INFORMATION TO USERS

This manuscript has been reproduced from the microfilm master. UMI films the text directly from the original or copy submitted. Thus, some thesis and dissertation copies are in typewriter face, while others may be from any type of computer printer.

The quality of this reproduction is dependent upon the quality of the copy submitted. Broken or indistinct print, colored or poor quality illustrations and photographs, print bleedthrough, substandard margins, and improper alignment can adversely affect reproduction.

In the unlikely event that the author did not send UMI a complete manuscript and there are missing pages, these will be noted. Also, if unauthorized copyright material had to be removed, a note will indicate the deletion.

Oversize materials (e.g., maps, drawings, charts) are reproduced by sectioning the original, beginning at the upper left-hand comer and continuing from left to right in equal sections with small overlaps. Each original is also photographed in one exposure and is included in reduced form at the back of the book.

Photographs included in the original manuscript have been reproduced xerographically in this copy. Higher quality 6" x 9" black and white photographic prints are available for any photographs or illustrations appearing in this copy for an additional charge. Contact UMI directly to order.



Bell & Howell Information and Learning 300 North Zeeb Road, Ann Arbor, Mi 48106-1346 USA 800-521-0600

	·		

DEVELOPMENT OF LAMINAR MORPHOLOGY IN SHEET EXTRUSION OF POLYMER BLENDS

by

Hamid Garmabi

A thesis submitted to the Faculty of Graduate Studies and Research
in partial fulfillment of the requirements of the degree of

Doctor of Philosophy

Department of Chemical Engineering

McGill University

Montreal, Quebec, Canada

December 1997

[©]Hamid Garmabi (1997)



National Library of Canada

Acquisitions and Bibliographic Services

395 Wellington Street Ottawa ON K1A 0N4 Canada Bibliothèque nationale du Canada

Acquisitions et services bibliographiques

395, rue Wellington Ottawa ON K1A 0N4 Canada

Your file Votre référence

Our file Notre référence

The author has granted a nonexclusive licence allowing the National Library of Canada to reproduce, loan, distribute or sell copies of this thesis in microform, paper or electronic formats.

The author retains ownership of the copyright in this thesis. Neither the thesis nor substantial extracts from it may be printed or otherwise reproduced without the author's permission.

L'auteur a accordé une licence non exclusive permettant à la Bibliothèque nationale du Canada de reproduire, prêter, distribuer ou vendre des copies de cette thèse sous la forme de microfiche/film, de reproduction sur papier ou sur format électronique.

L'auteur conserve la propriété du droit d'auteur qui protège cette thèse. Ni la thèse ni des extraits substantiels de celle-ci ne doivent être imprimés ou autrement reproduits sans son autorisation.

0-612-44435-X



To:

My parents, my wife, and my sons

ABSTRACT

The present work attempts to obtain deeper understanding of the development of laminar morphology in polymer blends and to optimize the production and properties of laminar polymer blends in ribbon extrusion. Studies of the microstructure of extruded ribbons of high density polyethylene (HDPE)/ polyamide-6 (PA-6) and polypropylene (PP) /ethylene vinyl alcohol copolymer (EVOH) blends have shown that it is possible to control the flowinduced morphology to generate thin, large and discontinuous overlapping platelets of PA-6 or EVOH dispersed phase in a HDPE or PP matrix phase, respectively. Such polymer blends are known as laminar polymer blends. The laminar blends of HDPE/PA-6 with only small amounts (20 wt%) of the barrier component, i.e. PA-6 resin, produced significant reduction (up to 45 times) in hydrocarbon permeability of extruded ribbons. The PP/EVOH laminar blends with 25 wt% of the barrier component, i.e. EVOH, yielded 10 times improvement in hydrocarbon permeability of the extruded ribbons. was achieved by optimizing material characteristics, processing conditions and flow field in the screw zone and in the die unit. In particular, an approach for controlling the mixing and melting steps in the screw zone was introduced, in order to maximize the size of melted particles of the dispersed phase upon entering the die unit. In the die region, extensional flow generated by incorporating converging and diverging sections in the die design, caused the large particles entering the die to be stretched in both directions (machine and transverse directions), thus, producing platelets in the plane of extrusion.

The effects of the following factors on morphology development and blend properties were considered and, when possible, manipulated to obtain large particles and deformations of dispersed phase particles: screw zone temperature profile, die temperature, screw design and configuration, composition, pre-compounding, die exit gap size, and cooling system. The influence of the rheology of the system, i.e. the viscosity and elasticity ratios of components, was studied and manipulated to obtain large deformations of dispersed phase particles. The effect of interfacial tension on the

morphology and barrier and mechanical properties was investigated and for the HDPE/PA-6 system, the interfacial tension was optimized by controlling the level of compatibilizer, in order to obtain maximum barrier and mechanical performance of the laminar blends. Pressure-Volume-Temperature (P-V-T) characteristics of the individual resins and blends of HDPE/PA-6 were studied, in order to calculate the interfacial tension values and other thermodynamic relationships for compatibilized and non-compatibilized blends of HDPE and PA-6. Various relationships were obtained for predicting the barrier and mechanical properties of the laminar blends from morphological data.

RESUMÉ

La présente étude tente de mieux comprendre le développement de la morphologie laminaire dans les mélanges de polymères et d'optimiser la production et les propriétés des mélanges laminaires de polymères dans le procédé d'extrusion de bandes. Différentes études de la microstructure de bandes extrudées de mélanges de polymères de polyéthylène haute densité (HDPE)/polyamide-6 (PA-6) et de polypropylène (PP)/éthylène vinyl alcool (EVOH) ont montré qu'il est possible de contrôler la morphologie induite par l'écoulement, afin de générer de minces, longues, discontinues et chevauchantes plaquettes de PA-6 ou EVOH respectivement dispersées dans une matrice de HDPE ou de PP. De tels mélanges de polymères sont connus sous le nom de mélanges laminaires de polymères. Les mélanges laminaires de HDPE/PA-6 avec de petites quantités de produits "barrières" (20% en poids), par exemple de la résine de PA-6, ont produit une réduction significative (jusqu'à 45 fois) de la perméabilité des bandes extrudées aux hydrocarbures. Ce résultat a été obtenu en optimisant les caractéristiques des matériaux, les conditions opératoires du procédé et le profil d'écoulement dans l'extrudeuse et dans la filière. Dans la filière, l'écoulement élongationnel obtenu en utilisant des sections convergentes et divergentes lors de la conception de la filière, a provoqué l'étirement des grosses particules entrant dans la filière suivant deux directions (axes machine et transversal), produisant donc les plaquettes dans le plan de l'extrusion.

Les effets des facteurs suivants sur le développement de la morphologie et les propriétés du mélange ont été considérés et, autant que possible manipulés afin d'obtenir de grosses particules et des déformations des particules des phases dispersées: profil de température dans l'extrudeuse, température de la filière, dimensionnement et configuration de la vis, composition, pré-mélange, dimension interne de la sortie de filière et système de refroidessement. L'influence de la rhéologie du système (viscosité et rapports d'élasticité de ses composantes) a été étudiée et manipulée dans le but d'obtenir d'importantes déformations des particules de la phase dispersée. L'effet de la

tension interfaciale sur la morphologie et les propriétés "barrières" et mécaniques ont été optimisées en contrôlant la quantité de compatibilisant afin d'obtenir une performance maximale barrière et mécanique des mélanges laminaires. Les caractéristiques Pression-Volume-Température (P-V-T) des résines et des mélanges de HDPE/PA-6 ont été étudiées afin de calculer les valeurs de tension interfaciale et d'autres relations thermodynamiques pour des mélanges de HDPE et PA-6 compatibilisés et non compatibilisés. Plusieurs relations ont été obtenues afin de prévoir les propriétés "barrières" et mécaniques des mélanges laminaires à partir de données morphologiques.

ACKNOWLEDGEMENT

There are many people who have contributed knowingly, or unknowingly, to the completion of this thesis. First of all, I would like to express my deep gratitude and sincere thanks to my research supervisor, Professor M. R. Kamal, for his guidance, support, encouragement, and for his contribution throughout the course of this project and preparation of this manuscript.

In addition, I would like to thank the following:

- The staff of the Chemical Engineering Department of McGill University who have contributed in their own way to the completion of this work.
- Messrs Alain Gagnon, Walter Greenland, Charles Dolan, Luciano Cusmich, Edward Siliauskas, Bill Habib, and Jean Dumont and Andy Krish who may have been forgotten, for their help in supplying, making and troubleshooting of the equipment.
- My colleagues in the Polymer Group including: Dr. Richard Lai-Fook, Dr. Furang Gao, Dr. Nicole Demarquette, Dr. Mehdi Rafizadeh, Dr. Mark Weber, Imad Ansari, Mazen Samara, Nadja Walling, Joachim Dehmel, Yalda Farhoudi, François Koran, Oi Wun Lee, Oscar Rodriguez, Tao Huang and Lei Wang for helpful discussions and for their friendship.
- The Natural Science and Engineering Research Council of Canada, Ministere de l'Education des Gouvernment du Quebec, Graduate Faculty of McGill University and Ministry of Culture and Higher Education of Islamic Republic of Iran for financial support.
- My parents for their continual and unlimited support throughout of my life as well as my parents-in-law for their support from so far away.

Finally, I would like to thank my wife, Dr. Farideh Bayan, for her understanding, encouragement, love, and unbelievable patience, who gave me the strength to finish this work; and last but not least, my little sons Ali and Mohammad, who were often neglected, because Daddy was busy.

Table of Contents

List of Figures	vii
List of Tables	xiv
Nomenclature	xv
CHAPTER 1 INTRODUCTION	1
CHAPTER 2 TECHNICAL BACKGROUND	4
2.1. Importance of Morphology Control in Immiscible Polymer Blends	4
2.2. Brief review of Theories of Microrheology of Emulsions	5
2.3. Experimental Studies of Drop Deformation in Emulsions	11
2.4. Drop Deformation and Morphology Development in Polymer Blends	13
2.5. Effect of Processing Conditions and Flow Field on Morphology	18
2.6. Droplet Coalescence and Compatibilizer Effect	21
2.7. Time Scale of Morphology Development in Polymer Blends	23
2.8. Development of Laminar Morphology in Polymer Blends	27
2.9. Summary and Conclusions	29
CHAPTER 3 SCOPE AND RESEARCH OBJECTIVES	31
2.1. Specific Research Objectives	31
CHAPTER 4 EXPERIMENTAL	33
4.1 Material Characterization	33
4.1.1 Materials	33
4.1.2 Rheological Measurements	34
4.1.2.1 Steady Shear Viscosity Measurements	35
4.1.2.2 Dynamic Measurements	36
4.1.3 Maleic Anhydride Content Determination	37
4.1.4 PVT Experiments	
4.1.4.1 Density Measurements at Room Temperature	
4.1.4.2 PVT Apparatus	38

4.1.4.3 Calibration Run	40
4.1.4.4 Experimental Procedure	41
4.1.4.5 LVDT Calibration	43
4.1.4.6 Method Used	43
4.1.5 Interfacial Tension Measurements	44
4.1.5.1. Pendant Drop Method	45
4.1.5.1.1 Theory	45
4.1.5.1.2 Experimental Assembly	47
4.1.5.1.3 Experimental Procedure	48
4.1.5.2 Spinning Drop Method	49
4.1.5.2.1 Theory	49
4.1.5.2.2 Experimental Apparatus	50
4.1.5.2.3 Experimental Procedure	52
4.1.5.2.4 Measurement of Optical Enlargement and Correction Factors	53
4.2 Processing	53
4.2.1 Processing Equipment	53
4.2.1.1 Twin-Screw Extruder	53
4.2.1.2 Single Screw Extruder	54
4.2.1.3 Die Unit	54
4.2.1.4 Take-off System	55
4.2.2 Processing Conditions	56
4.2.2.1 HDPE/PA-6	56
4.2.2.1.1 Single Screw Extrusion Using Dry Blends	56
4.2.2.1.2 Twin-Screw Compounding	57
4.2.2.2 PP/EVOH	60
4.3 Product Characterization	61
4.3.1 Microstructural Analysis	61
4.3.1.1 Sample Preparation	62
4.3.1.2 Scanning Electron Microscopy (SEM)	
4.3.1.3 Image Analysis	
4.3.2 Toluene Permeability Measurements	
4.3.2.1 Sample Preparation	

4.3.2.2	Toluene Permeability Setup	66
4.3.2.3	Calibration of the Apparatus	68
4.3.3 Oxy	gen Permeability Measurements	69
4.3.3.1	Sample Preparation	69
4.3.3.2	Oxygen Permeability Apparatus	70
4.3.4 High	h Speed Instrumented Impact Testing	70
CHAPTER 5	ANALYSIS OF MATERIAL PROPERTIES	74
5.1 Rheolog	gical Analysis	74
5.1.1 Stea	ndy Shear Viscosity	74
5.1.1.1	HDPE/PA-6 Blends	74
5.1.1.2	PP/EVOH Blends	78
5.1.2 Dyn	amic Measurements	80
5.1.2.1	HDPE/PA-6	80
5.1.2.2	PP/EVOH	82
5.2 Analysi	s of the PVT Behavior of Resins and Blends	84
5.2.1 Equ	ations of State	84
5.2.1.1	The Tait Equation	84
5.2.1.2	The Spencer-Gilmore Equation of State	87
5.2.2 HD	PE/PA-6 Blends	87
5.2.3 PP/I	EVOH Blends	100
5.3 Analysi	s of Interfacial Tension Results	105
5.3.1 Spir	nning Drop Results	105
5.3.1.1	PE/PA-6 System	105
5.3.1	.1.1 Density Measurements	105
5.3.1	.1.2 Measurement of the Optical Correction Factor	107
5.3.1	.1.3 Measurement of the Interfacial Tension of PE/PA-6 Pair	108
5.3.1	.1.4 Effect of Temperature	111
5.3.1	.1.5 Effect of the Maleation Content	111
5.3.1.2	PP/EVOH System	113
5.3.1	.2.1 Density Measurements	113
5.3.1	.2.2 Measurement of the Optical Correction Factor	114
5.3.1	.2.2 Measurement of Interfacial Tension of ADMER/EVOH Pair	116

5.3.	1.2.4 Effect of Temperature on Interfacial Tension	117
5.3.	1.2.5 Effect of Maleation Content on Interfacial Tension of PP/EVOH Pair	118
5.3.2 Eva	aluation of Spinning Drop Apparatus	119
5.3.3 Pre	diction of Interfacial Tension	121
CHAPTER 6	RESULTS AND DISCUSSION	. 123
6.1 Morph	ology of Blends	. 123
6.1.1 HD	PE/PA-6 Blends	123
6.1.1.1	Verification of Existence of Laminar Morphology	123
6.1.1.2	Variation of Microstructure across the Ribbon Thickness	125
6.1.1.3	Effect of Die Temperature on Morphology	128
6.1.1.4	Effect of Screw Zone Temperature on Morphology	129
6.1.1.5	Influence of Screw Design on Morphology	135
6.1.1.6	Effect of Die Exit Gap on Morphology	136
6.1.1.7	Effect of PA-6 Content on Morphology	140
6.1.1.8	Effect of Maleation Content on Morphology	143
6.1.1.9	Influence of Pre-compounding on Morphology	. 146
6.1.2 PP/	EVOH Blends	. 148
6.1.2.1	Variation of Microstructure across the Ribbon Thickness	. 148
6.1.2.2	Effect of Die Temperature on Morphology	. 152
6.1.2.3	Influence of Screw Design on Morphology	. 155
6.1.2.4	Influence of Low Temperature Screw Zone on Morphology	. 156
6.1.2.5	Effect of Die Exit Gap Size on Morphology	. 157
6.1.2.6	Effect of Cooling System on Morphology	. 159
6.2 Permea	bility Results	. 160
6.2.1 Tol	uene Permeability of HDPE/PA-6 Blends	. 162
6.2.1.1	Effect of Die Temperature on Permeability	. 162
6.2.1.2	Effect of Screw Temperature on Permeability	. 164
6.2.1.3	Influence of Screw Design on Permeability	. 165
6.2.1.4	Effect of Die Exit Gap Size on Barrier Performance	. 166
6.2.1.5	Influence of Composition on Permeability	. 168
6.2.1.6	Influence of MAH Content of PE on Permeability	. 169
6217	Effect of Pre-compounding on Permeability	170

6.2.1.8	Effect of Screw Speed on Permeability	171
6.2.1.9	Influence of Adapter Angle on Permeability	172
6.2.2. Per	meability of ADMER/EVOH Blends	173
6.2.2.1.	Effect of Die Temperature on Permeability	173
6.2.2.2.	Influence of Screw Design on Permeability	174
6.2.2.3.	Influence of Die Exit Gap Size on Permeability	175
6.2.2.4.	Influence of Cooling System on Permeability	177
6.2.3. Co	mparison of Permeability Results of HDPE/PA-6 Blends with Predi	ctions of
Th	eoretical Models	177
6.2.3.1.	HDPE/PA-6 Blends	180
6.2.3	.1.1. Toluene Permeability of HDPE/PA-6 Blends	180
6.2.3	.1.2. Oxygen Permeability of HDPE/PA-6 Blends	181
6.2.3.2.	ADMER/EVOH Blends	181
6.2.3	2.1. Toluene Permeability of ADMER/EVOH Blends	181
6.2.3	.2.2. Oxygen Permeability of ADMER/EVOH Blends	183
62 Evolue	time Mark suited Deuferman of Disards	101
o.s. Evalua	ting Mechanical Performance of Blends	104
	oact Strength of HDPE/PA-6 Blends	
6.3.1. Im		185
6.3.1. Imp	oact Strength of HDPE/PA-6 Blends	185 185
6.3.1. Imp 6.3.1.1. 6.3.1.2.	Dact Strength of HDPE/PA-6 Blends	185 185 187
6.3.1.1. 6.3.1.2. 6.3.1.3.	Influence of Die Temperature Effect of Screw Design and Screw Zone Temperature	185 185 187
6.3.1.1. 6.3.1.2. 6.3.1.3. 6.3.1.4.	Influence of Die Temperature Effect of Screw Design and Screw Zone Temperature Influence of MAH Content of PE on Impact Properties	185 185 187 189
6.3.1.1. 6.3.1.2. 6.3.1.3. 6.3.1.4. 6.3.1.5.	Influence of Die Temperature Effect of Screw Design and Screw Zone Temperature Influence of MAH Content of PE on Impact Properties Effect of Pre-compounding on Impact Properties of PE/PA-6 Blends	185 185 187 189 192
6.3.1. Imp 6.3.1.1. 6.3.1.2. 6.3.1.3. 6.3.1.4. 6.3.1.5. 6.3.1.6.	Influence of Die Temperature Effect of Screw Design and Screw Zone Temperature Influence of MAH Content of PE on Impact Properties Effect of Pre-compounding on Impact Properties of PE/PA-6 Blends Influence of PA-6 Content on Impact Properties of PE/PA-6 Blends	185 187 189 189 192
6.3.1. Imp 6.3.1.1. 6.3.1.2. 6.3.1.3. 6.3.1.4. 6.3.1.5. 6.3.1.6. 6.3.1.7.	Influence of Die Temperature Effect of Screw Design and Screw Zone Temperature Influence of MAH Content of PE on Impact Properties Effect of Pre-compounding on Impact Properties of PE/PA-6 Blends Influence of PA-6 Content on Impact Properties of PE/PA-6 Blends Effect of Screw Speed on Impact Properties of PE/PA-6 Blends	185 187 189 192 193
6.3.1. Imp 6.3.1.1. 6.3.1.2. 6.3.1.3. 6.3.1.4. 6.3.1.5. 6.3.1.6. 6.3.1.7. 6.3.2. Imp	Influence of Die Temperature Effect of Screw Design and Screw Zone Temperature Influence of MAH Content of PE on Impact Properties Effect of Pre-compounding on Impact Properties of PE/PA-6 Blends Influence of PA-6 Content on Impact Properties of PE/PA-6 Blends Effect of Screw Speed on Impact Properties of PE/PA-6 Blends Influence of Adapter Angle on Impact Properties of PE/PA-6 Blends	185 187 189 192 193 193
6.3.1. Imp 6.3.1.1. 6.3.1.2. 6.3.1.3. 6.3.1.4. 6.3.1.5. 6.3.1.6. 6.3.1.7. 6.3.2. Imp 6.3.2.1.	Influence of Die Temperature Effect of Screw Design and Screw Zone Temperature Influence of MAH Content of PE on Impact Properties Effect of Pre-compounding on Impact Properties of PE/PA-6 Blends Influence of PA-6 Content on Impact Properties of PE/PA-6 Blends Effect of Screw Speed on Impact Properties of PE/PA-6 Blends Influence of Adapter Angle on Impact Properties of PE/PA-6 Blends Influence of Adapter Angle on Impact Properties of PE/PA-6 Blends Strength of ADMER/EVOH Blends	185 187 189 192 193 193 194
6.3.1. Imp 6.3.1.1. 6.3.1.2. 6.3.1.3. 6.3.1.4. 6.3.1.5. 6.3.1.6. 6.3.1.7. 6.3.2. Imp 6.3.2.1. 6.3.2.2.	Influence of Die Temperature Effect of Screw Design and Screw Zone Temperature Influence of MAH Content of PE on Impact Properties Effect of Pre-compounding on Impact Properties of PE/PA-6 Blends Influence of PA-6 Content on Impact Properties of PE/PA-6 Blends Effect of Screw Speed on Impact Properties of PE/PA-6 Blends Influence of Adapter Angle on Impact Properties of PE/PA-6 Blends Influence of Adapter Angle on Impact Properties of PE/PA-6 Blends Effect of Die Temperature at Various Compositions	185 187 189 192 193 194 195
6.3.1. Imp 6.3.1.1. 6.3.1.2. 6.3.1.3. 6.3.1.4. 6.3.1.5. 6.3.1.6. 6.3.1.7. 6.3.2. Imp 6.3.2.1. 6.3.2.2. 6.3.2.3.	Influence of Die Temperature Effect of Screw Design and Screw Zone Temperature Influence of MAH Content of PE on Impact Properties Effect of Pre-compounding on Impact Properties of PE/PA-6 Blends Influence of PA-6 Content on Impact Properties of PE/PA-6 Blends Effect of Screw Speed on Impact Properties of PE/PA-6 Blends Influence of Adapter Angle on Impact Properties of PE/PA-6 Blends Influence of Adapter Angle on Impact Properties of PE/PA-6 Blends Effect of Die Temperature at Various Compositions Influence of Screw Design at Different Die Temperatures	185 187 189 192 193 194 195 198
6.3.1. Imp 6.3.1.1. 6.3.1.2. 6.3.1.3. 6.3.1.4. 6.3.1.5. 6.3.1.6. 6.3.1.7. 6.3.2. Imp 6.3.2.1. 6.3.2.2. 6.3.2.3. 6.3.2.4.	Influence of Die Temperature Effect of Screw Design and Screw Zone Temperature Influence of MAH Content of PE on Impact Properties Effect of Pre-compounding on Impact Properties of PE/PA-6 Blends Influence of PA-6 Content on Impact Properties of PE/PA-6 Blends Effect of Screw Speed on Impact Properties of PE/PA-6 Blends Influence of Adapter Angle on Impact Properties of PE/PA-6 Blends Effect of Die Temperature at Various Compositions Influence of Screw Design at Different Die Temperatures Effect of Cooling System on Impact Properties	185 187 189 192 193 194 195 195 198
6.3.1. Imp 6.3.1.1. 6.3.1.2. 6.3.1.3. 6.3.1.4. 6.3.1.5. 6.3.1.6. 6.3.1.7. 6.3.2. Imp 6.3.2.1. 6.3.2.2. 6.3.2.3. 6.3.2.4. 6.4. Theore	Influence of Die Temperature Effect of Screw Design and Screw Zone Temperature Influence of MAH Content of PE on Impact Properties Effect of Pre-compounding on Impact Properties of PE/PA-6 Blends Influence of PA-6 Content on Impact Properties of PE/PA-6 Blends Effect of Screw Speed on Impact Properties of PE/PA-6 Blends Influence of Adapter Angle on Impact Properties of PE/PA-6 Blends Influence of Adapter Angle on Impact Properties of PE/PA-6 Blends Effect of Die Temperature at Various Compositions Influence of Screw Design at Different Die Temperatures Effect of Cooling System on Impact Properties Influence of EVOH Content at Low Screw Temperature	185 187 189 192 193 194 195 198 198 198

			
СНАРТЕ	R 7	CONCLUSIONS AND RECOMMENDATIONS	209
7.1. C	onclu	sions	210
7.2. R	.ecom	mendation for Future Work	212
7.3. O	rigina	l Contributions	213
REFREN	CES.		215
Append	lix A	Detailed Design of Screw and Barrel of the Single Screw Extruder	I
Append	lix B	Sample Codes and Processing Conditions	V
Append	lix C	Error Analysis of Experimental Measurements	XI
Append	lix D	Normalization Procedure for Impact Tests	XVII
Append	lix E	Calculation of Shear Rates in Different Parts of the Die	.XXI
Append	lix F	Typical Load-Displacement Curves of Individual Resins and Blends	. XVI

List of Figures

2.1 :	Sinusoidally disturbed thread with definitions of R0, R, A, and A
2.2 :	Transition in the phase morphology type: from dispersed (left) to the stratified (right)
	induced by the change in sign of the principal normal stress difference
2.3 :	Dimensionless master curve of κ versus λ for the melt extrusion using a co-rotating
	twin screw extruder
2.4:	Dimensionless master curve of κ^{\bullet} versus viscosity ratio $(\eta_{r}^{\bullet} = \eta J \eta_{m})$ and dispersed
	phase concentration (φ_d) for PE/PA blends for a wide range of mixing conditions
	(G: shear rate, T: temperature) and dispersed phase concentration
2.5 :	Schematic of the droplet deformation process that would occur in the entrance and
	fully developed regions
2.6 :	Down-channel variations in the striation thickness (polystyrene/styrene-butadiene
	copolymer) a) lower film b) upper film
2. 7:	Schematic of dispersion of the minor phase during blending showing the transition
	from pellets to droplets
2.8 :	Number and weight average dispersed phase size as a function of position along the
	screw axis for PE/PA-6 without and with 5 phr of MASEBS (104)
2.9 :	Permeability (weight loss, g) as a function of nylon concentration, in laminar-walled
	containers
2.10 :	Comparison of measured oxygen transmission rates with model predictions for
	MAPP2/EVOH blends system, 1 Homogeneous blends, 2- — Co-extruded
	materials
4.1 :	Schematic drawing of the PVT apparatus
4.2 :	Pendant drop geometry46
4.3 :	Experimental assembly for pendant drop apparatus
4.4 :	Schematic of an elongated spinning drop
4.5 :	Schematic of the spinning drop apparatus
4.6:	Schematic of the die unit 55

4.7: Optimized screw configuration for twin-screw compounding of HDPE/ PA-6
blends
4.8: Alternative sequences of compounding and extrusion for HDPE/PA-6 blends 60
4.9: Locations of sampling for SEM and image analysis
4.10: Schematic of the toluene permeability measurements setup
4.11: Diagram of the coulumetric system used in measurements of oxygen permeability
coefficient71
4.12: Idealized deformation stages and transitions for impact testing using RIT-8000 73
5.1: Steady shear viscosity vs. shear rate for PE0 resin at different temperatures 75
5.2: Steady shear viscosity vs. shear rate for PE1 resin at different temperatures 75
5.3: Steady shear viscosity vs. shear rate for PE2 resin at different temperatures 76
5.4: Steady shear viscosity vs. shear rate for PA-6 resin at different temperatures 76
5.5: Viscosity ratio of PA-6/PE vs. shear rate at different temperatures
5.6: Steady shear viscosity vs. shear rate for ADMER and EVOH at 200 and 230 °C 79
5.7: Viscosity ratio of EVOH /ADMER vs. shear rate at different temperatures 79
5.8: Shear storage modulus for PE0, PE2, PA-6 resins and PE0/PE2/PA-6 blend at two
temperatures of 250 and 270 °C
5.9: Complex viscosity, $/\eta^*/$, vs. frequency for PE0, PE2, PA-6 resins and PE0/PE2/PA-
6 (60/20/20) blend at temperatures of 250 and 270 °C
5.10: Shear storage modulus of ADMER and EVOH at two temperatures of 200 and
230℃85
5.11: Specific volume of HDPE/PA-6 (80/20 wt%) blend at room temperature vs. MAH
content (wt%) of HDPE
5.12: Melt specific volume of resins and blends versus temperature at atmospheric
pressure
5.13: Crossplotted isobars of PE0 resin along with predictions of the Tait equation 93
5.14: Comparison of the experimental isotherms with predictions of Tait equation for PEO
Resin
5.15: Crossplotted isobars of PA-6 resin along with predictions of the Spencer-Gilmore
equation of state

5.16: Comparison of the experimental isotherms with predictions of Spencer-Gilmore
equation of state for PA-6 resin96
5.17: Comparison of the experimental isotherms with predictions of Tait equation of state
for PE0/PA-6 (80/20 wt%) blend
5.18: Comparison of the experimental isotherms with predictions of Tait Equation of state
for PE0/PE2/PA-6 (70/10/20 wt%) blend
5.19: Comparison of the experimental isotherms with predictions of Tait equation of state
for PE0/PE2/PA-6 (60/20/20 wt%) blend
5.20: Comparison of the experimental isotherms with predictions of Tait equation of state
for PE0/PE2/PA-6 (40/40/20 wt%) blend
5.21: Comparison of the experimental isotherms with predictions of Tait equation of state
for PE2/PA-6 (80/20 wt%) blend
5.22: Melt specific volume of ADMER and EVOH resins versus temperature at
atmospheric pressure
5.23: Cross-plotted isobars of ADMER resin along with predictions of Tait equation of
state
5.24: Comparison of the experimental isotherms with predictions of Tait equation of state
for ADMER resin
5.25: Cross-plotted isobars of EVOH resin along with predictions of Tait equation of
state
5.26: Comparison of the experimental isotherms with predictions of Tait equation of state
for EVOH resin104
5.27: Melt densities of PE0 and PA-6 resins vs. temperature at atmospheric pressure along
with the difference in melt densities
5.28: Optical correction factor (n) vs. temperature for PA-6 resin
5.29: Evolution of the radius of a drop of PE in PA-6 at 250 ℃
5.30: Interfacial tension between PE and PA-6 as a function of temperature
5.31: Interfacial tension between PE and PA-6 as a function of MAH content (wt.%) of
DE at 250 9°

5.32 :	Melt densities of ADMER and EVOH resins vs. temperature at atmospheric pressure
	along with the difference in melt densities
5.33:	Optical correction factor (n) vs. temperature for EVOH resin
5.34:	Evolution of radius of a drop of ADMER-PP(50-50) in EVOH at 220 ℃
5.35 :	Interfacial tension between ADMER and EVOH as a function of temperature 117
5.36 :	Interfacial tension between PP and EVOH as a function of MAH Content (wt.%) of
	PP at 220 ℃
5.3 7:	Comparing the interfacial tension between PE and PA-6 as a function of temperature
	using the spinning drop and pendant drop methods
6.1 :	Morphology of extruded ribbons of PE0/PE2/PA-6 (70/10/20 wt%) blend in 4
	locations indicated in 4.10
6.2 :	Variation of morphology of HDPE/PA-6 blends across the thickness of extruded
	ribbon (longitudinal), a- X151T012 b- X143702 c- X1537012
6.3 :	Variation of cross section area (length × thickness) and aspect ratio across the ribbon
	thickness for PE/PA-6 blends
6.4 :	SEM micrographs of PE0/PA-6 (80/20 wt%) blends showing the effect of die
	temperature on morphology. a- X133702 b- X143702
6.5 :	Effect of die temperature on the aspect ratio and cross section area of dispersed
	phase particles for PE0/PA-6 (80-/20 wt%) blend
6.6 :	SEM micrographs of PE0/PE2/PA-6 (70/10/20 wt%) blends showing the effect of
	screw zone temperature on morphology: a- X1537012 b- X1037012
	c-X1337012
6.7 :	Effect of screw zone temperature on the aspect ratio and cross section area of
	dispersed phase particles for PE0/PE2/PA-6 (70/10/20 wt%) blend
6.8 :	SEM micrographs of PE0/PE2/PA-6 (70/10/20 wt.%) blends showing the effect of
•	screw design on morphology. a- mixing screw b- metering screw
6.9 :	Effect of screw design on the aspect ratio and cross section area of dispersed phase
	particles for PE0/PE2/PA-6 (70/10/20 wt%) blend
610:	SEM micrographs of PE0/PA-6 (80/20 wt.%) blends showing the effect of die exit
	gap size on morphology. a- X133702 (1.0 mm) b-X533702 (0.5 mm)

6.11: Effect of die exit gap size on the aspect ratio and cross section area of dispersed
phase particles for PE0/PA-6 (80/20 wt%) blend
6.12: SEM micrographs of PE0/PE2/PA-6 blends showing the effect of PA-6 content on
morphology. a- X1537011 (78.6/11.4/10 wt%) b-X1537012 (70/10/20 wt%) 140
6.13: Effect of PA-6 content on the aspect ratio and cross section area of dispersed phase
particles for PE0/PE2/PA-6 blends
6.14: SEM micrographs showing effect of maleation content of PE on the morphology of
PE0/PE2/PA-6 blends. a- 80/0/20 wt% b-75/5/20 wt% (MAH content 0.007
wt%) c- 70/10/20 wt% (MAH content 0.014) d- 60/20/20 wt% (MAH content
0.028)144
6.15: Effect of maleation content of PE and pre-compounding on the aspect ratio and area
of dispersed phase particles for PE0/PE2/PA-6 blends
6.16:SEM micrographs showing effect of pre-compounding on the morphology of
PE0/PE2/PA-6 (70/10/20 wt%) blends. a- dry-blending b- PE0 and PE2 were pre-
mixed c- PE0, PE2, and PA-6 were pre-mixed in one pass d- PE0,PE2, and PA-6
were pre-mixed in two passes
6.17:Distribution of cross section area for SEM micrographs of 6.16 showing the effect of
pre-compounding on particle size of PE0/PE2/PA-6 (70/10/20 wt%) blends. a-
dry-blending b- PE0 and PE2 were pre-mixed c- PE0, PE2, and PA-6 were pre-
mixed in one pass d- PE0,PE2, and PA-6 were pre-mixed in two passes 149
6.18: SEM micrograph of ADMER/EVOH (75/25wt%) blend showing the variation of
morphology across the thickness of extruded ribbon
6.19: Variations of cross section area and aspect ratio across the ribbon thickness for
ADMER/EVOH (75/25 wt.%) blend
6.20: SEM micrographs of ADMER/EVOH (75/25 wt.%) blends showing the effect of die
temperature on morphology: a- 215 ℃ b- 225 ℃ c- 230 ℃
6.21: Effect of die temperature on the aspect ratio and area of dispersed phase particles for
ADMER/EVOH (75/25 wt%) blends
6.22: SEM micrographs showing effect of screw design on the morphology of
ADMER/EVOH (75/25 wt%) a- mixing screw b- metering screw

6.23: SEM micrograph of ADMER/EVOH (75/25wt%) blend showing the microstructure
obtained at low temperature screw zone
6.24: SEM micrographs showing effect of die exit gap size on the morphology of
ADMER/EVOH (70/30 wt%) blends. a- 0.25 mm b- 0.5 mm
6.25: Effect of die exit gap size on the aspect ratio and area of dispersed phase particles
for ADMER/EVOH (70/30 wt%) blends
6.26: SEM micrographs showing effect of cooling system on the morphology of
ADMER/EVOH (70/30 wt%) blends. a- air cooling b- water cooling 160
6.27: Effect of die temperature on toluene permeability of PE/PA-6 (80/20 wt%) blends.
6.28:Effect of screw zone temperature on toluene permeability of PEO/PE2/PA-6
(70/10/20 wt%) blends
6.29: Influence of screw design on toluene permeability of PE/PE2/PA-6 (70/10/20 wt%)
blends
6.30: Effect of die exit gap size on toluene permeability of PEO/PE2/PA-6 (70/10/20 wt%)
blends
6.31: Effect of PA-6 content on toluene permeability of HDPE/PA-6 laminar blends 168
6.32:Effect of maleation content and pre-compounding on toluene permeability of
PE0/PE2/PA-6 (70/10/20 wt%) blends extruded at low screw zone temperature. 170
6.33: Effect of RPM on toluene permeability of PEO/PA-6 (80/20 wt%) laminar blends 172
6.34: Effect of die temperature on toluene permeability of ADMER/EVOH (75/25 wt%)
blends
6.35: Influence of screw design on barrier performance of ADMER/EVOH blends 175
6.36: Influence of die exit gap size on barrier performance of ADMER/EVOH (70/30
wt%) blends
6.37: Influence of cooling system on barrier performance of ADMER/EVOH (70/30 wt%)
blends
6.38: Variation of toluene permeability with respect to PA-6 content along with Maxwell
and Series model predictions for HDPE/PA-6 blends

6.39: Variation of oxygen permeability with respect to PA-6 content along with Maxwell
and Series model predictions for HDPE/PA-6 blends
6.40: Variation of toluene permeability with respect to EVOH content along with Maxwell
and Series model predictions for ADMER/EVOH blends
6.41: Variation of oxygen permeability with respect to EVOH content along with Maxwell
and Series model predictions for ADMER/EVOH blends
6.42: Influence of die temperature on ultimate force and energy of PE/PA-6 blends 186
6.43: Variations of ultimate force and energy versus screw design and screw zone
temperature for PE0/PE2//PA-6 (70/10/20 wt%) blends
6.44: Influence of MAH content and pre-compounding on ultimate force and energy for
HDPE/PA-6 blends 190
6.45: Variation of ultimate force and energy versus PA-6 content for HDPE/PA-6
blends
6.46: Variation of ultimate force and energy versus Screw Speed for HDPE/PA-6
blends
6.47: Variation of ultimate energy and force versus die temperature for various
compositions of ADMER/EVOH blends
6.48: Variation of ultimate energy and force versus die temperature for various screw
designs for ADMER/EVOH (75/25 wt%) blends
6.49: Variation of ultimate energy and force versus cooling systems for ADMER/EVOH
(75/25 wt%) blends
6.50: Variation of ultimate energy and force versus EVOH content for ADMER/EVOH
blends extruded at low screw zone temperature
A1: Detailed Design of Metering Screw (C. W. Brabender Instruments Inc)
A2: Detailed Design of Mixing Screw (C. W. Brabender Instruments Inc)
A3: Heating/cooling Collar Design (C. W. Brabender Instruments Inc)
D1: Normalization curves for ultimate energy and ultimate force for PE0XIX
D2: Normalization curves for ultimate energy and ultimate force for PE0/PE2/PA-6
(60/20/20 wt%) blend

List of Tables

4.1 :	Typical Properties of the Resins as Supplied by the Manufacturers
4.2 :	Properties of Resins (measured in this study)
4.3 :]	Processing Conditions for HDPE/PA-6 Blends: Single Screw Extrusion
4.4 :	Processing Conditions for PP/EVOH System: Single Screw Extrusion
4. 5:	Outlet Pressure and Related Flows for Different Gases:
5. 1:	Coefficients of Tait Equation and Spencer-Gilmore Equation of States for Individual
	Resins: 90
5.2 :	Coefficients of Tait Equation of States for PE0/PE2/PA-6 Blends
5.3 : (Coefficients of Tait Equation of State for ADMER and EVOH:
6.1 : '	Toluene and Oxygen Permeability of Individual Resins
6.2 :	Comparison Between "f" Shape Factors Obtained From Equations (6.10) and (6.11)
	for HDPE/PA-6 Blends
6.3 :	Comparison Between "f" Shape Factors Obtained From Equations (6.10) and (6.11)
	for ADMER/EVOH Blends. 205
6.4 :	Comparison Between Predicted and Measured Elastic Modulus for PE0/PE2/PA-6
	(70/10/20 wt%) Blends
B1 : l	Processing Conditions Used for Extruding HDPE/PA-6 Blends:V
B2 : 1	Processing Conditions Used for Extruding ADMER/EVOH Blends:IX
E.1 :	Rabinowitsch Correction for PE and PA-6 ResinsXXII
E 2.	Estimated Shear Rates in Different Parts of the Die Unit XXIII

Nomenclature

Roman Letters

A	Total area of the particles
A	Area of the bellows in PVT apparatus
A	Amplitude of sinusoidal distortion
A	Area of the sample under permeability test
a	Drop diameter
a	Radius of the curvature of the pendant drop at the apex
a _i	Area of the i th particle
A_0	Amplitude of sinusoidal distortion at t=0
ā	Number average area of particles
− a _w	Weighted average area of particles
В	Drop width
В	Dimensionless quantity given by Equation (4.5)
В	Tait parameter
B ₀	Pre-exponential factor in Tait equation
ס	Rabinowitsch factor
С	Constant in Tait equation
D	Effective diffusion
D	Drop deformation
d	Diameter of the spinning drop
d*	Equilibrium drop diameter
d _{app}	Apparent diameter of drop or rod
d_{rod}	Actual diameter of the rod in spinning drop
E	Activation energy
E _{DK}	Macroscopic bulk breaking energy
EVA	Ethylene vinyl acetate
EVOH	Ethylene vinyl alcohol
E _c	Modulus of composite
$E_{\mathbf{f}}$	Modulus of flake
E_{m}	Modulus of matrix
EP	Ethylene-propylene terpolymer
F	Flow rate
f	Calibration factor

f Shape factor

GC Gas chromatograph
Gm Matrix shear modulus
G' Storage modulus

G'_m Storage modulus of matrix

G'_d Storage modulus of dispersed phase

G' Loss modulus
G* Complex modulus

g Gravitational acceleration

HDPE High density polyethylene

h_c Critical separation distance

J_D A constant in Equation (4.9)

K Factor includes the origins of weakening of composite

K Isothermal compressibility factor

L Length of the drop

L Deflection of the LVDT in PVT apparatus

LDPE Low density polyethylene

LVDT Linear variable differential transducer

M Maleation content

MRF Modulus reduction factor

MAH Maleic anhydride

m Parameter in Equation (5.20)
N Total number of particles

Nl_d First normal stress difference of dispersed phase

N₁ First normal stress difference of matrix

n Power law index
n Refractive index

P Viscosity ratio of zero shear viscosity of the dispersed phase and matrix

P Toluene permeability coefficient factor

PP Polypropylene

PAB Polymer alloys and blends

PA-6 Polyamide-6

PET Polyethyleneterephetalate

PS Polystyrene

PPO Polyphenylene oxide

PVT Pressure-volume- temperature

P_c Permeability of blend or composite

P_m Permeability of matrix

P_d Permeability of dispersed phase

pr Probability factor
Po Pre-exponential factor
q Toluene permeability rate
q Exponent of Equation (2.5)
R Universal gas constant

R₀ Diameter of the thread

R₂^{max} Drop curvature in the longitudinal direction taken at the point of maximum

width

Radius of curvature of the pendant drop
 Other radius of curvature of the pendant drop

R₀ Initial diameter of the spinning drop

 R_{∞} Equilibrium diameter of the spinning drop R_d Diameter of the die in capillary rheometry R_b Diameter of the barrel in capillary rheometry

RPM Rotation per minute
S Solubility factor

SBS Styrene-butadiene-styrene
SEM Scanning electron microscopy

S.W. Self wiping element S.E. Simple element

T Thickness of the drop

T Temperature

T_m Crystallization temperature

T⁰_m Crystallization temperature at zero pressure

t Thickness of the sample

t_c Coalescence or coagulation time

t Time

V Specific volume V^E Excess volume

V_b Specific volume of the blendV_f Volume fraction of the flake

V_E Extrusion speed in capillary rheometry
V_{init} Initialization volume in PVT studies

W Width of the drop wi Weight fraction

Greek Letters

α	Thermal expansion factor
α	Aspect ratio
α_0	Zero-pressure thermal expansion factor
$\bar{\alpha}$	Number average aspect ratio
$\bar{\alpha}_{w}$	Weighted average aspect ratio
β	Constant in equation (5.12)
β_m , β_d , β_c	Exponents as defined in Equation (2.10)
γ	Interfacial tension
·	Shear rate
γd	Strain rate for drop
γ _m	Strain rate for matrix
γο	Interfacial tension for a system with no maleation
γ _∞	Interfacial tension for highly maleated system
γм	Interfacial tension for a system with maleation content of M
γi	Interfacial tension of ith component
ΔΡ	Pressure drop
ΔV_{m}	Volume change during crystallization
$\Delta H_{\mathfrak{m}}$	Enthalpy change during crystallization
ΔG_{m}	Free energy of mixing
$\Delta S^{(e)}$	Excess energy of mixing
Δρ	Density difference
3	Elongation strain
ξ	Parameter in Equation (6.1)
$\eta_{\mathfrak{m}}$	Viscosity of matrix
η_d	Viscosity of dispersed phase
η*.	Modified viscosity ratio
η_b	Viscosity of blend
η	Complex viscosity
κ	Capillary number
κ*	Modified capillary number
Λ	Distortion wave length of thread
Λ	A parameter in Equation (6.13) indicating the adhesion
λ	Viscosity ratio
λ_d	Cauchy strain
ν	Interfacial tension

v_{dm} Interfacial tension in flow

v°_{dm} Interfacial tension in quiescent flow

 ρ Density τ Tortuosity

τ_w Shear stress at wall

τ_m Relaxation time of matrix

 τ_d Relaxation time of dispersed phase

 τ_1 Relaxation time as defined in Equation (2.9)

 ϕ Angle between the axis and R_1 in pendant drop geometry

 ϕ_d Volume fraction of dispersed phase

 ϕ_m Volume fraction of matrix

X^P Polarity

Ω Tabulated function in Equation (2.6)ω Rotational speed in spinning drop

CHAPTER 1

INTRODUCTION

Polymer blends are defined as mixtures of at least two polymeric components containing a minimum of 2 wt% of each component (1). Many polymeric materials of current industrial significance are polymer blends. The rise in use of polymer blends during the past two decades has been remarkable, and currently polymer alloys and blends, PAB, constitute over 30 wt% of polymer consumption (2). Polymer alloys and blends, represent a dynamic domain of plastic research and industrial applications. While synthesis of new polymers was the major focus in the early phase of plastics industry, emphasis has shifted to blending of existing polymers, because blending can usually be implemented more rapidly and economically than the development of new chemistry

Plastics continue to expand into food packaging applications traditionally served by metal and glass products. Melt-fabricated plastic articles with good solvent and vapour barrier properties offer a variety of advantages in comparison to metals and glass for use in applications such as packaging, gasoline tanks and even fuel pipeline systems for passenger cars (3-5). These advantages include light weight, flexibility, low cost and recyclability (6). One of the most important requirements for the use of plastics in packaging or gasoline tanks is impermeability to gases and hydrocarbons. Mechanical properties should also meet product specifications, especially impact properties. In most cases, one polymeric material cannot offer all the properties required; therefore a combination of polymers, i.e. polymer blends, is employed.

Currently, plastic containers with high-barrier properties are produced with a multilayer structure using co-extrusion technology (7-9). Co-extrusion is the simultaneous extrusion from a single die of two or more homogeneous melts, which form a lamellar structure. Coextruded materials incorporate layers of a barrier polymer like ethylene vinyl alcohol (EVOH) copolymer and a low cost polymer such as polypropylene. This technology, however, requires high capital and complex control, and presents recyclability limitations. However, a variety of other technologies have been developed to give enhanced barrier properties to plastic materials, e.g., surface modification by treatment with highly oxidizing gases and metallizing (10-12). Recently, a new approach employing immiscible polymer blends to improve solvent and gas barrier properties of plastic products has been introduced (13-28). Combination of a thermoplastic barrier material with a lower cost matrix material which then could be processed in a single step operation, if feasible, could offer process versatility and low product cost. Transformation of the spherical particles of dispersed phase in polymer blends into laminar morphology may have significant effect on the diffusion of gases and hydrocarbons through films (13-21) and container walls (22-28).

Immiscibility is an important criterion for selecting the components of barrier polymer blends. If the blend components are miscible, only minor improvement of barrier properties might be attained. Tailoring immiscible blends to achieve specific characteristics requires, among other things, control over the morphology or the spatial arrangement of the phases and the stability of these arrangements, once formed. Dispersed, fibrillar, co-continuous phases (interpenetrating networks) and stratified (laminar) are the main morphological types. The first three types of morphology provide average barrier properties, while laminar morphology leads to outstanding barrier properties. Controlling the morphology of immiscible polymer blends to achieve specific properties, needs knowledge of the parameters that affect morphology development. Among them, viscosity ratio, interfacial tension and elasticity ratio, are the most important material characteristics that affect the morphology. On the other hand, processing parameters such as temperature, shear stress/strain, flow field, and residence time affect the morphology of polymer blends substantially. It is also necessary to understand the mechanism behind the transition of the dispersed phase from the initial pellets to submicron size droplets.

This work evaluates the influence of the above parameters on the development of laminar blends with barrier properties comparable to co-extruded materials during ribbon extrusion of high density polyethylene-polyamide 6 (HDPE/PA-6) and polypropylene-ethylene

vinyl alcohol copolymer (PP/EVOH) blends. In particular, it proposes an approach based on controlling temperature to delay the melting of the dispersed phase in combination with special die design. The product exhibits substantial improvement in barrier properties of the blends, especially for the HDPE/PA-6 system. Optimizing the maleation level of high density polyethylene provides good mechanical performance for HDPE/PA-6 blends. The effect of pre-compounding in a twin-screw extruder on the mechanical and barrier properties of these blends is also reported and discussed. Previous research (19) has been used to select the optimum level of maleation content for the polypropylene resin. The above observations regarding the barrier and mechanical properties are supported by morphological studies and image analysis.

In order to understand and quantify the relationships between the processing conditions and product characteristics, particularly permeability and mechanical properties, it was necessary to obtain data regarding some of fundamental properties of the polymers in the blend. Interfacial tension, barrier and mechanical properties were measured for both systems. The influence of maleation content of the matrix and the effect of temperature on the interfacial tension were evaluated. As melt densities of resins are needed for interfacial tension calculations, the pressure-volume-temperature (PVT) behaviour of individual resins and of HDPE/PA-6 blends was evaluated.

CHAPTER 2

TECHNICAL BACKGROUND

2.1. Importance of Morphology control in immiscible Polymer blends

The rules governing miscibility or immiscibility of polymer blends are best understood through a thermodynamic approach by using the Gibbs free energy of mixing, ΔG_m . Free energy of mixing can vary with composition in different ways. Complete and stable miscibility exists only if $\Delta G_m < 0$ (29, 30), where ΔG_m is the free energy of mixing. These studies have profound consequences regarding the general miscibility of polymer blends, since they suggest that $\Delta G_m < 0$ only when $\Delta H_m < 0$ or $\Delta S^{(e)} > 0$, where ΔH_m and $\Delta S^{(e)}$ are enthalpy and excess entropy of mixing, respectively. Since mixing of polymers is generally endothermic ($\Delta H_m > 0$) and excess entropy is too small to result in a negative free energy of mixing, polymer binaries are most often immiscible. This is not a restriction in many applications, because miscibility is neither required nor desired. Immiscible polymer blends are providing new materials, and in some applications such as rubber toughening and barrier polymer blends, immiscibility is essential.

Adapting immiscible polymer blends to fulfill specific final properties requires, among other things, control over the flow induced morphology during melt processing and the stability of microstructure, once formed. The morphology of immiscible polymer blends depends on various parameters including material, processing, and flow field variables. The main morphological types are dispersed, co-continuous (interpenetrating networks), fibrillar, and laminar morphologies. The first three types of morphology result in "average" barrier properties and reduction of permeability. Even with substantial volume fraction of the minor phase, the effect is small (31,32). On the other hand, laminar morphology, as in the case of blends of barrier polymers (EVOH, PA-6 and PET) with

polyolefins (PE, PP), where small amounts of the former polymers are dispersed as essentially parallel, thin, large layers, produce substantial reduction of permeability in blow molded/extruded articles, even for small volume fraction of barrier minor phase (13,27,28).

2.2. Brief Review of Theories of Microrheology of Emulsions

In order to better understand the deformation and breakup of polymeric droplets suspended in another polymer, it is beneficial to review fundamental theories of drop deformation in emulsions. Physically, the problem of drop deformation would appear to be straightforward. A droplet immersed in a non-uniform velocity field will deform due to viscous stresses exerted on the fluid-fluid interface. The deformation is resisted by interfacial tension. If the velocity gradient is adequately large, in most cases the drop can not persevere a steady shape, but rather begin to continually stretch in the flow. This lack of a steady drop shape is generally called "drop burst" or "drop breakup".

Fundamental studies on the deformation and breakup of a liquid drop due to the motion of an immiscible, viscous suspending fluid dates back to the pioneering work of Taylor (33, 34). In order to provide a theoretical description of small deformations of a Newtonian drop in a Newtonian medium, Taylor used the method of domain perturbations (33,34). He derived equations for the internal and external velocity and pressure fields and also for deformation, D. He introduced two dimensionless parameters, the capillary number, κ , a ratio of shear stress, $\eta_m \gamma^{\bullet}$, and interfacial stress v/a; and viscosity ratio, λ :

$$\kappa = \frac{\eta_m \dot{\gamma} a}{\nu} \qquad \lambda = \frac{\eta_d}{\eta_m} \tag{2.1}$$

where η_m and η_d are the matrix and dispersed phase viscosities, respectively, γ^{\bullet} is the shear rate, a is the droplet diameter and ν is the interfacial tension.

At low strains, when the interfacial tension effect dominates the viscous effect (small λ),

Taylor's theory yields:

$$D = \frac{L-B}{L+B} = \kappa \left(\frac{19\lambda + 16}{16\lambda + 16}\right) \tag{2.2}$$

with L and B the length and width of deformed droplet, respectively. It can be seen from Equation (2.2) that, for λ values from 0 to infinity, $\kappa \le D \le 1.187 \kappa$. Equations (2.1) and (2.2) indicate that large interfacial tension and small drop diameter yields smaller drop deformations.

When the interfacial tension effect is negligible in comparison to the viscosity effect (large λ), this theory provides:

$$D = \frac{5}{4\lambda} \tag{2.3}$$

Cox's theory (35), which involves a perturbation in deformation and not in κ or λ , provides wider application than Taylor's theory:

$$D = \frac{5(19 \lambda + 16)}{4(\lambda + 1)((20 / \kappa)^2 + (19 \lambda)^2)^{1/2}}$$
(2.4)

It can be seen that Cox's theory reduces to Taylor's in the limiting cases.

To describe the motion of highly elongated shapes, characteristic of low-viscosity drops, Taylor introduced slender-body theory in 1964 (36) for low Reynolds number flows. The perturbation parameter in this theory was a parameter proportional to the slenderness ratio of the drop, which was assumed to be small. Subsequently, a number of researchers tried to modify these theories by considering higher orders of the perturbation parameter or a more suitable one that resulted in greater accuracy and wider applicability for larger drop deformations (37-46).

In 1975 Youngern and Acrivos (47) introduced the boundary-integral method, which is a numerical method that can consider large drop deformation and breakup of droplets without any limitation on λ . Other researchers applied this method to various problems (48-51). It should be stated that in these studies, the influence of viscoelastic properties and neighbouring drops was not considered.

Deformation and breakup of droplets was theoretically treated by Raleigh (52) and by Tomotika (53). According to them, deformation of spherical particles in shear flow might result in ribbon like entities that will become cylinder-like under the influence of the interfacial tension (this reduces the interfacial area). Further reduction of interfacial area can occur by the growth of distortions of the liquid cylinder, as indicated in Figure 2.1 (54).

Tomotika showed that for a Newtonian system, a sinusoidal distortion with amplitude of "A" grows exponentially with time:

$$A = A_0 \exp\{qt\} \tag{2.5}$$

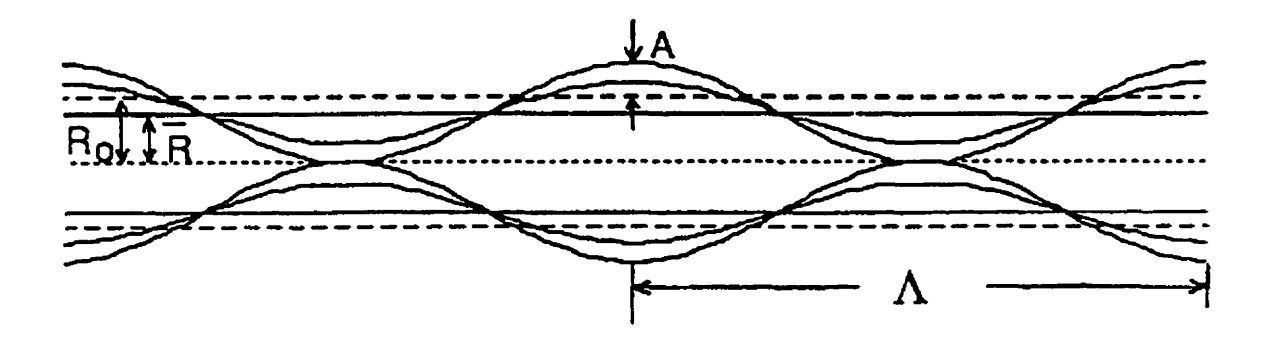


Figure 2.1: Simusoidally disturbed thread with definitions of R0, R, A, and A. (54)

where A₀ is the distortion at t=0 and

$$q = v.\Omega(\Lambda, \lambda)/2\eta_m R_0 \tag{2.6}$$

where Λ is the distortion wavelength, $\Omega(\Lambda,\lambda)$ is a tabulated function and R_0 is defined in Figure 2.1.

The thread break happens when A=R=0.81R₀. The time required to reach this stage can be calculated as:

$$t_b = (1/q) \ln \left[(0.81R_0)/A_0 \right]$$
 (2.7)

The wavelength of the dominant distortion that results in breakup and its growth rate depend on the viscosity ratio.

It should be pointed out that the theoretical treatment of droplet deformation is complicated and therefore, understandably, the majority of the studies reported in the literature are concerned with dilute Newtonian systems. Under flow conditions of practical interest, most of the polymeric systems exhibit non-Newtonian, viscoelastic behavior. Therefore, it is very important to have a better understanding of the role of viscoelastic properties of the individual components in determining the bulk rheological properties of two-phase systems and deformation behavior of drops in these systems.

Chin and Han (55) investigated the small extensional deformation of a viscoelastic droplet suspended in a viscoelastic medium, employing a perturbation technique. Their study took into account the effects of viscosity, elasticity and interfacial tension of the fluids concerned. Their model is restricted to dilute emulsions and small deformations. They made the following observations: (i) droplet deformation increases with capillary number; (ii) capillary number has a much greater influence on droplet deformation than the viscosity ratio and elasticity parameter; (iii) in steady elongational flow, the medium viscosity plays a much more important role in determining the droplet deformation than the droplet phase viscosity and medium elasticity.

Recently Palierne (56) introduced the linear theory of viscoelastic emulsions that was employed in the work of Delaby et al (57-59), for predicting drop deformations in uniaxial flow of a viscoelastic drop suspended in viscoelastic matrix. Palierne's linear model of viscoelastic emulsions led to expressions for the time-dependent drop deformation, assuming that both phases are Maxwell fluids with single relaxation times. They obtained the following equation:

$$\lambda_d(t) - 1 = \varepsilon \frac{5}{2p+3} \left[t + \frac{2p}{2p+3} \left(\tau_d - \tau_m \right) \left(1 - \exp\left\{ -\frac{t}{\tau_1} \right\} \right) \right]$$
 (2.8)

where λ_d is the Cauchy strain of the droplet, t is time in seconds, ϵ is the elongation strain rate in s⁻¹, p is the viscosity ratio of zero-shear viscosities of the dispersed phase and the matrix, τ_m and τ_d are the relaxation times of matrix and dispersed phase, respectively, in seconds and τ_1 is defined as

$$\tau_1 = \frac{2p\tau_m + 3\tau_d}{2p + 3} \tag{2.9}$$

Delaby et al. made the following theoretical and experimental observations: (i) for small deformations, good agreement with Taylor's theory was found; (ii) The drop deforms less than the matrix when the viscosity ratio is higher than 1, and it deforms more when viscosity ratio is less than 1; (iii) The drop is less deformed by a viscoelastic matrix than by a viscous matrix.

However, this linear model is restricted to small deformations and zero interfacial tension. Thus, it can be of little direct use in predicting the morphology during processing of polymer blends in complex flow fields of practical interest.

More recently, Stradins and Osswald (60) using the boundary integral method predicted the effect of viscosity ratio on mixing of polymer blends. They proposed Equation (2.10) as the best fit approximation to the simulated data for strain ratio as a

function of viscosity ratio. The relationship allows the strain in a drop to be predicted if the viscosity ratio and matrix strain are known. This can be used to determine the strain imposed on a drop when the strain imposed on the main matrix is known.

$$\frac{\gamma_d}{\gamma_m} = 2\left(1 - e^{\beta_m} - e^{\beta_d} - e^{\beta_c}\right) \tag{2.10}$$

where γ_d and γ_m are the strain rates for drop and matrix, respectively, $\beta_m=-1.22795$ $(\eta_m/\eta_d)^{0.7}$, $\beta_d=-1.22695(\eta_m/\eta_d)$ and $\beta_c=\beta_m+\beta_d$. They evaluated experimental results of Delaby et al. and found them of the same order of magnitude as predictions of numerical simulation.

Levitt and Macosko (61) used a stress balance approach to study the widening of viscoelastic drops in viscoelastic matrix (PP/PS) in simple shear flow and obtained the following equation:

$$0.6(G_m' - G_d') \approx \frac{v}{R_2^{\text{max}}}$$
 (2.11)

where $1/R_2^{max}$ is drop curvature in the longitudinal direction taken at the point of maximum width. As expected the largest widening was observed for the lowest drop/matrix elasticity ratio. However, for a viscosity ratio larger than unity and elasticity ratio above 2, no widening was observed.

Ghodgaonkar and Sundararaj (62) used a simple force balance to predict the effect of elasticity on drop diameter in mixing of polymer blends. They obtained the following equation for drop diameter:

$$D = \frac{2v}{\eta_m \gamma - 2(G_d^{\cdot} - G_m^{\cdot})}$$
 (2.12)

where D is the diameter of the drop. The force balance best predicts the behavior of dilute

systems (2% PS/PP). It should be noted that this equation gives qualitative information. To obtain quantitative values, the proportionality between forces due to effects of viscosity ratio and elasticity ratio, and direction of the forces must be determined. Their experimental results showed a minimum in drop diameter by increasing shear rate that can be explained through this equation. However, this was not observed for all systems.

2.3. Experimental Studies of Drop Deformation in Emulsions

Experimental studies of drop deformation have been used for evaluating theoretical approaches. Beside the researchers that introduced theoretical approaches for drop deformation (33-51), other investigators studied the phenomenon experimentally (54,63-70). On the basis of a review of theoretical and experimental studies of drop deformation, one may conclude that the principles and mechanisms governing drop deformation and breakup for Newtonian emulsion systems are generally understood. Based on this literature review the following general conclusions can be made:

- The viscosity ratio, interfacial tension, capillary number, breakup time, and flow field are important controlling parameters.
- In simple shear flow, breakup of droplets occur more easily when viscosity ratio, λ , is close to unity (0.3< λ <1.5). For viscosity ratios in excess of 3.8, no breakup can be achieved in simple shear flow, regardless of the value of interfacial tension. Since Cox's theory predicts deformations less than 0.32 (D<0.32), for infinite high values of κ , it is reasonable that such a deformation is not sufficient for breakup.
- A minimum viscosity ratio exists below which a droplet does not burst. In simple shear flow, values of 0.003-0.005 have been reported.
- Drop deformation increases with capillary number.
- At low interfacial tension and high viscosity of the matrix, the required shear rate for breakup is smaller.

- Droplet breakup is easier in extensional flow fields. The relative efficiency of the extensional flow substantially increases for $\lambda \ge 3$.

Deformation of Newtonian droplets suspended in a viscoelastic media has been covered in a few reports (66, 72-75). They made the following observations:

- In Couette flow, the droplet moves closer to the outer cylinder (72).
- Due to decrease in viscosity with increasing shear rate, a viscoelastic matrix causes droplet deformation to increase less at higher shear rates (73).
- In the viscoelastic medium, migration towards the tube axis was observed, and the equilibrium position was at R=0 (66,74).

Deformation of viscoelastic droplets in Newtonian media was reported by a number of researchers (55, 64, 72, 75-78). They recorded the following observations:

- Viscoelastic droplets are less deformable than the Newtonian droplets (55).
- Higher values of critical capillary number are observed than those determined for Newtonian droplets (72).
- -Contradictory observations were made concerning the stabilizing effect of droplet elasticity (77,78).

2.4. Drop Deformation and Morphology Development in Polymer Blends

Under the compounding and processing conditions encountered in processing of polymer blends, molten polymers exhibit non-Newtonian viscoelastic behavior. In viscoelastic systems, the drop deformation is determined not only by the viscous and interfacial forces, but also by the pressure distribution around the droplet arising from the elasticity (70,71). Therefore, the parameters involved and the mechanism of drop deformation in viscoelastic systems might be quite different from those in Newtonian emulsions. In contrast to the Newtonian systems, little has been published on drop deformation and breakup in

viscoelastic systems.

During the past two decades, much work on immiscible polymer blends has attempted to establish the relationship between morphology and rheological/physical properties of the individual components. Of particular interest are the experimental and theoretical studies of Van Oene (70) and the work of Starita (71). They reported that in addition to the viscosity and equilibrium interfacial tension of the two components, the elasticity of polymer melts plays an important role in deformability of dispersed phase droplets and in determining the morphology of two-phase polymer blends. Van Oene, in his rheo-thermodynamics theory, attempted to characterize the dispersion in terms of droplet size, interfacial tension and differences in the viscoelastic properties of species and derived an expression for dynamic interfacial tension during flow of a Weissenberg fluid (i.e. N_2 =0):

$$v_{dm} = v_{dm}^{0} + (1/6)a[N_{1d} - N_{1m}]$$
 (2.13)

where v_{dm} is interfacial tension in flow (or dynamic interfacial tension), v_{dm}° is the interfacial tension in a quiescent polyblend, N_{1d} and N_{1m} are the first normal stress differences of the dispersed phase and matrix, respectively. If dispersed phase is more elastic than the matrix, i.e. $N_{1d} > N_{1m}$, Equation (2.13) predicts higher interfacial tension in flow or more stable dispersed phase morphology. On the other hand, for $N_{1d} < N_{1m}$ and $|v_{dm}^{\circ}| > |a| (N_{1d} - N_{1m})/6|$, the dependence predicts lower dynamic interfacial tension. Thus the flow tends to reduce interfacial tension. In other words, the flow is inclined to enhance the dispersing process, i.e. flow compatibilization. It also predicts, for a certain droplet size, v_{dm} may be zero and only droplets smaller than this size are stable. Since v_{dm} can not be negative, for larger differences of the normal stress differences or larger drop diameter, the dispersed morphology translates into stratified morphology, for which Equation (2.13) is no longer valid. It should be mentioned that due to neglecting the flow inside the drop, the predictions of Van Oene theory of dynamic interfacial tension and minimum droplet size for stable dispersed morphology, might be incorrect for some

systems.

On the basis of Van Oene's theory, Plochocki (79,80) predicted if N_{lm} is quite larger than N_{ld} , the minor phase no longer preserves droplet shape and stratifies (Figure 2.2).

The problem of droplet deformation and breakup was investigated by Wu (81) for blends of PA-6 and PET with EP terpolymer processed by twin screw extrusion. On the

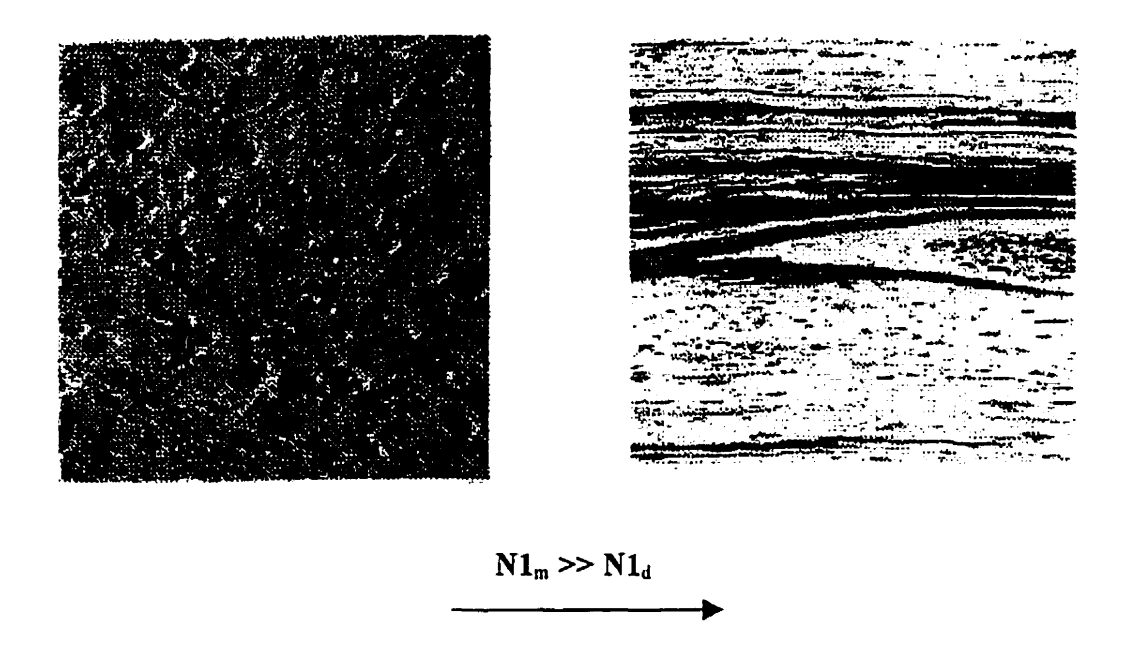


Figure 2.2: Transition in the phase morphology type: from dispersed (left) to the stratified (right) induced by the change in sign of the principal normal stress difference (78).

basis of obtained results, he plotted capillary number, κ , versus viscosity ratio, λ (Figure 2.3) and obtained a master curve defined by the following equations:

$$\frac{\eta_m \cdot \gamma \cdot \alpha}{v} = \kappa = 4(\lambda)^{0.84} \tag{(\lambda>1)}$$

$$\frac{\eta_m \cdot \gamma \cdot a}{\nu} = \kappa = 4(\lambda)^{-0.84} \qquad (\lambda < 1)$$

Therefore, small interfacial tension, large shear rates and high matrix viscosity enhance the

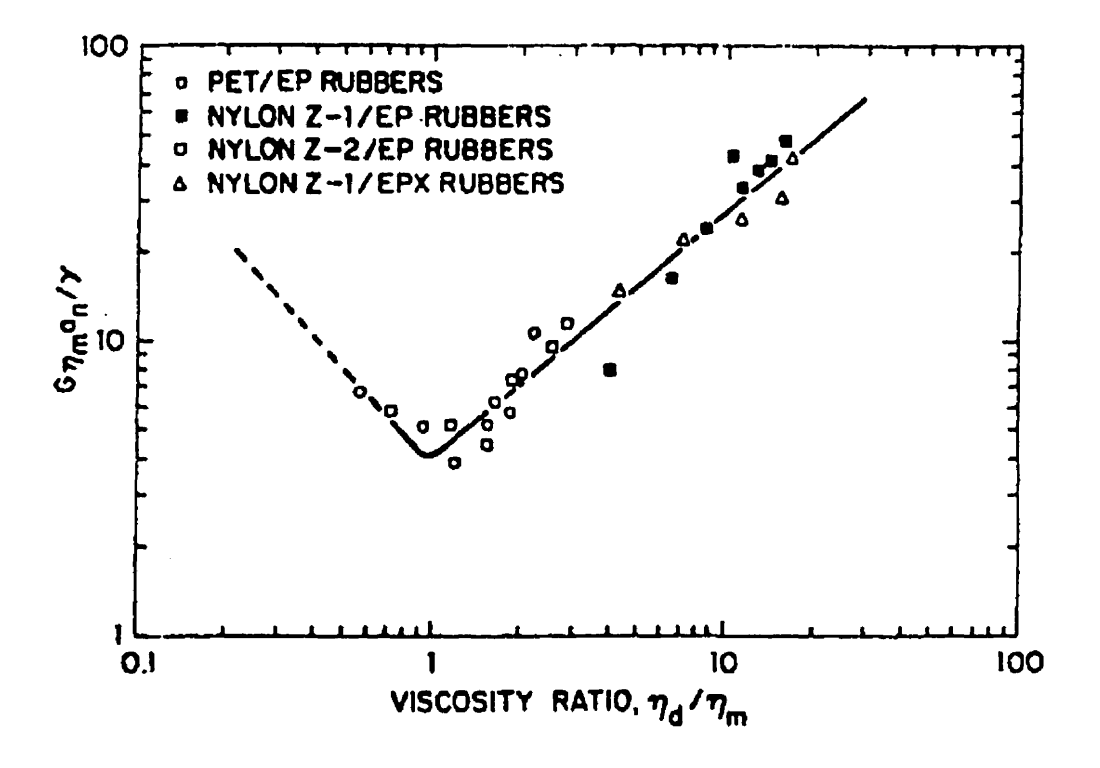


Figure 2.3: Dimensionless master curve of κ versus λ for the melt extrusion using a corotating twin screw extruder (81).

deformation and breakup of droplets during mixing. He observed that capillary number appears to have the lowest value at $\lambda \cong 1$. This suggests that the smallest particles are obtained when the viscosity ratio is about unity and as the viscosity ratio moves away from unity, the dispersed phase particles become larger. He concluded that particle size is directly proportional to interfacial tension and interfacial tension is a more effective means for controlling the particle size, because the interfacial tension can be more easily varied over a wide range than the viscosity with little effects on bulk properties.

Serpe et al (82) suggested some modification for Wu's equation as follows:

- (i)- they replaced the viscosity of continuous phase, η_m , by the viscosity of blend, η_{b} ;
- (ii)- an increase of the average particle size with concentration of dispersed phase was observed, therefore, keeping Wu's formulation, they defined:

$$F(\phi) = 1 - 4(\phi_d \phi_m)^{0.8}$$
 (2.16)

So, in the treatment of particle deformation for viscoelastic systems under shear flow, the proposed correction (viscosity and composition) lead to a modified capillary number (κ^{\bullet}) defined as:

$$\kappa^{\bullet} = \frac{\eta_b \cdot \gamma \, a \left(1 - 4(\phi_d \phi_m)\right)}{\nu} \tag{2.17}$$

They found that data points for various blends over a large range of composition and mixing conditions fall on a master curve (Figure 2.4) defined by the following equations:

$$\kappa^* = 4(\eta_r^*)^{0.84} \qquad (\eta_r^* > 1)$$
(2.18)

$$\kappa^* = 4(\eta_r^*)^{-0.84} \qquad (\eta_r^* < 1)$$

where $\eta_r^* = \eta_d/\eta_b$. As in Wu's approach, the smallest particles are obtained when η_r^* is about unity.

The effect of material characteristic on morphology development of polymer blends has been the subject of various experimental studies (44, 54, 63, 73, 76, 83-89). They made the following general observations:

- In Couette flow, long cylinders for $\lambda > 1$ and spheroids for $\lambda < 1$ was observed (83).

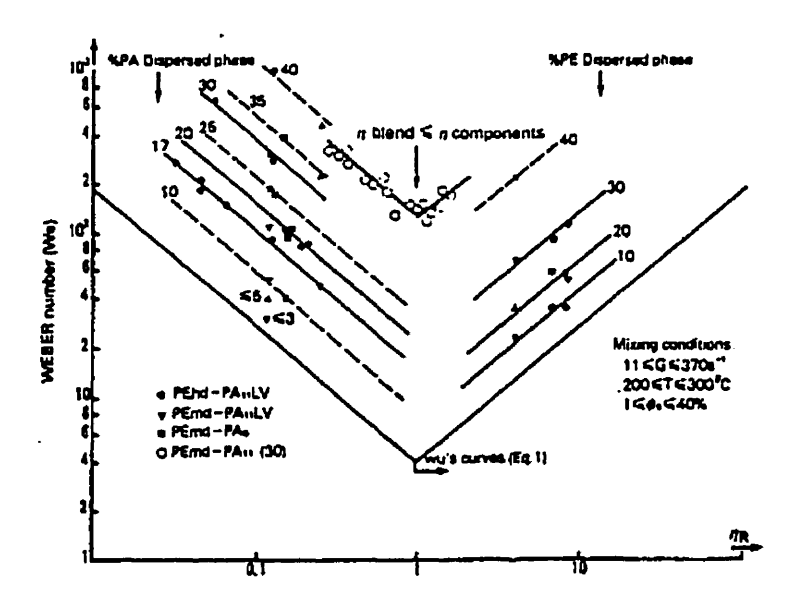


Figure 2.4: Dimensionless master curve of κ^* versus viscosity ratio $(\eta_r^* = \eta_b/\eta_m)$ and dispersed phase concentration (ϕ_d) for PE/PA blends for a wide range of mixing conditions (G: shear rate, T: temperature) and dispersed phase concentration (82).

- -Elevated interfacial tension and high elasticity of the drop enhances resistance to both deformation and breakup (76) and droplets with larger elasticity are hydrodynamically more stable (73).
- The critical shear rate for breakup is lower in a high viscosity suspending medium than a low viscosity suspending medium (76).
- Highly viscoelastic media give rise to large deformations of droplets (89).
- Minimum particle size was obtained for viscosity ratio of unity, $\lambda \cong 1$, and compatibilized blends are less sensitive to the value of λ (84, 85).
- A more decisive role is played by the viscosity ratio than by elasticities of the components, since the viscosities are high and vary by several orders of magnitude, while elasticities vary only within one order of magnitude (87).
- The longitudinal morphology of PE/PS blend extrudates is influenced by the viscosity ratio. If λ <0.7, fibrillar structure is formed; for 0.7 < λ <1.7, the droplets become undulant fibers; and for λ >2.1, undeformed droplets are observed (86).

2.5. Effect of Processing Conditions and Flow Field on Morphology

Processing operations in melt blending may be separated into; (i) compounding operations where the blend components are initially mixed and prepared, and (ii) shaping operation where the resulting blends are extruded or molded into desired shapes. During shaping operations, the phase morphology of the blends may be modified and the dispersed phase is frequently drawn or elongated.

Beside the material variables that were discussed in the previous section, processing parameters are determined to play a key role in deformation of dispersed phase particles and morphology development (76, 85, 90-93). The most important processing variables affecting morphology development include: shear rate/shear stress, time of mixing (in mixer) or residence time (in extruder), temperature, type of mixer or screw

design, flow rate and stretch ratio. The flow field, especially in the final shaping step, influences the deformation of dispersed phase particles and determines the obtained morphology (76, 90,17-21).

Shi and Utracki (90) studied development of polymer blend morphology in a twin-screw extruder. Dependency of predicted morphology on processing variables was also investigated. They found that increasing the screw rotating speed or decreasing the throughput, i.e. increasing the residence time, lead to finer morphology. However, the effect of throughput was found to be more pronounced than the influence of screw speed. The decrease in scale of dispersed phase morphology with capillary die extrusion rate has also been noted by various earlier investigators (82, 86, 91).

Tsai and Min (92) investigated the flow induced morphology of fluoroelastmer and polycarbonate blend in an internal mixer. They determined the effect of shear rate on morphology and found that when the shear stress is low $(7\times10^4 \text{ Pa})$, the spherical particles of dispersed phase do not deform. The transition from sphere to fiber occurs in the range of shear stress 7×10^4 Pa and 15.8×10^4 Pa. When the shear stress is larger than 15.8×10^4 Pa, the fibers will break into a series of small droplets.

Favis (85) studied the effect of processing parameters on the morphology of PP/PC blends in an internal mixer. He observed that a fourfold change in the apparent shear rate or doubling the apparent matrix shear stress had little effect on the dispersed phase distribution.

Serpe et al. (82) reported the effect of temperature on phase morphology of PE/PA blends. They observed that depending on the value of the activation energy of dispersed phase and matrix viscosities, increasing the temperature might increase or decrease the particle size. In some cases, temperature does not influence the morphology.

Han and Funatsa (76) studied droplet deformation and breakup in pressure driven flows through converging and uniform channels. They determined that elongational flow is more efficient in deforming the dispersed phase particles than shear flow. They found that droplet breakup happens when the droplet, elongated into a thread-like cylinder in the

converging section, recoils in the region of stress relaxation (Figure 2.5).

Utracki et al.(93) studied the behavior of HDPE/PA-6 blends in capillary flow. The intensity of the extensional flow in the converging inlet zone was shown to be sufficient to cause coalescence and fibrillation of PA-6 spheres at temperatures 69°C below the PA-6 melting point. At the low temperature of 150°C the high viscosity PA-6 migrated toward the center axis. At 250°C, the lower viscosity PA-6 was found to concentrate in the outer shell of the strand.

In the study of Wu (81) in a co-rotating twin-screw extruder, drop breakup occurs even when λ >4. This appears to arise from a combination of several factors including the viscoelastic effects, complex transient shear, complex viscosity/temperature profile along the extruder barrel, and perhaps more importantly the presence of elongational field in the extruder.

Kamal et al. (17,21) studied the morphology of PP/EVOH blends in a single screw extruder. They reported that incorporating converging and diverging sections in the die unit, results in large deformations of dispersed phase and obtaining laminar structure.

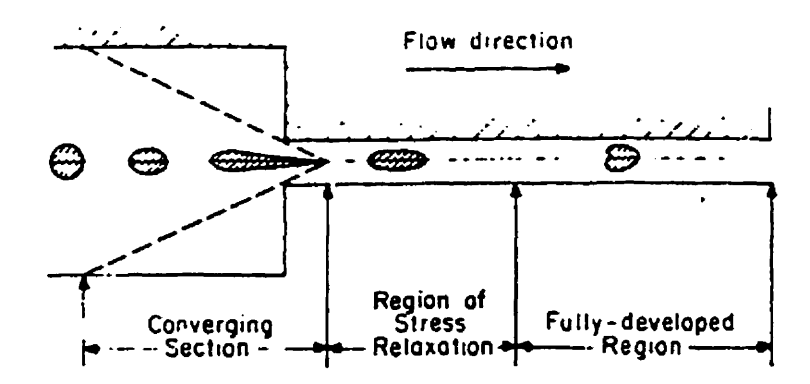


Figure 2.5: Schematic of the droplet deformation process that would occur in the entrance and fully developed regions (76).

It is evident from the above that elongational flow affects morphology more efficiently than shear, and the presence of elongational flow in the extruder and inlet of the die (17, 18, 94) indicates its importance in morphology development during processing of polymer blends.

2.6. Droplet Coalescence and Compatibilizer Effect

The effect of droplet coalescence on the morphology of immiscible polymer blends should be considered, even at low concentration of the dispersed phase, $\phi_d \ge 0.005$ (54). Various theories have been developed to interpret the coalescence effect (95-101). An extensive relevant review has been reported by Utracki et al. (54). Two important parameters predicted by these theories are the time for onset of coalescence or coagulation time, t_e , and the equilibrium drop diameter, d^e .

Tokita (96) derived the following equation to predict the equilibrium diameter of coagulation:

$$d^{*} = (24/\pi) p_{r} v \phi_{d} / \left[\eta_{m} \dot{\gamma} - (4/\pi) p_{r} E_{DK} \phi_{d} \right]$$
 (2.20)

where p_r is the probability that collision will result in a coalescence and E_{DK} is the macroscopic bulk breaking energy. This equation indicates that the equilibrium drop diameter should increase with concentration, interfacial tension, and decrease with shear stress.

Elmendorp's theory of coalescence (97, 98), which is often cited in the literature (99, 100, 102, 103), provides the coagulation time:

$$t_c = 3\kappa \left[\ln \left(d/4h_c \right) \right] / 4\gamma \tag{2.21}$$

where κ is the capillary number and h_e is the critical separation distance. This relationship, derived for dilute systems, predicts that the coagulation time should increase with viscosity of the matrix phase and with drop diameter but decrease with an increase of interfacial tension. Therefore, high concentration of the dispersed phase, low viscosity of the matrix, small particle size and high interfacial tension favor coalescence.

Generally, simple blending of different polymers results in coarse unstable phase morphology that lacks adhesion at the interface and produces poor mechanical properties. These deficiencies can be improved by incorporating small amounts of a third ingredient, usually referred to as "compatibilizer" or "interfacial agent". The presence of a compatibilizer can lower the interfacial tension between polymers and therefore, reduces the energy needed to break large particles during blending. This gives rise to a significant reduction in the size of dispersed phase and an increase in the interfacial adhesion. There is voluminous literature reports concerning the effect of compatibilizer on morphology, processing and properties of polymer blends (.84, 91, 104-111). Review of these papers reveals the effects of compatibilizer that are listed below.

- Compatibilizing agents produce significant increase in the rate of mixing and also reduce the scale of phase morphology (104, 105 and 108).
- Due to the high viscosity of the polymer matrix, much larger quantities than actually required for interface covering are usually needed (104).
- Some compatibilizers like SEBS-g-MAH, may be partly located at the interface as a compatibilizer but also partly incorporated as a rubbery impact modifier in the resin (107).
- The addition of compatibilizer stabilizes the phase dimensions (105).
- Some compatibilizers can produce substantial improvement in the ultimate properties (109).
- The influence of the compatibilizer on both particle size and final properties is substantial at low concentration of compatibilizer and levels off after a specific amount of compatibilizer (110).

2.7. Time Scale of Morphology Development in Polymer Blends

The understanding of the dispersion process in polymer blends and of the different stages of morphology formation starting from mm size pellets and ending with sub-micron size dispersed phase particles, should be of great help in controlling and developing special morphology for immiscible polymer blends. A small number of literature reports provide some useful guidelines for this purpose (85, 90, 103, 104, and 112-120).

Lindt (112), in studying the mathematical modeling of polymer melts in a single screw extruder, found substantial reduction in the thickness of solid bed width along the screw length. His experimental and theoretical results revealed that solid bed width reduces more than 70% within a screw length of L/D of 2. Lee and Han (115) observed similar results in investigating the performance of plasticating single-screw extruders. However, their experimental results did not show very sharp change of solid bed thickness. Breakup of the solid bed occurred at an L/D of 10.5. Lindt et al. (113,114) studied the morphology development for blends of polystyrene and styrene-butadiene-styrene (PS/SBS) and polystyrene-ethylene vinyl acetate (PS/EVA) blends. Their results, which are shown in Figure 2.6, confirmed that the melting zone plays a very important role during extrusion of polymer blends. They observed that within the residence time of the melt in the melting zone, the blend undergoes a continuous but rapid change in its developing morphology. Within a fraction of a second, the scale of mixing drops by several orders of magnitude. The results reported by them and other investigators (114, 115, 118) show that within a few seconds the scale of segregation is reduced by orders of magnitude.

Favis (85) studied the morphology of polypropylene-polycarbonate (PP/PC) blend from 2 to 20 min of mixing and did not observe notable changes over this time period. Therefore, he too concluded that a major portion of the morphology development occurred during the melting of the pellets.

Scott and Macosko (119) used an internal mixer for polystyrene-polyamide (PS/PA) system and found that the initial morphology (1.0 min of mixing) of the dispersed

phase consisted of sheets and ribbons containing holes about 10 microns wide. They also reported irregular shapes, which may have originated from breakup of the lace structure. This research was followed by Sundararaj et al. (116) in a twin-screw extruder for the same blend and polystyrene-polypropylene (PS/PP) blend. They also observed that very large changes in dispersed phase size occurred during the softening stage. The particle size changed less after the polymers were completely melted. Similar results were obtained with a batch mixer. The formation of sheets in polymer blends was seen to occur in twin-screw extruders. This sheeting mechanism caused the dispersed phase size to rapidly decrease in the first stage of mixing (during the melting and softening period). Most of the significant morphology development and size reduction in the extruder happened within 30 mm of the first point of melting, and most of the important size reduction in the batch mixer occurred within 1.0 min. The breakup mechanism involved

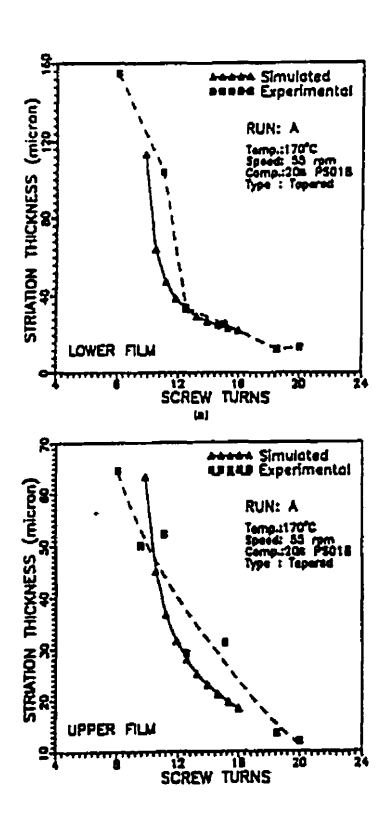


Figure 2.6: Down-channel variations in the striation thickness (polystyrene/styrene-butadiene copolymer) a) lower film b) upper film (112).

hole formation, which might be caused by impurities in the blend. Levitt and Macosko (118) studied deformation, breakup, and coalescence of the dispersed phase by means of visualization technique. They considered deformation of droplets and thin, pre-made viscoelastic sheets inside a viscoelastic matrix. They were interested in conditions where large stretching without breakup could be achieved. The most stretched sheets were observed for polymer pairs with closely matched viscosities and small interfacial tension. On the basis of previous reports and their observations, they proposed the schematic of dispersion of the minor phase during blending process (Figure 2.7).

Shi and Utracki (90) studied the problem theoretically, and they too reported substantial reduction of particle size of dispersed phase with length of the twin screw extruder. Lim and White (104) studied the development of polyethylene-polyamide

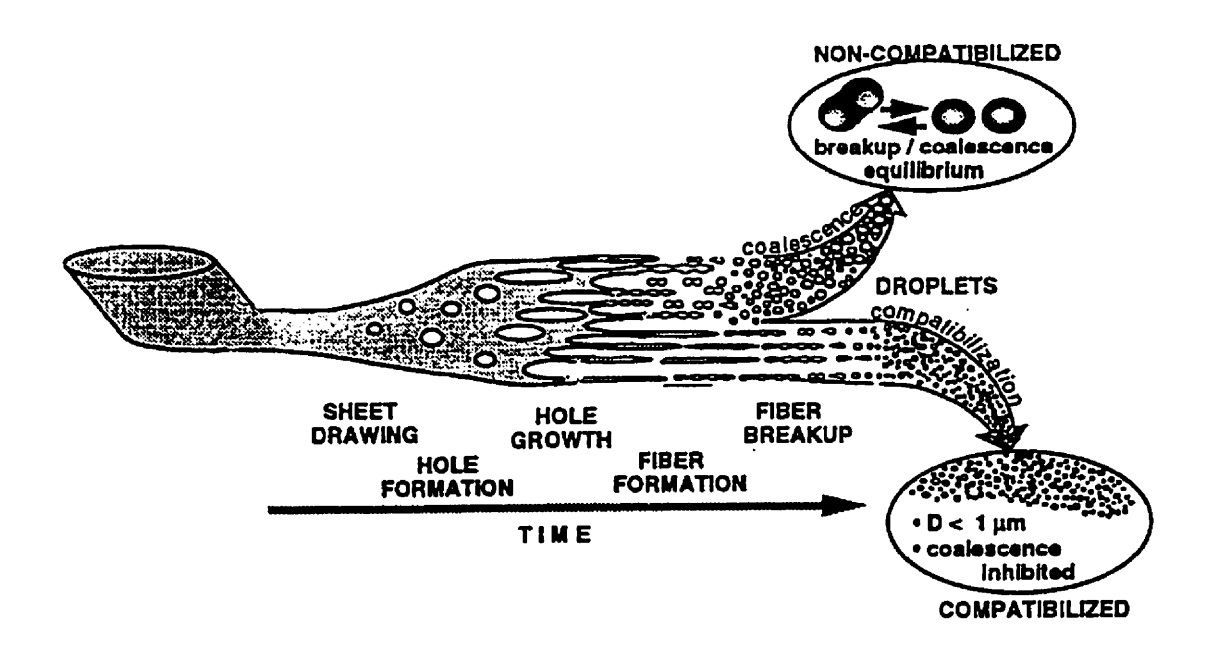


Figure 2.7: Schematic of dispersion of the minor phase during blending showing the transition from pellets to droplets (118).

(PE/PA) blend in a modular intermeshing co-rotating twin screw extruder with and without compatibilizer. They observed significant reduction of particle size along the screw length. These changes were more substantial in the case of compatibilized blends (Figure 2.8).

The above reveals the importance of the very early stages of mixing in the development of morphology in polymer blends. It also suggests that it should be possible to obtain large particles of the dispersed phase at the die exit by delaying the melting process. Application of an optimized temperature profile and control of shear heating by optimizing the screw design should help in this regard. However, also material variables should be taken into consideration.

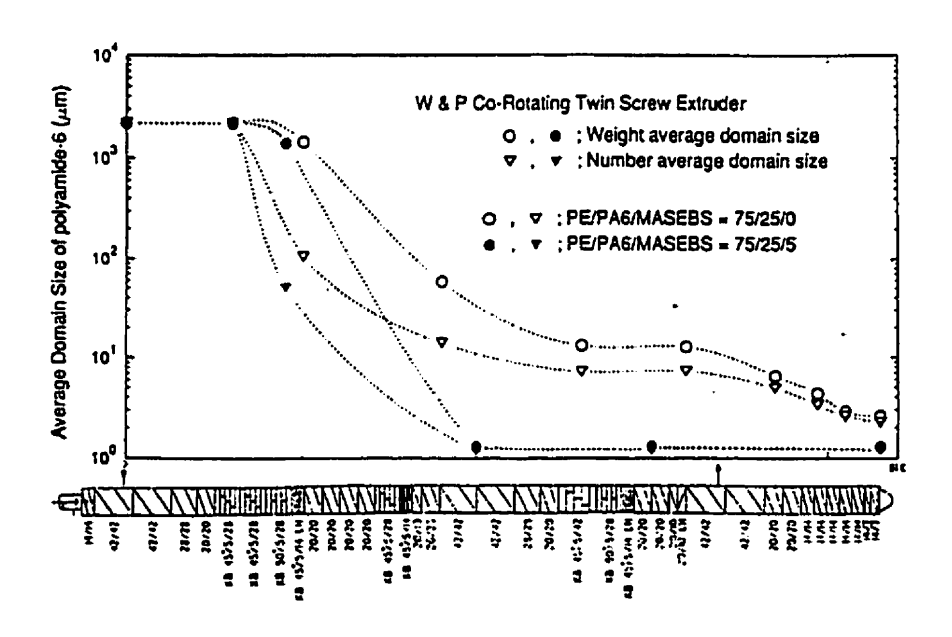


Figure 2.8: Number and weight average dispersed phase size as a function of position along the screw axis for PE/PA-6 without and with 5 phr of MASEBS (104).

2.8. Development of Laminar Morphology in Polymer Blends

There is great demand for barrier plastic materials in applications such as food packaging, gasoline tanks and fuel pipeline systems for passenger cars, where low permeability to moisture, gases, solvents and hydrocarbons are essential. Polymer blends with laminar structure, where small amounts (5-20 wt%) of a barrier polymer dispersed as essentially parallel, thin and large layers in the matrix of a low cost resin, provide orders of magnitude reduction in oxygen or hydrocarbon permeability in blow-molded/extruded articles (13-28).

Subramanian et al. (22-27) employed "SELAR", i.e. adhesion modified nylon, in laminar blends with HDPE to produce blow molded containers with improved barrier properties (Figure 2.9). They also developed HDPE/PET laminar blends in film extrusion. Although, they obtained substantial reduction in permeability of HDPE/PA containers (up to 200 times), extruded HDPE/PET laminar blends showed only 10 times improvement in toluene permeability. It appears that the principal reason for excellent barrier properties of HDPE/PA containers and moderate barrier performance of HDPE/PET films is the nature of two processes used to produce these articles. In the blow molding process, the possibility of obtaining extension ratios in both directions (machine and transverse directions), is a significant advantage, while in the case of sheet extrusion, the possibility of achieving desired extension ratios is not high.

Kamal et al. (17) and Lohfink (18) chose a slit die to study the possibility of manipulating microstructure and developing laminar morphology in ribbon extrusion. They achieved laminar morphology in PP/EVOH blends with good barrier properties, using a specially designed die and process manipulation. The die design incorporated converging and diverging sections in order to help in stretching dispersed phase particles in two directions (machine and transverse directions). Figure 2.10 presents the oxygen permeability of some of their samples.

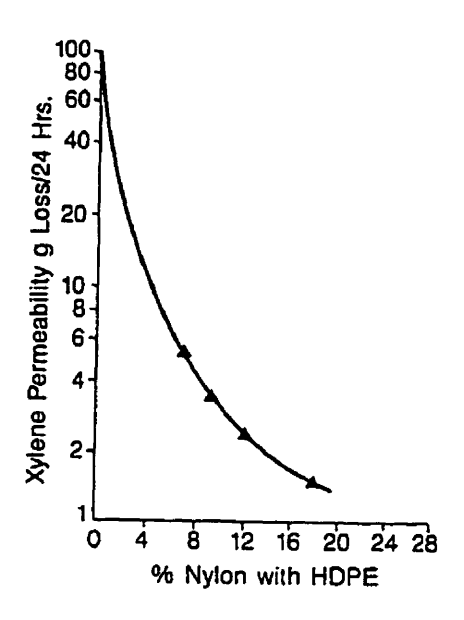


Figure 2.9: Permeability (weight loss, gr.) as a function of nylon concentration, in laminar-walled containers (27).

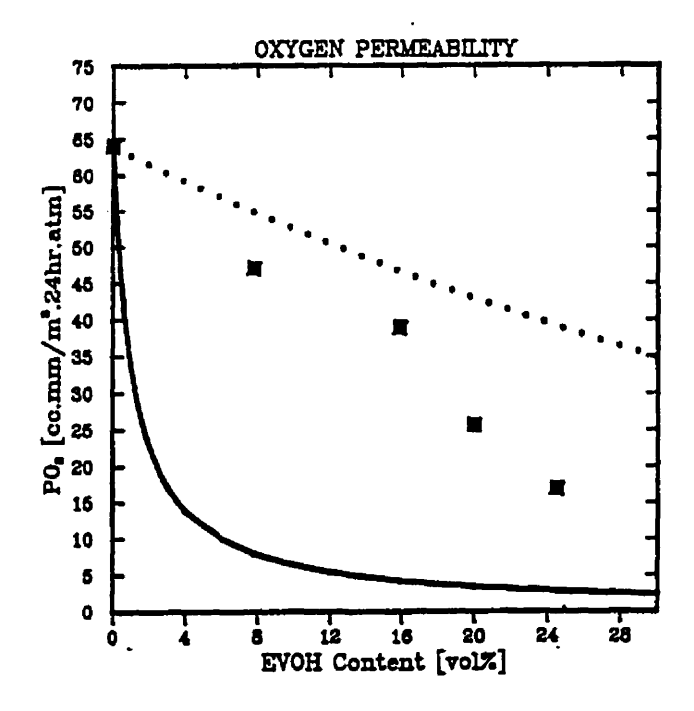


Figure 2.10: Comparison of measured oxygen transmission rates (■) with model predictions for MAPP2/EVOH blends system, I-.... Homogeneous blends, 2-—Co-extruded materials (21).

Recently, Lee and Cho (28) and Lee and Kim (121) studied LDPE/EVOH system in blow molding, film blowing, and sheet extrusion. While, they obtained substantial improvement in oxygen permeability of blow molded containers (300 times), the film blowing and sheet extrusion results were not very promising. They obtained up to 20 times improvement in film blowed samples and only 2 times enhancement in oxygen permeability of samples produced by sheet extrusion.

2.9. Summary and Conclusions

The above survey of the status of knowledge regarding morphology development during the processing of blends leads to the following conclusions:

(1) Some rules have been proposed with regard to particle size distribution as a result of deformation in simple flow fields. These rules incorporate rheological, processing and interfacial parameters. The most extensively explained effect relates to the viscosity ratio of the dispersed phase and matrix. Yet, this effect is not thoroughly understood, and some of the experimental observations appear to lead to contradictory conclusions. However, it is evident that high viscosity ratio is not desirable for large drop deformations needed for developing laminar morphology. For this purpose, viscosity ratio close to unity is advantageous.

Although elasticity of the components and the differences between first normal stress differences have been reported to be important from experimental observations and theoretical considerations, the status of knowledge in this area remains very weak due to difficulties in measurement of the relevant elasticity parameters and the lack of dependable rheological constitutive equations that could provide dependable predictions of these parameters. Also, presently, there is no proven theory capable of describing large deformations of viscoelastic systems encountered in polymer blends. However, from experimental and limited theoretical observations, it is apparent that high elasticity ratio of dispersed phase and matrix is not advantageous for large deformations. Therefore, as Van Oene's theory (70) also predicts, higher elasticity of matrix than dispersed phase is necessary to produce laminar morphology in polymer blends. Moreover, it is established that elongational flow is more effective in

producing large deformations of the dispersed phase, even at high viscosity ratio. The effect of interfacial parameters is ambiguous at least, since no reliable interfacial tension data are available regarding the relevant polymer melts. In general, lower interfacial tension coefficient is more beneficial for large drop deformation and it is known that high interfacial tension causes resistance against deformation.

(2) The key references regarding the development of laminar morphology are the works of Subramanian (22-27), Lohfink (18), and recently Lee et al. (28,121). Literature reports of the work of Subramanian are sketchy, in large part due to the commercial aspects of the work. Therefore, very little guidance may be derived from this work. However, it should be noted that their results for sheet extrusion were not promising. The thesis of Lohfink provides more details and specific information. Subsequent research by Hozhabr-Ghelichi (19) and Arghyris (20) adds to Lohfink's database. However, the main aspects of the work of the last three researchers have relied heavily on qualitative observations of the morphology and its relation to compositional, design and processing parameters. The findings are restricted to one polymer blend system (PP/EVOH). There is great need to improve these results and to extend and test the corresponding observations to another commercially important polymer blend systems like HDPE/PA-6 blends. Recent research (112-120) regarding morphology development in single and twin-screw extruders, might be beneficial for this purpose. Furthermore, reliable interfacial tension data are needed to better understand the effect of interfacial tension on morphology development in polymer blends.

CHAPTER 3

SCOPE AND RESEARCH OBJECTIVES

In light of the literature review in the preceding chapter, this research, which is an extension of an integrated program comprising the efforts of three researchers (18, 19, 20), attempts to fill some of the existing gaps. Emphasis in this work is placed on the understanding and development of criteria for the production of laminar blends and applying such findings in developing laminar morphology for the first time in sheet extrusion of HDPE/PA-6 blends and also to upgrade the results obtained for PP/EVOH system. The development of these criteria has been guided by the results of other studies reported in the literature review section.

2.1. Specific Research Objectives

The specific goals and objectives of this research were:

- to study the effects of rheology of blend components on the development of blend morphology and to tailor rheology to aid in developing laminar structure in sheet extrusion of blends. In particular, the effects of elasticity and viscosity ratios were evaluated and optimized to obtain laminar morphology.
- 2. to investigate the influence of compatibilizer on the development of laminar morphology and final properties in HDPE/PA-6 system, and to optimize the level of compatibilizer by modifying HDPE with different contents of maleic anhydride; the optimum maleation level is determined with the aid of interfacial tension measurements at different temperatures and maleation levels (for both PP/EVOH and HDPE/PA-6 systems);

- 3. to evaluate the influence of composition, flow field and processing parameters, i.e. shear rate (screw rotation speed), temperature profile in the screw zone and die temperature, screw design, twin-screw compounding and sequence of blending, and cooling system on morphology and barrier and mechanical properties of blends;
- 4. to obtain relationships for predicting barrier and mechanical properties of blends from morphological data.

CHAPTER 4

EXPERIMENTAL

4.1 Material Characterization

4.1.1 Materials

Two blend systems were employed in the present study:

- (i) Polypropylene/Ethylene vinyl alcohol copolymer (PP/EVOH): As the matrix phase, a maleic anhydride grafted polypropylene, ADMER QF500A, supplied by Mitsui Petrochemical Industries was used. The maleation level of this resin was 0.07 wt%. EVOH, an excellent barrier polymer, was chosen for the dispersed phase. The EVOH grade used in this study, EP-F101A, manufactured by EVAL® Company of America has a 32 mol% ethylene content (122).
- (ii) High density polyethylene/Polyamide-6 (HDPE/PA-6): A blow molding grade high density polyethylene, Sclair 58A designated as PE0 was used as the matrix. Two maleic anhydride grafted high density polyethylene, CXA 4003 (PE1) and CXA 4006 (PE2) were used as either potential compatibilizer or to replace the matrix. By mixing different proportions of PE0 and PE2, different levels of maleation content for polyethylene can be achieved. All these three resins are supplied as commercial grades resins by Du Pont Canada Inc. A blow molding grade polyamide-6, Ultramid B5, supplied by BASF Corporation was used as the dispersed phase. PA-6 is known as a good barrier polymer for hydrocarbons (123).

Table 4.1: Typical Properties of the Resins as Supplied by the Manufacturers

	Resin							
Property	ADMER	EVOH	PE0	PE1	PE2	PA-6		
Solid Density (g/cm³)	0.90	1.19	0.955	0.951	0.950	1.13		
Melt Index (dg/min)	3.0 (230°C)	1.3 (190°C)	0.43 (190°C)	1.3 (190°C)	0.6 (190°C)	_		
Vicat Softening Point (°C)	143	-	125	129	128	_		
Melting Point (°C)	160	181	135	136	136	220		
Tensile Yield Strength (MPa)	24.5	25	31	_	-	80		
Ultimate Tensile Strength (MPa)	31.5	80	-	-	-	-		

Typical properties of the resins used in this work, as supplied by the manufacturer, are shown in Table 4.1. Some of the physical and mechanical properties of the resins needed in this study are presented in Table 4.2.

4.1.2 Rheological Measurements

Based on the literature review in chapter 2, viscosity ratio and elasticity ratio of blend components are among the parameters that affect morphology development under various

Table 4.2: Properties of Resins (measured in this study)

		Resin					
Property	ADMER	EVOH	PE0	PE1	PE2	PA-6	
Solid Density (g/cm³)	0.90	1.19	0.955	0.951	0.950	1.13	
Toluene Permeability (mg.mm/m².day)	176	0.004	24.8	30.7	32.9	0.11	
Oxygen Permeability (cm ³ .mm/m ² .day.atm)	61.5	0.01	23.5	-	25	0.71	
Impact Strength (J/mm)	2.5	0.4	1.5	-	1.8	2.8	
Elastic Modulus (MPa)	-	-	778	-	-	1210	
Maleation Content (wt%)	0.069	0.0	0.0	0.093	0.113	0.0	

processing conditions. Thus, steady shear viscosity and dynamic measurements were made to obtain these parameters.

4.1.2.1 Steady Shear Viscosity Measurements

An Instron Capillary Rheometer (model TT-CM) was used to measure the steady shear viscosity of the resins. The capillary rheometer was calibrated for temperature distribution along the barrel. Viscosity measurements for HDPE's and PA-6 were done at three different temperatures of 230, 250 and 270°C. For ADMER and EVOH resins, the results

of Lohfink (18) were used. In order to cover a wider range of shear rates, two different dies with diameter of 0.762 and 2.54 mm were used. For shear rates higher than 10 s⁻¹, die with diameter of 0.762 mm and L/D ratio of 40 was used. To consider the entrance effects, two other dies with L/D ratio of 5 and 20 were used and the Bagley correction was calculated. To determine the true wall shear rate and viscosity of polymer melts, the Rabinowitsch correction was calculated using the following equation:

$$b = \frac{d \log \gamma_{app}}{d \log \tau_{w}} \tag{4.1}$$

Then the value of shear rate at the wall was obtained using Equation (4.2):

$$\dot{\gamma}_{w} = \frac{4Q}{\pi R^3} \left(\frac{3+b}{4} \right) \tag{4.2}$$

Viscosity measurements showed that at low shear rates, the Bagley correction is negligible. Therefore, for shear rates less than 10 s⁻¹, the die with diameter of 2.54 mm was used, and the Bagley correction factor was neglected. To consider the non-Newtonian behavior of the resins, the Rabinowitsch correction was calculated. The calculation procedure to determine the viscosity is described in details in various references (124).

4.1.2.2 Dynamic Measurements

In this study a Bohlin Rheometer CS was used to measure the shear storage modulus and loss modulus of PE0, PE2 and PA-6 resins as well as a PE0/PE2/PA-6 (60/20/20) blend. Test samples were prepared by compression molding of resins at 230°C. The rheometer was preheated up to the desired temperature, plates were adjusted to the exact distance, i.e. 1 mm, samples were placed between the plates, and heating was continued until steady state conditions was reached. The following settings were used for all the experiments:

Temperature: 250 and 270°C

Gap size: 1 mm

Shear strain (constant): 1.0E-2

Frequency range: 0.01-10 HZ

For the ADMER/EVOH system, results obtained by Lohfink (18) were used.

4.1.3 Maleic Anhydride Content Determination

Maleated polyethylene (PE1 and PE2) is obtained by grafting maleic anhydride on the polyethylene backbone and ADMER is anhydride modified polypropylene. Anhydride modified polyolefins are made to overcome the non-polarity of these polymers which results in lack of adhesion to other polymers or they could be used as potential compatibilizers for polyolefin blends. Two different methods might be used to determine maleic anhydride content of maleated ployolefins. These two methods include, Furier Transform Infrared Spectroscopy (FTIR) and the acid/base titration. Previous work (18, 19) showed that low maleic anhydride levels (below 1%) cannot be identified by FTIR. Thus, the titration method, which yields reasonable accuracy (125) was used to measure the maleic anhydride content of resins.

About 1-1.5 grams of polymer was weighed exactly and dissolved in hot, refluxing water saturated xylene. The solution was constantly stirred to assure the homogeneity. The hot solution was titrated with 0.005 N, KOH in isopropyl alcohol, using 6-7 drops of thymol blue in DMF as the indicator. The end point was detected by the change of the solution color from yellow to blue. 1 ml excess KOH solution was added and the dark blue color of solution was back titrated to yellow by using 0.005 N, HCL in isopropyl alcohol. It should be mentioned that because of the precipitation of the polymer, the solution process was limited to 1.5 grams of polymer in 150 ml of xylene. The results of MAH content measurements of individual resins are shown in Table 4.2. The MAH contents of blends were also measured and found to follow the addition rule closely.

4.1.4 PVT Experiments

To measure the interfacial tension of polymer pairs, melt density of resins at different temperatures is needed. To our knowledge, there are no reported pressure-volume-temperature (PVT) data for maleated polyolefins and EVOH resins or their blends. Few reports have been published concerning the PVT behavior of polymer blends (123). Therefore, it was decided to conduct a detailed evaluation of the PVT behavior of resins used in this study, including the HDPE/PA-6 blends and the effect of level of compatibilizing agent on PVT behavior of blends of HDPE and PA-6.

4.1.4.1 Density Measurements at Room Temperature

To study the PVT behavior of resins, the specific volume/density of the resins at room temperature and atmospheric pressure is needed. For the individual resins, the values of specific volume provided by manufacturers of the resins were used. Specific gravity and density of blends were measured according to test method ASTM-D792-B. A 25 ml pycnometer equipped with a thermometer having five divisions per °C was used. As the density of the blends is slightly more than that of water, air-free distilled water was used as the immersion liquid. Each measurement was repeated three times, and average of three values is reported.

4.1.4.2 PVT Apparatus

The apparatus used is a commercially available PVT apparatus based on principles described by Zoller (126, 127). Figure 1 shows the schematic drawing of the PVT apparatus. 1-2 grams of the polymer are weighed and placed in a steel cell with flexible bellows at one end. The total volume of the cell is 7.0-7.5 cm³. The cell is filled with mercury as the confining fluid. Other fluids may be used as well, provided they do not interact with the sample and their PVT properties are known. However, the PVT behavior of any arbitrary confining fluid might be measured in the PVT apparatus itself in a previous

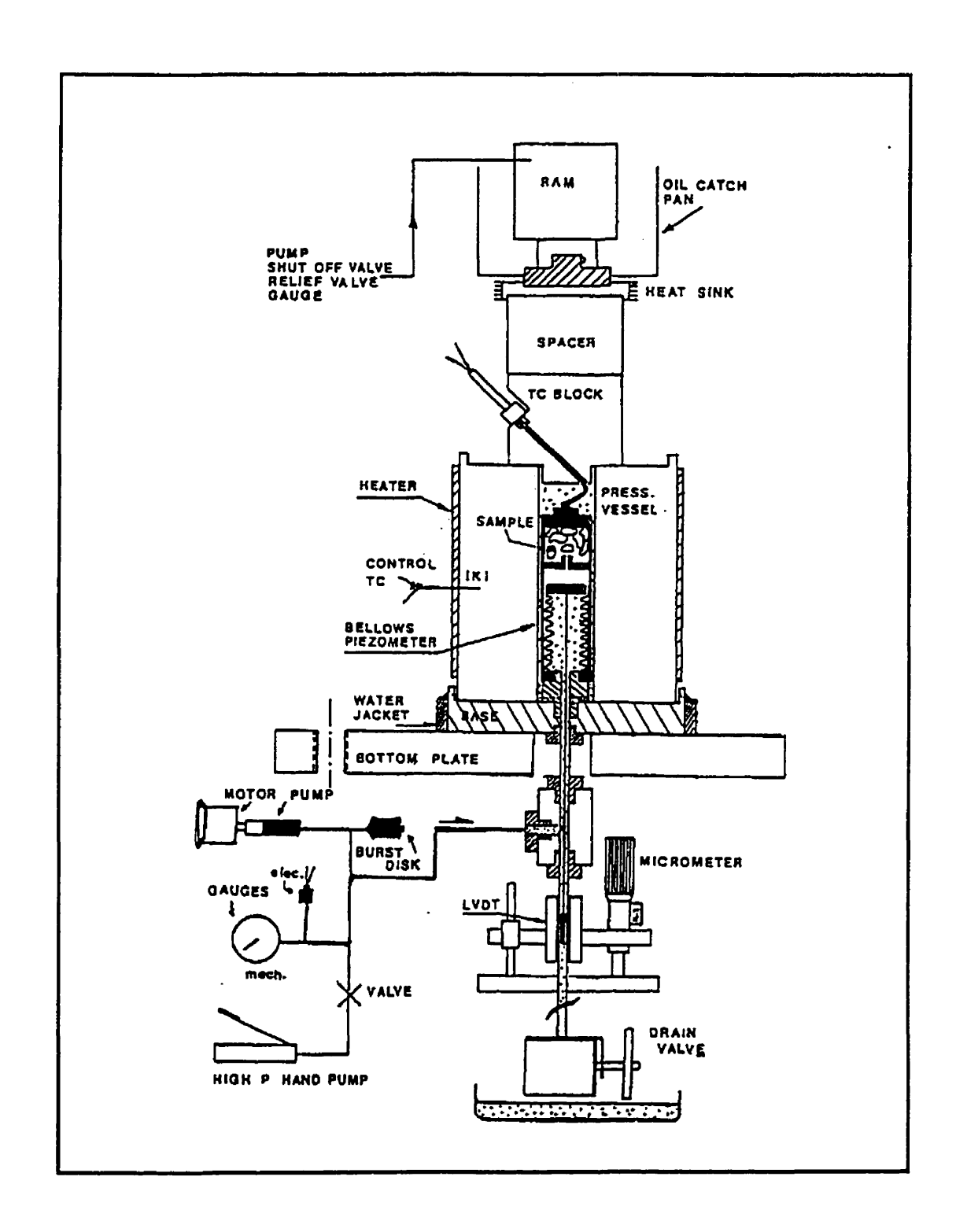


Figure 4.1: Schematic drawing of the PVT apparatus

run. The sealed cell is placed inside a vessel that is under the hydraulic pressure of a special silicon oil (Dow Corning 210H). The hydrostatic pressure of silicon oil is produced by a high pressure motorized/manual pump. The pump can provide pressures up to 200 MPa. This pressure is transmitted to the contents of the cell, including the polymer sample, by the flexible bellows. The deformation of the bellows is a measure for volume changes of the contents of the cell, provided the effective cross section of the bellows is known. A linear variable differential transducer (LVDT) located below the pressure vessel, measures the deflection of the bellows as a result of temperature and/or pressure changes. The deflection is measured with a resolution of 0.001 mm, representing a volume change of approximately 0.0001cm³. Using the known PVT properties of the confining fluid (mercury), the deflections are converted to volume changes of the sample. pressure vessel is sealed in two places (at the interface to the base and to the thermocouple block on top) by vertical force of a 25 ton hydraulic ram, mounted on a support plate above the PVT apparatus assembly. The thermocouple block on top includes a high pressure thermocouple (type K). The sheathed end is located in the steel closing nut of the cell, close to the sample in the cell. This thermocouple measures the sample temperature. A separate thermocouple is used for the temperature controller, which is located in a hole drilled about 1.3 cm into the side of the pressure vessel. This thermocouple measures the metal temperature. A temperature calibration is needed to relate the sample temperature to the controlled temperature. The calibration should be redone whenever any changes or repair is carried out.

4.1.4.3 Calibration Run

It is necessary to do a calibration run for each cell and confining fluid being used for the measurements. For a calibration run, the piezometer cell is filled with confining fluid only. Then, the cell is put in the apparatus and a calibration run is done between room temperature and 400°C and pressure from 0 to 200 MPa. In order to compensate for the associated volume changes of the mercury, the obtained results are kept in a file and are

used as the basis for all the runs with the same cell. Also, these results could be used to check the accuracy of the apparatus.

4.1.4.4 Experimental Procedure

The polymer sample, in the shape of pellets or small pieces cut from the extruded ribbons, was dried overnight in a vacuum oven at 80°C. A small nickel cup was made from nickel foil with the use of a supplied aluminum conical mandrel and weighed to 0.01 mg. use of the nickel cup is for keeping the hydrostatic pressure for both the solid and molten polymer sample inside the cell. All parts of the cell were weighed to 0.001 gram. bellows was mounted on the filler base, which was used to fill the cell with mercury. The filler had a cylindrical steel container with a base, on which the piezometer cell could be screwed. Next the bellows was either compressed or stretched so that it had a relaxed length which required a slight compression (about 0.5 mm) to constrain it to the fixed length determined by a set screw in the filler base. This step is to assure that the whole volume of the cell would be filled with the mercury and the sample. The bellows was then removed from the filler base. The nickel cup was placed in the sample compartment which is a part of the cell assembly. The length of the nickel cup was such that the partition of the cell slightly compressed the rim of the cup. The polymer sample was weighed to 0.01 mg and placed in this cup. Then, different parts of the cell including the sample compartment, central piece and the bellows were put together with the help of ring nuts. Gasket rings were placed between parts to seal the cell assembly properly. The cell parts were tightened.

The next step was to fill the assembled cell with confining fluid, i.e. mercury. The assembled cell was mounted on the filler base. To fix the overall volume of the cell for the run, the constraining rod was inserted and threaded into the end of the bellows. The rod was positioned so that the set screw in the filler base was engaged in the groove in the constraining rod. The cell was connected to the reservoir of mercury with a flexible tube. While the filler base was placed in a tray inside the hood, employing a syringe about 10-12 cm³ of fresh, clean mercury was poured into the mercury reservoir. Then, the cell

assembly mounted on filler base, was placed in the vacuum vessel with the reservoir on top and piezometer cell on the bottom. While keeping the vessel in the 45° position, the whole assembly was connected to a vacuum pump, to a vacuum of better than 4×10^{-2} mm When the required vacuum was reached, the vessel was tilted slowly past the Hg. horizontal, until it came to rest against the stop provided. This tilting would permit the mercury to flow from the reservoir into the sample cell. The assembly was kept 3-5 min in this position to assure of filling of the cell. While the vacuum vessel was still against the stop, the vacuum pump was turned off. Over a period of 15 seconds, the air was admitted through the valve to reduce the vacuum to about 15 inches of Hg. vacuum vessel was moved back to its upright position. The valve was opened completely to reach atmospheric pressure. The vessel was opened and the filler base was withdrawn from it. The flexible tube was disconnected from the filler, and the remaining mercury in the tube was emptied into the end of the cell. Employing a vacuum suction device, the excess mercury was sucked up until the meniscus of the fluid was exactly at the top of the small bore leading into the sample compartment. A steel sealing disk was placed into the end piece, was centered, and with the use of cell closure nut, the seal was sealed. The set screw in the base of the filler device was released from the groove in the restraining rod. The assembled cell was unscrewed from the base, and the fully assembled cell was weighed to 0.001 gram to find the mass of mercury used.

At this step, the assembled cell, containing nickel cup, polymer sample, and mercury should be mounted to the base of the PVT apparatus. The LVDT core, which was mounted at the end of a long thin tube, was lifted up far enough to be able to screw its end into the inside end of the bellows. The sample cell was screwed to the adapter piece in the base of the PVT apparatus. The pressure vessel, which is a thick steel cylinder with heaters, was put in place by carefully lowering it over the sample cell. The control thermocouple was placed into the side-hole of the pressure vessel. Then, the thermocouple block was put in place on top of the pressure vessel, making sure that the thermocouple tip entered the conical opening in the piezometer cell closure nut. The spacer was added to the top of the thermocouple block and the finned aluminum heat sink was added to the top of the spacer block. Then, the ram piston was lowered with the help

of the hand pump and a pressure of 62 MPa was applied to the ram. A pressure of 200 MPa was applied manually to the pressure vessel with the high pressure pump to fill the pressure vessel with the silicon oil and for inspecting of any possible leakage.

4.1.4.5 LVDT Calibration

There should be a linear relationship between the output voltage and the micrometer reading. The purpose of the LVDT calibration is to find this linear relationship, which might be different from one run to another one. Therefore, initially the output voltage of the LVDT was set at zero to within 0.01 volt, by moving the micrometer. The corresponding micrometer reading and the exact voltage were the zero point for the run. Then, the micrometer was moved in steps of 1.0 mm (within 0.1 mm) within a range of ±4.0 mm from the zero point, and the corresponding voltage and micrometer readings were read. After the final reading, a linear regression was done on the micrometer readings and the output voltage by the PVT software. If the deviation between the experimental and fitted values was less than 0.003 mm, the LVDT calibration was accepted; if not, another calibration was conducted.

4.1.4.6 Method Used

This study covers the temperature range of 30-290°C and pressures up to 100 MPa. In order to obtain the required PVT data, the isothermal mode of the apparatus was used. Selecting of the isotherms depends on the materials and their transitions and processing temperatures. For all the samples, a few runs around room temperature were done, to get the values of additional volume. These isothermal runs were done at 30, 40, 50, and 60°C. Therefore, the specific volume at zero pressure and initialization temperature was obtained. The PVT apparatus indicates the changes in the specific volume, and knowing the additional volume at initialization conditions yields the exact value of specific volume. For materials like EVOH and PA-6 which show a T_g above room temperature, a few isotherms with intervals of

10°C were selected around the T_g as well as around the melting range of all the polymers. To cover the whole range of the temperature, some isotherms before the melting point were considered. The required data for this study are the data above the melting point, i.e. in the range of processing temperature. To avoid degradation of polymers, the intervals above the melting point was 20°C. Although the apparatus can be used up to 200 MPa, in order to avoid thermal degradation of the polymers and to minimize the residence time of the polymers at high temperatures, the maximum pressure was fixed at 100 MPa. This pressure covers the applicable pressure range for processing of the polymers. For better accuracy, a holding time of 20 sec was used at each pressure. The pressure was changed from 10 to 100 MPa in 10 MPa increments. The value for zero pressure was calculated by extrapolation.

4.1.5 Interfacial Tension Measurements

As explained earlier (chapter 2), interfacial tension is one of the key parameters that affect morphology development during processing of polymer blends. Furthermore, the final properties of the polymer blends are determined, to a large extent, by the morphology as well as the interfacial adhesion between the blend components in the solid state. Interfacial adhesion in the solid state, is determined directly by the interfacial tension of molten polymers. Therefore, knowledge of interfacial tension is of great interest for blend technology.

Different methods have been used to measure the interfacial tension of polymer pairs. The most versatile method is the pendant drop method in which a drop of one of the molten polymers (more dense polymer) is suspended into a pool of the other molten polymer (lower density polymer) and is allowed to reach the equilibrium shape under influence of gravity (128-130). This technique relies on a force balance between interfacial tension and gravitational forces. Although, the pendant drop method provides reliable results, it tends to be a slow and time consuming process. In the case of viscous polymer melts, which are encountered in this study, many hours are needed for the equilibrium shape to be obtained. This problem presented a most serious limitation for the PEO/PA-6

pair. Another major limitation that makes the pendant drop method unpractical for "maleated PE/PA-6" and "ADMER/EVOH" pairs is due to the strong interaction at the interface of the two polymers which prohibits the drop from reaching the equilibrium shape.

Another technique that is used to measure the interfacial tension of polymer pairs is the spinning drop method (131,132). In this technique, a drop of the less dense polymer is placed in a pool of the polymer melt of higher density contained in a horizontal glass tube. The glass tube is spun at constant high speed. Depending on the speed of the rotation, the drop will form an equilibrium cylindrical shape that is determined by centrifugal deformation forces being balanced by the interfacial tension. Due to the large centrifugal field, the time to reach to equilibrium is much shorter for the spinning drop method compared to the pendant drop technique. Thus, using the spinning drop technique, the two major limitations of the pendant drop method might be overcome. The pendant drop method was used to check the accuracy of the spinning drop technique.

4.1.5.1. Pendant Drop Method

4.1.5.1.1 Theory

Starting from the force balance between the gravity and surface tension, the mechanical equilibrium of a drop of one polymer immersed in a liquid matrix of another polymer is given by Laplace's equation (133):

$$\frac{1}{R_1} + \frac{1}{R_2} = \frac{\Delta P}{\gamma} \tag{4.3}$$

where R_1 is the radius of curvature in the plane of Figure 4.2, R_2 is the radius of curvature in a plane perpendicular to Figure 4.2, ΔP is the pressure difference across the curved interface and γ is the interfacial tension. Using Equation (4.3), Bashforth and Adams (133) proposed the following equation:

$$\frac{1}{R/a} + \frac{\sin\phi}{X/a} = B\frac{Z}{a} + 2 \tag{4.4}$$

where ϕ is the angle between the Z axis and R_1 , a is the radius of curvature at the apex of the drop, X is the abscissa, and the dimensionless quantity B is given by:

$$B = \frac{a^2 g \Delta \rho}{\gamma} \tag{4.5}$$

 $\Delta \rho$ is the density difference between two fluids and g is the gravitational acceleration.

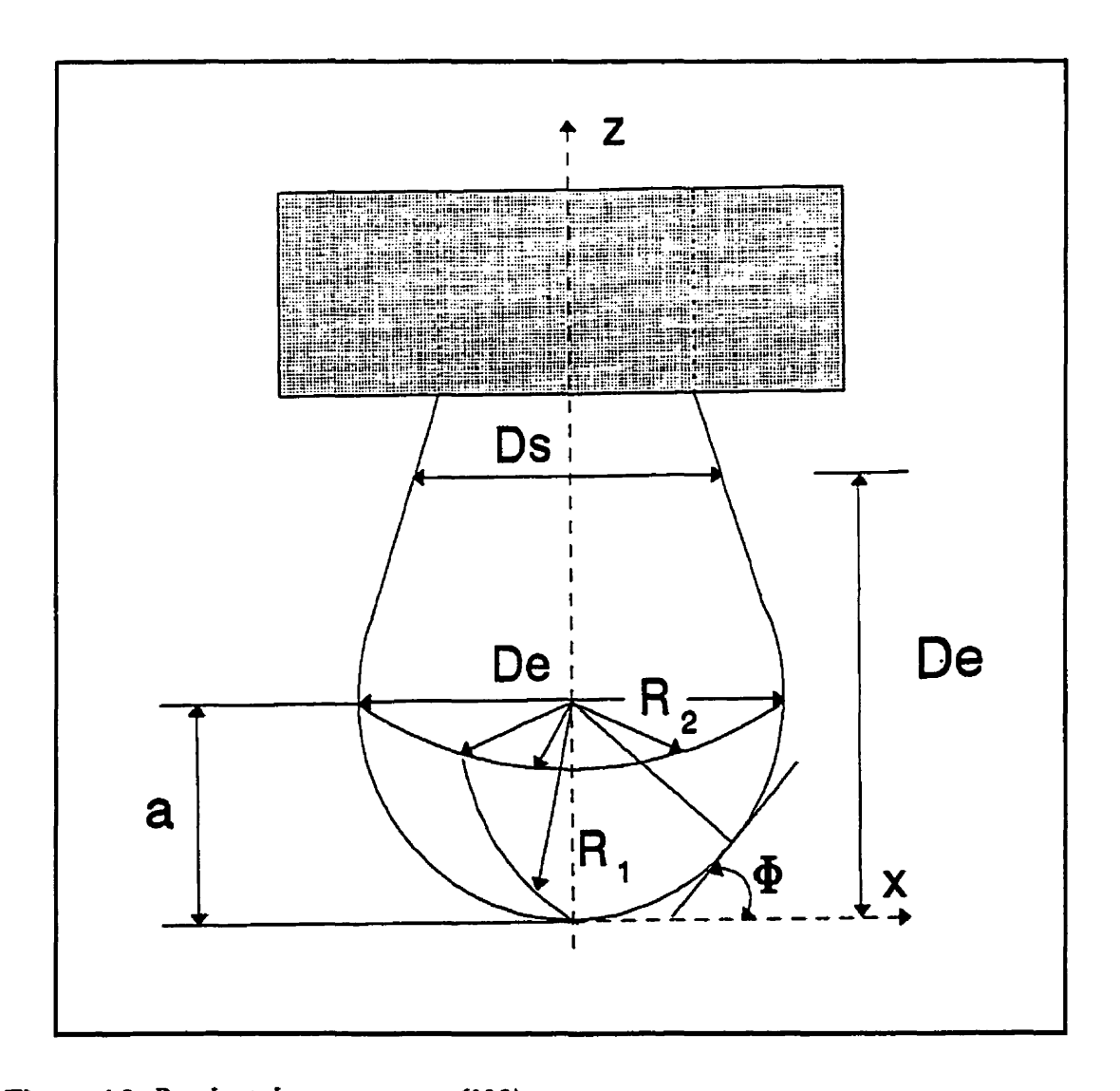


Figure 4.2: Pendant drop geometry (129)

 R_1 and ϕ are geometrical functions and are given below:

$$R_1 = \frac{ds}{d\phi} = \frac{\left\{1 + (dz/dx)^2\right\}^{3/2}}{d^2z/dx^2}$$
 (4.6)

$$\sin \phi = \frac{dz/dx}{\{1 + (dz/dx)^2\}^{1/2}}$$
(4.7)

The Bashforth and Adams equation, which relates the drop profile to interfacial tension, is a non-linear differential equation between x and z. In this equation R, x, and z appear as ratios to the radius of curvature at the apex of the drop. Thus, for the same value of B, the drop keeps the same shape, irrespective of its volume.

4.1.5.1.2 Experimental Assembly

The core part of the apparatus consists of an oven in which a quartz cell filled with the less dense polymer and the drop insertion device, containing the polymer with lower density, are heated. The other parts of the apparatus include the light source, an optical system to capture the digitized image of the drop, and a data acquisition system with a PC computer to compute the interfacial tension from the drop profile. Figure 4.3 shows the different parts of the apparatus. The apparatus has been described in more detail by Demarquette and Kamal (129).

Computer programs are used for edge detection, smoothing the drop profile and finally shape comparison program, which provides the optimal value of the dimensionless parameter of B (134). The value of a, radius of the curvature at the apex of the drop, is obtained using a curve fitting program. The criterion to accept the value of a is, having overall error of less than 1% between the experimental drop profile and the fitted circle, with the biggest radius of curvature at the apex. Then, the interfacial tension is obtained from the following equation:

$$\gamma = \frac{a^2 g \Delta \rho}{B} \tag{4.8}$$

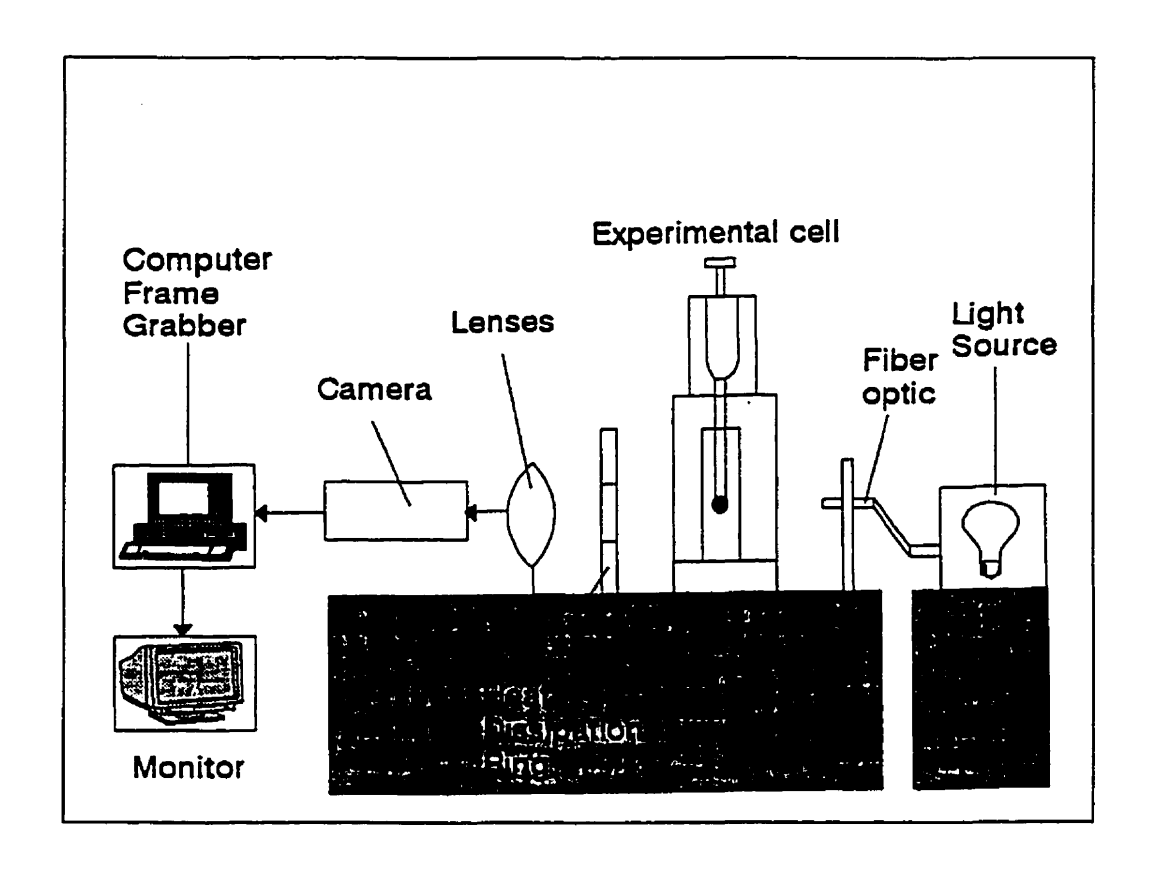


Figure 4.3: Experimental assembly for pendant drop apparatus (134)

where B is the dimensionless quantity described by Equation (4.5).

4.1.5.1.3 Experimental Procedure

The heavier phase (PA-6 and EVOH) was shaped by extrusion in a Capillary Rheometer using a die with diameter of 0.762 mm. The less dense polymer (HDPE and ADMER) was compression molded and then cut to the dimensions of the experimental cell. The samples were dried in a vacuum oven overnight at 80°C. The syringe (drop insertion device) containing the higher density polymer was assembled in the controlled temperature support. The syringe (containing the heavier phase) and the cell (containing the lower density phase) were heated up to the desired temperature. The syringe was then pushed

into the pool (less dense polymer) until the tip of the syringe reached the level of the optical path. The experiment started 15 min after thermal equilibrium was reached. The drop of the polymer with higher density was then gently extruded into the pool. The experimental cell was sealed and was kept under a small positive pressure of argon to protect the polymers from degradation.

The drop profile was analyzed every 15 min during the experiment until two consecutive measurement of interfacial tension, using Equation (4.8), varied by less than 2%. Thereafter, measurements were taken every 10 min for 2 hr. If no variation of more than 2% between the measurements was observed, it was assumed that the mechanical equilibrium of the drop was reached, and the value of interfacial tension during the last 2 hours were averaged and reported as the interfacial tension at the desired temperature.

4.1.5.2 Spinning Drop Method

4.1.5.2.1 Theory

This method was first introduced by Vonnegut (135) and later was modified by different investigators (131, 132, 136 and 137). In this method a drop of fluid 1 (lighter phase) is made to rotate inside a glass tube which is filled with fluid 2 (denser phase). The axis of the cylinder is strictly horizontal and rotation speed is high enough for gravity effects to be negligible. The drop elongates until it reaches its equilibrium shape. Interfacial tension γ can be determined by doing a balance between the centrifugal forces and tension due to interfacial forces (Figure 4.4). This results in the following equation:

$$\gamma = \frac{\Delta \rho \omega^2 d^3}{8J_D(l/d)} \tag{4.9}$$

where

 γ = interfacial tension (dyne/cm)

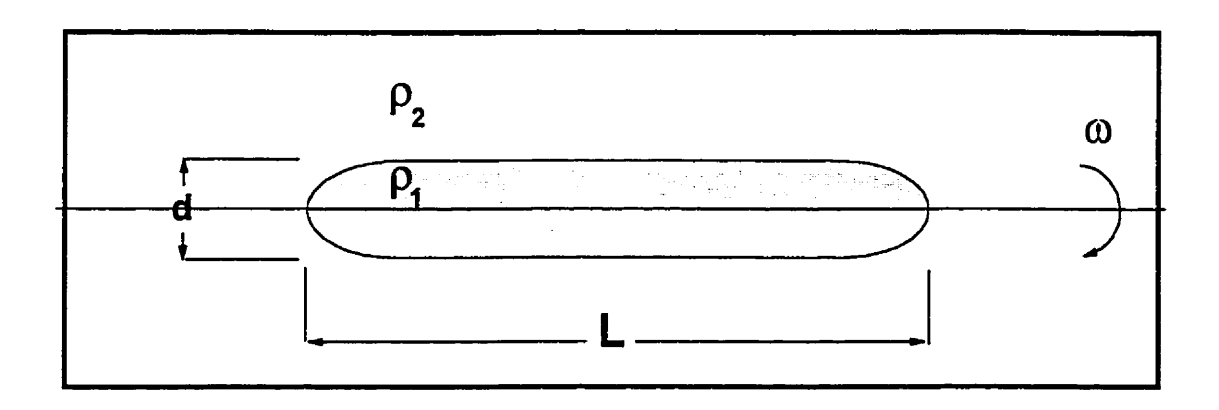


Figure 4.4: Schematic of an elongated spinning drop

 $\Delta \rho$ =density difference ($\rho_2 - \rho_1$) between the two fluids (gr/cm)

 ω = rotational speed (rpm)

d = the diameter of the cylindrical droplet (cm).

 J_D is a constant which is equal to 4 where 1/d > 4, as reported in Seeto (138). If the rotation speed is sufficiently high and/or the initial volume of the drop is selected properly, 1/d > 4 could be satisfied. Thus, Equation (4.9) can be reduced to:

$$\gamma = \frac{\Delta \rho \omega^2 d^3}{32} \tag{4.10}$$

It has been shown that Equation (4.10) introduces an error of about 0.4% when 1/d=4 (138). More details about the evaluating J_D (1/d) can be found in Manning (139).

4.1.5.2.2 Experimental Apparatus

The apparatus consists of a motor that rotates the shaft attached to a glass tube containing the polymers, an oven and a capacitance probe. The motor was a DC motor (from Nu-

Tech Ind.), and rotation speed was controlled with the power supply up to 40,000 rpm. The speed of the motor was checked independently using a Tachometer. The motor and the bearing are mounted on precision rods (for precise alignment) away from the oven to avoid heating. The special high speed ball bearings are located on cooling fans. The oven consists of two parts, the top one is removable and the bottom one sits on a maronite support to thermally isolate it from the aluminum table. It contains two windows (one on each side of the oven), allowing the viewing of the glass tube and polymer. A light source provides the illumination of the polymer. Two thermocouples inserted at the center of the oven, connected to two P.I.D. controllers, provide the accurate control of the oven temperature to within ±0.5°C. The glass tube with outside diameter of 1/2 inch and inside diameter of 3/8 inch is made of borosilicate glass. A schematic representation of the apparatus is shown in Figure 4.5. More details about the different parts of the apparatus are available elsewhere (134).

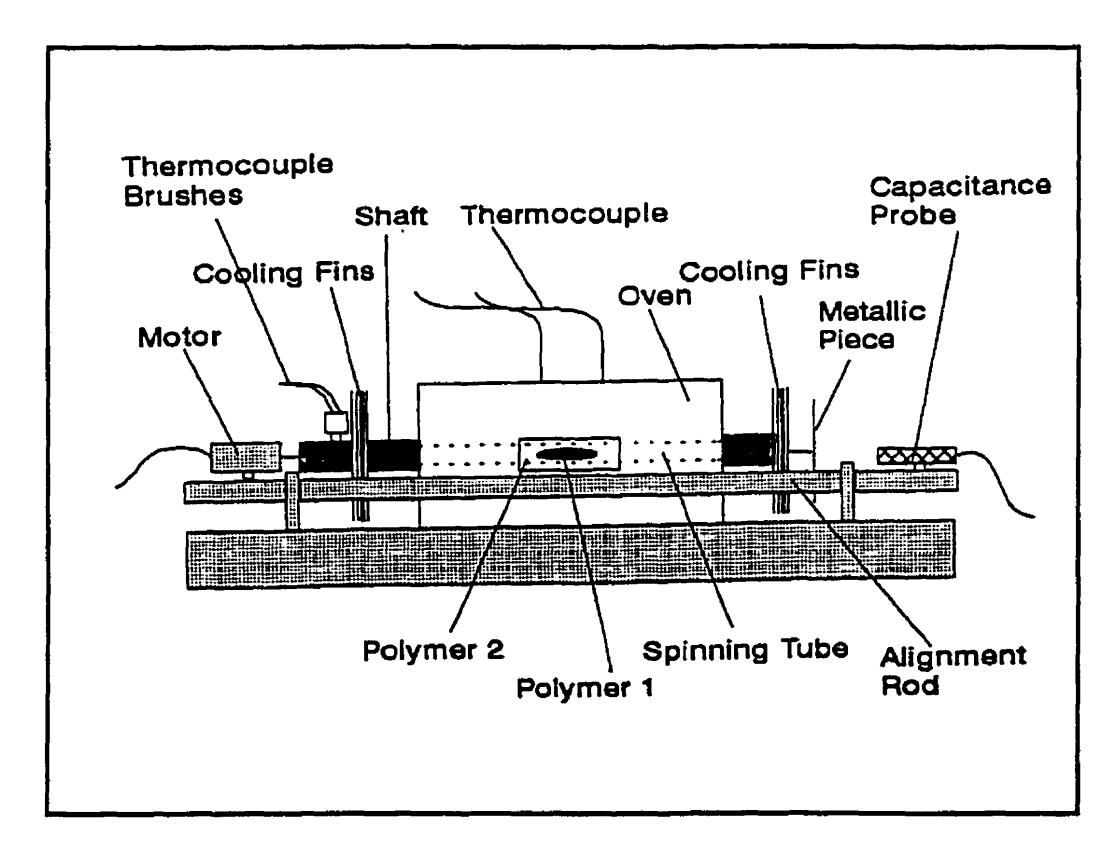


Figure 4.5: Schematic of the spinning drop apparatus (134).

4.1.5.2.3 Experimental Procedure

The denser phase (EVOH and PA-6) was extruded in the shape of the rods using a single screw extruder. The extruder was a Brabender type 125-25 with a screw diameter of 31.75 mm and a L/D ratio of 25. The diameter of the rod was controlled through changing the speed of the take-off system. Then the extruded rod was cut to the desired length and a hole was drilled in the center. In order to keep the melted polymer inside the hole, the hole length was shorter than the diameter of the rod. The polymer forming the drop (ADMER and HDPE) was prepared using a twin-screw extruder. The twin-screw extruder was a 25 mm, co-rotating intermeshing extruder and L/D ratio of 28 was used. The extrudate was led into a pelletizer to get the cylindrical pellets with desired diameter. Then a pellet was inserted inside the hole of the cylinder made from the heavier phase.

The polymers were dried in a vacuum oven at 80°C overnight. Then they were introduced inside the glass tube between the two plungers. One plunger is sealed using vacuum grease and the other one is left unsealed to apply vacuum to the glass tube. The tube was then mounted in place in the shaft of the apparatus. The vacuum was applied and the sample was heated progressively to prevent the glass tube from breaking by thermal stresses. Once the polymers were melted, the vacuum was discontinued and the polymers were left to reach the desired temperature. When the set point in temperature was reached, the plunger was locked in place to avoid movement during rotation and to prevent polymer and air leakage. Using the OCULUS-TCX/MX frame grabber software from CORRECO, the image of the drop was taken every 10 min and the length and diameter of the drop was measured. To record the rapid changes of the drop at the early stages of the experiment, the image was taken every 30sec. Once the diameter of the drop did not change for 1 hr, it was assumed that the equilibrium has been reached and the values of diameter during the last 1 hour were averaged and interfacial tension was calculated using Equation (4.10). As there is some discrepancy between the temperature of the polymer and the measured temperature of the oven, a temperature calibration was conducted for each polymer.

4.1.5.2.4 Measurement of Optical Enlargement and Correction Factors

The measured dimensions of the drop should be corrected for optical enlargement of the system and for the combined refractive index of polymer 2 (matrix) and the glass. A standard rod was used to obtain the optical enlargement factor. There are two methods for measuring the optical correction factor. Although, theoretical approaches have been developed to evaluate the combined refractive index of two materials (138), it is easier to determine the optical correction factor experimentally as reported in earlier work (139). A standard rod with known diameter (d rod) was inserted in polymer 2 (matrix) inside the glass tube that was filled with molten polymer. The apparent diameter of the rod, d app was measured at different temperatures. The optical correction factor was defined as follows:

$$n = \frac{d_{app}}{d_{md}} \tag{4-11}$$

4.2 Processing

4.2.1 Processing Equipment

4.2.1.1 Twin-Screw Extruder

The twin-screw extruder was used for compounding the materials prior to processing in the single screw extruder and to achieve desired level of distributive mixing, while avoiding extensive dispersive mixing. The twin-screw extruder was a 25 mm, co-rotating intermeshing extruder with L/D ratio of 28, manufactured by BERSTORFF (model ZE25). The twin-screw extruder was used either for compounding of PE0 with PE2 to obtain the desired level of maleation or for compounding of PE0, PE2 and PA-6 and for preparing pellets of blend to feed to the single screw extruder.

4.2.1.2 Single Screw Extruder

The single screw extruder was a Brabender 125-25 with screw diameter of 31.75 mm and L/D ratio of 25. Two types of screw design, metering and mixing, were used to demonstrate the feasibility of developing laminar morphology in both cases. The two screws were designed to provide the same extrusion characteristics, except in the metering zone where the mixing screw had an extra channel with higher pitch which provides more mixing. Detailed design of screws and barrel are given in Appendix A.

4.2.1.3 Die Unit

The single screw extruder was equipped with a slit die, specifically designed for producing extensional deformations, which are believed to assist in stretching the minor phase particles and developing laminar morphology (18). The die and adapter were designed so that the dispersed phase undergoes two-dimensional stretching in the plane of the flow, as shown in Figure 4.6. In sections A and C, the flow field is dominated by converging extensional flow; in section B shear flow is dominant; in section D (in the X-Y plane), shear flow is dominant, while in the X-Z plane, diverging extensional flow prevails. In section E, converging extensional flow becomes dominant again, while in section F shear flow prevails. Therefore, in sections A, C and E the fluid particles are stretched in the flow direction and in section D in the transverse direction. This biaxial stretching is expected to produce platelets and to develop laminar morphology. Detailed analysis of flow kinematics inside the die (18) has verified the deformation pattern indicated. To evaluate the effect of coalescence on the obtained morphology, two adapters with 30° and 70° were used.

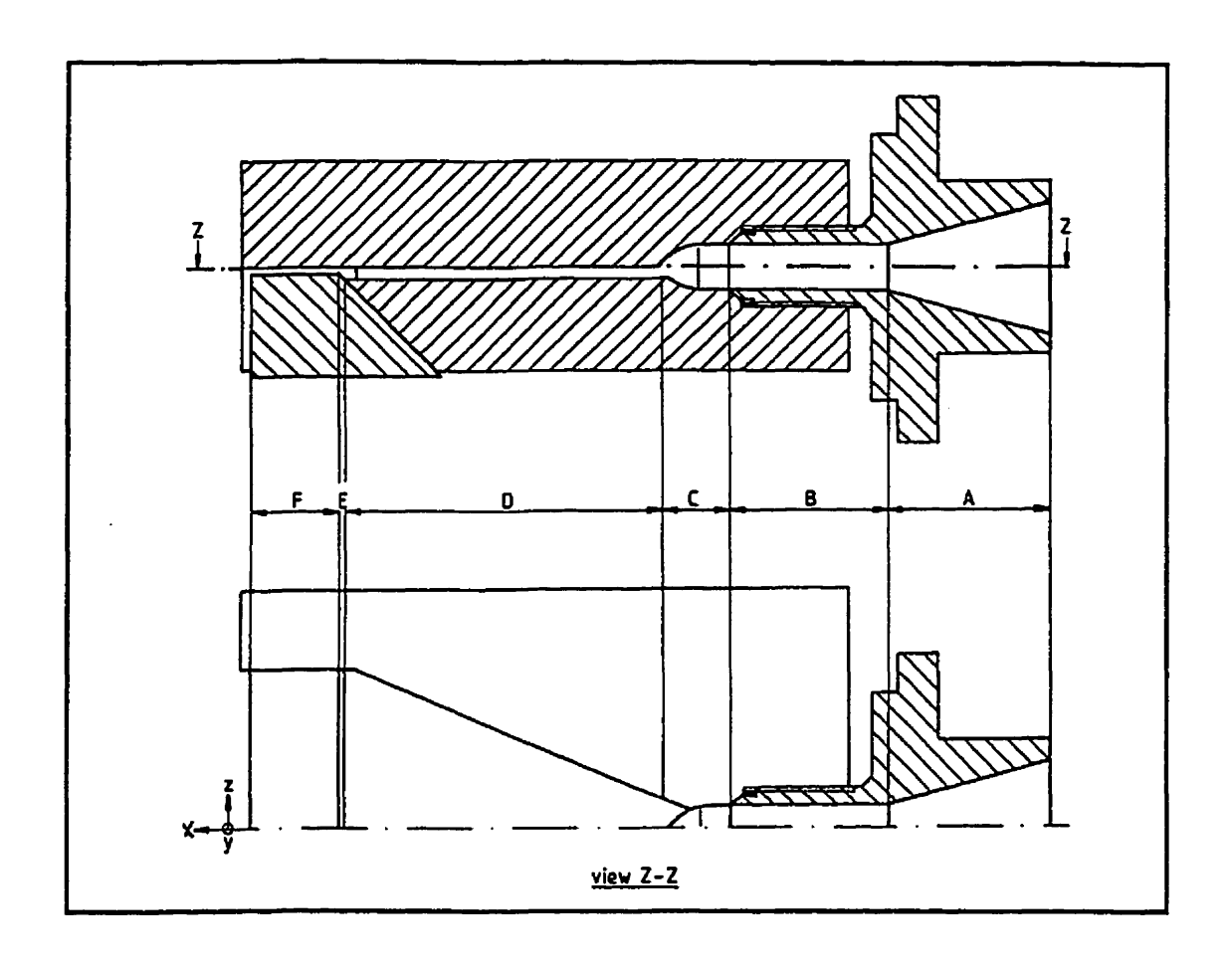


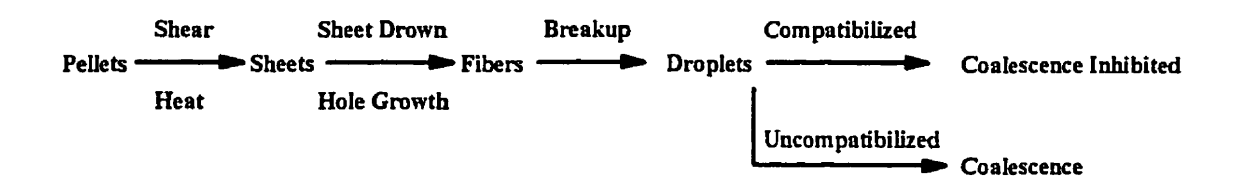
Figure 4.6: Schematic of the die unit (18).

4.2.1.4 Take-off system

A variable speed flat belt conveyer served as the take-off system. The take-off speed was adjusted to be the same as extrudate velocity, in order to prevent stretching of the extrudate after exiting from die. Two different systems of cooling were used: air-cooling and water-cooling. In the case of air cooling, a series of air fans were used. In order to prevent sticking of polymer melt to the cooling apparatus, TEFLON coated rods were used for the support.

4.2.2 Processing Conditions

During the mixing process, pellets of the minor phase undergo five main stages of deformation and breakup which can be summarized as follows (118):



To develop laminar morphology, it is necessary to stop the above steps of deformation and breakup after the sheets of the minor phase are formed. To achieve this goal, the temperature in the screw zone should be kept as low as possible and preferably below the melting point of the minor phase (i.e. the higher melting point component). In order to assure the melting of the polymer mass before entering the die, the last zone should be kept above the melting point of the minor phase. In view of the above, it is important to have precise control of process heaters, shear rates, shear heating, and residence time of the melt inside the extruder.

4.2.2.1 HDPE/PA-6

4.2.2.1.1 Single Screw Extrusion Using Dry Blends

Due to the large difference between the melting points of the two components (135°C for HDPE and 220°C for PA-6), the processing window is wide enough to satisfy the desired temperature profile in the screw zone. To evaluate the effect of processing temperature distribution, five different temperature profiles along the barrel and die were examined. Although, a die temperature of 250°C provides the viscosity ratio of about unity (section 5.1) that is believed to produce maximum deformation of PA-6 particles, two other die temperatures, 230 and 270°C were also examined. Both mixing and metering screws were used to demonstrate the feasibility of producing laminar morphology in the two cases.

Table 4.3: Processing Conditions for HDPE/PA-6 Blends: Single Screw Extrusion

Processing Parameter	Tested Condition		
Temperature profile #1: Temperature profile #2: Temperature profile #3: Temperature profile #4: Temperature profile #5:	215, 220, 225, 230 Die=230°C 220, 230, 240, 250 Die=250°C 220, 240, 260, 270 Die=270°C 190, 200, 210, 230 Die=250°C 180, 190, 200, 225 Die=250°C		
Screw Design (single screw extruder)	Mixing, Metering		
Die Exit Gap (mm)	0.25, 0.5, 1.0		
Adapter Angle (°)	30,70		
RPM	30,60		
Composition (HDPE/PA-6 wt %)	90/10, 80/20, 70/30		
MAH Content	0.0, 0.0035, 0.007, 0.014, 0.028, 0.056		

Different MAH contents were utilized, in order to find the optimum level of MAH needed to achieve both good mechanical properties and good barrier properties. A summary of the processing conditions is presented in Table 4.3. Detailed processing conditions for each sample are listed in Appendix B.

4.2.2.1.2 Twin-Screw Compounding

In order to optimize twin-screw compounding, three important parameters should be manipulated carefully. These parameters are screw configuration, temperature profile, and blending sequence.

(a) Screw Configuration: In order to obtain good distributive mixing while maintaining low dispersive mixing, it was decided to use only conveying elements throughout the screw

length. The temperature profile was chosen in a way that melting of PA-6 is delayed until the last zone of extruder. To ensure the melting of the polymer mass before entering the die, a kneading block was placed as the last element. This screw configuration provides both low shear rate and minimum residence time inside the extruder.

The following screw configuration, which is shown in Figure 4.7, was used for all the twin-screw runs:

1×25mm	7×37.5	2×37.5	8×25	6×25	1×37.5	
s.w.	S.E.	s.w.	S.E.	s.w.	K.B.(45°)	

Where S.W. stands for self-wiping, S.E. for simple element, and K.B. for kneading block. Using the above screw configuration at 60 RPM and feeder rate of 350 provides a residence time of about 50 sec.

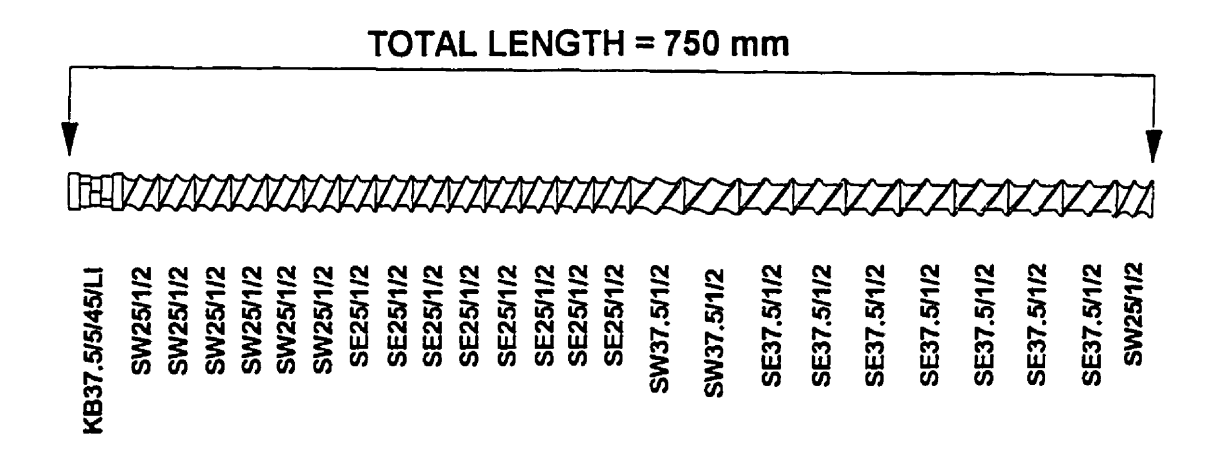


Figure 4.7: Optimized screw configuration for twin-screw compounding of HDPE/PA-6 blends

(b) Processing Temperature: The temperature profile along the screw should be chosen in a way that the dispersed phase melted just before entering the die. Considering the melting point of PA-6, i.e. 220°C, after some preliminary runs, the following temperature profile was found to be close to the optimum processing temperature to achieve the desired goals:

zone 1	zone 2	zone 3	zone 4	zone 5	head flange
180°C	190°C	200°C	200°C	225°C	230°C

Therefore, it is expected that melting of the dispersed phase (PA-6) particles starts in zone #5, and before any extra mixing the melt reaches the end of the screw zone and enters the die. Considering the total residence time of 50 sec., it is estimated that the residence time of melted PA-6 in the screw zone should be less than 10 sec.

(c) Blending Sequence: To evaluate the effect of sequence of blending, different methods were used to mix the components of the blend (i.e. PE0, PA-6, and PE2). Figure 4.8 shows the different sequences of compounding and extrusion that were used.

4.2.2.2 PP/EVOH

As the temperature difference between the melting points of the two components is small (160°C for ADMER and 181°C for EVOH), the processing window is narrow for this system. Therefore, it was not easy to satisfy the conditions explained in 4.2.2 in single screw extrusion of ADMER/EVOH blends. Based on the previous research at McGill University (17-21), the processing conditions shown in Table 4.4 were used. ADMER, i.e. a maleic anhydride grafted polypropylene with maleation content of 0.07 wt%, was used as the matrix for all the blends. Hozhabr (19) found that the maleation content of 0.07 wt% was the optimum value, considering both barrier and mechanical properties for PP/EVOH blends. Twin-screw compounding of this system was not considered.

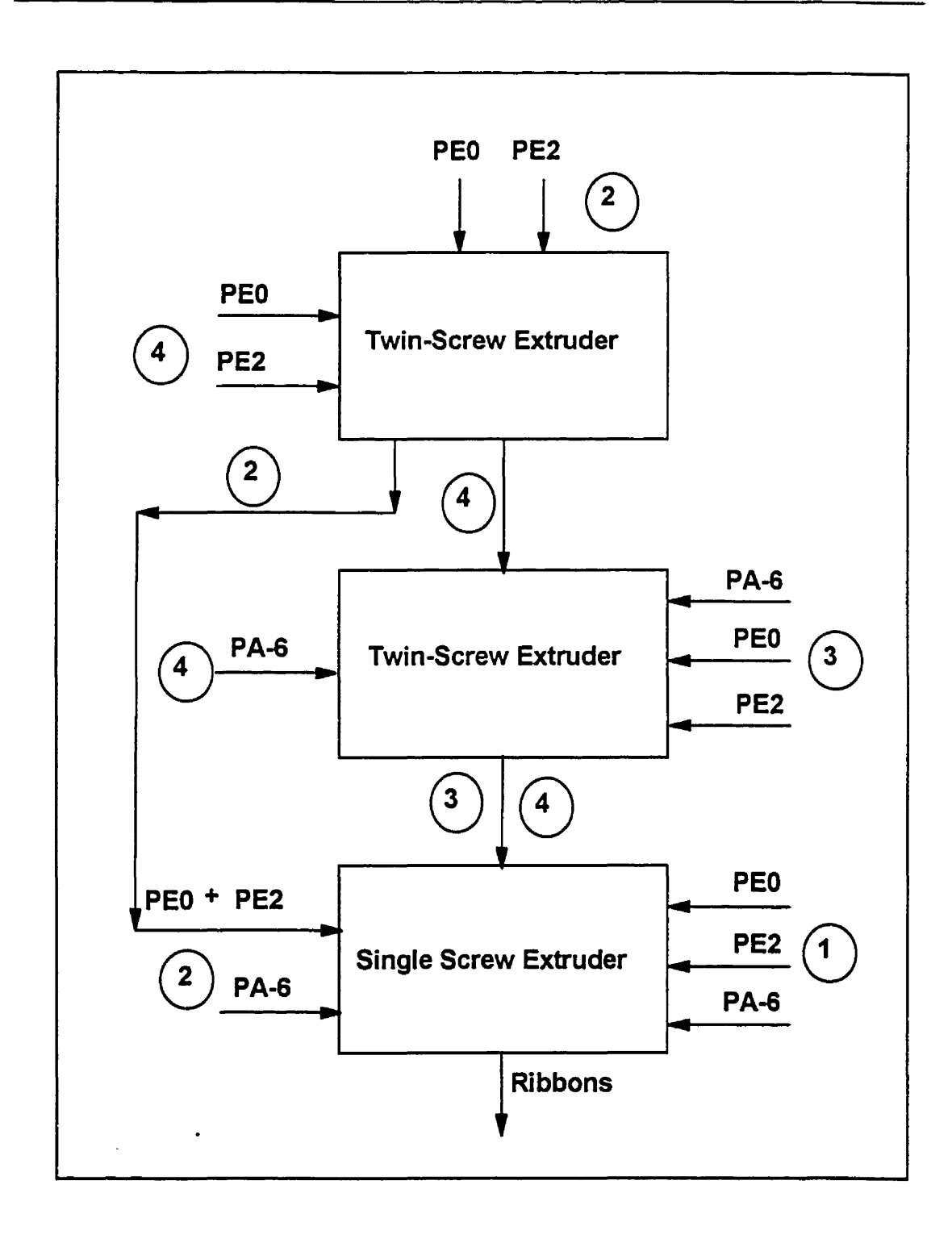


Figure 4.8: Alternative sequences of compounding and extrusion for HDPE/PA-6 blends

Table 4.4: Processing Conditions for PP/EVOH System: Single Screw Extrusion

Tested condition	Processing parameter		
Temperature profile #1: Temperature profile #2: Temperature profile #3: Temperature profile #4:	180, 200, 210, 220 Die=215°C 180, 205, 215, 230 Die=225°C 180, 205, 220, 235 Die=230°C 160, 160, 170, 180 Die=225°C		
Screw Design	Mixing, Metering		
Die Exit Gap (mm)	0.25, 0.5, 1.0		
Adapter Angle (°)	30,70		
RPM	30,60		
Composition (PP/EVOH wt%)	80/20, 75/25, 70/30		
Cooling System	Air Cooling, Water Cooling		

4.3 Product Characterization

4.3.1 Microstructural Analysis

Laminar structure implies that the minor phase exhibits large deformations both parallel and perpendicular to the flow direction. Thus, samples were examined in both the flow and transverse directions. Figure 4.9 shows the sample locations chosen for the microstructural study of the extruded ribbons. Samples 1 and 4 are parallel to the flow direction, and samples 2 and 3 are perpendicular to the flow direction. To evaluate the morphology variations across the width of the sample, locations 1 and 2 are chosen at the center of the ribbon, while locations 3 and 4 are selected close to the edge of the ribbon.

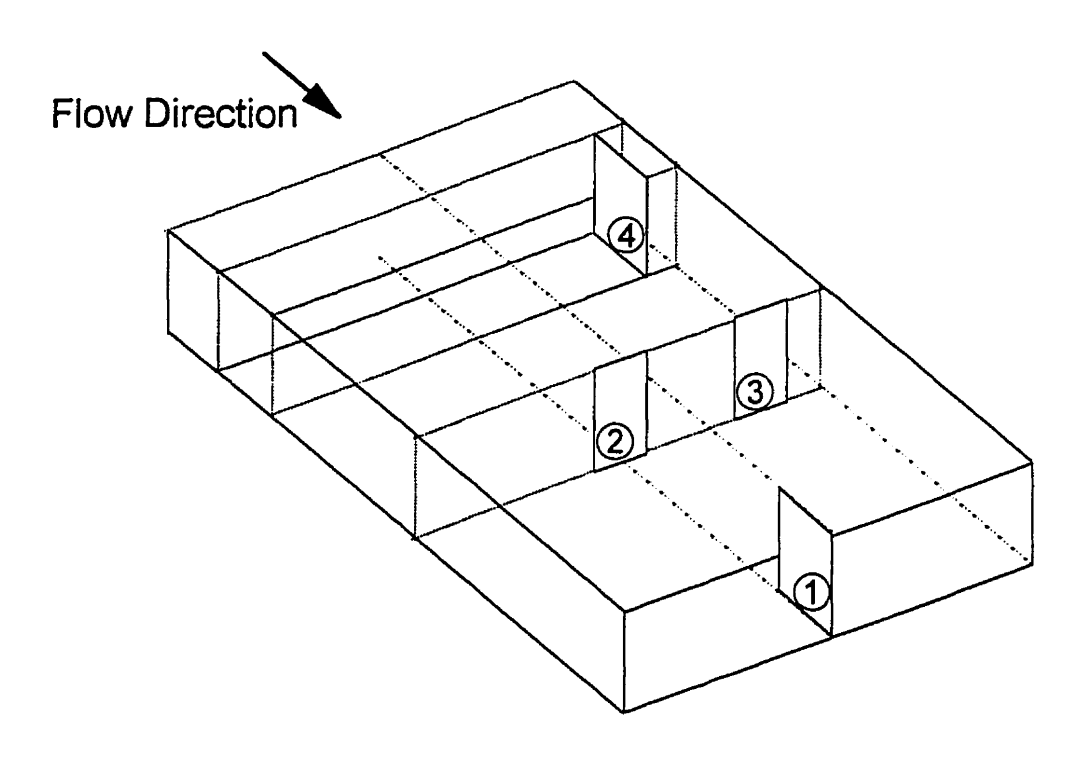


Figure 4.9: Locations of sampling for SEM and image analysis

4.3.1.1 Sample Preparation

Samples were cut from the above locations using a cutter, and the relevant faces of the samples were marked. In order to obtain undeformed plane face, the samples were microtomed cryogenically using a Reichert Ultracut S/FCS. A temperature of -170°C was selected for HDPE/PA-6 blend, and for the PP/EVOH blend, the set temperature was -100°C. In the case of HDPE/EVOH blend, HDPE has the lowest Tg, i.e. -110°C, and PP with Tg of -25°C has the lowest Tg for the PP/EVOH blend. Cooling the polymers below or near their Tg, increases their stiffness and makes them less likely to deform and smear during microtoming. Subsequently, the dispersed phase was etched out using appropriate solvent. The HDPE/PA-6 blends were etched for 1 hour with 88% formic acid, while 1,1,1,3,3,3,-hexafluro-2-propanol was used for the same period to etch the PP/EVOH blends. Then, to prepare the samples for scanning electron microscopy, they were coated with a gold/palladium alloy under vacuum in an Anatech Ltd. Hummer VI sputtering

system. The samples were coated to provide an electrically conductive layer, to suppress surface charges, to minimize radiation damage and to increase electron emission.

4.3.1.2 Scanning Electron Microscopy (SEM)

The morphology of the samples was studied using a Jeol 840 scanning Electron Microscope. After testing different accelerating voltages between 10 and 20 KV, an accelerating voltage of 20 KV that appeared to provide optimum resolution, was used. A working distance of 39 mm was used throughout this study. In order to view the whole length of the elongated particles, especially in HDPE/PA-6 samples, the minimum magnification that provided good resolution was used. Depending on the morphology of the sample, this magnification was between 80X and 600X. The areas where the dispersed phase was etched out, appeared as dark areas, whereas the matrix was more pale.

4.3.1.3 Image Analysis

A TN-8500 image analysis system was used to analyze the morphology quantitatively. Since larger particles play a more important role in determination of final product properties than smaller ones, an "area weighted average" was used to obtain the numerical values for aspect ratio (L/T) and average particle area (L×T) of dispersed phase particles. These two parameters were defined as follows:

number average area =
$$\overline{a} = \frac{\sum_{i=1}^{n} a_i}{N} = \frac{A}{N}$$
 (4-12)

weighted average are
$$a = \overline{a}_w = \frac{\sum_{i=1}^{n} (a_i)^2}{\sum_{i=1}^{n} a_i} = \frac{\sum_{i=1}^{n} (a_i)^2}{A}$$
 (4-13)

number average aspect ratio =
$$\overline{\alpha} = \frac{\sum_{i=1}^{n} \alpha_i}{N} = \frac{\sum_{i=1}^{n} (L/T)_i}{N}$$
 (4-14)

weighted average aspect ratio =
$$\overline{\alpha}_{w} = \frac{\sum_{i=1}^{n} a_{i} \alpha_{i}}{A} = \frac{\sum_{i=1}^{n} a_{i} (L/T)_{i}}{A} = \frac{\sum_{i=1}^{n} a_{i} (L/T)_{i}}{\sum_{i=1}^{n} a_{i}}$$
 (4-15)

where:

A= total area covered by all particles

N= total number of particles

 a_i = area of ith particle

 $\alpha_i = (L/T)_I = \text{aspect ratio of i}^{th} \text{ particle}$

L =length or maximum projection of the particle

T = thickness of the particle

The obtained numerical results were then used to evaluate the effect of processing conditions on morphology.

4.3.2 Toluene Permeability Measurements

4.3.2.1 Sample Preparation

To obtain smooth samples, as needed for permeability measurements, extruded ribbons of individual resins and blends of HDPE/PA-6 and ADMER/EVOH were compression molded at low temperature and pressure. The main restriction was to avoid changing the morphology of the samples. Therefore, temperature and pressure were controlled strictly to prevent such changes. The compression molding was done at temperatures below the

melting point of blend components and close to the melting point of the matrix, i.e. the lowest melting point component. The pressure was set at a value such that the surface area of the sample after compression molding was about 15% more than the original area before compression molding. Therefore, the particles of the dispersed phase were stretched less than 4% during compression molding. It is believed that this small amount of deformation does not affect the permeability measurements considerably. To verify this claim, permeability of the samples before and after compression molding was compared and the result showed that the difference was less than 5%, which is within the experimental error of the test. The conditions used for compression molding of the two systems are as follows:

1- HDPE/PA-6: As the melting point of HDPE is about 135°C, the following conditions were used for compression molding of HDPE/PA-6 system:

- temperature: 120°C±4

- pressure: 750 psi ±50

- pre-heating time: 7 min.

- heating time: 2 min.

- cooling time: 6 min.

Tap water was used as the coolant. As mentioned above, the compression molding temperature is well below the melting point of the dispersed phase (PA-6), i.e. 220°C. Thus, the dispersed phase morphology is not affected significantly by the compression molding.

2- ADMER/EVOH: The melting point of the ADMER is 161°C; therefore, the following molding conditions were used:

- temperature: 148°C±4

- pressure: 1500 psi°C100

- pre-heating time: 8 min.

- heating time: 2 min.

- cooling time: 7 min.

4.3.2.2 Toluene Permeability Setup

Toluene permeability of the samples was measured according to ASTM F739 method with the help of a gas-chromatograph (GC) supplied by Hewlett Packard (type 5890 series II) which was equipped with additional accessories. As the permeability of some of the resins, especially EVOH, depended on the relative humidity of the test sample, the samples were conditioned at 23°C and 50% relative humidity for 96 hours. Then the sample was placed in a glass cell. Thus, the cell was separated into two chambers by the sample. One side of the sample was filled with toluene, while the other side was flushed with helium as the carrier gas. Toluene diffused through the polymer film and after a breakthrough time, it appeared on the other side of the cell. The helium carried the diffused toluene to the FID detector (flame ionization detector) of the GC, and the mixture was analyzed for the concentration of toluene. Due to low permeability of the samples with laminar morphology, long time was needed to reach steady state. Therefore, the setup was designed to measure the steady state permeability of 4 samples simultaneously.

Figure 4.10 shows a schematic of the toluene permeability measurement setup. When valve #2 is off, the helium carrier gas (helium stream #1) goes directly to the detector to provide the baseline. At the same time, depending on the position of valve #1, stream #2A or 2B fills the loop and is directed to the loop vent while another stream goes to the cell vent. When sufficient time has elapsed (50 min.), valve #2 is turned on in order to purge the loop from the previous run. The helium carrier flow (stream #1) is directed to the loop and then to the FID detector. Therefore, the gas sample is analyzed and the concentration of the toluene will be known.

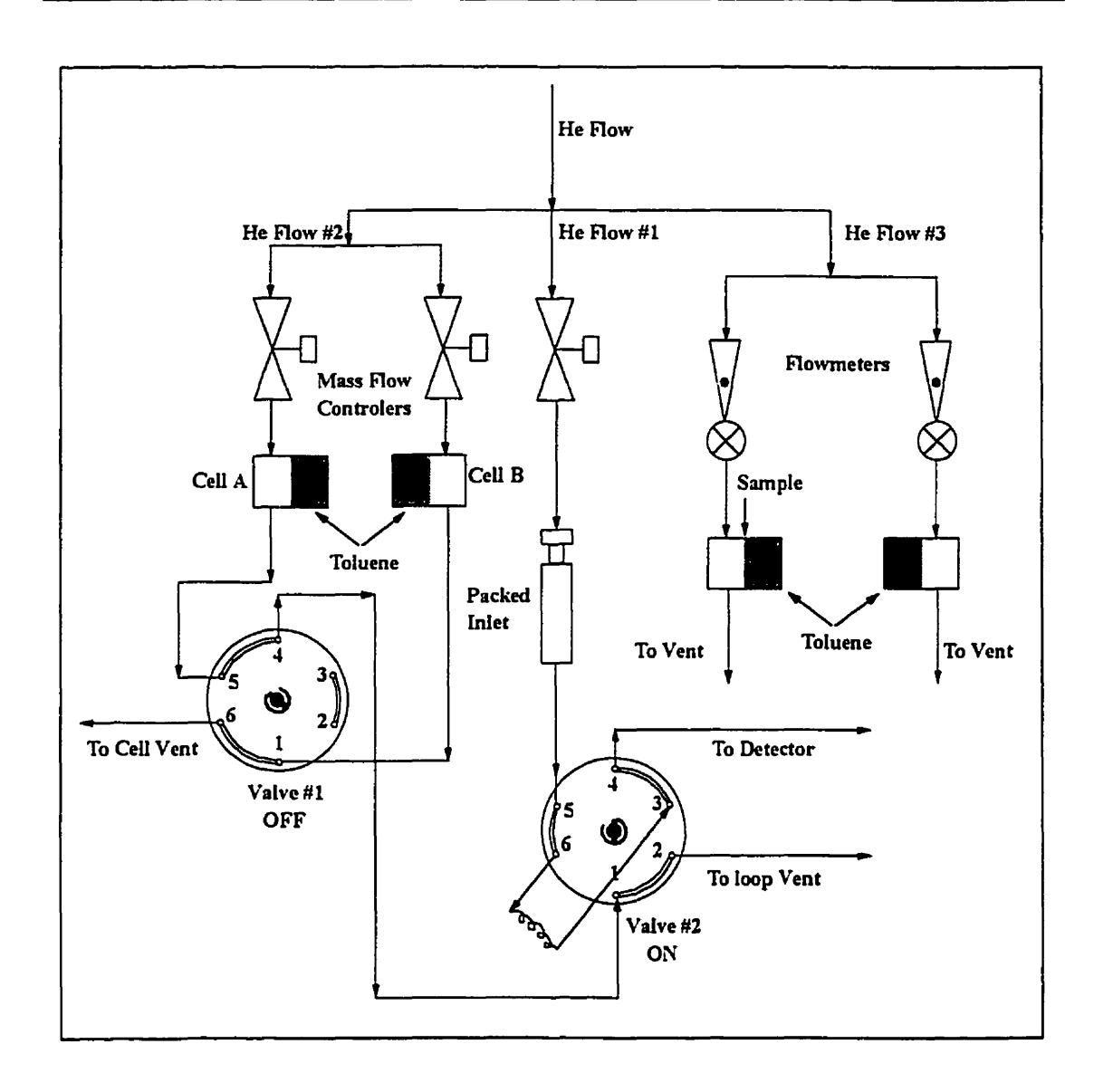


Figure 4.10: Schematic of the toluene permeability measurement setup

Permeability can be calculated using the following equation:

$$q = c\frac{F}{A} \tag{4.16}$$

where q is toluene permeation rate in mg/m².min, c is the concentration of toluene in the gas mixture, F represents the flow rate of helium and A is the exposed area of the sample

to toluene, i.e. 18.86 cm². The permeability coefficient depends on the thickness of the sample as defined below:

$$p = q \times t \tag{4-17}$$

where p is permeability coefficient in mg.mm/m².min, and t is the thickness of the sample in mm. As permeability is a function of temperature, room temperature was monitored and the permeability results were corrected for the effect of temperature using an Arrhenius type equation as follows:

$$p = p_0 \left(\exp \frac{-E}{RT} \right) \tag{4.18}$$

4.3.2.3 Calibration of the Apparatus

To calibrate the GC for toluene permeability measurements, standard 10 liter Mylar bags were filled with air. Then specific amount of toluene, 10-50 µl, was injected into the air filled bags. Therefore, the concentration of toluene in the bags was already known. The mixture was left for at least 4 hours to form a homogeneous gas mixture. Then, the mixture was pumped into the system under the same conditions that were used during the sample runs. The pump produced constant and accurate flow rate. Using different concentrations of toluene, the required parameters including retention time and amount/area were found. The GC provided accurate results for the concentration of toluene in the different bags. A standard deviation of 1% for the same bag, and 2% for different bags was achieved. Table 4.5 shows the pressure and related flow rates for calibration and sample runs.

Table 4.5: Outlet Pressure and Related Flows for Different Gases:

Gas	Cylinder Pressure (KPa)	Flow Rate (ml/min)
Pneumatic air	414	-
Air	241	350
Hydrogen	107	30
Helium #1 (detector)	276	30
Helium #2 (cell #1)	276	50
Helium #3 (cell #2)	276	50

4.3.3 Oxygen Permeability Measurements

4.3.3.1 Sample Preparation

The procedure explained in section 4.3.2.1 was used for providing the smooth sample for oxygen permeability measurements. Then, the sample was sandwiched between two aluminum foil masks with an opening of 18.86cm². The standard aluminum foil masks have an opening of 5cm², which is not large enough for samples with low permeability such as EVOH resin. Thus, the obtained voltage was too low for the detection. Therefore, a mold was made to provide aluminum foil masks with larger opening of 18.86cm². The samples were conditioned at 23°C and 50% relative humidity for 96 hours prior to measurements.

4.3.3.2 Oxygen Permeability Apparatus

A Mocon coulometric oxygen detector incorporated into a device similar to Ox-Tran mode 100, as shown in Figure 4.11, was used to measure the oxygen permeability of the samples. The apparatus consisted of a cell separated into two chambers by the sample. One side of the sample was flushed continuously with extra dry oxygen. On the other side of the sample, dry nitrogen carrier gas containing 3% hydrogen swept the permeating oxygen molecules to the sensor. Through an electrochemical reaction, sensor produced a current, which is a linear function of the mass flow rate of oxygen into the sensor. The nitrogen gas carrier contained 3% hydrogen, which by passing through a platinum catalyst caused the hydrogen to react with any residual oxygen in the system. Both oxygen and carrier gas vented directly to the atmosphere, and when the mass flow rates are identical, there is no pressure difference across the sample. To remove any absorbed oxygen in the samples and aluminum foil masks, the cell was conditioned between 12 and 48 hours, with dry nitrogen passing on both sides of the sample. When no voltage was observed, it was assumed that the sample was free of absorbed oxygen. The temperature of the cell was monitored, and the results were corrected for the effect of temperature using the Arrhenius equation, as indicated earlier (see Equation (4.18)).

4.3.4 High Speed Instrumented Impact Testing

Impact performance of polymeric materials is of great importance in many applications. Impact strength of polymer blends is a good indicator of the quality of adhesion between blend components. A Rheometrics Variable-Speed Impact Tester (RIT-8000) was used to evaluate the impact properties of the samples. RIT-8000 is a controlled velocity impact tester, in which an electrically controlled hydraulic system drives a dart shape probe to impact a flat specimen fixed between sample retaining rings. The force exerted on the probe, as a result of impacting the specimen, is measured by a load cell positioned at the tip of the rod and is plotted against the distance traveled (displacement). The test imposes

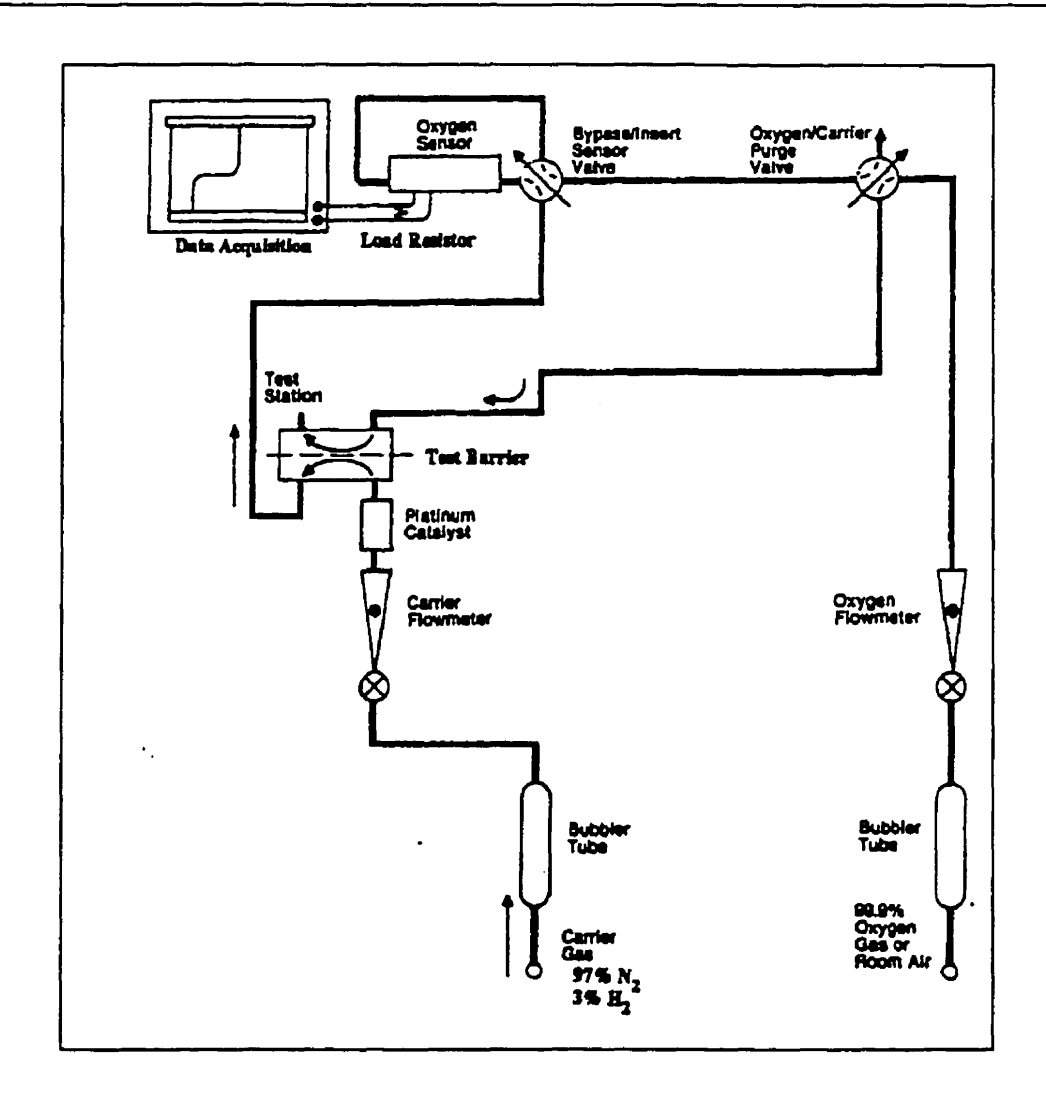


Figure 4.11: Diagram of the coulometric system used in measurements of oxygen permeability coefficient.

a biaxial flexural deformation on the sample that is similar to the loading conditions which are encountered in many applications. The extruded ribbons were conditioned at 23°C and 50% relative humidity for 96 hours. The average thickness of the samples was measured with a micrometer within 0.01 mm precision and tests were done at room temperature. Samples were clamped between the 3.15 cm diameter rings. A hemi-spherical probe with diameter of 1.26cm was used for all the tests. Based on previous research (20), impact

speed of 0.432 m/sec (1000 in/min) was used. As the probe impacted the specimen, force was measured as a function of displacement and was displayed on a CRT screen. The shape of the load-deflection curve depends on the behavior of the material under impact load and it may consist of all, or portions of, the idealized stages shown in Figure 4-12, which is explained below.

- Stage A: Perturbations; are usually small.
- Stage B: Linear load-deflection deformation; where specimen behaves elastically.
- Transition B: Yield point; plastic deformation of sample starts.
- Stage C: First major permanent deformation; where, because of distributed damage, a decrease in load is not observed.
- Transition C: Maximum load; which is usually associated with the first appearance of visible cracks in the specimen.
- Stage D: Stable deformation; which is after the maximum load.
- Transition D: End of test; the specimen looses its structural integrity.

The following data were collected and discussed for all the samples:

- The ultimate force (transition C), which shows the rigidity of the samples.
- The ultimate energy, which is the area under the curve up to point C, and is an indication of impact strength of the samples.

A normalization procedure was used (Appendix D) to compare the samples with different thicknesses. The values presented in this study are averaged over 10 samples.

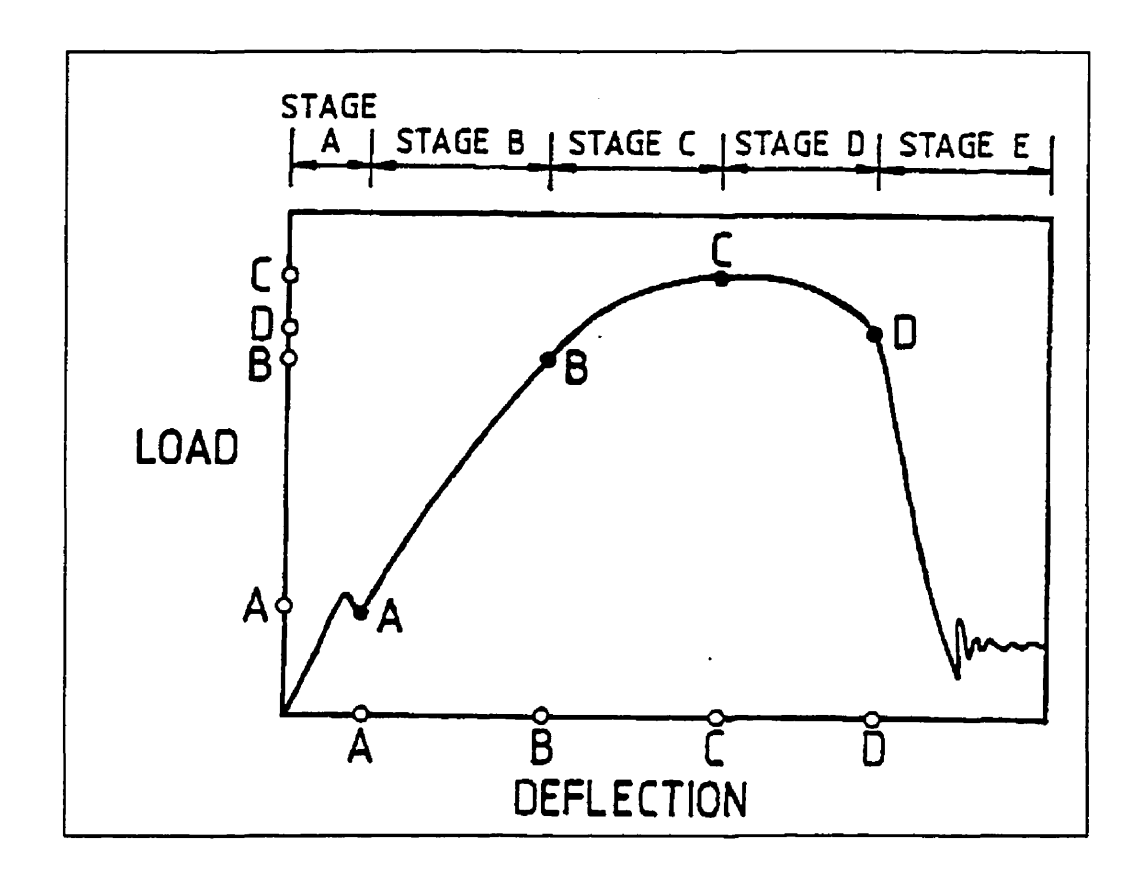


Figure 4.12: Idealized deformation stages and transitions for impact testing using RIT-8000.

CHAPTER 5

ANALYSIS OF MATERIAL PROPERTIES

5.1 Rheological Analysis

5.1.1 Steady Shear Viscosity

The review in chapter 2 indicated that viscosity of blend components or the viscosity ratio of the dispersed phase to the matrix phase is one of the most important parameters that affect the deformation and breakup of dispersed phase particles. Developing laminar morphology in polymer blends deals with large deformations of dispersed phase particles. Therefore, knowledge of the rheological behavior of blend components is a necessity in this study.

5.1.1.1 HDPE/PA-6 Blends

The viscosity-shear rate data for resins were obtained using both Bagley and Rabinowitsch correction factors. These data for PE0, PE1, PE2, and PA-6 at three different temperatures of 230, 250, and 270°C are shown in Figures 5.1-5.4. The viscosity-shear rate curves of the three grades of HDPE, Figures 5.1-5.3, are similar, and none of them could be fitted well to the power law model over the whole range of shear rates. Also, the viscosity-shear rate curve of the PA-6, Figure 5.4, could not be fit to the power law model. While PA-6 viscosity shows strong temperature dependency (Figure 5.4), the viscosities of PE0, PE1, and PE2 resins (Figures 5.1-5.3) do not change significantly in this temperature range. This is an advantage of HDPE/PA-6 blend and provides flexibility in optimizing the processing temperature in the screw zone and inside the die region for

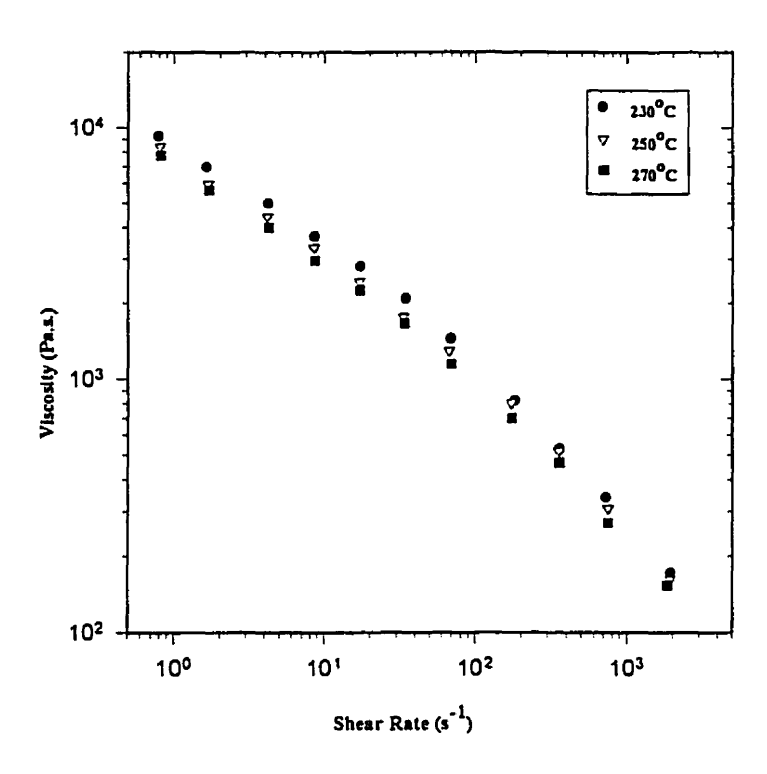


Figure 5.1: Steady shear viscosity vs. shear rate for PE0 resin at different temperatures

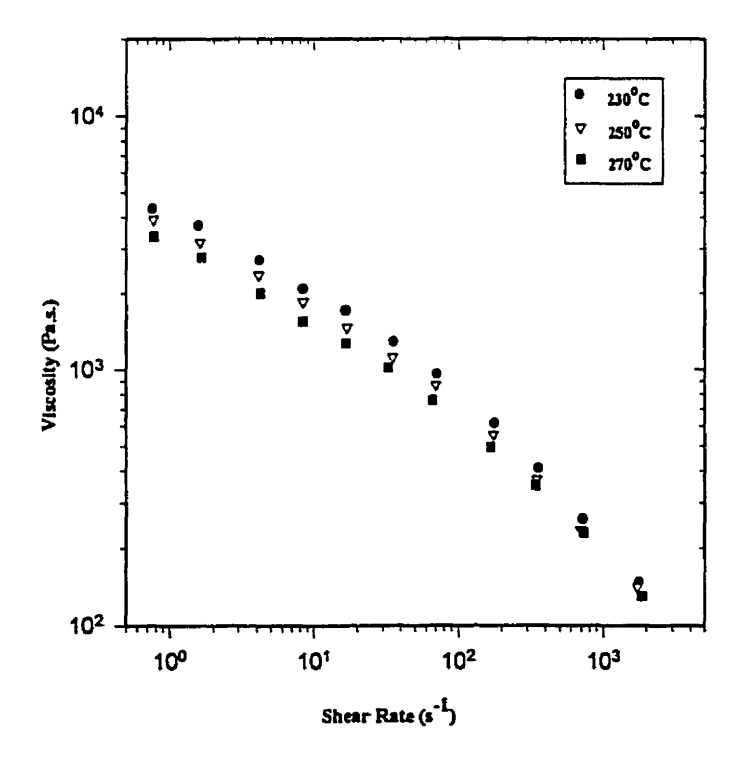


Figure 5.2: Steady shear viscosity vs. shear rate for PEI resin at different temperatures

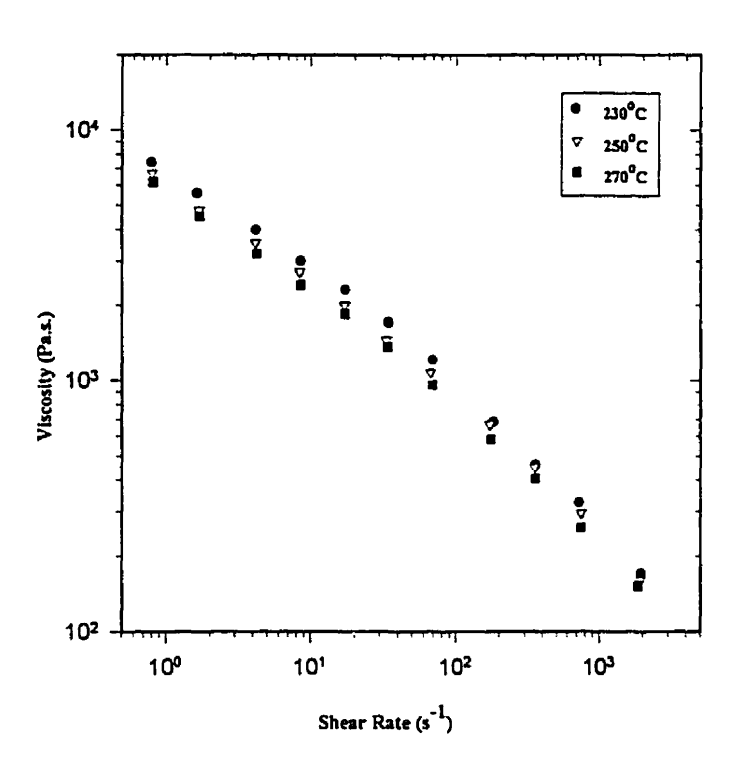


Figure 5.3: Steady shear viscosity vs. shear rate for PE2 resin at different temperatures

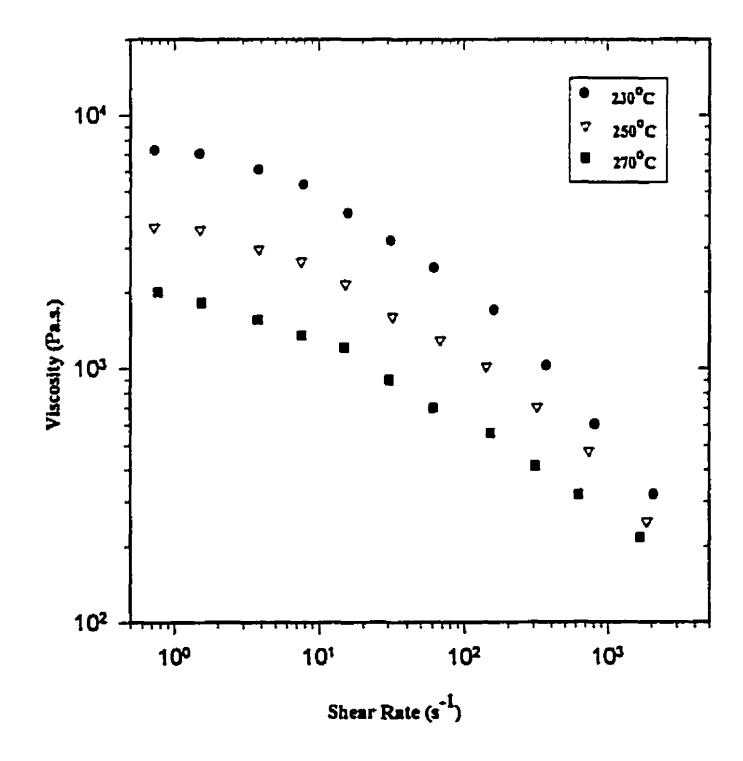


Figure 5.4: Steady shear viscosity vs. shear rate for PA-6 resin at different temperatures

obtaining ideal viscosity ratios.

As mentioned earlier, the viscosity ratio of dispersed phase to the matrix phase (λ) is an important parameter that affects mixing characteristics in the screw zone and consequently, the size of the dispersed phase particles entering the die. It is also an important parameter in determination of deformation of dispersed phase particles in the die region. Figure 5.5 shows the viscosity ratio of PA-6 to the PE0 and PE2 vs. shear rate at different temperatures. Due to strong dependency of the viscosity of PA-6 to the temperature, a wide range of viscosity ratios (0.2-2.1) is observed. The shear rate at various parts of the die has been calculated and reported in Appendix E. The range of the

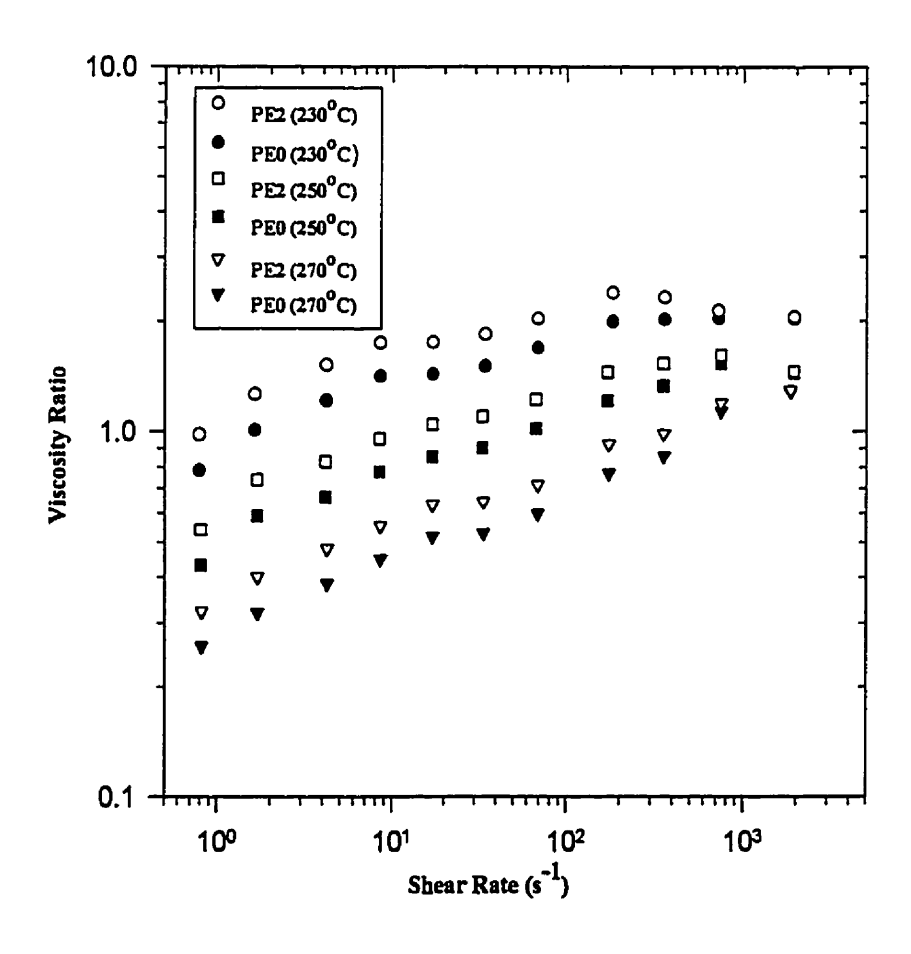


Figure 5.5: Viscosity ratio of PA-6/PE vs. shear rate at different temperatures

shear rate encountered in different parts of the die is between 0.5 and 160 s⁻¹. As Figure 5.5 shows, for this range of shear rate at temperature of 230°C, the viscosity ratio is greater than one (λ >1). It can be seen that at 250°C, the viscosities of the dispersed phase (PA-6) and matrix (PE0) are closely matched. Thus, the viscosity ratio at temperature of 250°C is close to unity (0.7> λ >1.3) and its value decreases at 270°C. As discussed earlier, a viscosity ratio greater than unity in the screw zone, is desirable in order to avoid size reduction of PA-6 particles, and a viscosity ratio of close to 1 in the die region, is the ideal condition for the large deformations that are needed in this study (81,82).

As explained in section 4.2.2, a low temperature profile below the melting point of the dispersed phase (PA-6), i.e. 220°C, is preferred in the screw zone. For providing a homogenized polymer melt entering the die, it is necessary to raise the temperature in the last zone of the extruder. Although, this temperature rise is essential, a temperature of 230°C that provides a viscosity ratio greater than unity is recommended in order to prevent any size reduction, even in the last zone of the extruder. This temperature is not likely to cause significant breakup of the dispersed phase particles. As the objective of this study is to develop laminar morphology which requires large deformations of dispersed phase particles, a die temperature of about 250°C, which provides a viscosity ratio close to unity, is expected to yield maximum deformation of PA-6 particles in the die. Since the viscosities of PE0 and PE2 are similar, the above conditions are applicable to both resins and blends thereof. Thus, it should be easy to manipulate compatibilizer content with using the same extrusion conditions.

5.1.1.2 PP/EVOH Blends

The viscosity-shear rate data for ADEMR and EVOH at two different temperatures of 200 and 230°C are shown in Figure 5.6 (18). It is apparent that the dispersed phase material, EVOH, exhibits higher viscosity at both temperatures for the whole range of shear rate. This observation is clearer in Figure 5.7 that shows the viscosity ratio of the dispersed

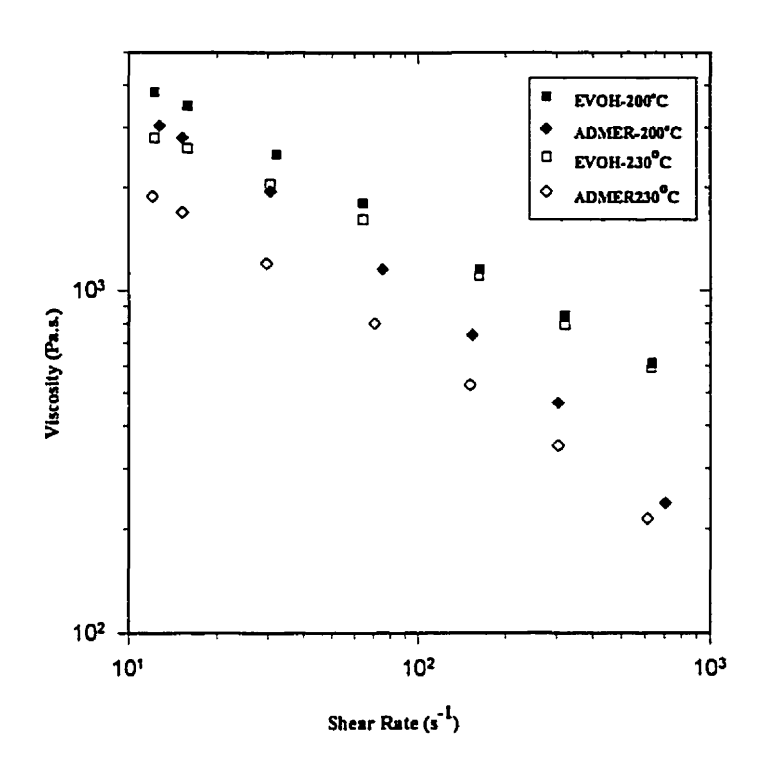


Figure 5.6: Steady shear viscosity vs. shear rate for ADMER and EVOH at 200 and $230\,\mathrm{C}$

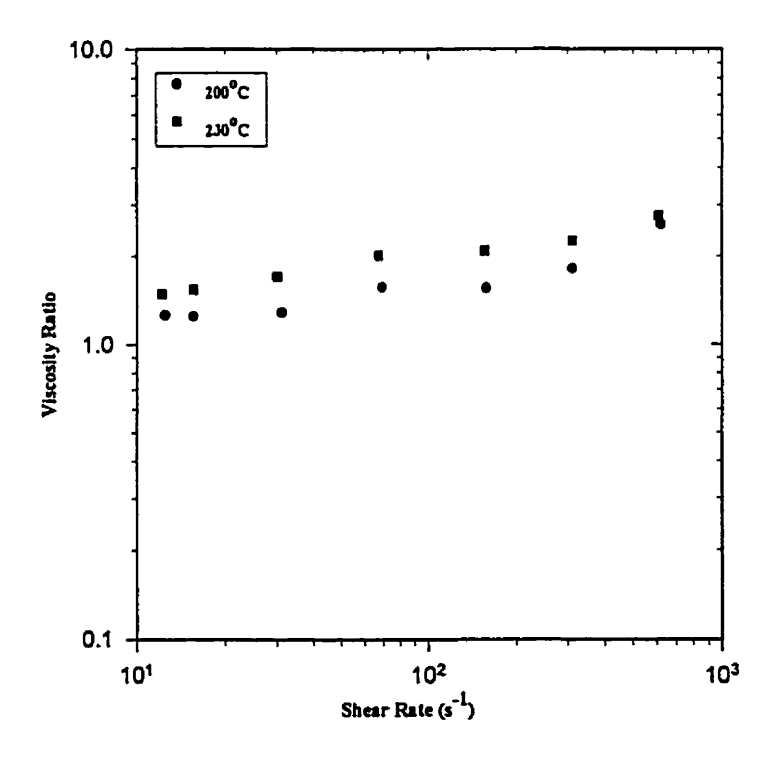


Figure 5.7: Viscosity ratio of EVOH /ADMER vs. shear rate at different temperatures

phase to the matrix phase as a function of shear rate. Figures 5.6 and 5.7 also indicate that the viscosities of the ADMER and EVOH do not change significantly at different temperatures. As a result, changing the temperature by 30°C in Figure 5.8, does not change the viscosity ratio considerably. Therefore, the viscosity ratio is above one (λ >1) for the all shear rate range and throughout the processing window for ADMER/ EVOH blend. This is not an ideal condition for large deformation of the dispersed phase, which is needed inside the die region for developing laminar morphology. This is a disadvantage of the present ADMER/EVOH blend which limits the possibility of achieving maximum barrier properties for this system. Using other grades of maleated polypropylene and ethylene vinyl alcohol (EVOH) with closer viscosities in the processing range could help in achieving larger deformations.

5.1.2 Dynamic Measurements

Elasticity of blend components is one of the important material characteristics that affect morphology development during processing of polymer blends. In oscillatory rheometry, the dynamic storage modulus (G') represents the elastic component of the viscoelastic melt. Therefore, the G' of blend components were used to compare their elasticities.

5.1.2.1 HDPE/PA-6

Figure 5.8 presents the dynamic shear storage modulus, G', of PEO, PE2, and PA-6 resins and one of the prepared blends, i.e. PEO/PE2/PA-6 (60/20/20), as a function of frequency at two different temperatures of 250 and 270°C. At both temperatures, the matrix, i.e. PEO, has higher elasticity than PA-6, which forms the dispersed phase. Although, due to limitations of the apparatus, the data do not cover higher frequencies, it is clear that the crossover happens out of the range of shear rate (frequencies) encountered inside the die (0.5-160 s⁻¹). Chin and Han (88,89) observed that a highly viscoelastic medium gave rise to large deformations of droplets. Therefore, the elasticity ratio of this system is also in

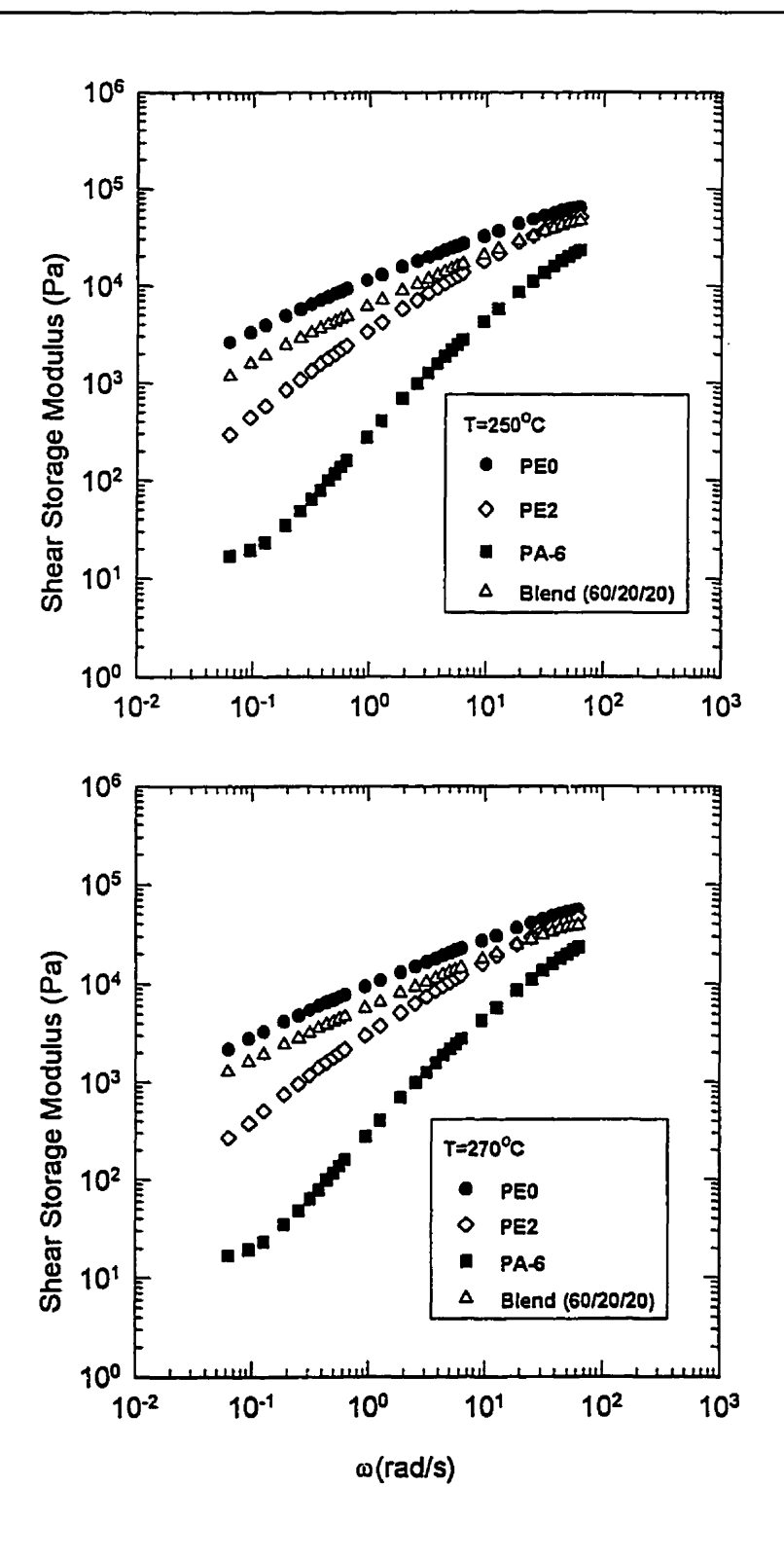


Figure 5.8: Shear storage modulus for PE0, PE2, PA-6 resins and PE0/PE2/PA-6 (60/20/20 wt%) blend at two temperatures of 250 and 270 °C.

favor of providing the large drop deformations that are necessary for developing laminar morphology. The storage modulus of PE2 is smaller than PE0, while the storage modulus of the blend lies between moduli of the PE0 and PA-6 resins.

Figure 5.9 shows the complex viscosity of the individual resins and a typical blend, i.e. PE0/PE2/PA-6 (60/20/20 wt%). The complex viscosity curve results from the following equation:

$$\left|\eta *\right| = \frac{1}{\omega} |G *| \tag{5.1}$$

where $|\eta^*|$ is the magnitude of complex viscosity, ω is frequency (rad/s), and $|G^*|$ is the complex modulus defined as follows:

$$|G^*| = \sqrt{(G')^2 + (G'')^2}$$
 (5.2)

where G' and G" are the storage and loss moduli, respectively.

The complex viscosity of PA-6 at 270°C is lower than the viscosity of PE0 for the whole range of frequency. The viscosities of PA-6 and PE0 resins are closer to each other at 250°C, and the viscosities are almost identical for the frequencies higher than 10 rad/s. The graphs show that the viscosities of PE0 and PE2 obey the power law model, however, the viscosity of PA-6 does not. The viscosity of the blend lies between the viscosities of PE0 and PA-6 resins and it can not be fitted to the power law model.

5.1.2.2 PP/EVOH

Figure 5.10 shows the storage modulus, G', of ADMER, designated in this figure as MAPP2, and EVOH resins as a function of frequency at two different temperatures of 200

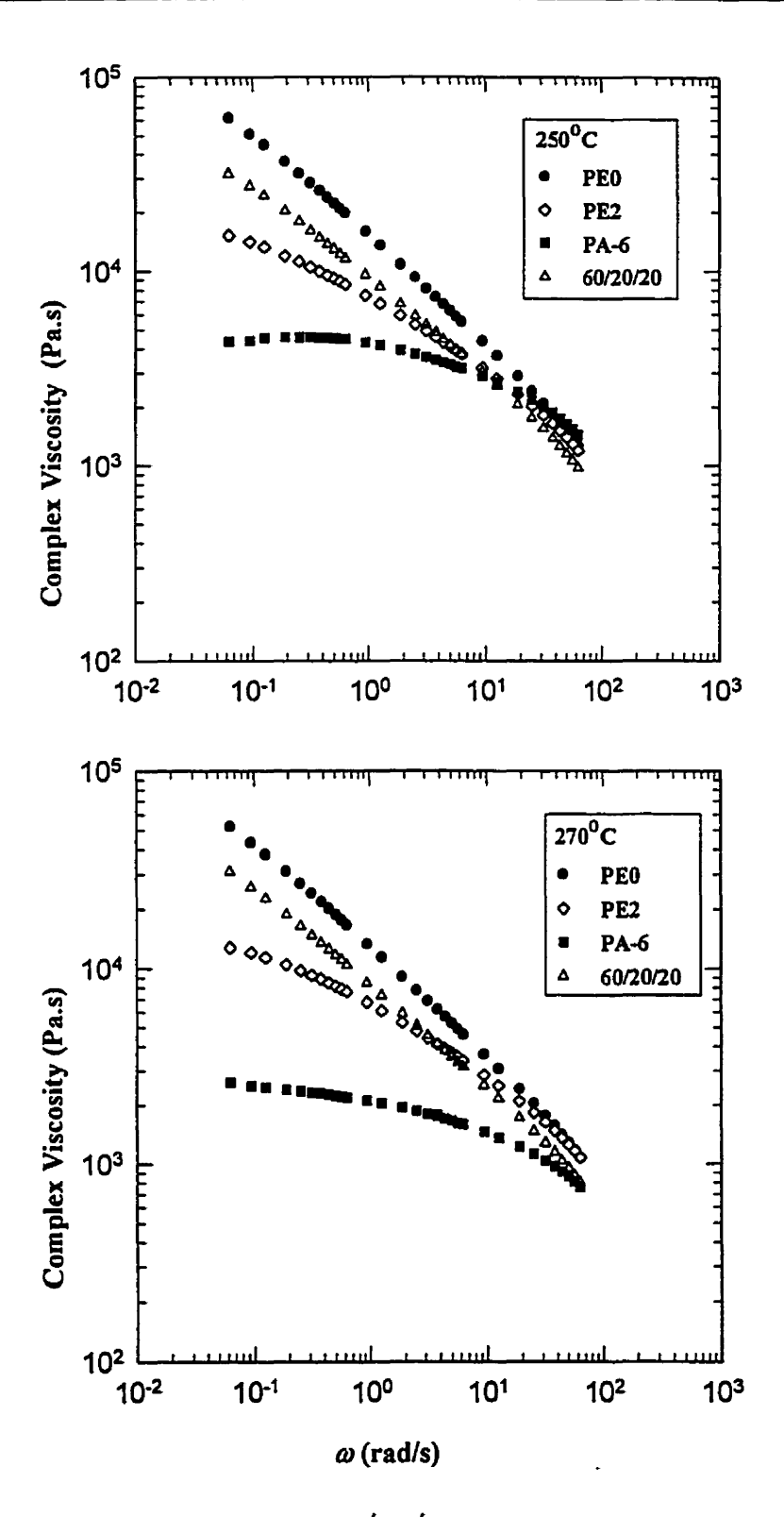


Figure 5.9: Complex viscosity, $/\eta^*/$, vs. frequency for PE0, PE2, PA-6 resins and PE0/PE2/PA-6 (60/20/20) blend at temperatures of 250 and 270 °C.

and 230°C (18). At 200°C, the shear modulus or elasticity of ADMER (MAPP2), is higher than the elasticity of EVOH at lower frequencies and a crossover happens at a frequency of about 10 rad/s. Above this frequency, in the range of shear rates encountered in the die region, the EVOH, i.e. the dispersed phase, is more elastic than the ADMER matrix. Based on Van Oene's Theory (70) and Chin and Han (88,89), this condition is generally not favorable for large deformations of the dispersed phase particles. The situation is slightly improved at 230°C, where the crossover point can be marked at frequency of 50 rad/s. Thus, both the viscosity ratio which is higher than unity (Figure 5.7) and the elasticity ratio of ADMER and EVOH resins are not in favor of large deformations of EVOH particles, as needed for developing laminar morphology.

5.2 Analysis of the PVT Behavior of Resins and Blends

5.2.1 Equations of State

A number of equations of state have been proposed for predicting the specific volume of polymers as a function of pressure and temperature. The purely empirical Tait equation of state has been used frequently with a wide range of polymers, both in the glassy and melt states (123). Another empirical equation of state is the Spencer-Gilmore equation of state (140), which normally leads to larger deviations. Among the theoretical equations of state for melts, the Simha-Somcynsky equation (141) consistently gives the best representation of the data over extended ranges of temperature and pressure (142). In this study, the Tait equation of state has been used for fitting the PVT data of all the individual resins and HDPE/PA-6 blends, with the exception of PA-6 resin, for which the Spencer-Gilmore equation of state provided better predictions.

5.2.1.1 The Tait Equation

The Tait equation (143) predicts the volume along an isotherm in terms of the volume at zero pressure, V (0,T), and the Tait parameter B (T), which depends only on temperature.

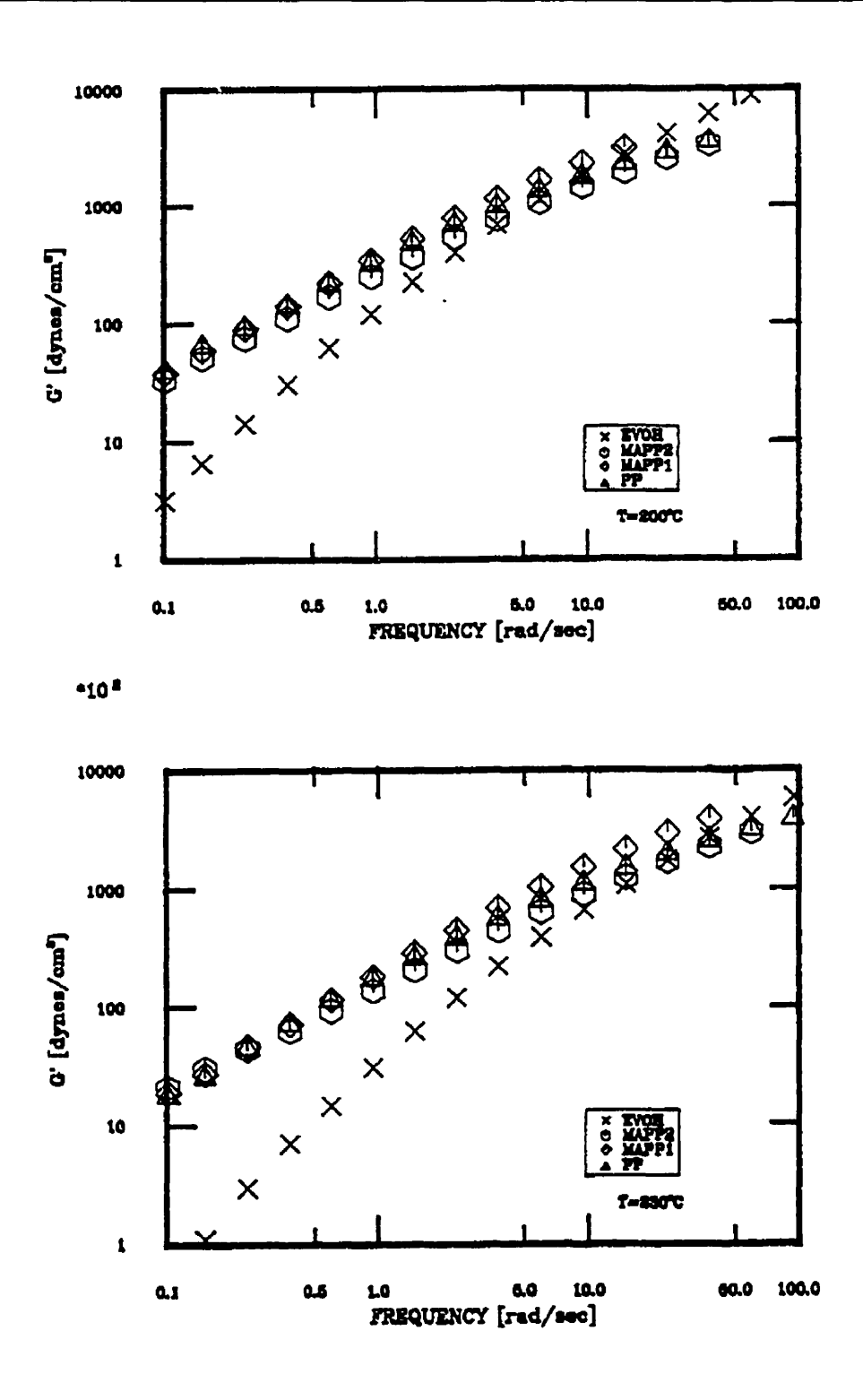


Figure 5.10: Shear storage modulus of ADMER and EVOH at two temperatures of 200 and 230 °C (18).

It is generally written as

$$V(P,T) = V(0,T) \times [I - C \ln[I + P/B(T)]]$$
(5.3)

C is a constant and its standard value is 0.0894. Although, it may not be suitable for describing PVT data for all polymers, it may be estimated by fitting PVT data to the equation. The temperature dependence of B (T) is exponential:

$$B(T) = B_0 \exp(-B_1(T)) \tag{5.4}$$

For V(0,T), a polynomial similar to Equation (5.5) is normally used

$$V(0,T) = A_0 + A_1 T + A_2 T^2$$
(5.5)

The Tait equation does not yield a good representation of compression isotherms of some semi-crystalline polymers. Therefore, sometimes it is used with a Tait parameter that decreases linearly with temperature rather than exponentially. In the present report, both fits were examined and the exponential form yielded smaller standard deviation.

The Tait equation and a suitable fit to the zero-pressure isobar together provide fairly simple expressions for the derived quantities of the isothermal compressibility K(P,T) and the volume or thermal expansion coefficient $\alpha(P,T)$.

$$K(P,T) = -(\partial \ln V / \partial P)_T = -\frac{1}{V} \left(\frac{\partial V}{\partial P}\right)_T = \left[C/(P+B)\right] \cdot \left[1 - C\ln(1+P/B)\right]$$
 (5.6)

and

$$\alpha(P,T) = \left(\frac{\partial \ln V}{\partial T}\right)_P = (1/V)\left(\frac{\partial V}{\partial T}\right)_P = \alpha_{\bullet} - P \cdot B \cdot K(P,T)$$
 (5.7)

where α_0 is the zero-pressure thermal expansivity, given by the expression for V(0,T).

$$\alpha_{\circ} = \frac{1}{V(0,T)} \times (A_1 + 2A_2T)$$
 (5.8)

5.2.1.2 The Spencer-Gilmore Equation of State

The Spencer-Gilmore equation of state (140) can be written as:

$$(P+\pi)(v-\omega) = \frac{RT}{M}$$
 (5.9)

where P is the pressure in bar, ν is specific volume in cm³/g, T is the temperature in K, and R is the universal gas constant in cm³ bar mol⁻¹ k⁻¹ and π , ω and M are equation parameters that are calculated by fitting the equation to the experimental data using the least square method.

5.2.2 HDPE/PA-6 Blends

Figure 5.11 presents the specific volume of HDPE/PA-6 (80/20) blends versus maleation content of HDPE at room temperature. The additive rule as defined in Equation (5.10) is also shown for the comparison purposes.

$$V_b = w_1 V_1 + w_2 V_2 ag{5.10}$$

Where w_i is the weight fraction of each component, V_i is the specific volume of each component and V_b is the specific volume of the blend. Mixing different proportions of PE0 and PE2 in the twin screw extruder produces the different levels of MAH content. At low concentration of MAH between 0.01 and 0.1 wt%, the specific volume of compatibilized blends follows a linear relationship with the MAH content. However, deviation of up to 0.008 cm³/g from the additive rule is observed. There is an important

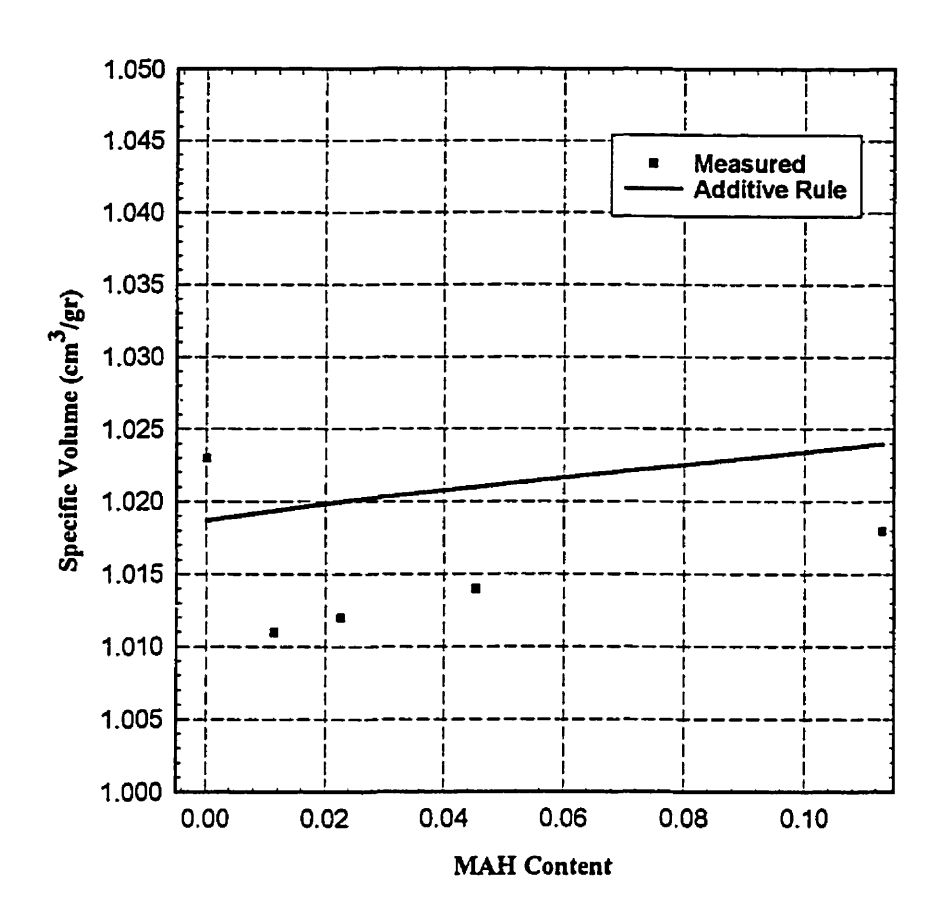


Figure 5.11: Specific volume of HDPE/PA-6 (80/20 wt%) blend at room temperature vs.

MAH content (wt%) of HDPE

difference between the compatibilized and non-compatibilized blends, i.e. the blend with MAH content of zero. The non-compatibilized blend shows a positive deviation from the additive rule, while the compatibilized blend presents a negative deviation. This difference is also evident in Figure 5.12, for the variations of melt specific volume with temperature at atmospheric pressure. The negative deviation from the mixing rule is referred to as negative excess volume in the literature, which is defined as follows:

$$V^{E} = V_{b} - (w_{1}V_{1} + w_{2}V_{2})$$
 (5.11)

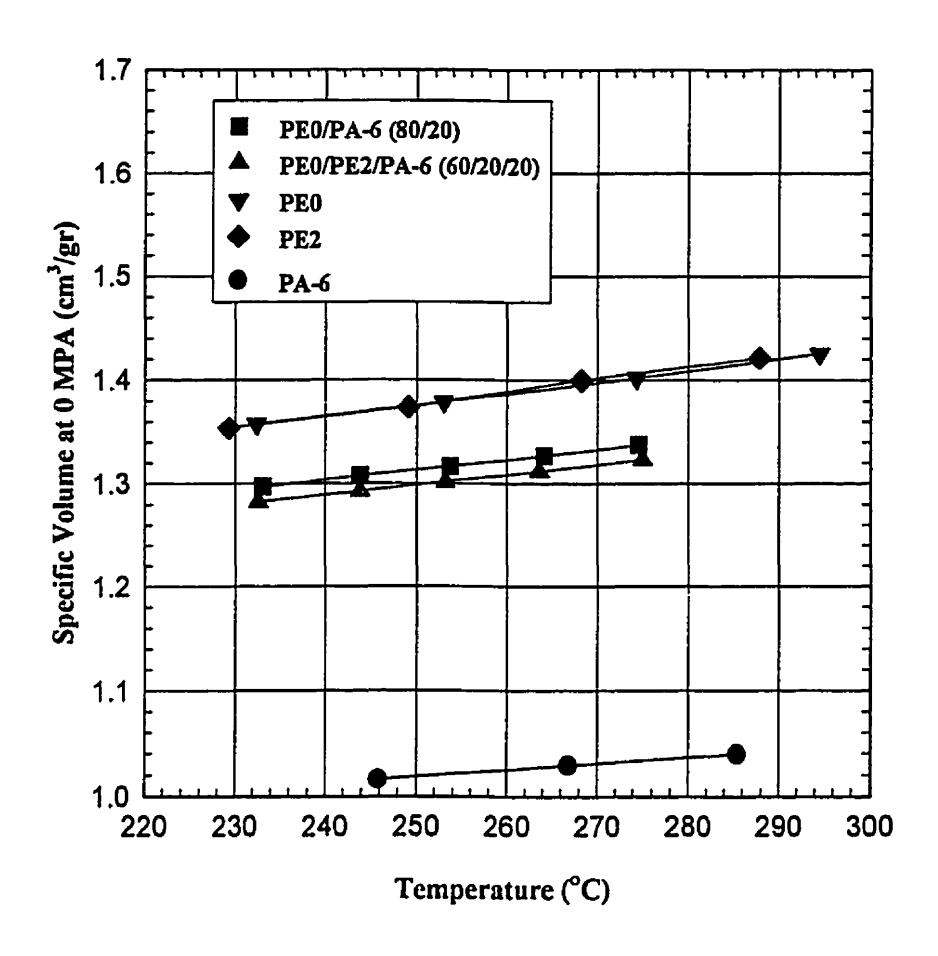


Figure 5.12: Melt specific volume of resins and blends versus temperature at atmospheric pressure

where V^E, V_b, and V_i are the excess, mixture, and component specific volumes, respectively. Some studies on PVT behavior of polymer blends (144-147) have reported a negative excess volume for compatibilized polyphenylene oxide/ polystyrene (PPO/PS) blends. Such a negative excess volume of mixing has been taken as an indication of specific interactions favoring compatibility. As indicated, the negative excess volume for compatibilized blends of HDPE/PA-6 in this study could be a sign of compatibility of the system. While, in the case of non-compatibilized blends, a positive excess volume suggests lack of any interaction at the interface.

Table 5.1: Coefficients of Tait Equation and Spencer-Gilmore Equation of states for Individual Resins:

Material	PE0	PE0	PE2	PA-6
B ₀ ×10 ⁻² (MPa)	3.603	2.078	2.030	•
B ₁ ×10 ³ (°C)	5.239	5,387	5.290	-
A ₀ (cm ³ /g)	1.048	1.157	1.170	-
A ₁ ×10 ³ (cm ³ /g°C)	-0.0529	0.6855	0.5129	-
A ₂ ×10 ⁶ (cm ³ /g°C)	5.322	0.76814	1,2650	-
С	0.08931	0.08916	0.08940	-
SD	0.0026	0.00035	0.0008	0.0007
T (°C)	30-120	159-294	160-287	-
P (MPa)	0-100	0-100	0-100	0-100
π (Bar)	_	-	-	4585
ω (cm³/g)	-	-	-	0.7893
M	•	-	-	33.5

Table 5.1 presents the coefficients of Tait and Spencer-Gilmore equations of state for the individual resins. There is good agreement between the experimental and predicted values from the Tait equation for the PE's and from the Spencer-Gilmore equation for the PA-6. A maximum standard deviation of 0.0026 cm³/g is observed for the solid state of PE0.

To evaluate the effect of compatibilizer level on the PVT behavior of the HDPE/PA-6 resins, extensive studies were done on the PE0/PA-6 (80/20 wt.%) blends with different levels of compatibilizer, i.e. the PE2. The Tait equation, which was used

successfully for the PE resins, was found to be applicable for the blends of PE and PA-6 resins. Due to the high concentration of PE in the blend, i.e. 80 %wt., this is to be expected. Three transition points that should be considered in planning PVT experiments:

- Glass transition temperature (T_g) of the PA-6 resin (60°C)
- Melting point (T_m) of the HDPE (135°C)
- Melting point (T_m) of the PA-6 (220°C)

Therefore, four different temperature zones were used to fit the experimental data to the Tait equation:

- 30-50°C, i.e. $T < T_g$ of the PA-6 resin"
- 68-110°C, i.e. " T_g of the PA-6 resin" $< T < "T_m$ of the HDPE"
- 165-213°C, i.e. " T_m of the HDPE" $< T < "T_m$ of the PA-6"
- 233-276°C, i.e. T > " T_m of the PA-6"

Table 5.2 presents the parameters of the Tait equation for HDPE/PA-6 resins containing different levels of compatibilizer. As indicated by the small values of the standard deviation (maximum of 0.0005 cm³/g), the Tait equation with appropriate parameters, provides good prediction of the PVT behavior of HDPE/PA-6 resins. The range of pressure for all the blends and resins is 0-100 MPa. The value of the Tait parameter (C) for all the blends is close to the standard value of 0.0894. Error analysis of PVT measurements is given in Appendix C. The reproducibility of the measurements was found to be better than 0.005 cm³/g.

Figure 5.13 presents the cross-plotted isobars (based on the isothermal data) of PEO in pressure increments of 20 MPa. At zero pressure, the PVT data show a melting point of 137°C which is 2°C higher than the T_m reported by the supplier based on DSC

Table: 5.2: Coefficients of Tait Equation of states for PEO/PE2/PA-6 Blends

	 	1	1				T .			·
Blend Comp. PE0/PE2/PA-6	80/0/20	80/0/20	80/0/20	80/0/20	70/10/20	70/10/20	70/10/20	70/10/20	60/20/20	60/20/20
B ₀ ×10 ⁻² (MPa)	3.4831	5.3746	2.2256	2.1780	3.516	4.786	2.362	2.186	3.5922	5.0915
B ₁ ×10 ³ (°C)	3.215	9.789	5.233	5.01	4.013	8.56	5.514	4.98	4.231	9.408
A ₀ (cm ³ /g)	1.10417	1.03669	1.113	1.135	1.02982	1.01963	1.10999	1.1333	1.09302	1.02808
A ₁ ×103 (cm ³ /g°C)	-3,685	-0.3398	0.5660	0.4683	-0.9525	-0.2379	0.3922	0.5153	-3.7781	-0.4122
A ₂ ×106 (cm ³ /g°C)	0.4545	6.190	0.8682	0.9836	15.19	5.642	1.352	0.8723	47.09	6.607
С	0.08906	0.08875	0.08908	0.08922	0.08877	0.08954	0.089	0.08943	0.08945	0.08857
SD	0.00013	0.00049	0.00048	0.00044	0.00014	0.00047	0.00042	0.00032	0.00010	0.00044
T (°C)	30-50	68-110	166-213	233-275	30-50	68-110	165-213	230-275	30-50	68-110
P (MPa)	0-100	0-100	0-100	0-100	0-100	0-100	0-100	0-100	0-100	0-100
Blend Comp.	60/20/20	60/20/20	40/40/20	40/40/20	10/40/20	40/40/20	0/80/20	0/80/20	0/80/20	0/80/20
B ₀ ×10 ⁻² (MPa)	2.2898	2.2536	3.6162	5.0996	2.3042	2.0226	3.66825	4.94284	2.27384	2.30212
B ₁ ×10 ³ (°C)	5.44	5.169	4.901	9.622	5.389	4.66	5.964	9.887	5.366	5.229
A ₀ (cm³/g)	1.10638	1.11217	1.094	1.02215	1.10436	1.16546	1.03352	1.03224	1.12634	1.15435
A ₁ ×103 (cm³/g°C)	0.4669	0.541	-3.764	-0.2268	0.4836	0.1009	-0.7931	-0.3163	0.2833	0.2095
A ₂ ×106 (cm³/g°C)	1.155	0.8234	46.84	5.597	1.067	1.686	14.14	6.218	1.624	1.488
С	0.08888	0.08922	0.0826	0.08850	0.08891	0.08911	0.08930	0.08858	0.08907	0.08925
SD	0.00051	0.00057	0.00160	0.00043	0.00046	0.00037	0.00011	0.00041	0.00042	0.00043
T (°C)	166-213	232-275	30-50	68-110	165-213	232-274	30-50	68-110	165-213	233-276
P (MPa)	0-100	0-100	0-100	0-100	0-100	0-100	0-100	0-100	0-100	0-100

measurements. This small difference has been reported for other semi-crystalline polymers (148). Increasing the pressure shifts the melting point of the PE0 towards higher temperatures, and increasing the pressure by 100 MPa results in the raising the melting point by up to 20° C. The Clausius-Clapeyron equation (149) gives a good theoretical estimation of the effect of pressure on T_m :

$$\frac{dT_m}{dP} = T_m^0 \frac{\Delta V_m}{\Delta H_m} = \beta \tag{5.12}$$

where T_m° is the crystallization temperature at zero pressure; ΔV_m and ΔH_m are the volume

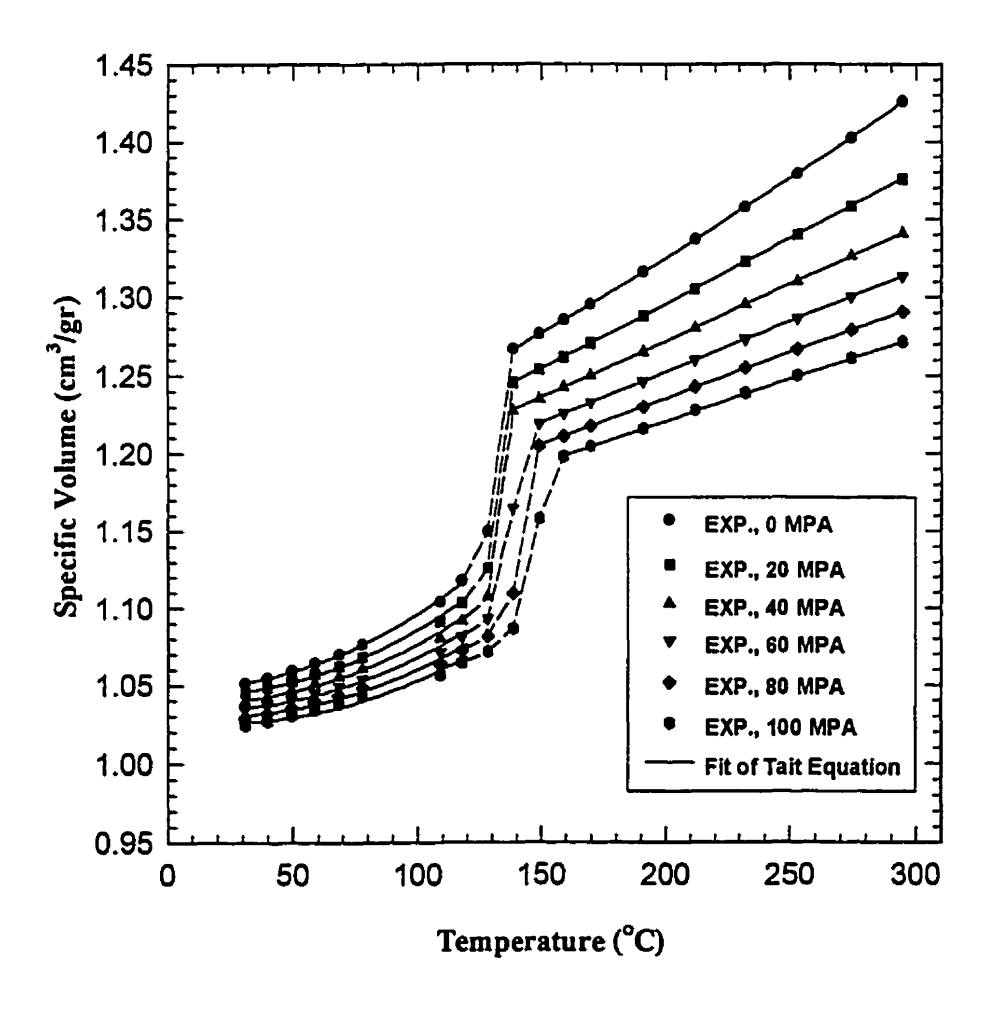


Figure 5.13: Crossplotted isobars of PE0 resin along with predictions of the Tait equation

and enthalpy changes upon crystallization; and β is a constant. Van Krevelen (150) showed that for large pressure variations:

$$P - P_0 = a \left[\left(\frac{T_m}{T_m^0} \right)^c - 1 \right]$$
 (5.13)

where a and c are constants. For high density polyethylene, $T_m^{\circ} = 409^{\circ}\text{K}$, $a \approx 3$ Kbar and c = 4.5. This gives a rise in T_m of 20°K at 1 Kbar (100MPa), which confirms the experimental findings.

Figure 5.14 shows the experimental and predicted isotherms for PE0 resin. Although, the isothermal experiments were one in increments of 10°C, due to better resolution of the data output, only some of the isotherms are shown in this figure. There is a good agreement between the predicted and experimental results. However, the agreement is better for the melt state than the solid state. The Tait equation, like other equations of state, cannot predict the PVT behavior of polymers during the transitional melting stage.

Figure 5.15 shows the cross-plotted isobars (based on the isothermal data) for PA-6 resin. It seems that, within the pressure range tested in this study, i.e. 0-100 MPa, the pressure does not have an important effect on the melting point of PA-6 resin. The zero pressure data yield T_m of 222°C, which is very close to the reported T_m of 220°C by the supplier using the DSC method. The Spencer-Gilmore equation of state was judged to give satisfactory prediction for the PVT behavior of PA-6 resin in the melt state.

Figure 5.16 presents the experimental isotherms along with the predictions of the Spencer-Gilmore equation of state for the PA-6 melt. The agreement between the experimental and prediction values for temperatures lower than 270°C is good. However, the experimental isotherm at 285.4°C, seems to give slightly higher values than the predicted values. Possibly, some degradation at high temperatures could explain this small disagreement, although we had no direct evidence for degradation. It has been reported

that some polymer samples degrade, producing higher than expected volumes especially at low pressures (151).

Figure 5.14 shows that the increase in the specific volume of PE0 during the melting is larger and sharper than in the case of PA-6, Figure 5.16.

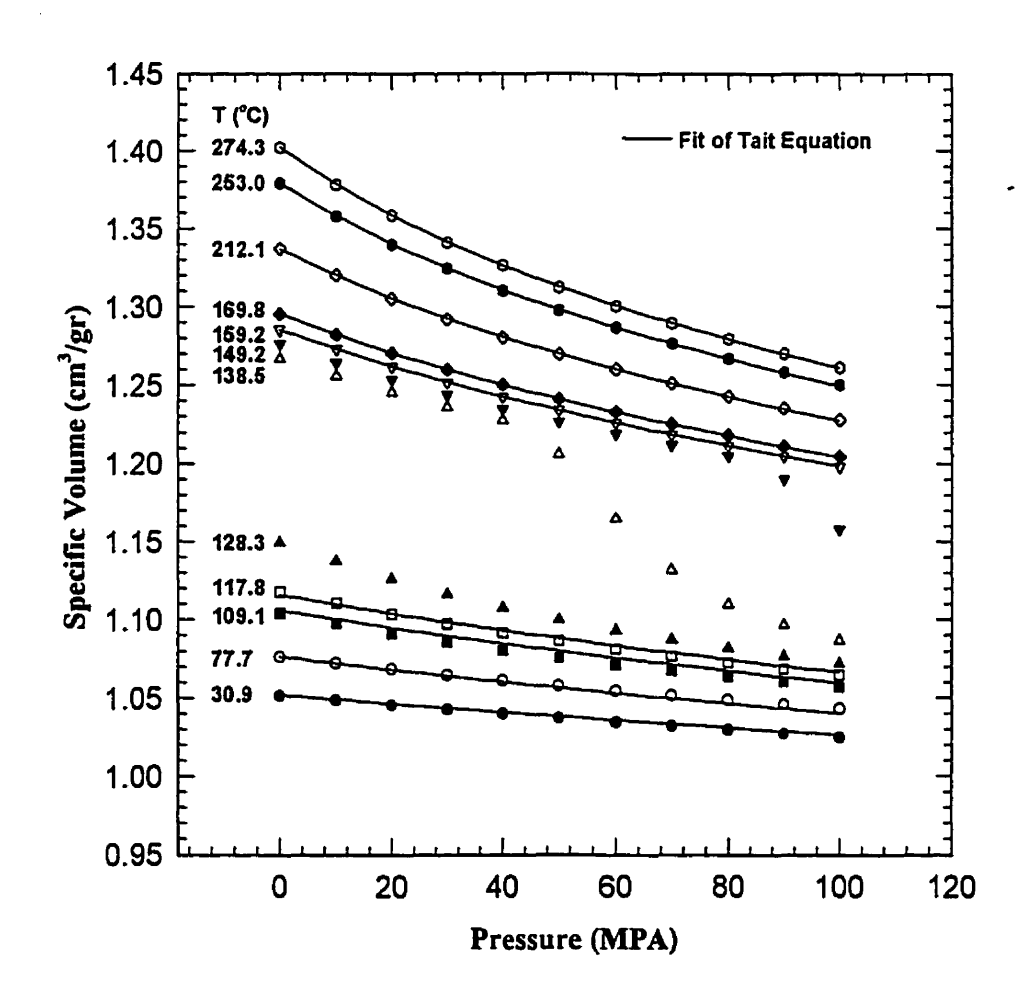


Figure 5.14: Comparison of the Experimental Isotherms with Predictions of Tait

Equation for PE0 Resin

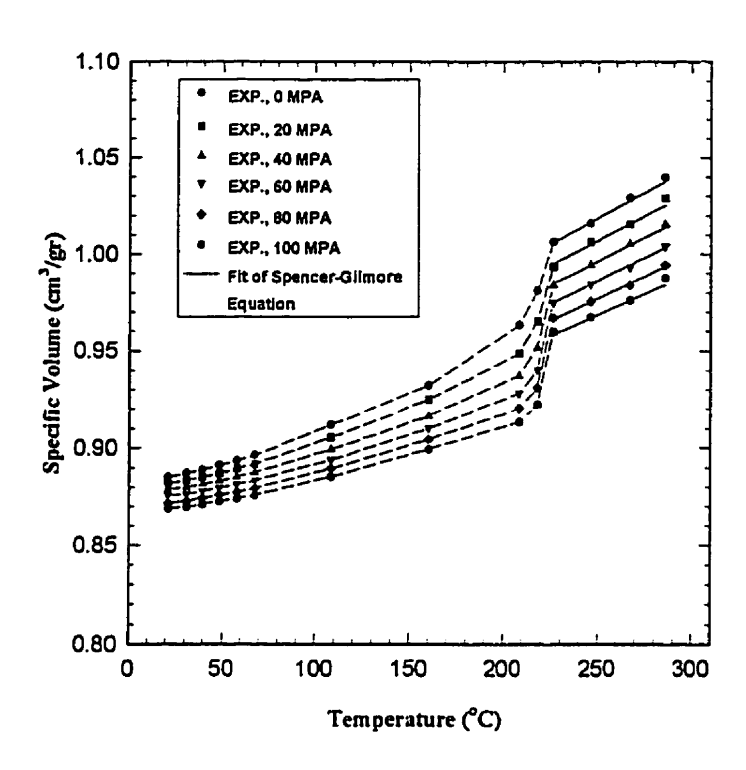


Figure 5.15: Crossplotted Isobars of PA-6 resin along with predictions of the Spencer-Gilmore equation of state

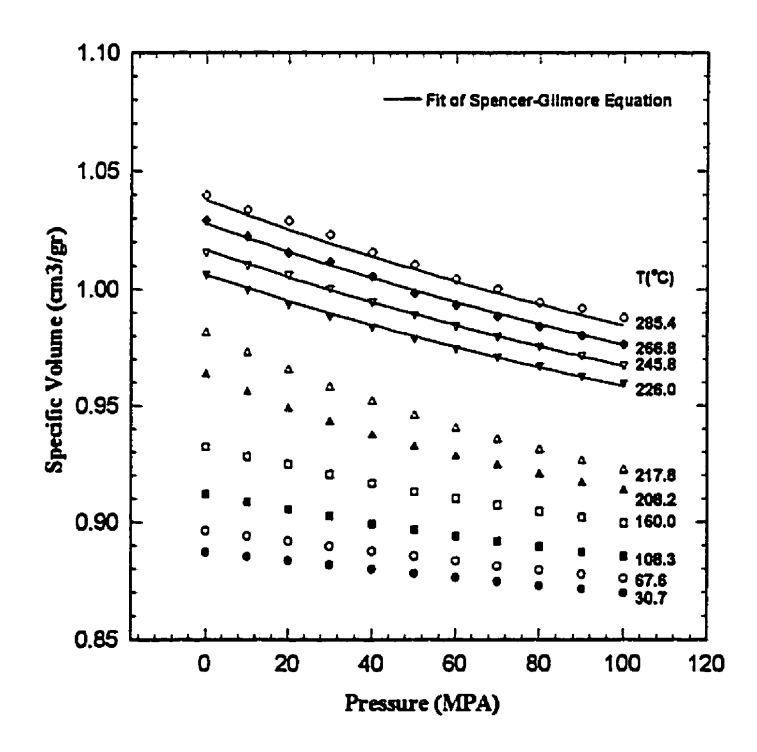


Figure 5.16: Comparison of the experimental isotherms with predictions of Spencer-Gilmore equation of state for PA-6 resin

Figures 5.17 to 5.21 present the experimental isotherms of PE/PA-6 (80/20 wt%) blends with different levels of compatibilizer. The Tait equation yields very good predictions for both the solid and the melt states of these blends. This is to be expected, because 80% of the blend is polyethylene and the Tait equation describes the PVT behavior of PE well. The specific volume of PE0 at different temperatures and pressures match closely the literature reports (152).

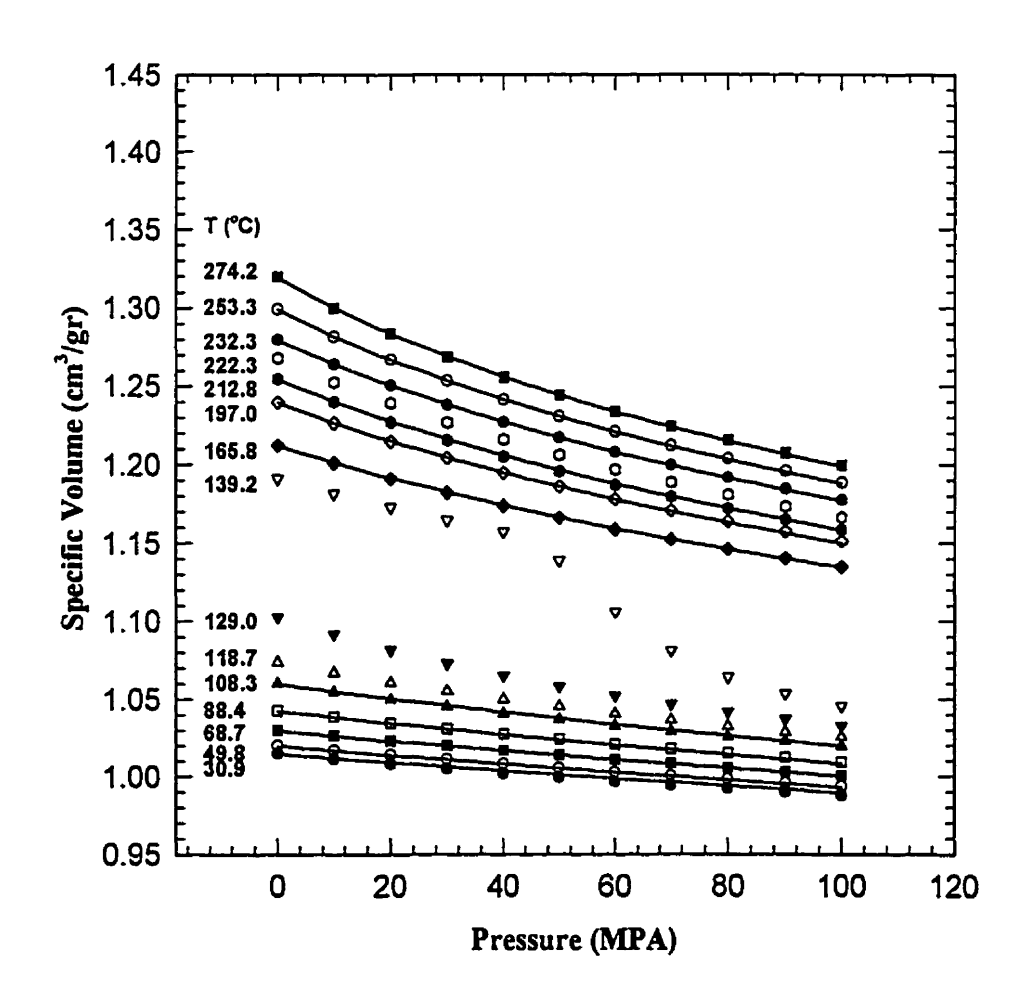


Figure 5.17: Comparison of the experimental isotherms with predictions of Tait equation of state for PEO/PA-6 (80/20 wt%) blend

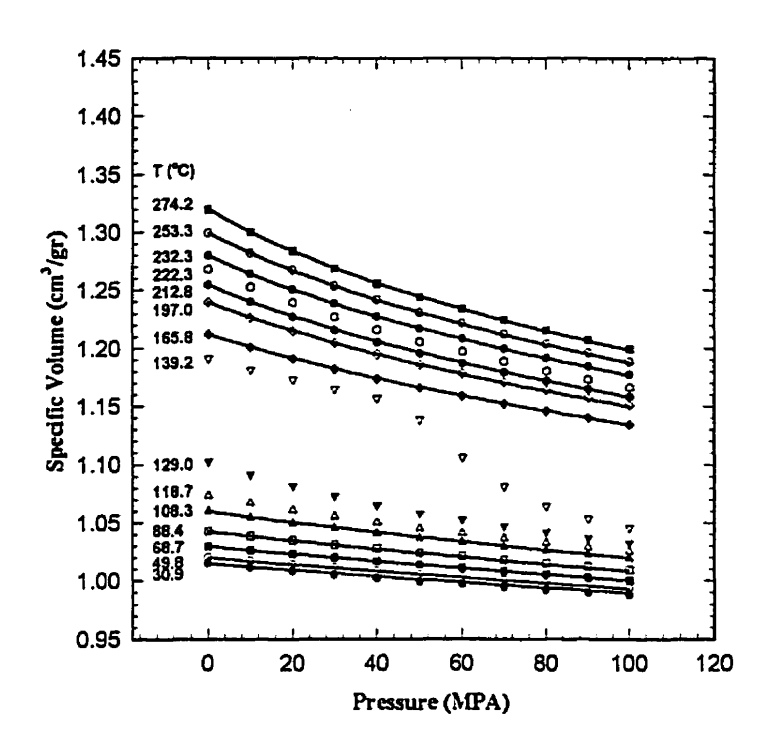


Figure 5.18: Comparison of the experimental isotherms with predictions of Tait Equation of state for PEO/PE2/PA-6 (70/10/20 wt%) blend

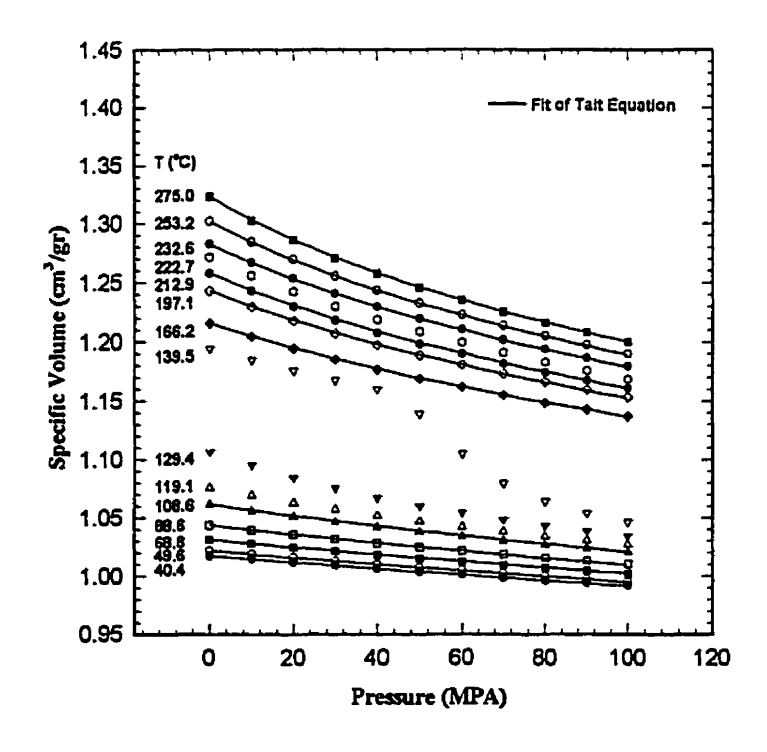


Figure 5.19: Comparison of the experimental isotherms with predictions of Tait equation of state for PE0/PE2/PA-6 (60/20/20 wt%) blend

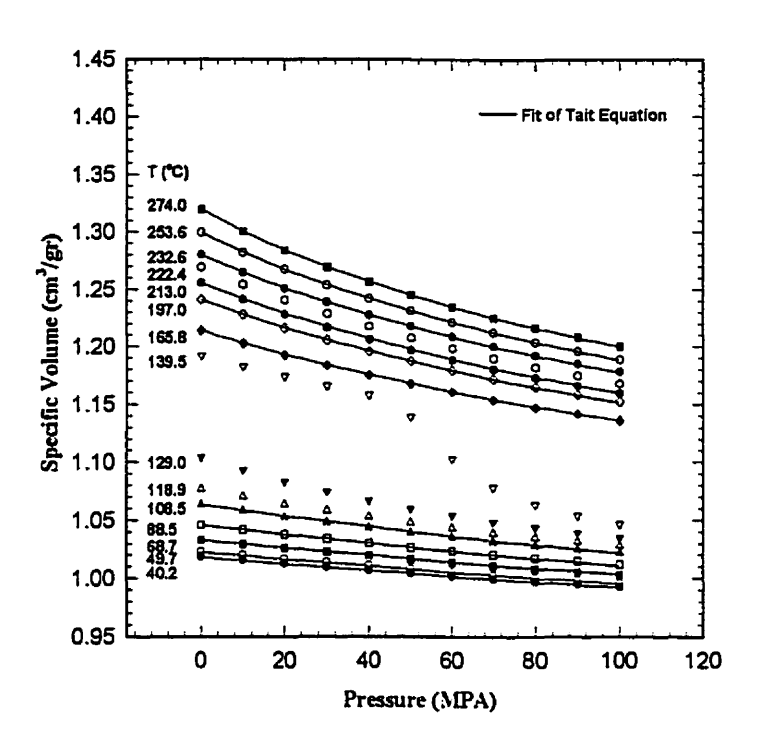


Figure 5.20: Comparison of the experimental isotherms with predictions of Tait equation of state for PE0/PE2/PA-6 (40/40/20 wt%) blend

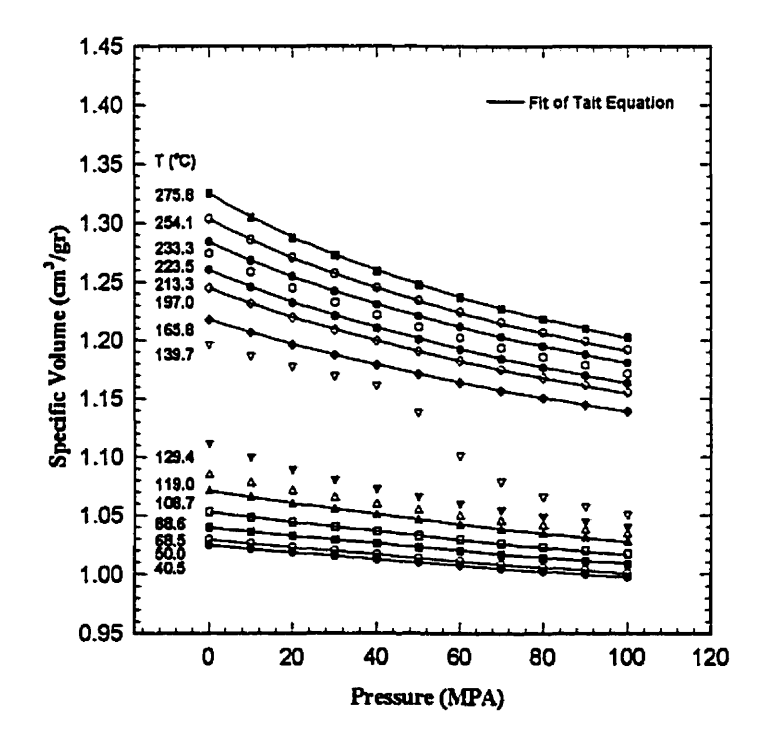


Figure 5.21: Comparison of the experimental isotherms with predictions of Tait equation of state for PE2/PA-6 (80/20 wt%) blend

5.2.3 PP/EVOH Blends

Figure 5.22 presents the specific volume of molten EVOH and ADMER at zero pressure and different temperatures. The data show the specific volume up to 250°C. Due to the possibility of thermal degradation of EVOH above 240°C, extra care should be taken when using the data above this temperature. Since short residence time was employed above this high temperature in the present work, the risk of degradation has been reduced.

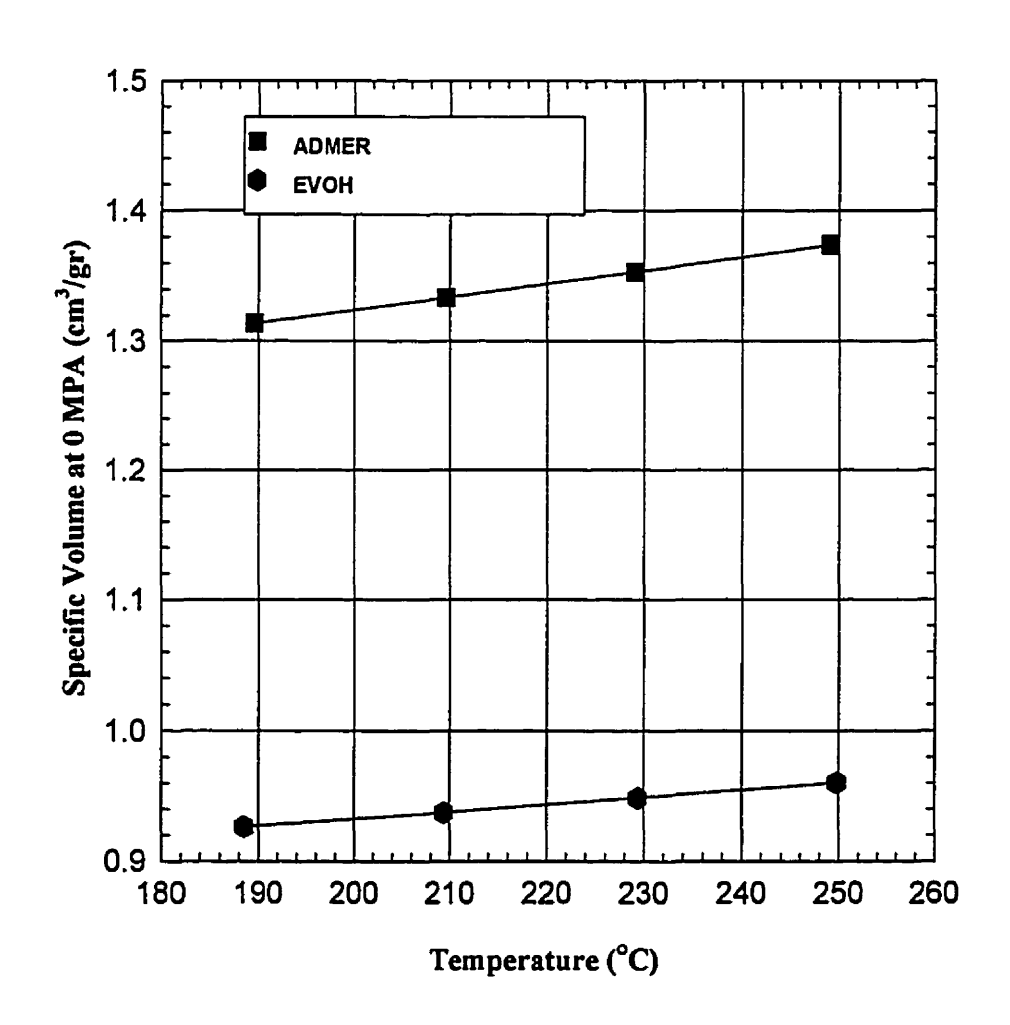


Figure 5.22: Melt specific volume of ADMER and EVOH resins versus temperature at atmospheric pressure

Table 5.3: Coefficients of Tait Equation of state for ADMER and EVOH:

Material	ADMER	EVOH	
B ₀ ×10 ⁻² (MPa)	1.6828	4.0454	
B ₁ ×10 ³ (°C)	4.901	3.691	
A ₀ (cm ³ /g)	1.152	0.8599	
A ₁ ×10 ³ (cm ³ /g°C)	0.7342	0.1986	
A ₂ ×10 ⁶ (cm ³ /g°C)	0.6360	0.8236	
С	0.0894	0.0894	
SD	0.0002	0.0001	
T (°C)	188-249	188-249	
P (MPa)	0-100	0-100	

Table 5.3 shows the coefficients of the Tait equation for molten ADMER and EVOH resins for the pressure range of 0-100 MPa. As indicated by the small value of the standard deviation (0.0001-0.0002), there is good agreement between the experimental results and the predictions of the Tait equation. For both ADMER and EVOH, the standard value of Tait parameter, i.e. 0.0894, provides good predictions of the specific volume at different temperatures and pressures. The values of isothermal compressibility K(P,T) and thermal expansivity $\alpha(P,T)$ coefficients for ADMER and EVOH could be obtained, using Equations (5.6) and (5.7). The numerical values of the parameters are presented in table 5.3.

Figure 5.23 presents the cross-plotted isobars (based on the isothermal data) of ADMER in pressure increments of 20 MPa. Due to the wide temperature interval (20°C) of the isothermal experiments, it is not possible to identify the end of melting precisely. The pressure dependence of the end of melting interval cannot be measured in the

isothermal mode of experimentation employed in this study. The predicted specific volume by the Tait equation matches closely the experimental data.

Figure 5.24 shows the experimental isotherms for solid and molten ADMER, i.e. from room temperature to 249°C. Again, the Tait equation provides good prediction of the PVT behavior of molten ADMER at different pressures and temperatures.

Figure 5.25 presents the cross-plotted isobars (based on the isothermal data) for EVOH resin in pressure increments of 20 MPa. Although, the pressure dependence of the end of melting interval cannot be measured in the isothermal mode, it is shown, as in the case of PA-6 resin, that the melting point of EVOH does not change significantly with pressure. The predictions of the Tait equation are in good agreement with the experimental data. Figure 5.26 shows the experimental isotherms along with the predictions of Tait equation for molten polymer. It confirms the good agreement indicated above.

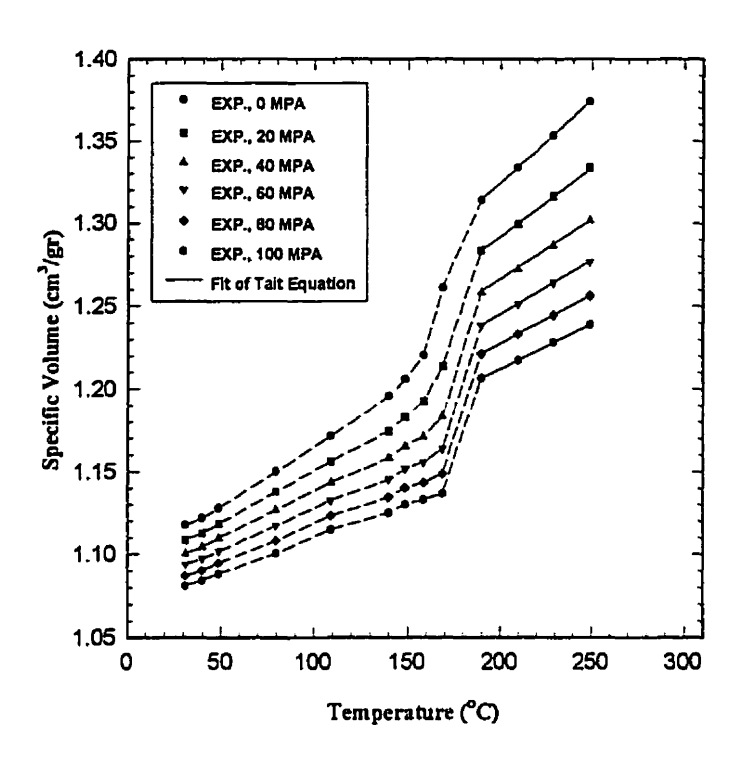


Figure 5.23: Cross-plotted isobars of ADMER resin along with predictions of Tait equation of state

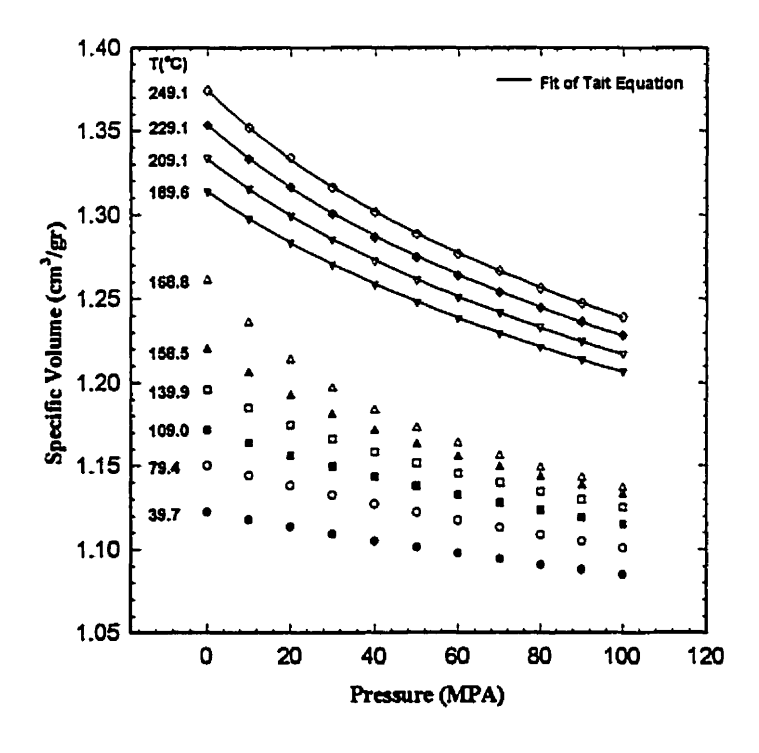


Figure 5.24: Comparison of the experimental isotherms with predictions of Tait equation of state for ADMER resin

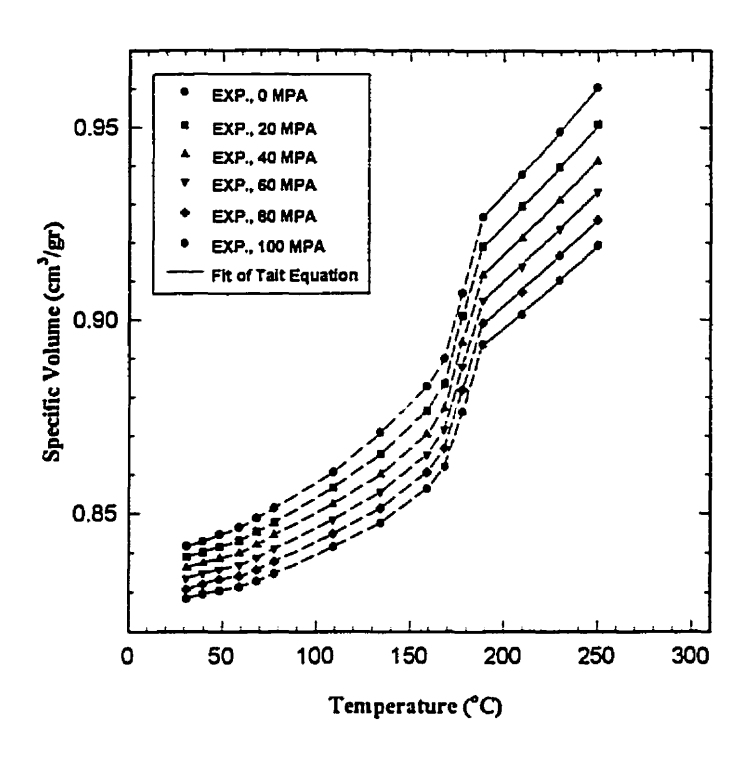


Figure 5.25: Cross-plotted isobars of EVOH resin along with predictions of Tait equation of state

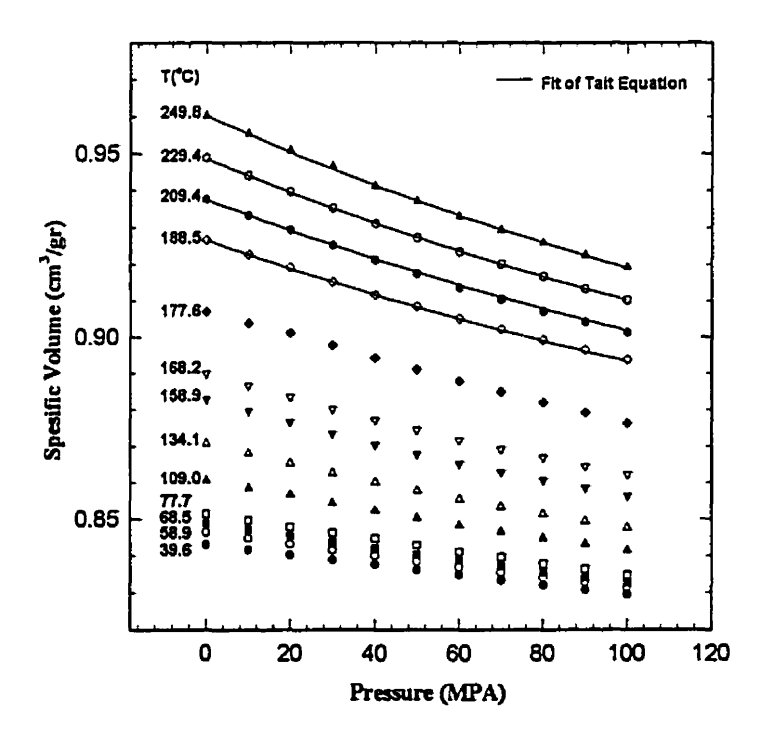


Figure 5.26: Comparison of the experimental isotherms with predictions of Tait equation of state for EVOH resin

5.3 Analysis of Interfacial Tension Results

The purpose of interfacial tension measurements in this study is to evaluate the effect of temperature and compatibilizer level on the interfacial tension of PE/PA-6 and PP/EVOH systems. This should help in the optimization of the interfacial adhesion between phases and, consequently, the mechanical and barrier properties of laminar blends of these polymers can be improved. To our knowledge, there are no reports of such measurements in the literature.

5.3.1 Spinning Drop Results

Due to the limitations indicated in section 4.1.5, the spinning drop method was used for interfacial tension measurements. In particular, this method was chosen versus the pendant drop method due to the high viscosity of the resins and also high interaction at the interface of compatibilized systems. However, the pendant drop method was used for evaluating the accuracy of the spinning drop technique, and to compare the two techniques.

Based on Equations (4.10) and (4.11), four parameters need to be measured in order to find the value of interfacial tension. These are the density difference between the two phases, the angular velocity, the diameter of the spinning drop, and the composite index of refraction for the glass and matrix resin. Among the above, the angular velocity is the easiest to measure. The rotation speed of the motor is shown digitally and a tachometer has been used to calibrate the motor.

5.3.1.1 **PE/PA-6** System

5.3.1.1.1 Density Measurements

The results extracted from section 5.2.2 were used to calculate the density of PE and PA-6 resins at atmospheric pressure. Figure 5.27 presents the melt densities of PE0 and PA-6 resins at atmospheric pressure and different temperatures. In the same figure, the

difference in the densities of the two resins, i.e. $\Delta \rho$, is plotted, too. Least square curve fitting was used to describe the densities of PE and PA-6 resins as well as the difference in the densities, $\Delta \rho$. Due to overlapping of the density curves for PE0 and PE2, the PE2 curve is not shown in this figure. The following equations describe the behavior of the resins at atmospheric pressure:

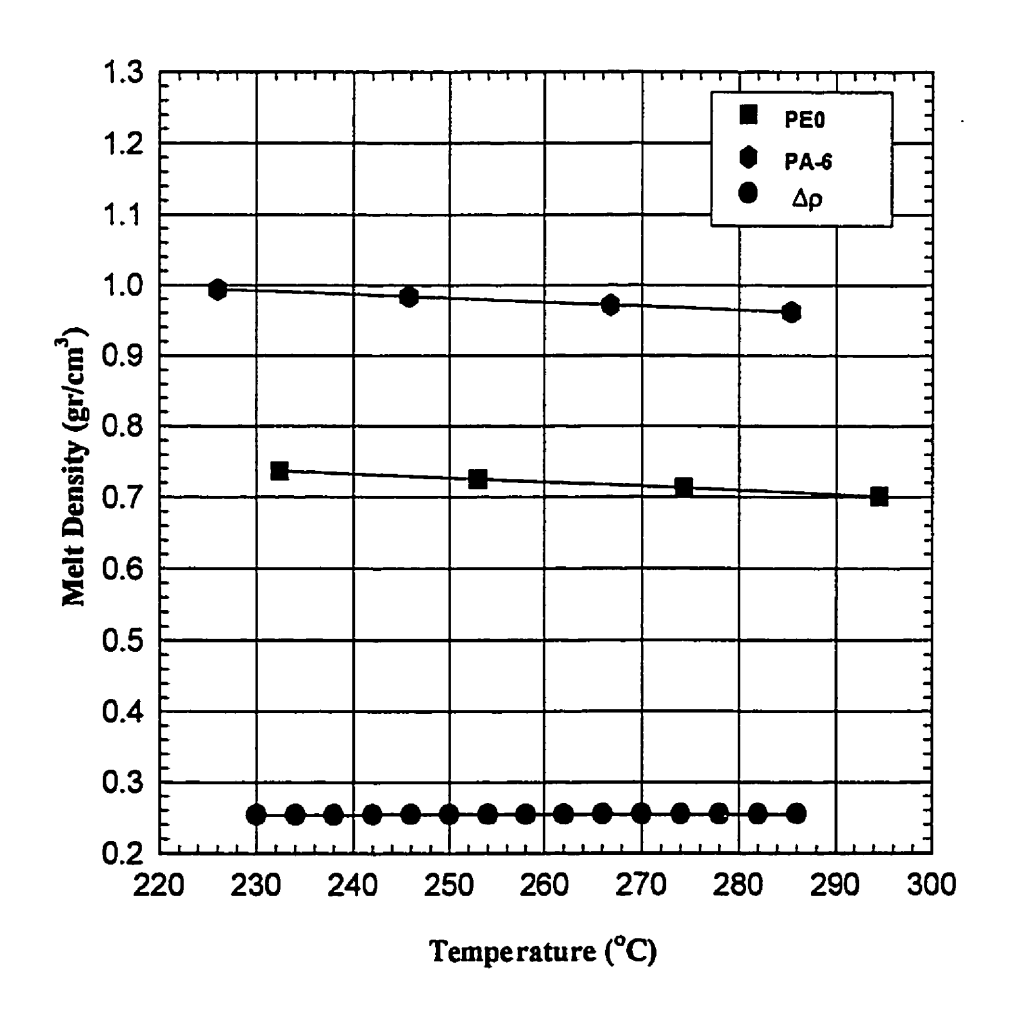


Figure 5.27: Melt densities of PE0 and PA-6 resins vs. temperature at atmospheric pressure along with the difference in melt densities

where T is temperature in °C and ρ is density in g/cm³. For different mixtures of the PE0 and PE2, the additive rule (based on wt%) was used to calculate the density and density difference. As Figure 5.29 shows and also the small value of temperature coefficient in equations 5.17 and 5.18 indicates, temperature does not affect $\Delta \rho$ significantly. This is due to the similar and small temperature coefficients for densities of PE and PA-6 resins, as shown by equations 5.14, 5.15, and 5.16.

5.3.1.1.2 Measurement of the Optical Correction Factor

To obtain the real diameter of the spinning drop from the apparent diameter measurements, it is necessary to evaluate the combined refractive index or optical correction factor at different temperatures. The optical correction factor was measured based on the method explained in section 4.1.5.2.4. The thermal expansion of the rod was found negligible. Figure 5.28 shows the optical correction factor as a function of temperature for PA-6 resin. The optical correction factor decreases linearly with temperature. Applying a least square regression to the experimental data leads to the following equation:

$$n = 1.558 - 3.9 \times 10^{-4} T \tag{5.19}$$

where n is the optical correction factor and T is temperature in degrees Celsius. This equation is valid within the temperature range of 230-270°C.

5.3.1.1.3 Measurement of the Interfacial Tension of PE/PA-6 Pair

Two methods were used to evaluate the value of interfacial tension using the spinning drop technique. The first method is applying the equilibrium diameter of the spinning drop in Equation (4.10). This method is believed to provide the most accurate results for most of the polymer pairs. All the results presented in this study are obtained using this method.

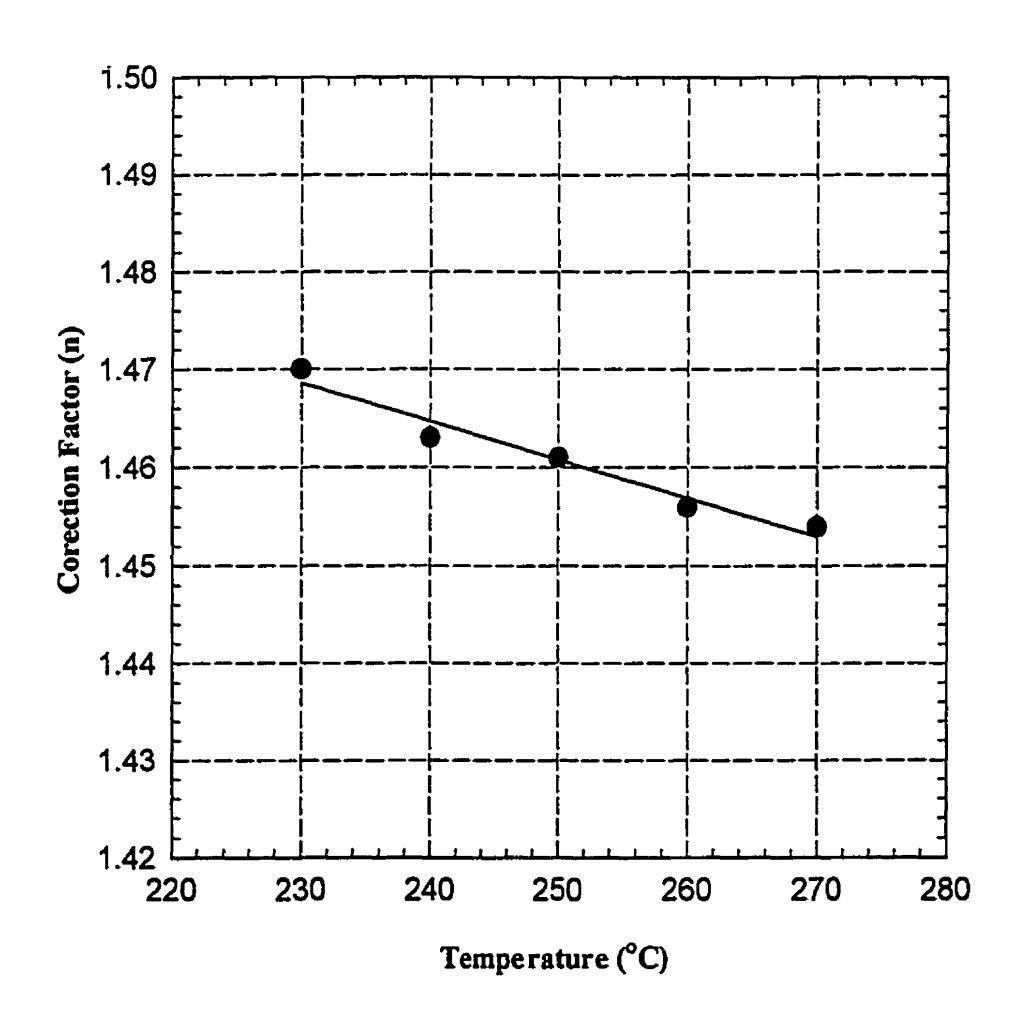


Figure 5.28: Optical correction factor (n) vs. temperature for PA-6 resin

Another method that has been found useful for temperature sensitive polymers is the method of Joseph (132). Joseph and co-workers developed a theory of experimental fitting to cope with the long equilibrium time needed for some polymers. This method is also useful for the polymers that may degrade before reaching mechanical equilibrium. Joseph proposed the following exponential equation:

$$R(t) = R_{\infty} + (R_0 - R_{\infty})e^{-m(t-t_0)}$$
(5.20)

where R(t) is the radius of the spinning drop at time t, R_{∞} is the equilibrium radius, R_0 is the initial radius of the drop, and m is a parameter related to the relaxation time of the system.

Figure 5.29 presents the radius of a spinning drop of maleated PE in the matrix of

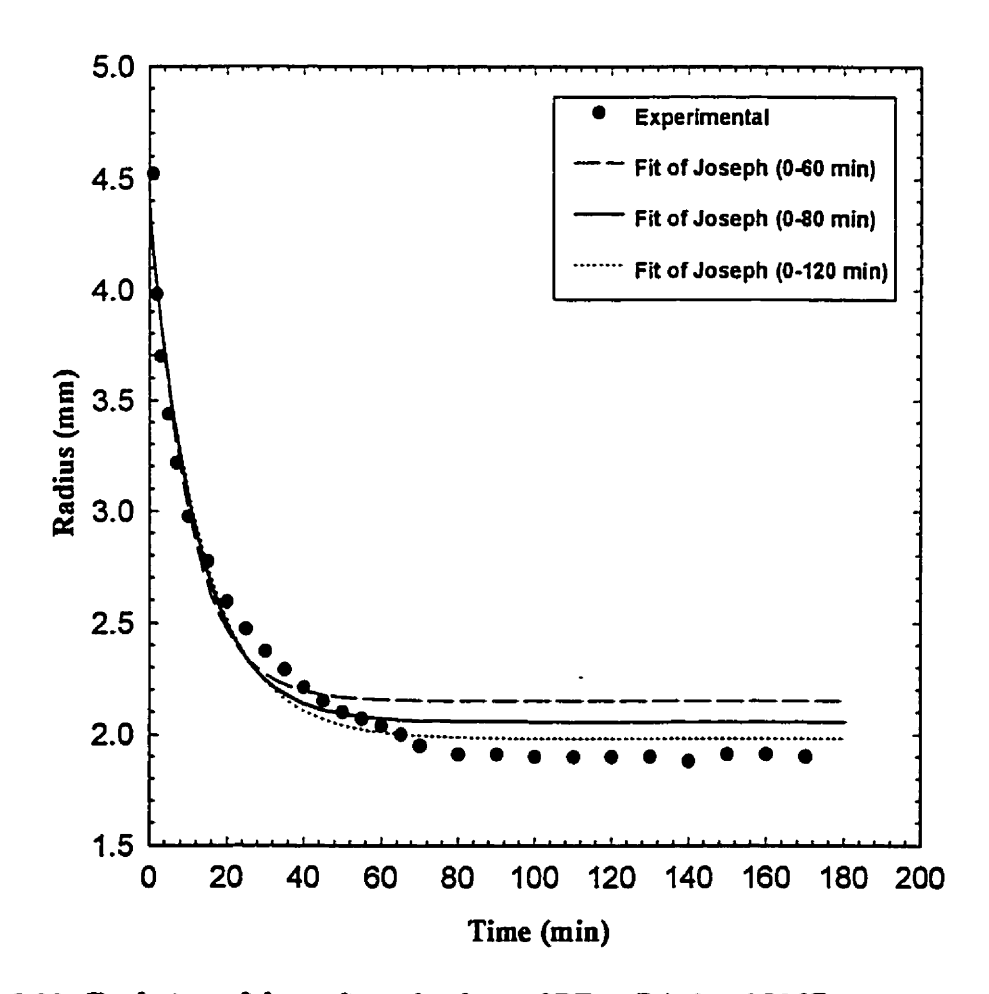


Figure 5.29: Evolution of the radius of a drop of PE in PA-6 at 250 °C

PA-6 resin at 250°C as a function of time. If we consider the equilibrium value of the radius, i.e. the first method, an interfacial tension value of 2.3 dyne/cm is obtained. By using the fit of Joseph to the first 80 min of experimental data, the values of m and R_{∞} are obtained as m=0.083 and R_{∞} =2.05 mm. This method yields a value of 2.7 dyne/cm, which is a fair estimate for the interfacial tension of this system. If this method is used with the first 60 and 120 min of the experimental data, interfacial tension values of 2.8 and 2.4 are obtained, respectively. However, for systems which are sensitive to the temperature, longer times are not recommended.

5.3.1.1.4 Effect of Temperature

The influence of temperature on the interfacial tension of the PE/PA-6 pair was studied, and the results are presented in Figure 5.30. The study covers the practical processing temperature range for PE/PA-6 blends, i.e. 230-270°C. Theoretically, raising the temperature decreases the free energy of mixing at the interface, resulting in the lower interfacial tension values. Therefore, it is expected that the interfacial tension should decrease with increasing temperature. As Figure 5.30 shows, this theoretical trend has been verified. The interfacial tension decreases linearly with increasing temperature. Applying a least square regression to the experimental data, results in the following equation for the temperature dependency of interfacial tension of the PE/PA-6 pair:

$$\gamma = 29.04 - 0.036T$$
 $r^2 = 0.966$ (5.21)

where γ is the interfacial tension in dyne/cm, and T is temperature in degrees Kelvin. The temperature coefficient of 0.036 of interfacial tension is in the range of temperature coefficients reported for most of polymer pairs (153, 154). This equation gives a value of 11.0 dyne/cm for the interfacial tension of PE/PA-6 pair at 230°C. This value is slightly smaller than the reported value of 12.30 dyne/cm by Chen and White et al (105) using the

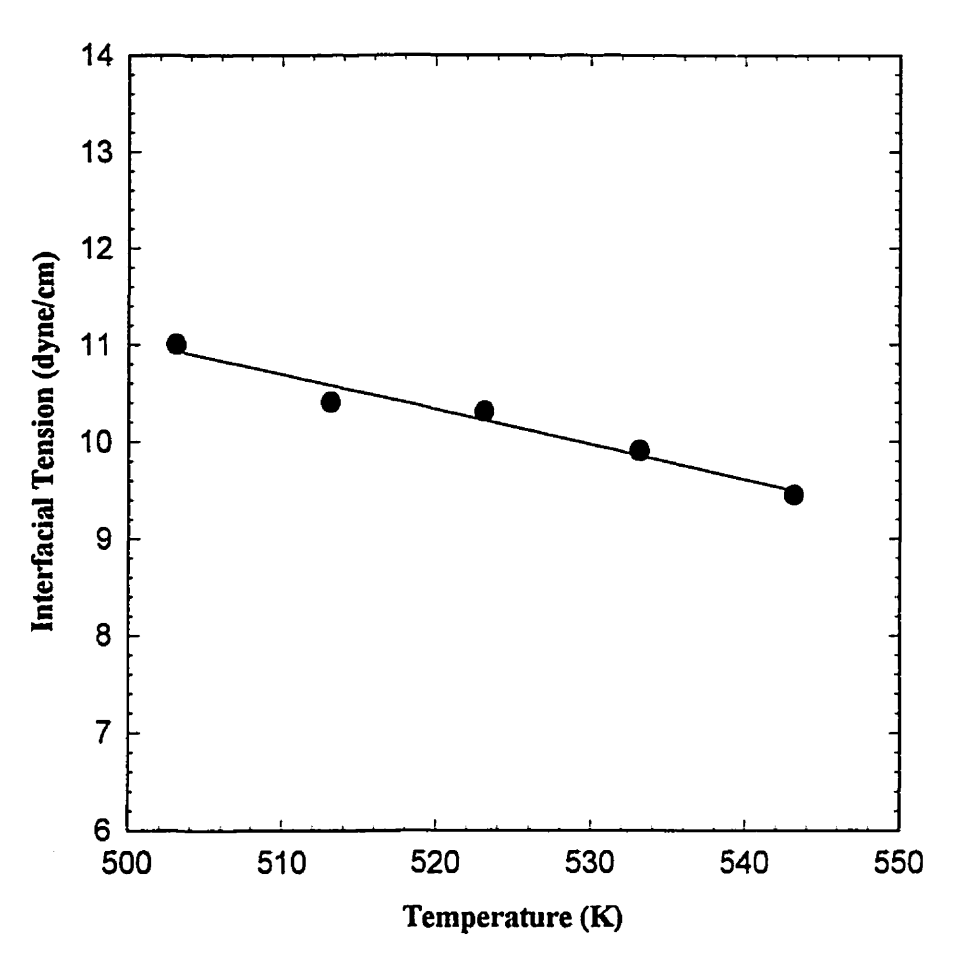


Figure 5.30: Interfacial tension between PE and PA-6 as a function of temperature

pendant drop method. This difference could be due to the small amount of additives that is usually added to commercial grades of resins. However, we shall show later that the spinning drop technique tends to yield lower interfacial tension values than the pendant drop method.

5.3.1.1.5 Effect of the Maleation Content

The magnitude of the interfacial tension is determined primarily by the disparity in the polarities of the two phases. The greater the polarity difference, the greater will be the interfacial tension. Polyethylene is a non-polar polymer with polarity of $X^P=0$. On the

other hand, polyamide-6 is a polar polymer with polarity of X^P=0.188 (123). Therefore, the interfacial tension for PE/PA-6 pair would be high. However, modifying polyethylene with maleic anhydride changes the polarity of this resin and provides polar polyethylene chains. So, it is expected that maleation would lower the interfacial tension between these two polymers.

Figure 5.31 shows the interfacial tension between PE and PA-6 as a function of MAH content of polyethylene. Interfacial tension decreases exponentially with increasing the maleation content of polyethylene and levels off to a value of 1.5 dyne/cm. The figure indicates that from the economical point of view, maleation content of more than 0.03% is

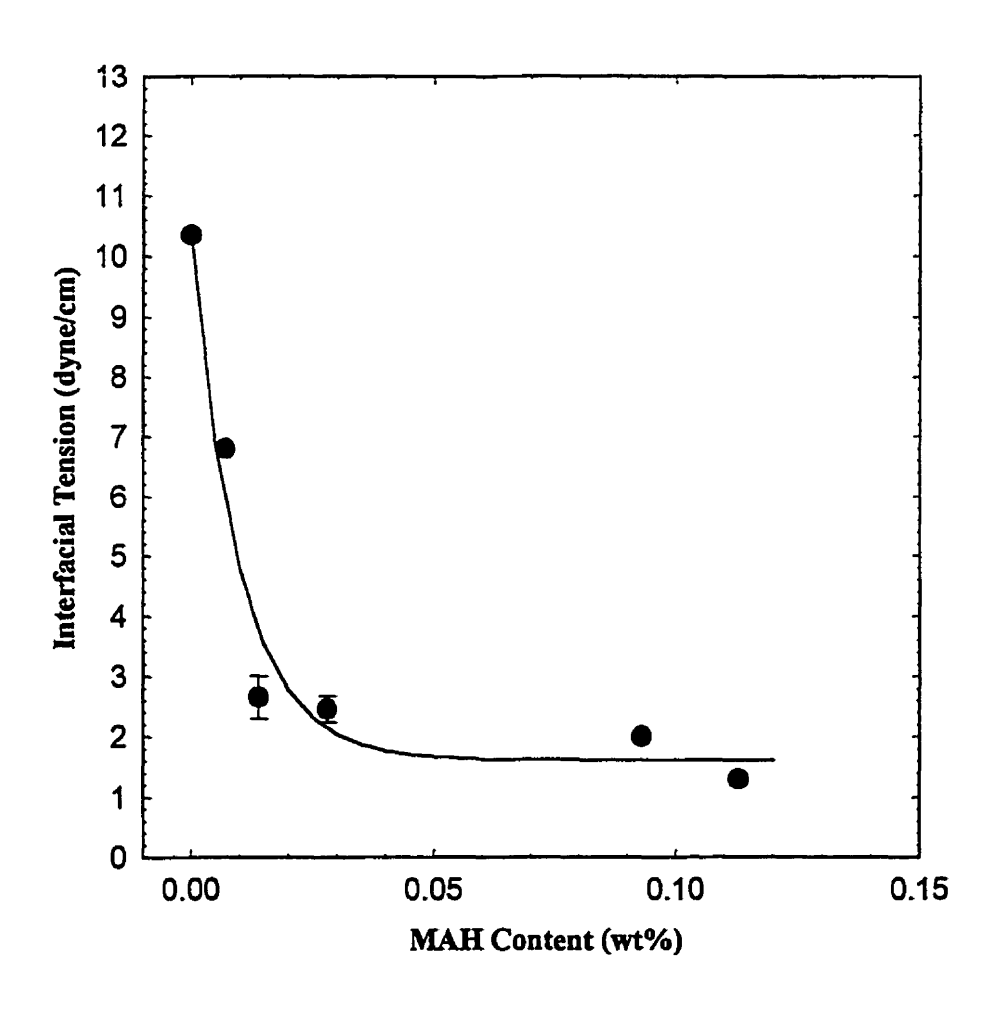


Figure 5.31: Interfacial tension between PE and PA-6 as a function of MAH content (wt.%) of PE at 250°C.

not necessary. Patterson et al (131) observed this typical behavior for polydimethylsiloxane and a copolyester fluid. The following exponential equation provides a good estimate of the dependency of interfacial tension on maleation content of PE at 250°C, within the range of experimental error of the technique.

$$\frac{\gamma_M - \gamma_{\infty}}{\gamma_0 - \gamma_{\infty}} = e^{-nM} \tag{5.22}$$

where $\gamma_{\infty}=1.62$, $\gamma_{0}=10.35$, and n=101.07. In this equation, γ_{M} is the value of interfacial tension of PE/PA-6 pair at the maleation level of M in dyne/cm, γ_{∞} is interfacial tension for high maleation content, γ_{0} is the value of interfacial tension for a system with no maleation, M is the maleation content of polyethylene in wt.%, and n is a parameter that determines the effectiveness of the maleation on lowering the interfacial tension.

5.3.1.2 PP/EVOH System

5.3.1.2.1 Density Measurements

The PVT studies of individual resins, reported in section 5.2.3 were used to extract the required data. Figure 5.32 shows the melt densities of ADMER and EVOH resins as well as the difference between the densities of these two resins. Using least square curve fitting yields the following equations for the densities of ADMER and EVOH resins within the temperature range of 188<T<250°C.

$$\rho_{ADMER} = 0.8674 - 5.600 \times 10^{-4} T \tag{5.23}$$

$$\rho_{EVOH} = 1.1963 - 6.205 \times 10^{-4} T \tag{5.24}$$

$$\Delta \rho = \rho_{EVOH} - \rho_{ADMR} = 0.3289 - 6.01 \times 10^{-5} T$$
 (5.25)

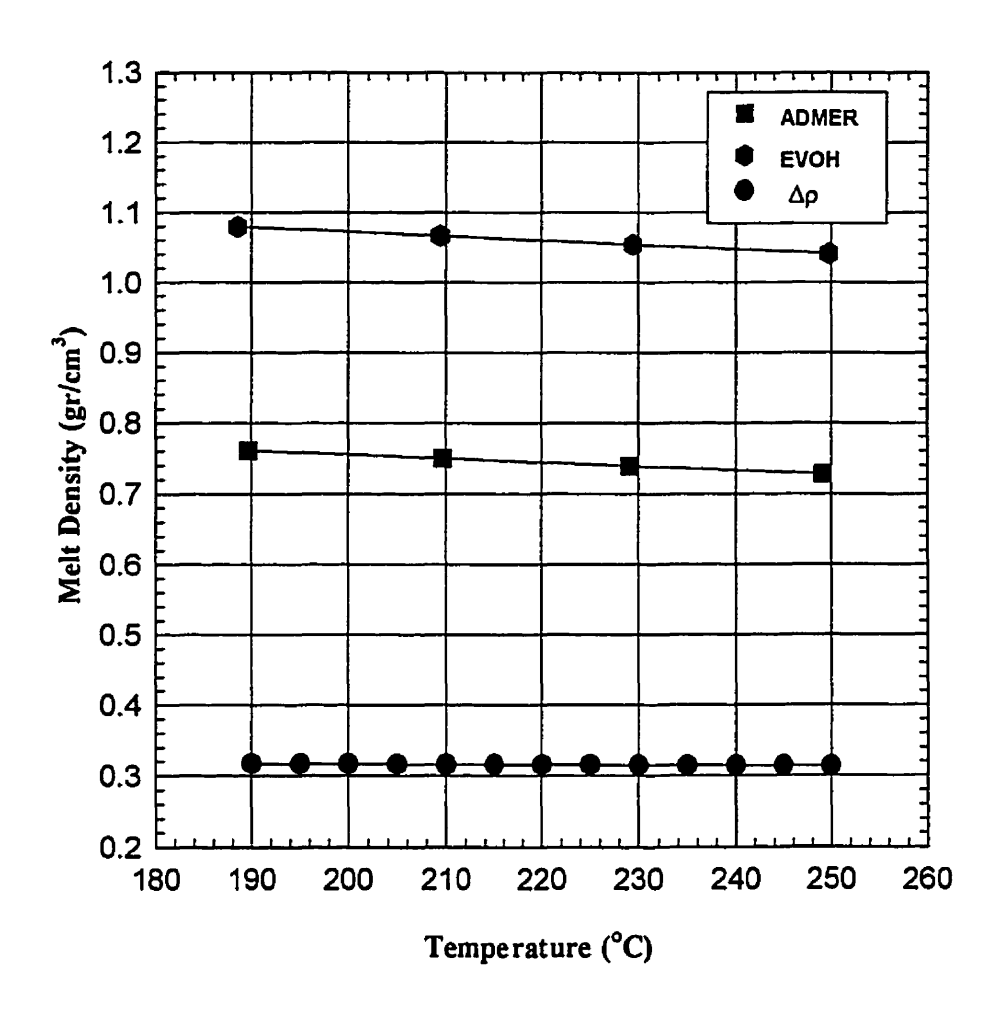


Figure 5.32: Melt densities of ADMER and EVOH resins vs. temperature at atmospheric pressure along with the difference in melt densities

Due to similar and small temperature coefficients of Equations (5.23) and (5.24), the temperature coefficient of Equation (5.25), is small. It indicates that the difference between the densities of the ADMER and EVOH is almost constant, and it does not change significantly with temperature.

5.3.1.2.2 Measurement of the Optical correction Factor

Figure 5.33 presents the optical correction factor of EVOH and ADMER resins as a function of temperature. Similar to the PE/PA-6 system, the optical correction factor that

is a combined refractive index effect, decreases linearly by increasing the temperature. The following equation, obtained from least square curve fitting of the experimental data, gives the value of the optical correction factor at different temperatures.

$$n = 1.5555 - 3.80 \times 10^{-4} T \tag{5.26}$$

This equation is valid within the temperature range of 210-240°C. However, extrapolation to lower and higher temperatures can be used if needed.

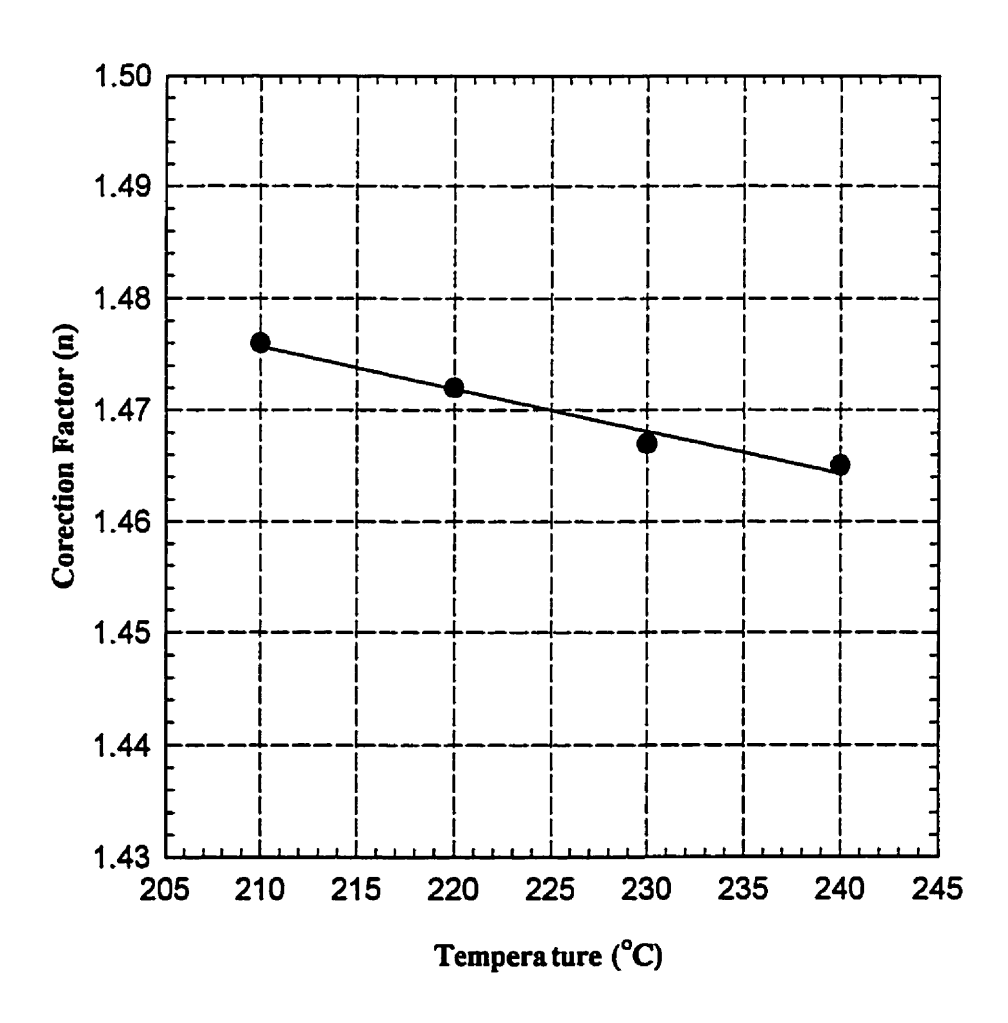


Figure 5.33: Optical correction factor (n) vs. temperature for EVOH resin

5.3.1.2.2 Measurement of Interfacial Tension of ADMER/EVOH Pair

Figure 5.34 shows the evolution of the radius of a drop of EVOH in the matrix of ADMER at 220°C. The Method of Joseph, i.e. equation 5.20, can be used to predict the value of interfacial tension for ADMER-PP(50-50)/EVOH pair. Applying the fit of Joseph to the first 80 min of the experimental data, yields the value of 0.1115 and 2.2879 mm for the m and R_{∞} , respectively. This method gives a value of 4.1 dyne/cm for the interfacial tension of this system at 220°C. Using the equilibrium value of the radius results in a value of 3.6 dyne/cm for the same system. Employing this method for the first 60 and 120 min of the experimental data yields values of 4.3 and 3.8 for the interfacial tension, respectively. The second method, i.e. the equilibrium value of radius, which proved to be more accurate has been used for all the interfacial tension measurements of PP/EVOH system.

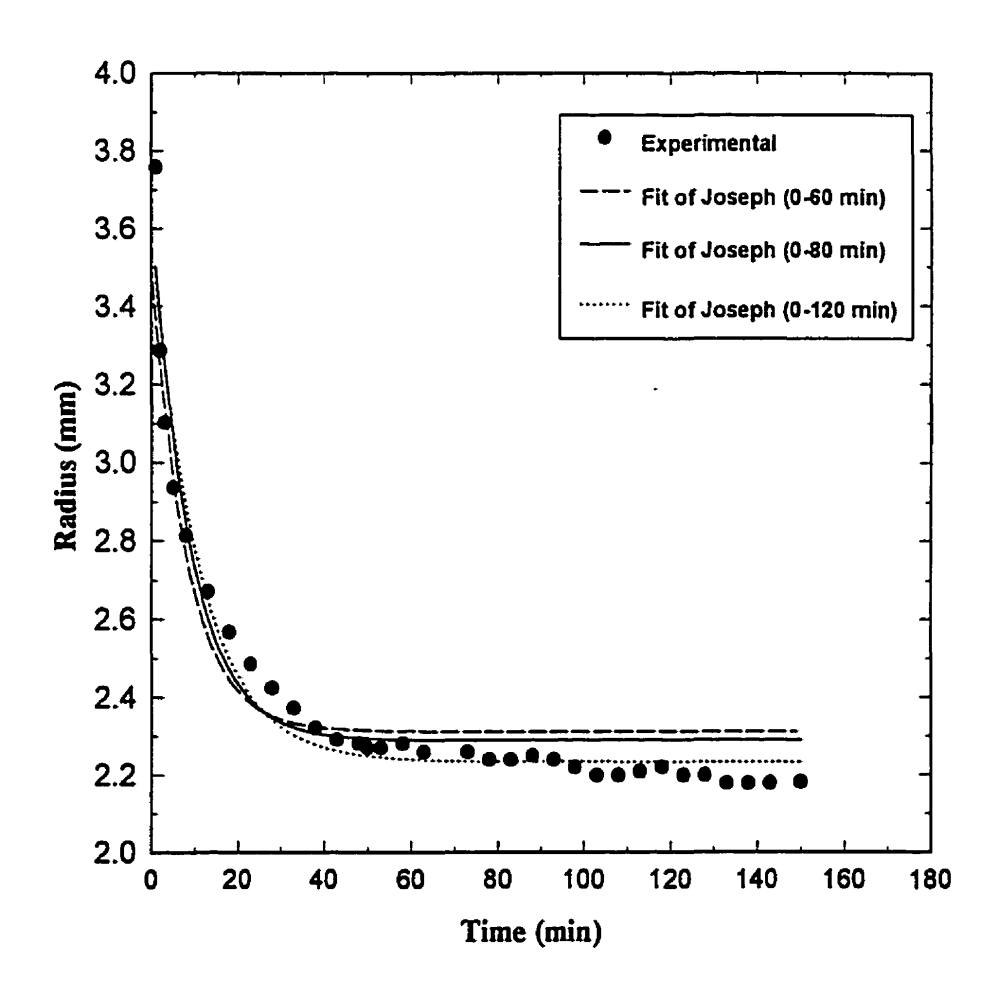


Figure 5.34: Evolution of radius of a drop of ADMER-PP (50-50) in EVOH at 220 $^{\circ}$ C.

5.3.1.2.4 Effect of temperature on Interfacial Tension

The interfacial tension of ADMER/EVOH pair was measured within the temperature range of 210-240°C with temperature interval of 10°C. The results are given in Figure 5.35. As was expected from literature reports (153, 154) and also from the results of PE/PA-6 system, the interfacial tension decreases linearly with increasing temperature. Applying a least square curve fitting to the experimental data, yields the following equation for the temperature dependency of interfacial tension of ADMER/EVOH pair.

$$\gamma = 47.4 - 0.087T$$
 $r^2 = 0.988$ (5.27)

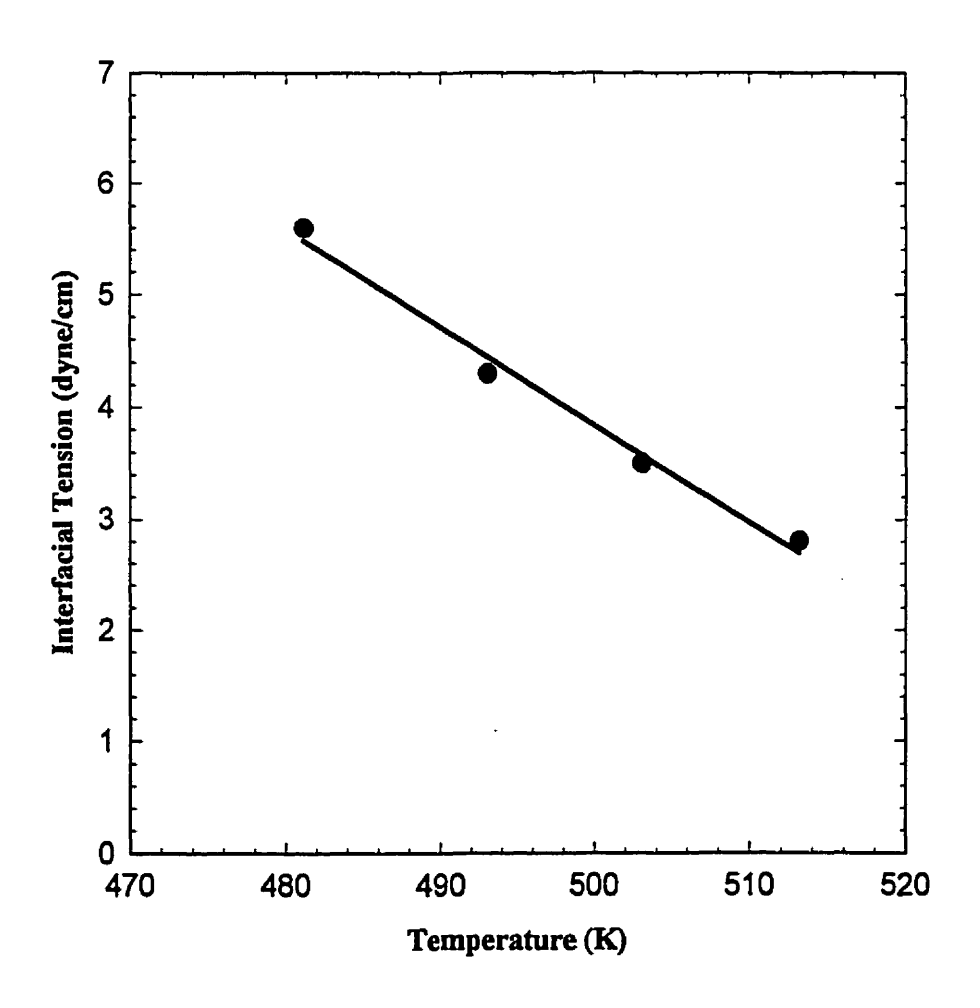


Figure 5.35: Interfacial tension between ADMER and EVOH as a function of temperature

The temperature coefficient of 0.087 for interfacial tension of ADMER/EVOH is higher than the range of reported temperature coefficients of other polymers (153), including the reported results in section 5.3.1.1.4 of this study for PE/PA-6 pair. However, Kamal et. al. (154) reported a similar value of 0.08 for the temperature coefficient of PP/PS pair. The presence of reactive groups of maleic anhydride at the interface and the increased activity of these groups at higher temperatures, contribute to accelerated lowering of interfacial tension, thus leading to the higher temperature coefficients. The temperature coefficient of the PP/EVOH system might provide information regarding the behavior of this system at different temperatures.

5.3.1.2.5 Effect of Maleation Content on Interfacial Tension of PP/EVOH Pair

Polypropylene is a non-polar polymer with polarity of 0.02. On the other hand EVOH is a polar polymer. However, there are no reported data on polarity of ethylene vinyl alcohol resin. Modifying the polypropylene with maleic anhydride groups increases the polarity of this resin and provides a smaller polarity difference between PP and EVOH resins. Therefore, it is expected to obtain lower interfacial tension by increasing the maleic anhydride content of polypropylene.

Figure 5.36 shows the influence of maleation content of polypropylene on interfacial tension of PP/EVOH system at 220°C. This figure shows an unusual behavior for interfacial tension of maleated PP and EVOH. By increasing the maleation content of PP, the interfacial tension decreases, as expected and after a critical maleation content, it increases. One explanation for this unusual behavior might be the result of a chemical reaction that causes saturation at the interface. For highly maleated systems, faster methods of measuring the interfacial tension might be needed. The imbedded fiber retraction method or the breaking thread method might yield the interfacial tension data in shorter times. They should be explored for these highly maleated systems.

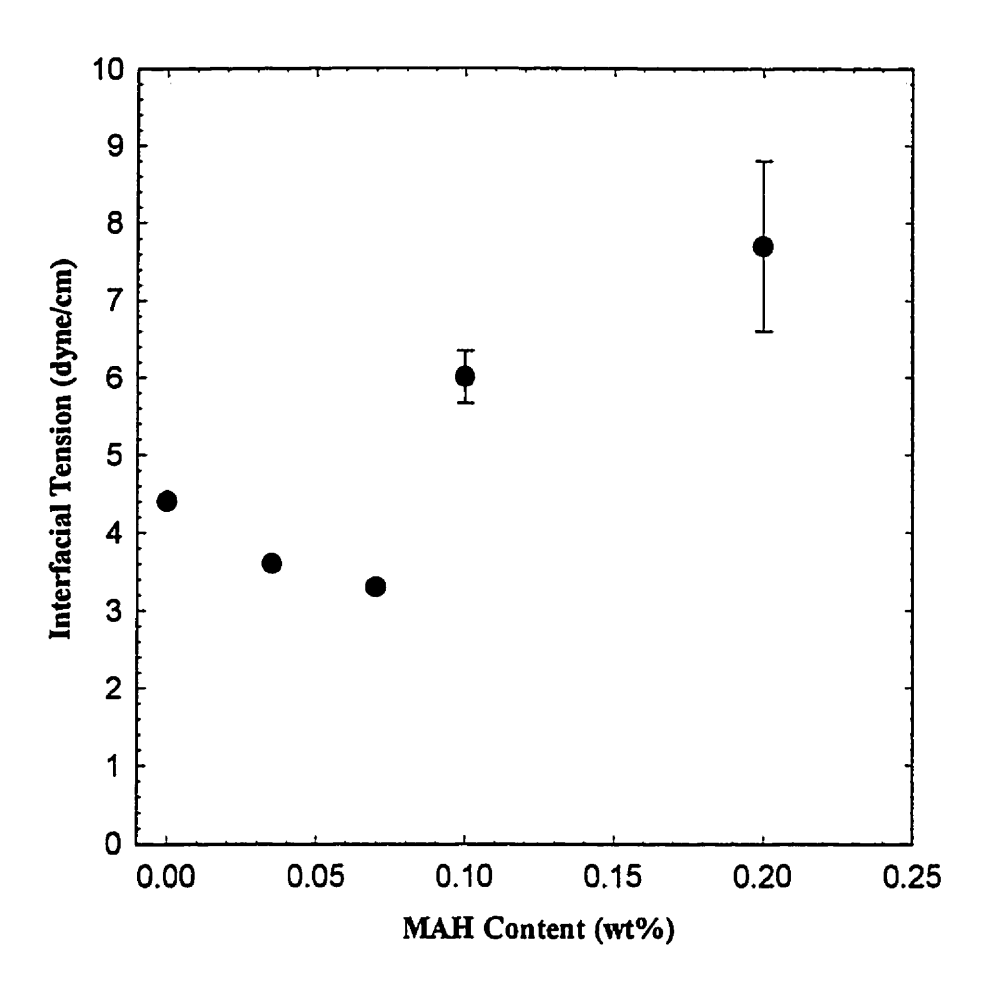


Figure 5.36: Interfacial tension between PP and EVOH as a function of MAH Content (wt.%) of PP at 220 $^{\circ}$ C

5.3.2 Evaluation of Spinning Drop Apparatus

The pendant drop apparatus that has been shown to yield reliable interfacial tension results (128-130, 134, 154) was used to evaluate the accuracy of the spinning drop apparatus. Due to the high viscosity of PE0, it was not possible to use this resin with the pendant drop apparatus. Therefore, it was decided to use a low viscosity polyethylene with the same PA-6 resin and to carry out the interfacial tension measurements using both the spinning drop and pendant drop methods. The polyethylene used was Sclair 2908 produced by Dupont Co. with a melt index of 6.0. The complete specification of this resin is reported elsewhere (155). The measurements were conducted at two temperatures:

240 and 260°C. Figure 5.37 presents the interfacial tension as a function of temperature for Sclair 2908 resin/PA-6, with both methods, i.e. the spinning drop and pendant drop methods. For comparison purposes, the interfacial tension of PE0 is also given. The spinning drop method gives interfacial tension values that are 10-15% lower than the pendant drop technique. The above difference between the interfacial tension values obtained using the two different techniques is within the experimental error of the spinning drop method, i.e. 15%. Applying the least square curve fitting, the following equations are obtained for the temperature dependency of interfacial tension of PE/PA-6 pair.

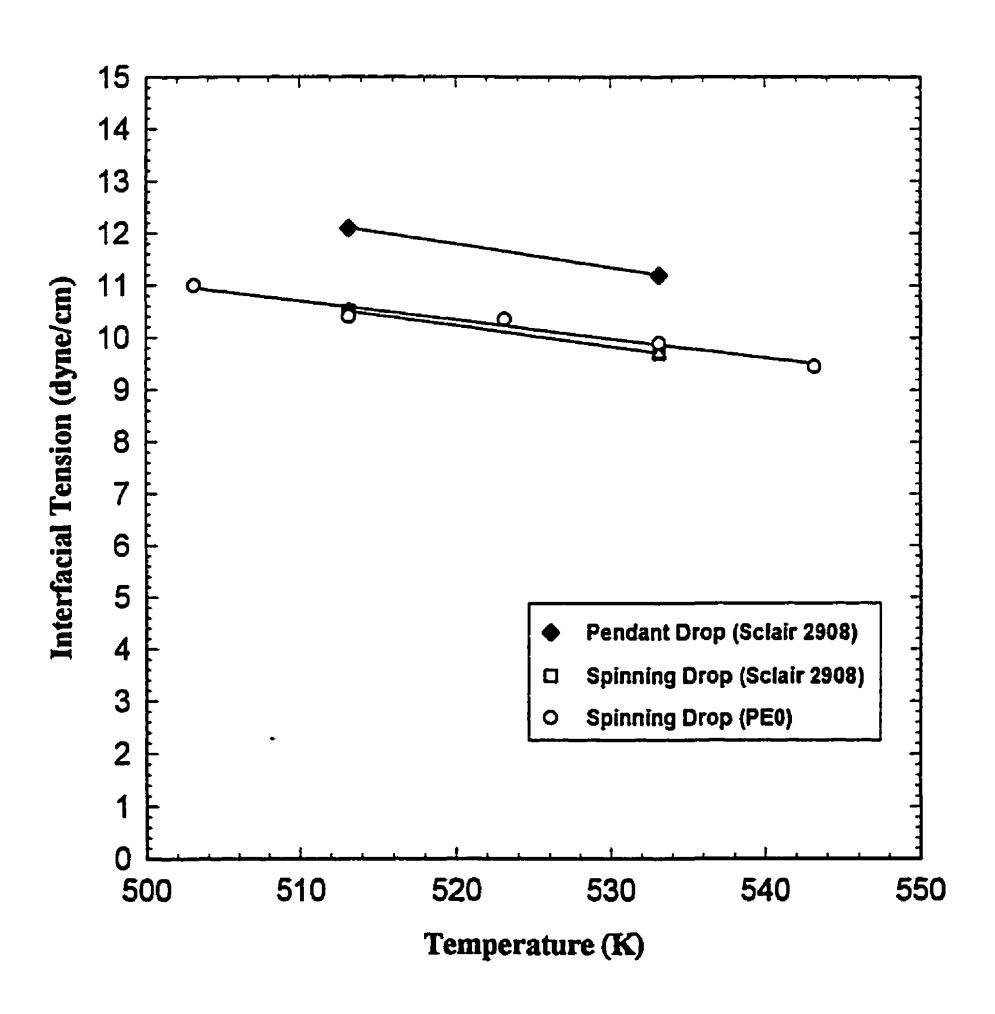


Figure 5.37: Comparing the interfacial tension between PE and PA-6 as a function of temperature using the spinning drop and pendant drop methods

$$\gamma = 29.04 - 0.036T$$
 Spinning Drop, PEO/PA-6 (5.31)

$$\gamma = 31.03 - 0.040T$$
 Spinning Drop, Sclair 2908/PA-6 (5.32)

$$\gamma = 35.2 - 0.045T$$
 Pendant Drop, Sclair 2908/PA-6 (5.33)

Considering the experimental error of both techniques, the temperature coefficients given by the different methods and reins are similar with an average of 0.04 dyne/cm.°C.

5.3.3 Prediction of Interfacial Tension

There are different thermodynamic theories to predict the interfacial tension between polymers (156-160). Among them, the mean field theory and the square gradient theory are more often used. A recent evaluation of these theories with experimental data has been reported by Kamal et. al. (154). However, to employ these theories, the value of the Flory-Huggins interaction parameter for the polymer pairs is needed. In the absence of reliable experimental Flory-Huggins interaction parameter, the harmonic-mean field equation theory is shown to predict well the interfacial tension between polymers (153). Detailed derivation of this theory has been explained in the same reference and the final equation is given here:

$$\gamma_{12} = \gamma_1 + \gamma_2 - \frac{4\gamma_1^d \times \gamma_2^d}{\gamma_1^d + \gamma_2^d} - \frac{4\gamma_1^p \times \gamma_2^p}{\gamma_1^p + \gamma_2^p}$$
 (5.34)

where γ_{12} is the interfacial tension between two polymers, γ_1 and γ_2 are the surface tension of two polymers, γ_i^p is the polar, and γ_i^d is the non-polar or dispersive component of the surface tension and are defined here:

$$\gamma = \gamma^d + \gamma^p \tag{5.31}$$

$$\gamma^{P} = \gamma \cdot \chi^{P} \tag{5.32}$$

and

$$\gamma^d = \gamma \cdot \chi^d = \gamma \cdot (\chi^p - 1) \tag{5.33}$$

where χ^p is the polarity of polymer.

The value of polarities of polyethylene and polyamide-6 are reported zero and 0.188, respectively. The surface tension values for PE and PA-6 are reported 21.9 and 35.8 dyne/cm, respectively. Applying these values in Equations (5.30) through (5.34), results in a value of 7.8 dyne/cm for interfacial tension of PE/PA-6 at 260°C. Experimental results give a value of 9.6 dyne/cm for the same system at the same temperature. Considering the 15% experimental error for the spinning drop method, the theoretical prediction of harmonic-mean equation is a fair estimate for the interfacial tension of PE/PA-6 pair. More accurate parameters used in the theoretical analysis, and better experimental results could improve the discrepancy between two approaches.

CHAPTER 6

RESULTS AND DISCUSSION

6.1 Morphology of Blends

6.1.1 HDPE/PA-6 Blends

To evaluate morphology development in HDPE/PA-6 blends, three types of blends were studied:

- Blends of PE0/PA-6 without using any compatibilizer.
- Blends of PE0/PE2/PA-6, where PE2 is a maleic anhydride grafted polyethylene and used as a compatibilizer.
- Blends of PE1/PA-6 or PE2/PA-6, where the maleated polyethylene was used as the matrix.

The main processing parameters that are expected to affect the morphology of extruded ribbons are given in Table 4.3. These effects are evaluated and discussed in details here.

6.1.1.1 Verification of Existence of Laminar Morphology

To ensure the existence of laminar morphology rather than fibrillar structure in the extruded ribbons, the samples were examined at 4 locations, both in the flow and transverse directions, as explained in section 4.2.2. Figure 6.1 shows the morphology of a 70/10/20 (PE0/PE2/PA-6 wt%) blend at 4 locations as indicated in Figure 4.9. The elongated particles of PA-6, shown in dark color, are present in all micrographs. However, these elongated particles are longer in micrographs "a" and "d", i.e. in the flow

direction. This is due to differences in the extension ratio in the flow and transverse directions. The extension ratio is 270% in the transverse direction, while in the flow direction, for the die exit gap of 1.0 mm, it is 1000%. Although, the stretch ratio in the transverse direction is relatively small, it is sufficient to the development of layers, which should result in good barrier properties. The above calculated stretch ratios are for the matrix, and, depending on the viscosity ratio, the stretch ratio of the dispersed phase may be higher or lower.

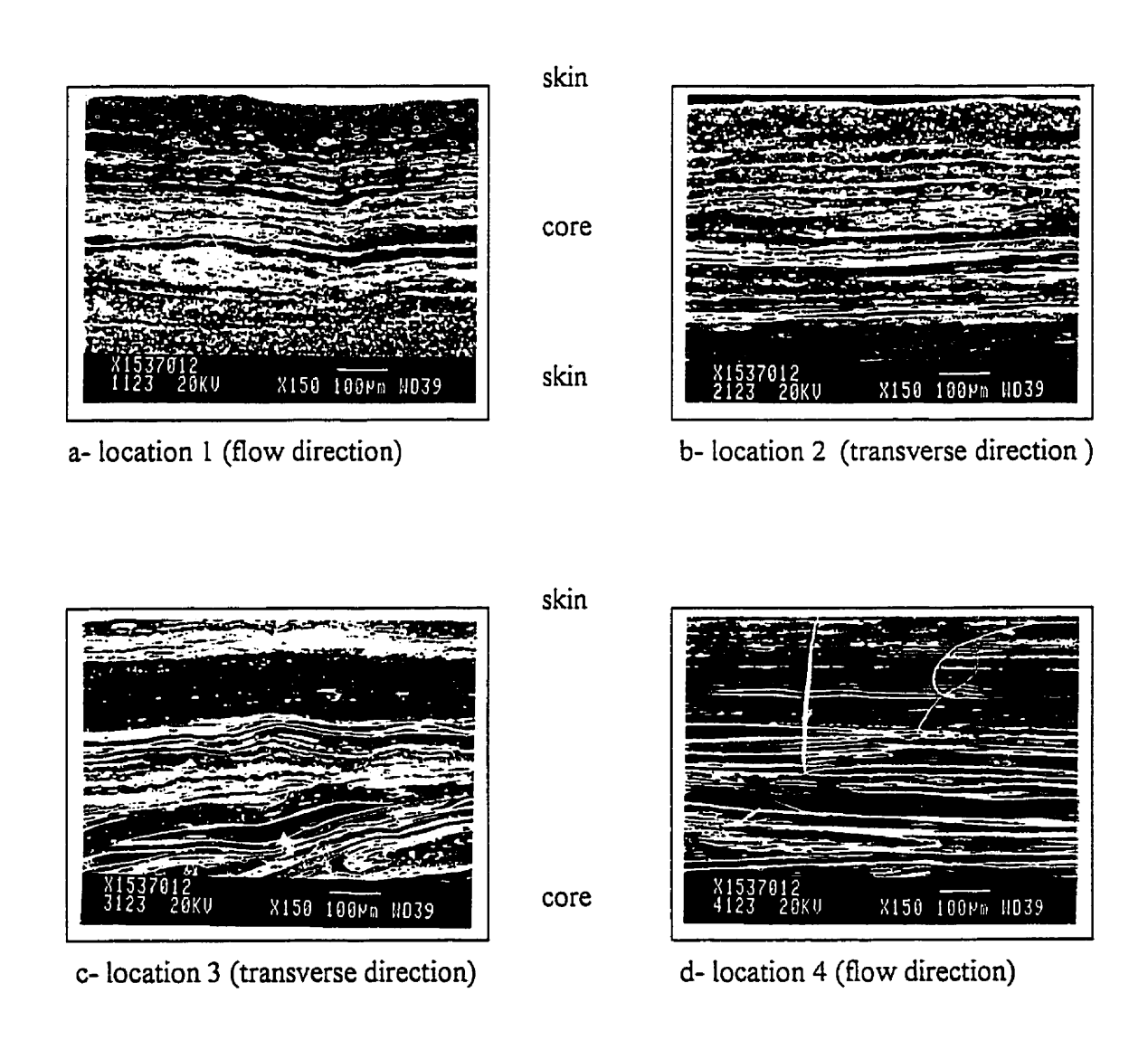


Figure 6.1: Morphology of extruded ribbons of PE0/PE2/PA-6 (70/10/20 wt%) blend in 4 locations indicated in Figure 4.10.

6.1.1.2 Variation of Microstructure across the Ribbon Thickness

The morphology changes across the ribbon thickness may vary, depending on the processing conditions and blend composition. However, a general trend has been observed in all the blends and different processing conditions. Across the thickness, the extruded ribbon is divided into three zones: core, intermediate and skin. Generally the core and intermediate zones have the same type of morphology, and there is no clear distinction between them. In these two regions, extensional flow is dominant and layered structure is observed. Depending on the processing conditions and composition, the length, thickness and overlapping area of the layers vary. As the skin is approached, the shear flow becomes dominant and dispersed phase particles appear as spheres, ellipsoids and agglomerates. The thickness of skin, core, and intermediate zone depends on the processing conditions.

Figure 6.2 presents the morphology, in the longitudinal direction, of three different samples of PE/PA-6 blends across the thickness of extruded ribbons. For all three blends, the percentage of PA-6 resin was kept constant at 20 wt%. Micrograph 6.2.a is a blend which prior to extrusion in the single screw extruder, had already been pre-compounded in the twin screw extruder. In this sample, the skin zone is large, and in the core and intermediate zone, the layered structure is observed. However, the layers are small in length and number and overlap is not large. Figure 6.2.b involves a blend with stronger laminar structure, where the skin region is thinner and, in the core and intermediate zone, longer particles having more overlap area are observed. Micrograph 6.2.c shows a sample where a large number of elongated layers of dispersed phase cover all the length of the picture, and the skin zone occupies a small area. This micrograph presents profound laminar morphology. Although, the morphologies of these three samples are quite different, the general trend of variation of morphology across the thickness of the ribbon is similar.

Figure 6.3 shows the results of the image analysis for micrographs 6.2.a and 6.2.b. Two parameters, which are important in evaluation of the laminar structure, are aspect

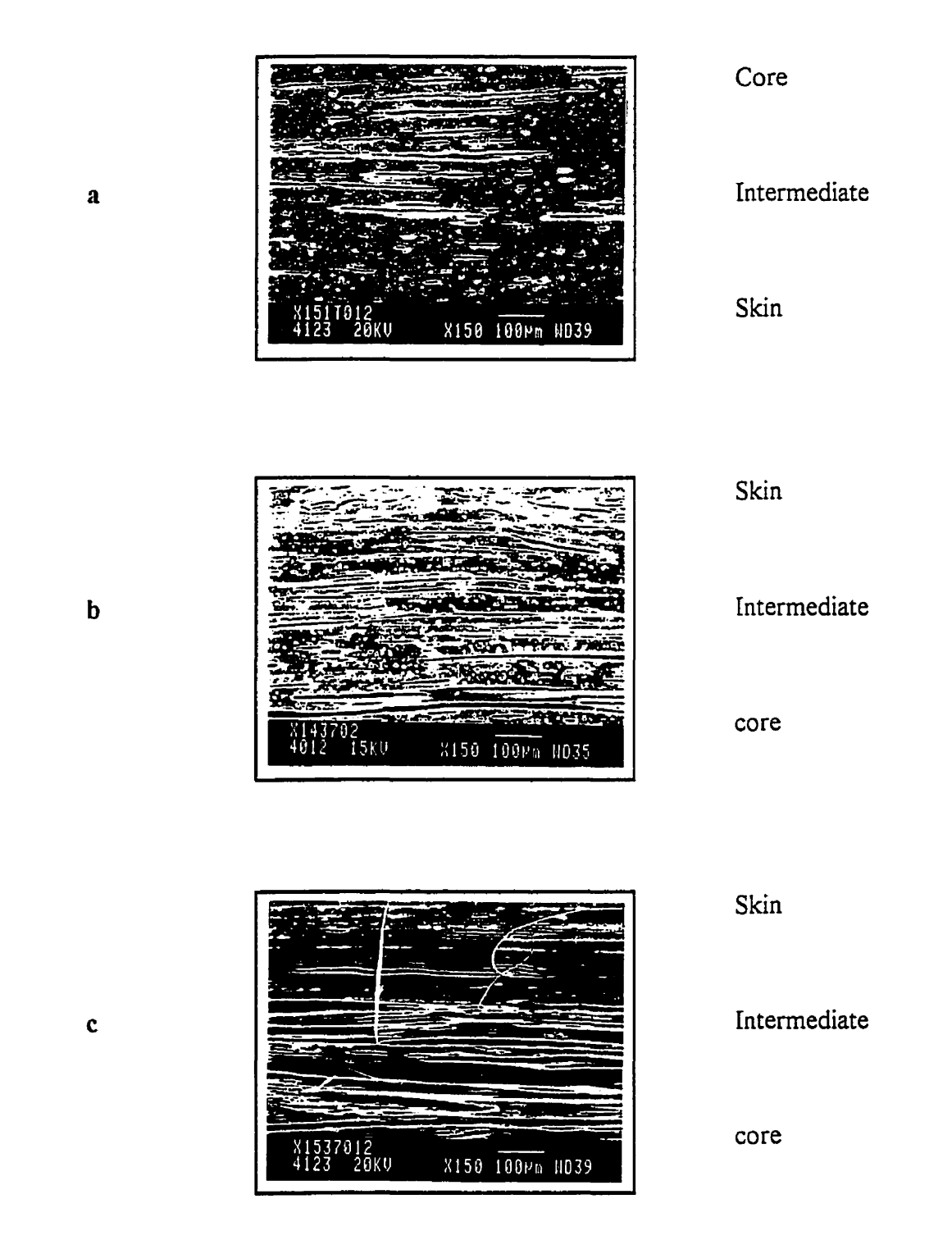
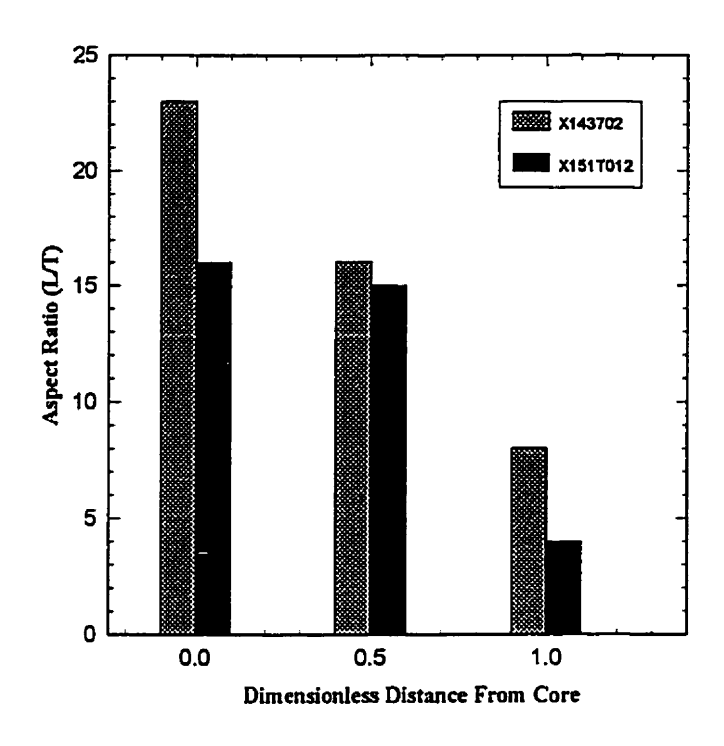


Figure 6.2: Variation of morphology of HDPE/PA-6 blends across the thickness of extruded ribbon (longitudinal), a-X151T012 b-X143702 c-X1537012



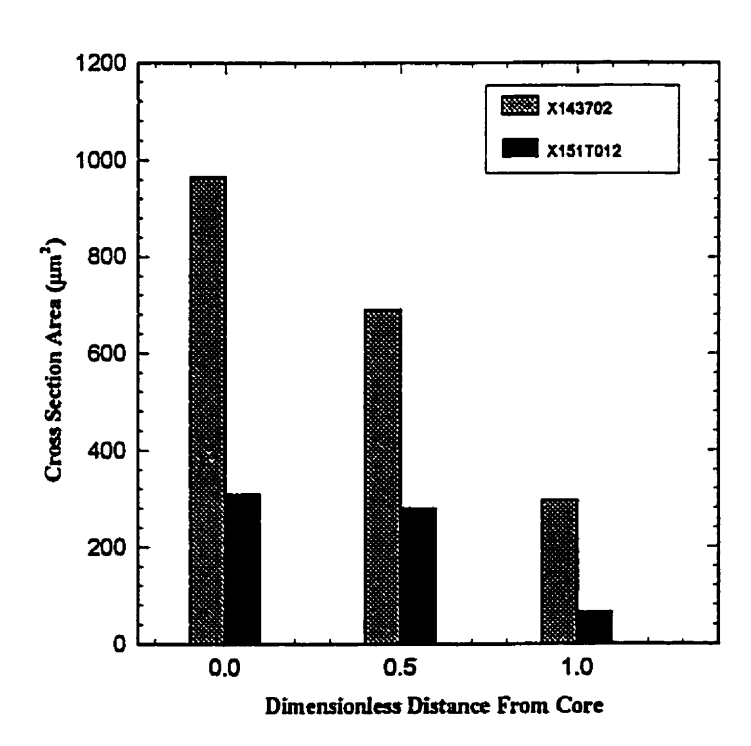


Figure 6.3: Variation of cross section area (length×Thickness) and aspect ratio across the ribbon thickness for PE/PA-6 blends

ratio and area of particles. These are presented in this figure. The general trend observed in the three micrographs of Figure 6.2, is verified quantitatively in Figure 6.3. In the core and intermediate regions, where the extensional flow is dominant, the particles are more elongated. As the skin area is approached, the shear flow becomes dominant. Therefore moving from core to the skin is associated with smaller aspect ratios. In the case of sample X143702, the change is gradually, while for the other sample, the core and intermediate zone show similar aspect ratios. The aspect ratio drops abruptly for the skin zone. The variations of particle area shows a similar trend. In the case of sample X143702, which is an uncompatibilized blend, the gradual and smooth change of particle size might be related to the effect of coalescence. During the flow of blend through the converging sections of the die unit, the PA-6 particles coalesce more in the core region. The effect of coalescence diminishes as the distance from the wall decreases. So, a gradual decrease in the particle size is observed. In the case of sample X151T012, which is a compatibilized blend, coalescence does not occur to the same extent. Thus, the particles tend to be smaller. The processing temperature in the screw zone used to extrude sample X151T012, is mostly lower than the melting point of PA-6 resin. Therefore, the PA-6 particles are conveyed as solid during more than 75% of the length of the screw zone. Moreover, the PA-6 particles do not break in this region, especially, in the core of the melt mass. However, the particles, which are close to the walls, i.e. close to screw or barrel, are more likely to experience higher temperatures and shear rates. For the early stages of mixing, Lindt and Ghosh (113) calculated 40 and 70°C temperature difference between the solid part in the core with the melt film of the polymer at the screw and barrel surfaces. respectively. The particles in the melt undergo breakup due to the stress and strain fields in the system. This explains the sudden decrease of particle size in the skin for this sample.

6.1.1.3 Effect of Die Temperature on Morphology

The stretching of spherical particles of the dispersed phase into two-dimensional platelets occurs mainly in the die unit. As discussed in sections 4.2.2 and 5.1.1, it is generally agreed that a viscosity ratio of unity provides the maximum deformation of dispersed

phase particles without breaking them up. The processing window for polyethylene is so wide that it does not limit the processing window for the PE/PA-6 blends. Therefore, considering the optimum processing window for PA-6 (161) and taking into account the influence of temperature on the value of viscosity ratio, three different temperatures of 230, 250 and 270°C were chosen for the die unit. Preliminary runs revealed that die temperature of 230°C is very low and is not easy to work with. Therefore, die temperatures of 250 and 270°C were selected for further studies. Rheological studies in section 5.1.1.1 showed that a die temperature of 250°C provides a viscosity ratio close to unity for the range of shear rates encountered inside the die unit. On the other hand, a temperature coefficient of 0.036 for the interfacial tension of PE/PA-6 pair, presented in Figure 5.30 and Equation (5.21), indicates that by increasing the temperature from 250 to 270°C, interfacial tension decreases 0.7 dyne/cm. Thus, interfacial tension changes due to temperature do not play a major role in the deformation of PA-6 particles inside the die.

Figure 6.4 presents a comparison between the morphology of a sample extruded at die temperature of 250°C, i.e. sample X133702, with the morphology of a sample extruded at die temperature of 270°C, i.e. X143702. The composition and other processing conditions are the same for the two samples. They are listed in Appendix B.

Figure 6.5 shows the results of image analysis on the same samples shown in Figure 6.4. Although, the micrographs in Figure 6.4 appears to be similar, one can distinguish more elongated particles in Figure 6.4.a, i.e. sample X133702, which is extruded at a die temperature of 250°C. Figure 6.5 confirms this visual inspection. The size of dispersed phase particles for the sample extruded at die temperature of 250°C is slightly larger, and the aspect ratio of this sample is about 30% higher than the sample extruded at die temperature of 270°C.

6.1.1.4 Effect of Screw Zone Temperature on Morphology

As indicated in section 4.2.2, it is important to stop the chain of deformation and breakup of dispersed phase particles right after the formation of sheets of minor phase. In order to

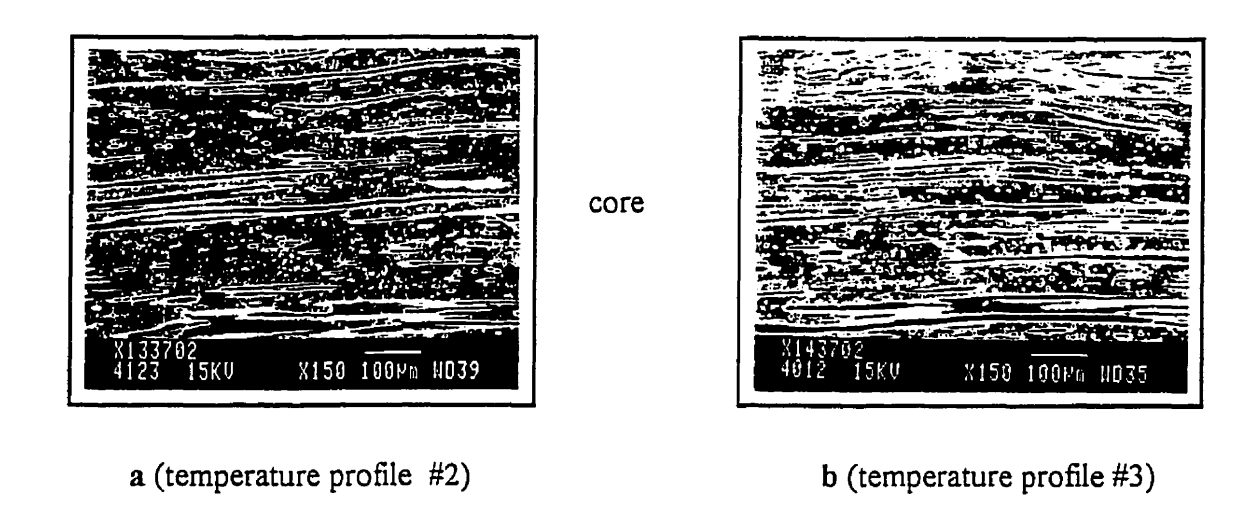


Figure 6.4: SEM micrographs of PEO/PA-6 (80/20 wt%) blends showing the effect of die temperature on morphology. a-X133702 b-X143702

achieve this, it is necessary to control and optimize shear rate, residence time, and heat generation in the melt. Employing an appropriate temperature profile in the screw zone helps to regulate the heat generation and residence time of the polymer melt inside the extruder. It has been reported that the bulk of size reduction occurs in the very early stages of melt mixing. (113-120). Therefore, optimizing the temperature profile in the screw zone is of prime importance.

One of the critical concepts proposed and implemented in this work for the development of laminar morphology in sheet extrusion of polymer blends, is to delay the melting of the dispersed phase until the last zone of the extruder, just before reaching the die. In other words, it is important to keep the processing temperature below the melting point of the dispersed phase up to the third zone of extruder and to raise the temperature in the last zone of the extruder. This special temperature profile provides enough dispersive mixing of the dispersed phase during the solid conveying and mixing step and assures melting of dispersed phase particles, before entering the die. It should be mentioned that during the early stages of mixing, the temperature should be above the glass transition temperature (T_g) of the dispersed phase, i.e. 60°C for PA.6. The low

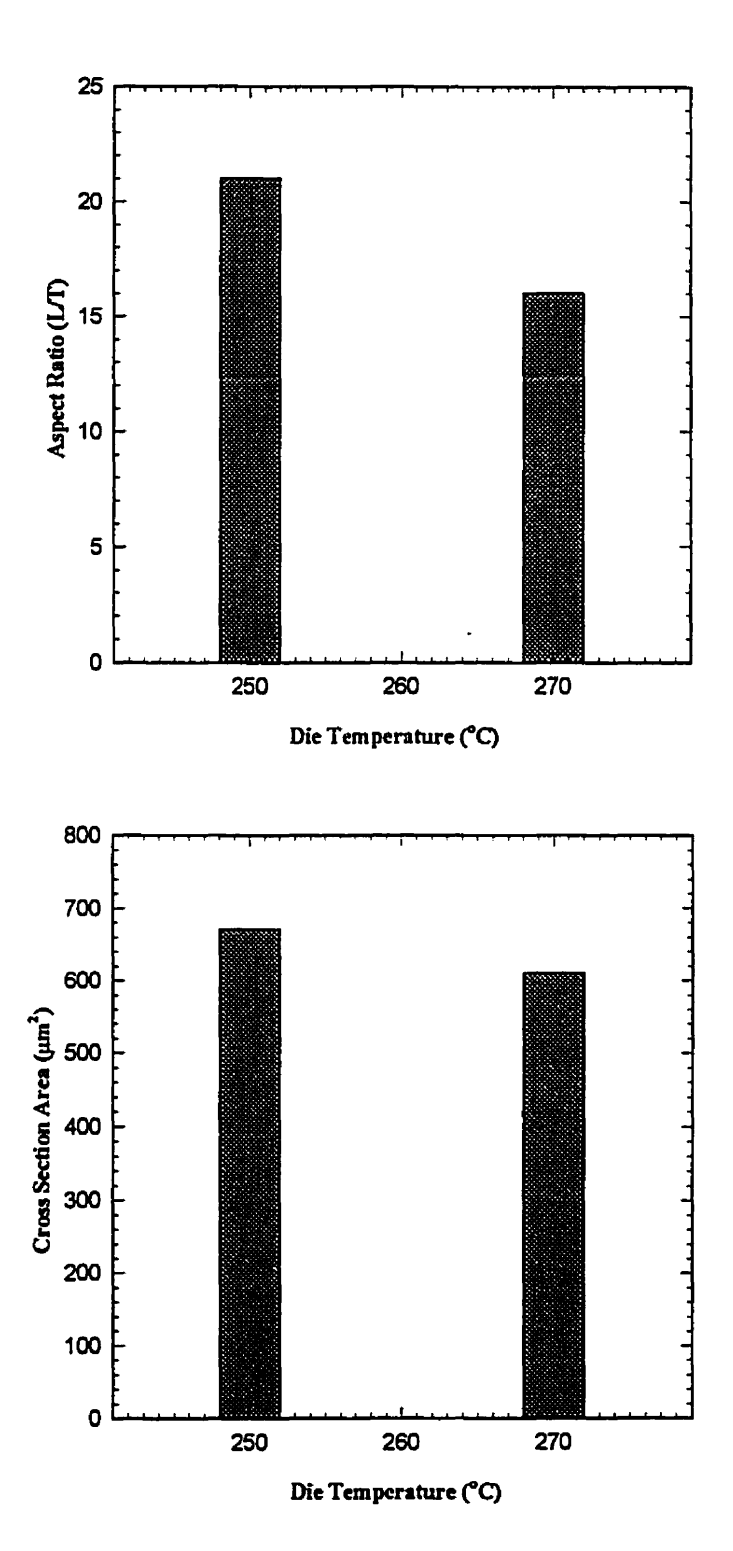


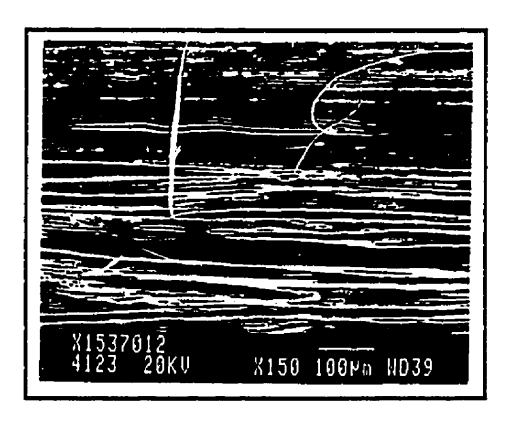
Figure 6.5: Effect of die temperature on the aspect ratio and cross section area of dispersed phase particles for PEO/PA-6 (80-/20 wt%) blend

concentration of PA-6 and its low T_g made it possible to process the blend below the melting point of the minor component. Figure 6.6 demonstrates the important influence of the temperature profile in the screw zone on the morphology of PE0/PE2/PA-6 (70/10/20 wt%) blends.

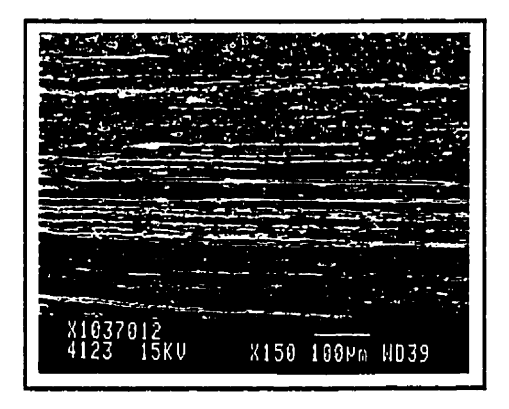
Micrograph 6.6.a shows the morphology of the sample using the lowest temperature profile in the screw zone, i.e. temperature profile of #5 in Table 4.3. Large and elongated particles of PA-6 cover all the length of the micrograph at low magnification of 150X. Even at a magnification of 80X that has been used for image analysis, elongated PA-6 particles, which are in the order of mm, cover all the length of the picture. Micrograph 6.6.b shows a sample that has been produced using temperature profile #3, where the temperatures are slightly higher but still up to zone 3, the temperature is kept below the melting point of PA-6. It is quite clear that the morphology changes considerably. It seems that melting of the PA-6 phase starts slightly earlier inside the extruder and earlier melting results in smaller and shorter PA-6 particles. In Figure 6.6.c, where temperature profile #2 has been used, the PA-6 particles melt in the earlier stages inside the extruder and morphology changes dramatically. The size and length of PA-6 particles have decreased dramatically. The die temperature in all three temperature profiles of 2, 3, and 5 was kept at 250°C, which was found to be the optimum die temperature for maximum deformation of the dispersed phase particles inside the die unit. These micrographs support the microstructure pattern in the early stages of mixing in a single screw extruder reported by Lindt and Ghosh (113).

Figure 6.7 shows the same results quantitatively. The aspect ratio of PA-6 particles changes more than one order of magnitude, by changing the temperature of zone 3 from 200 to 240°C. This is even more dramatic for the particle size, since cross section area changes more than 1.5 order of magnitude. This dramatic change of aspect ratio and particle size indicates a substantial dependence of the morphology of samples extruded on extrusion temperature profiles.

a (temperature profile #5)



b (temperature profile #4)



c (temperature profile #2)

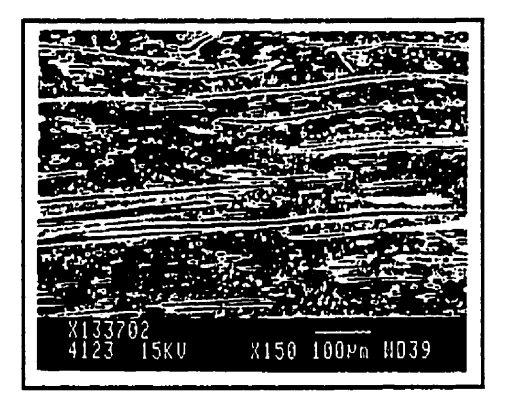
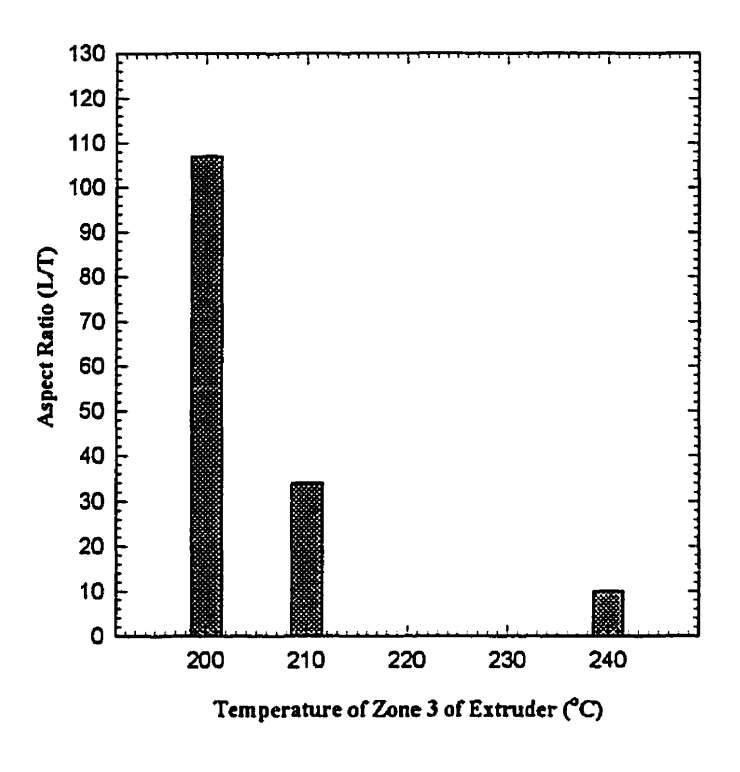


Figure 6.6: SEM micrographs of PE0/PE2/PA-6 (70/10/20 wt%) blends showing the effect of screw zone temperature on morphology:

a- X1537012

b-X1037012

c-X1337012



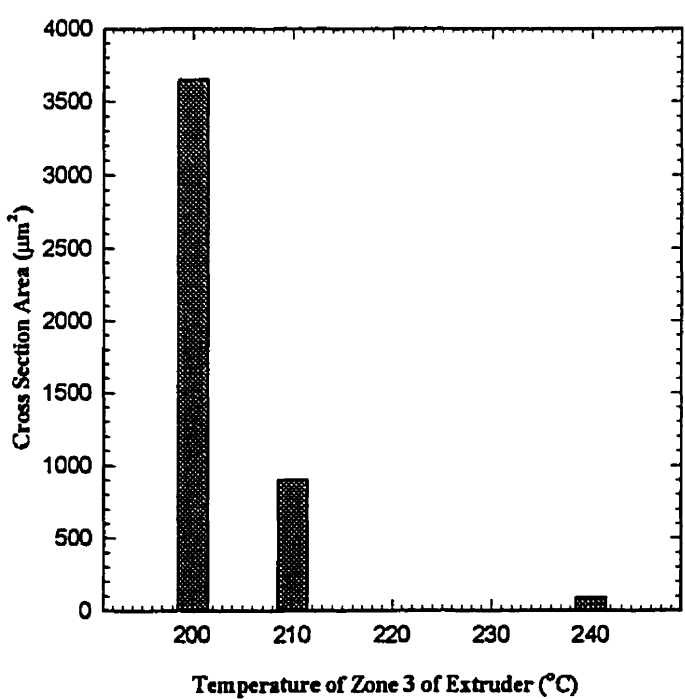


Figure 6.7: Effect of screw zone temperature on the aspect ratio and cross section area of dispersed phase particles for PEO/PE2/PA-6 (70/10/20 wt%) blend

6.1.1.5 Influence of Screw Design on Morphology

Shear rate is a parameter that changes the intensity of mixing of blend components and the extent of particle breakup. Consequently, it affects the particle size of the dispersed phase. Different screw designs provide varying ranges of shear rates in the different zones of the extruder. Therefore, it would be of interest to compare the morphological patterns obtained with a mixing screw to those obtained with a low mixing screw, i.e. metering screw.

Figure 6.8 compares the microstructure obtained using mixing and metering screws for identical processing conditions. The temperature profile #2, where the screw zone temperature is above the melting point of PA-6, has been used for both screw designs. In micrograph 6.8.a (the mixing screw case), the PA-6 particles are smaller and are more uniformly distributed in the matrix. However, only in the core and a part of the intermediate region, layered structure is observed. In large sections of the micrograph, the particles are small, and they are not elongated. Micrograph 6.8.b shows the morphology of a sample obtained using a metering screw. In this sample (the metering screw case);

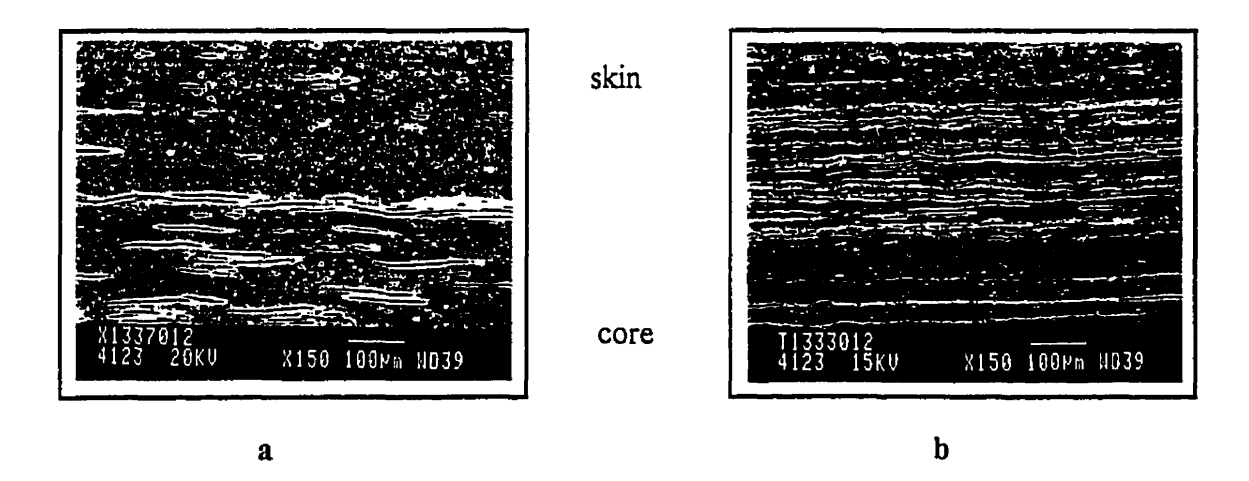


Figure 6.8: SEM micrographs of PE0/PE2/PA-6 (70/10/20 wt.%) blends showing the effect of screw design on morphology. a-Mixing screw b-Metering screw

PA-6 particles are larger and layered structure is observed in the entire core and intermediate region. In a small area close to the skin, where shear flow is dominant, PA-6 particles are not elongated and they are present in the shape of oriented ellipsoids. Lohfink (18) obtained similar results for PP/EVOH system.

Figure 6.9 presents the results of the image analysis on the same micrographs of Figure 6.8. Both the aspect ratio and particle size for the sample obtained with the metering screw are larger than for the sample produced with the mixing screw. Aspect ratio of the sample obtained with the metering screw is 80% higher than for the other sample, and particle size is higher by more than 100%. Therefore, under usual processing conditions, where the screw zone temperature is above the melting point of both components, the metering screw produces better layered structure. However, as discussed in section 6.1.1.4, the desired temperature profile for developing laminar structure requires the screw zone temperature to be mostly below the melting point of PA-6 resin. It is believed that under this condition, due to short residence time of the polymer melt in the screw zone, the effect of screw design could be less significant.

6.1.1.6 Effect of Die Exit Gap on Morphology

The special die design used in this study incorporates diverging and converging sections, in order to produce extensional flow in the die unit. The existence of extensional flow is of great importance in stretching the spherical particles of the dispersed phase entering the die, to generate two-dimensional platelets and develop laminar structure. Therefore, the dimensions of the die exit gap become an important parameter in determination of performance of extensional flow inside the die unit. Therefore, it is necessary to investigate how changes of die exit gap size influences the microstructural pattern in extruded ribbons of laminar blends. Although, three different gap sizes of 0.25, 0.5, and 1.0 mm were used in this study, it was not possible to work with a gap size of 0.25 mm due to high viscosity of blends and technical limitations of the extruder. However, other studies revealed that there is no advantage in using this low gap size.

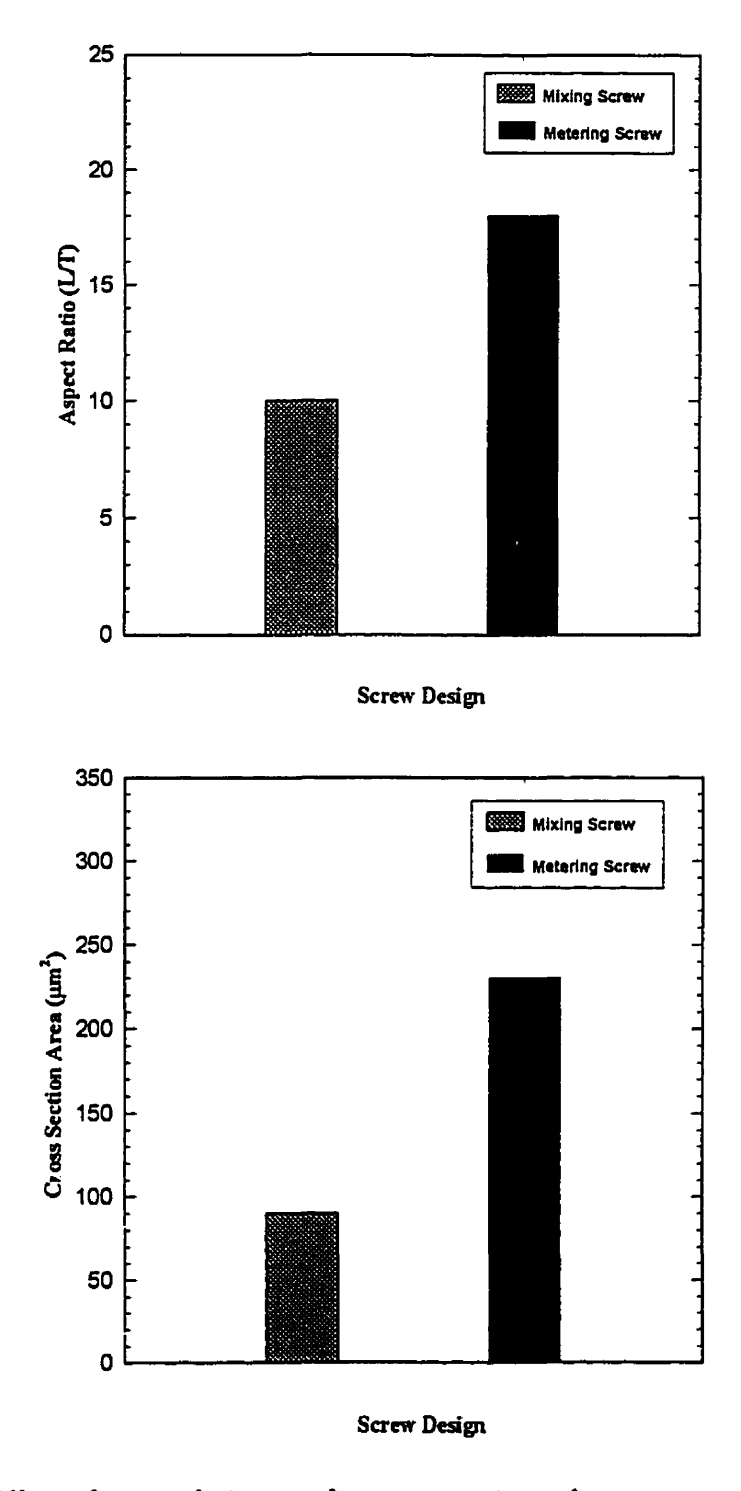


Figure 6.9: Effect of screw design on the aspect ratio and cross section area of dispersed phase particles for PEO/PE2/PA-6 (70/10/20 wt%) blend.

Figure 6.10 presents the effect of die exit gap size on the morphology of extruded ribbons in the flow direction. Micrograph 6.10.a reveals the morphology of a sample obtained with a gap size of 1.0 mm where the extension ratio is 10.3 in the flow direction and 2.7 in the transverse direction in the plane of extrusion. In micrograph 6.10.b, the morphology of a sample obtained using die exit gap of 0.5 mm is indicated. The extension ratios are 20.7 and 2.7 in the flow and transverse directions, respectively. Using the small gap size of 0.5 mm results in very high extension ratios that might originate the disruption of PA-6 particles. The existence of shorter and smaller particles of PA-6 in the micrograph of 6.10.b verifies this assumption. Subramanian (26) reported similar trend in developing laminar morphology in blow-molded containers of HDPE/PA-6 blends. He recommended an elongation of 100 to 300 percent. He added that avoidance of excessive stretching is important as far as excessive elongation of the melt may lead to rupture of the dispersed phase particles.

Figure 6.11 displays the quantitative analysis of micrographs shown in the previous figure. Reduction of aspect ratio about 20% and particle size up to 50%, confirms the hypothesis that increasing the stretch ratio beyond a critical value, might lead to breakup

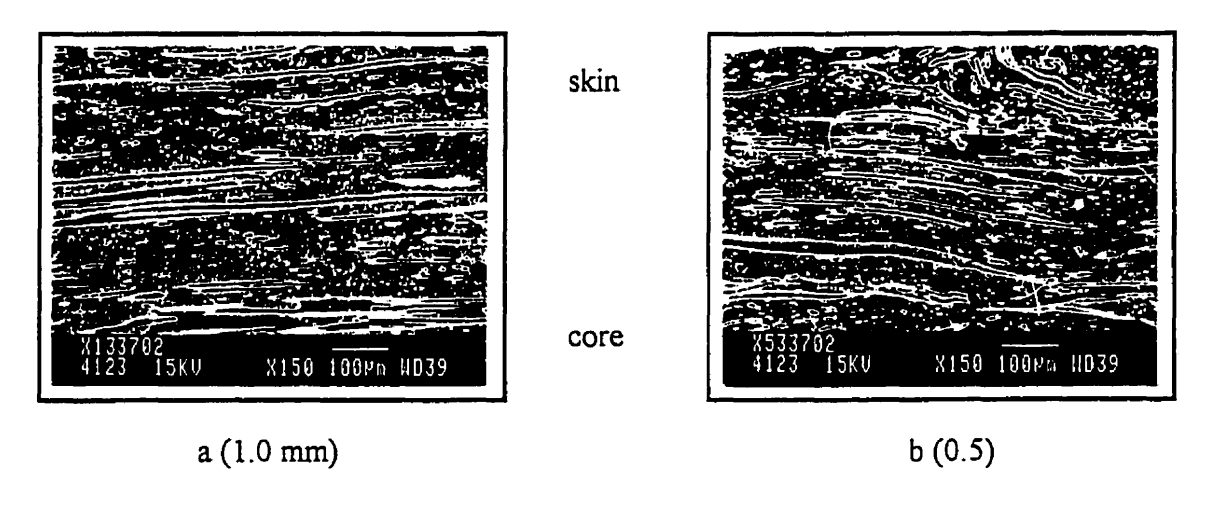


Figure 610: SEM micrographs of PEO/PA-6 (80/20 wt.%) blends showing the effect of die exit gap size on morphology. a- X133702 (1.0 mm) b-X533702 (0.5 mm)

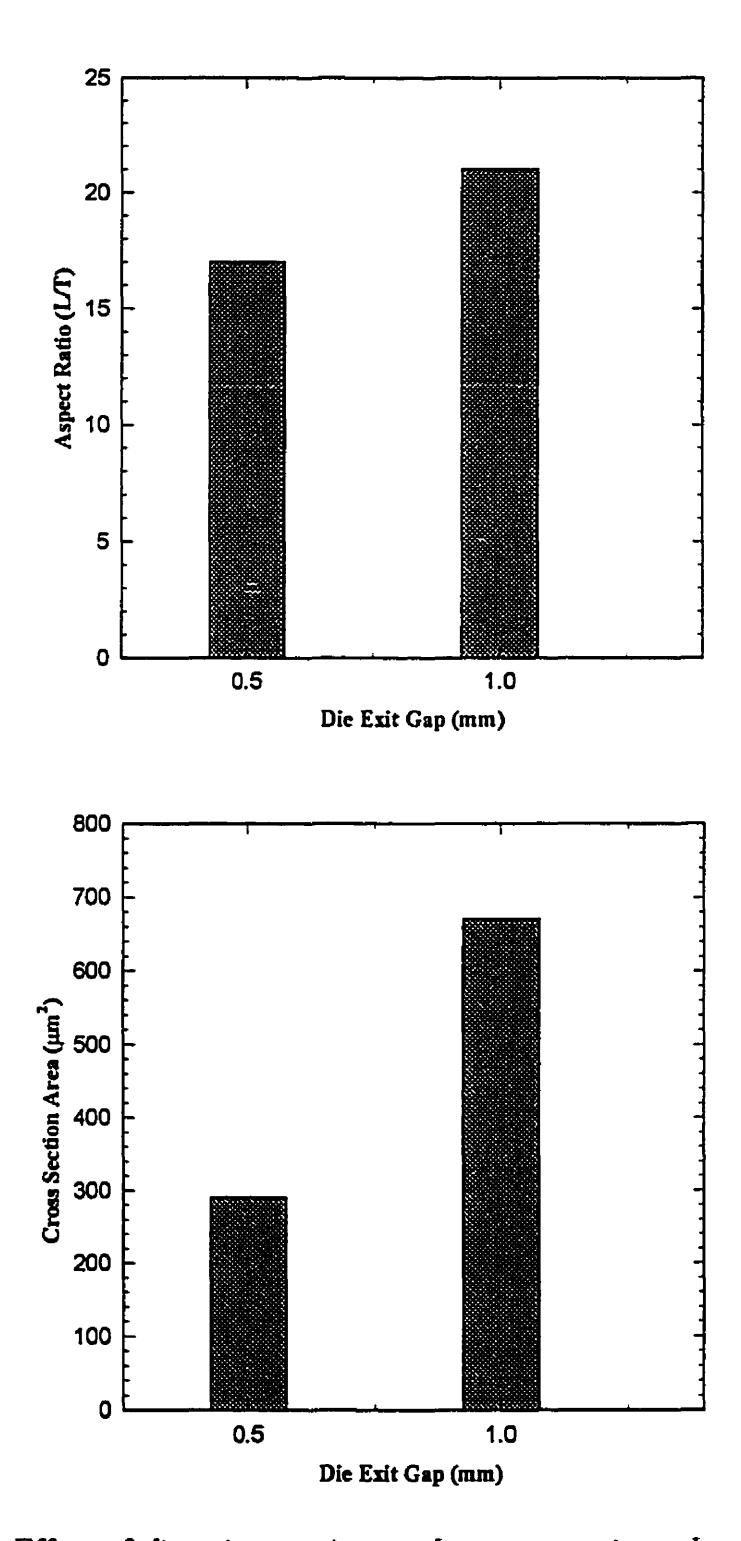


Figure 6.11: Effect of die exit gap size on the aspect ratio and cross section area of dispersed phase particles for PEO/PA-6 (80/20 wt%) blend.

of dispersed phase particles. Therefore, it seems that extension ratios in the range of 10 are more desirable to develop laminar morphology in blends of HDPE and PA-6, and increasing the extension ratio much beyond this value is not recommended.

6.1.1.7 Effect of PA-6 Content on Morphology

Figure 6.12 presents the influence of PA-6 content on the morphology of extruded ribbons of HDPE/PA-6 blends. Micrograph 6.12.a and 6.12.b reveal the microstructure for a 78.6/11.4/10 (PE0/PE2/PA-6 wt%) blend and 70/10/20 blend, respectively. All the processing conditions and level of compatibilizer are kept constant for both blends. In micrograph 6.12.a, where the percentage of the dispersed phase is 10wt%, the PA-6 particles are small in size and number, although they are generally elongated. At this low concentration, PA-6 particles are not present in all the area. In micrograph 6.12.b, where the amount of PA-6 is 20wt%, large and long particles of the dispersed phase cover more area and produce a tortuous path that is expected to reduce the permeability dramatically. Figure 6.13 shows the image analysis results for the same samples of Figure 6.12. By

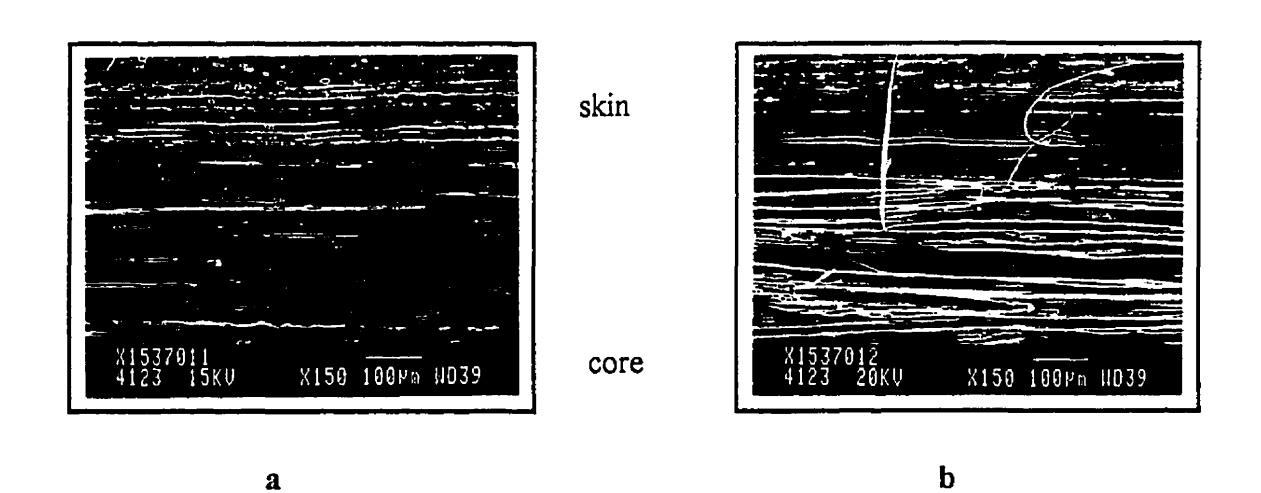


Figure 6.12: SEM micrographs of PE0/PE2/PA-6 blends showing the effect of PA-6 content on morphology: a- X1537011 (78.6/11.4/10 wt%) b-X1537012 (70/10/20 wt%)

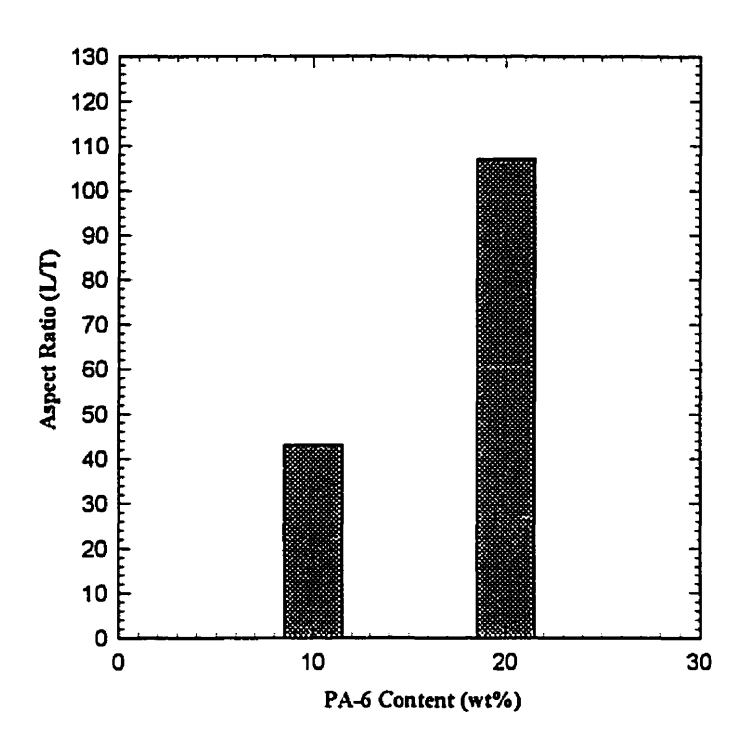
changing the PA-6 content from 10 to 20wt%, an increase of 300% in aspect ratio and 600% in particle area is observed.

The above results suggest that, at larger concentrations of the dispersed phase, the additional PA-6 is distributed so that both the number and size of droplets increase. The increase in number of drops is a direct result of the rise in concentration. The size of the drops is probably partly a result of coalescence, which becomes more likely as the proximity of the particles increases due to larger concentration. However, it has been reported that the coalescence frequency is less likely for highly compatibilized blends (54,102,118). On the other hand, there is a possibility that the required heat for melting the PA-6 phase is provided earlier for low concentration blends. Therefore, the residence time of PA-6 melt in the screw zone rises and accordingly the particle size decreases.

The significant change of aspect ratio can be explained by the theories of drop deformation and interfacial tension. Acrivos and Lo (38) obtained the following relationship for large drop deformations using the slender body theory and the volume conservation conditions:

$$\kappa \lambda^{1/6} = \left[1/20\right]^{1/2} \frac{\xi^{1/2}}{1 + 4/5\xi^3} \tag{6.1}$$

where κ is the capillary number. This equation implicitly relates the dimensionless length, $\xi = L\lambda^{1/3}/a$, to the flow strength. It can be seen that a large capillary number indicates large drop diameter for the same shear rate and matrix. Therefore, large drops are associated with large ' ξ ', and consequently, large values of L/a. The same conclusions can be made using the Cox Theory (35). However, Cox theory is proved to be valid for small deformations. It has been also observed (18) that larger particles of EVOH are easier to deform in the PP matrix in the shear and experimental fields encountered in the adapter and die unit.



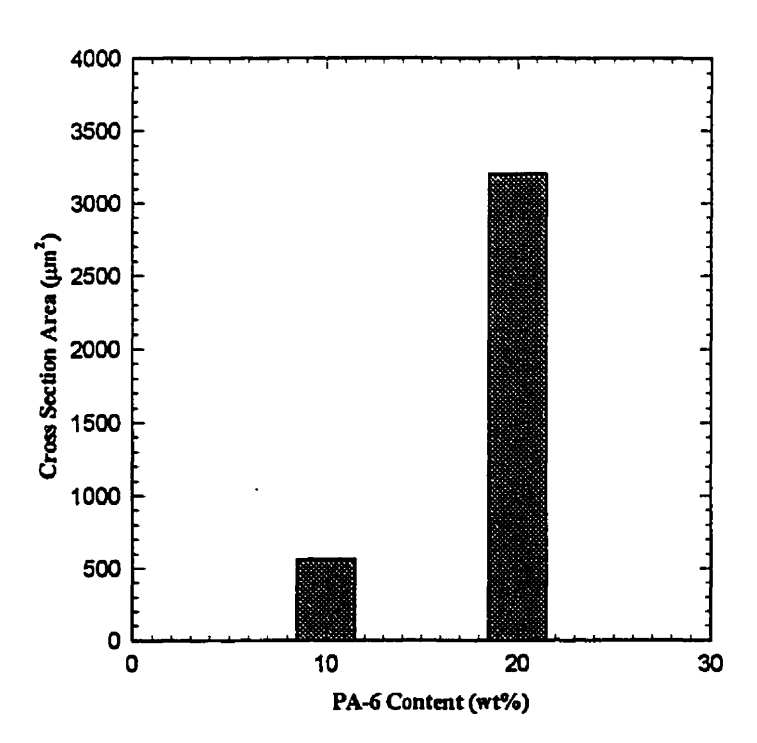


Figure 6.13: Effect of PA-6 content on the aspect ratio and cross section area of dispersed phase particles for PE0/PE2/PA-6 blends.

6.1.1.8 Effect of Maleation Content on Morphology

It is well known that using a compatibilizer in blends reduces the interfacial tension between the two components (104-110). The extensive investigation regarding the interfacial tension of PE/PA-6 in section 5.3 reveals that increasing the maleation content of polyethylene, reduces the interfacial tension between PE and PA-6 dramatically, and then it levels off. Therefore, under usual processing conditions, increasing the maleation content of PE facilitates the deformation and breakup of PA-6 particles and provides smaller particles, which is not desirable for developing laminar morphology. Due to the special processing conditions used in this study, as a result of short residence time and low temperature in the screw zone, the particles of the dispersed phase entering die tend to be large, even for a compatibilized blend. Then, under the extensional flow prevailing inside the die unit, deformation of PA-6 particles in a matrix of maleated PE is greater than in a matrix of standard PE. Therefore, it is expected to have thinner and longer particles of dispersed phase for compatibilized blends.

Figure 6.14 shows the influence of maleation content of PE on the morphology of PEO/PA-6 (80/20 wt%) blends, fed as a dry blend and extruded under the low temperature profile (#5). The mixing screw and a die exit gap size of 1.0 mm were used for extruding all the samples. By increasing the maleation content from zero in micrograph 6.14.a to 0.028 wt% in micrograph 6.14.d, the PA-6 particles become thinner and larger in area. In micrograph 6.14.a, where thick and large particles are present, the interface is smooth, suggesting poor adhesion at the interface. In micrographs c and d, where maleation content is 0.014 and 0.028 wt%, respectively, elongated particles cover the entire length of the picture. However, due to thinner particles in micrograph d, larger particle area in the plane of extrusion is expected. Both micrographs c and d, show a rough interface that indicates good adhesion and thus potentially better mechanical properties.

In Figure 6.15, the image analysis results for these 4 micrographs are shown. It is seen that by increasing the maleation content, both the aspect ratio and particle area in the plane of extrusion increases. Thus thinner and larger platelets of dispersed phase, i.e. PA-6, are spread in the PE matrix. This is expected to increase the tortousity of the sample

towards the diffusion of gases and hydrocarbons and thus reduces the permeability considerably. It appears that maleation content between 0.014% to 0.028 wt% is the optimum range of maleation for developing laminar morphology in dry blended alloys of PE and PA-6. Figure 5.31 that presents an optimum value of 0.03 wt% for the maleation content, on the basis of interfacial tension measurements, is in agreement with morphological findings.

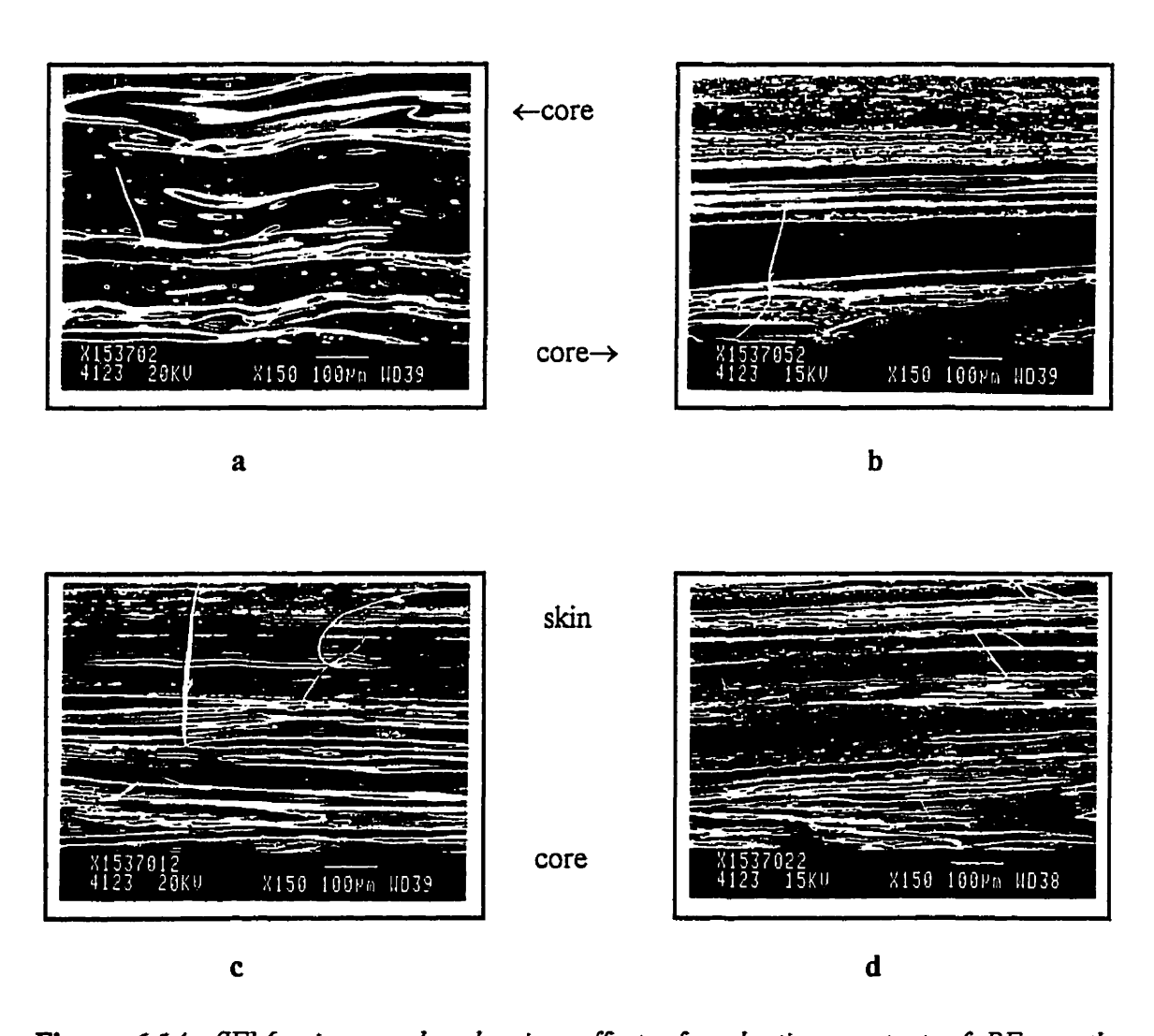
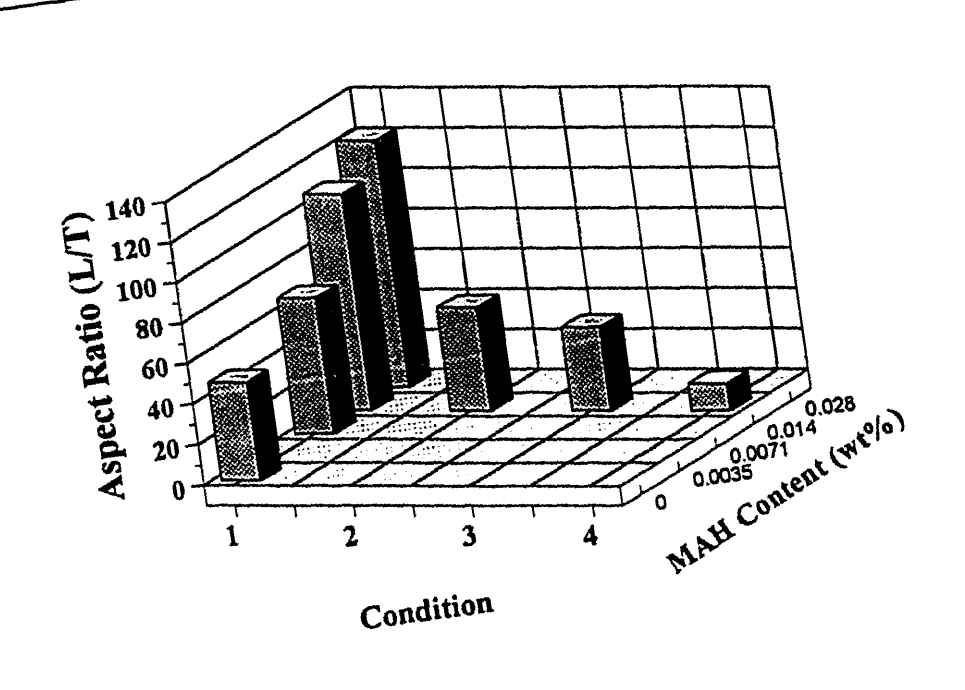


Figure 6.14: SEM micrographs showing effect of maleation content of PE on the morphology of PE0/PE2/PA-6 blends. a- 80/0/20 wt% b-75/5/20 wt% (MAH content 0.007 wt%) c- 70/10/20 wt% (MAH content 0.014%) d-60/20/20 wt% (MAH content 0.028%)



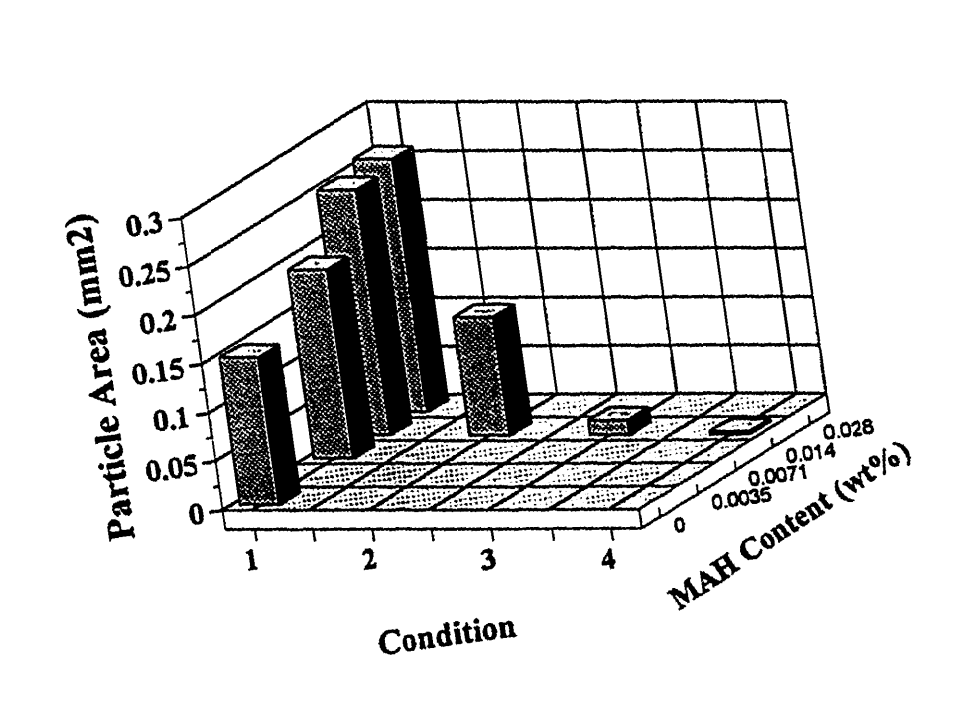


Figure 6.15: Effect of Maleation content of PE and pre-compounding on the aspect ratio and area of dispersed phase particles for PE0/PE2/PA-6 blends.

6.1.1.9 Influence of Pre-compounding on Morphology

The twin- screw extruder is known to be an efficient commercial mixer for polymer blends. In order to obtain more homogeneous blends and in order to supply a feed to the extruder in the form of blend pellets, which is preferred by industry rather than a dry mixture of pellets of the individual components, a blend was produced in the twin-screw extruder. The objective was to attain a maximum amount of distributive mixing and to avoid excessive dispersive mixing. The effect of sequence of blending on the morphology of PE/PA-6 blends was investigated using an optimized twin-screw configuration and temperature profile as explained in section 4.2.2. Figure 4.8 presents the different sequences of blending and extrusion used in this study.

Figure 6.16 reveals the morphology of samples obtained employing 4 different methods of blending, and Figure 6.15 presents the quantitative analysis of these micrographs. In picture 6.16.a, dry blending was used, while in micrograph 6.16.b, PEO was first mixed with the compatibilizer (PE2) in the twin-screw extruder to provide the required level of maleation. Then the pre-blended PE was dry-mixed with PA-6 and extruded using the single screw extruder. Sequences 3 and 4, which employ one pass and two passes in the twin-screw extruder, respectively, were used to obtain micrographs 6.16.c and d. Micrograph 6.16.a, shows that dry-blending provides elongated and large particles of the dispersed phase. By increasing the mixing intensity, the PA-6 particles become smaller and shorter. Thus, micrographs 6.16.c and d are as expected. However, the morphology obtained in picture 6.16.b and the corresponding image analysis results of condition 2 in Figure 6.15, were not anticipated. If micrograph 6.16.a, designated as condition 1 in Figure 6.15, is compared with picture 6.16.b, designated as condition 2, it may be concluded that the pre-mixing of PE0 and PE2 reduces both the aspect ratio and particle area by 50%. It seems that when PE2 is pre-mixed with PE0, i.e. condition 2, the contact between the PA-6 and compatibilized matrix is more effective, suggesting a lower overall interfacial tension that promotes particle breakup. On the other hand, when all the components are mixed in one step, i.e. condition 1, there is smaller chance for the PA-6 particles to contact the compatibilized polyethylene, suggesting that the effective

interfacial tension is higher in comparison to condition 2. Lim and White (104) found that, due to the high viscosity of the polymer matrix, a much larger quantity of compatibilizer than actually needed, is required for interface covering. Therefore, the PA-6 particles exhibit more resistance to breakup and remain larger. Although, both the aspect ratio and particle area decrease substantially by passing the blend through the twin-screw extruder, reduction of particle area is more severe. This may be due to differences in residence time of the polymer melt in the screw zone, which increases for any extra mixing step.

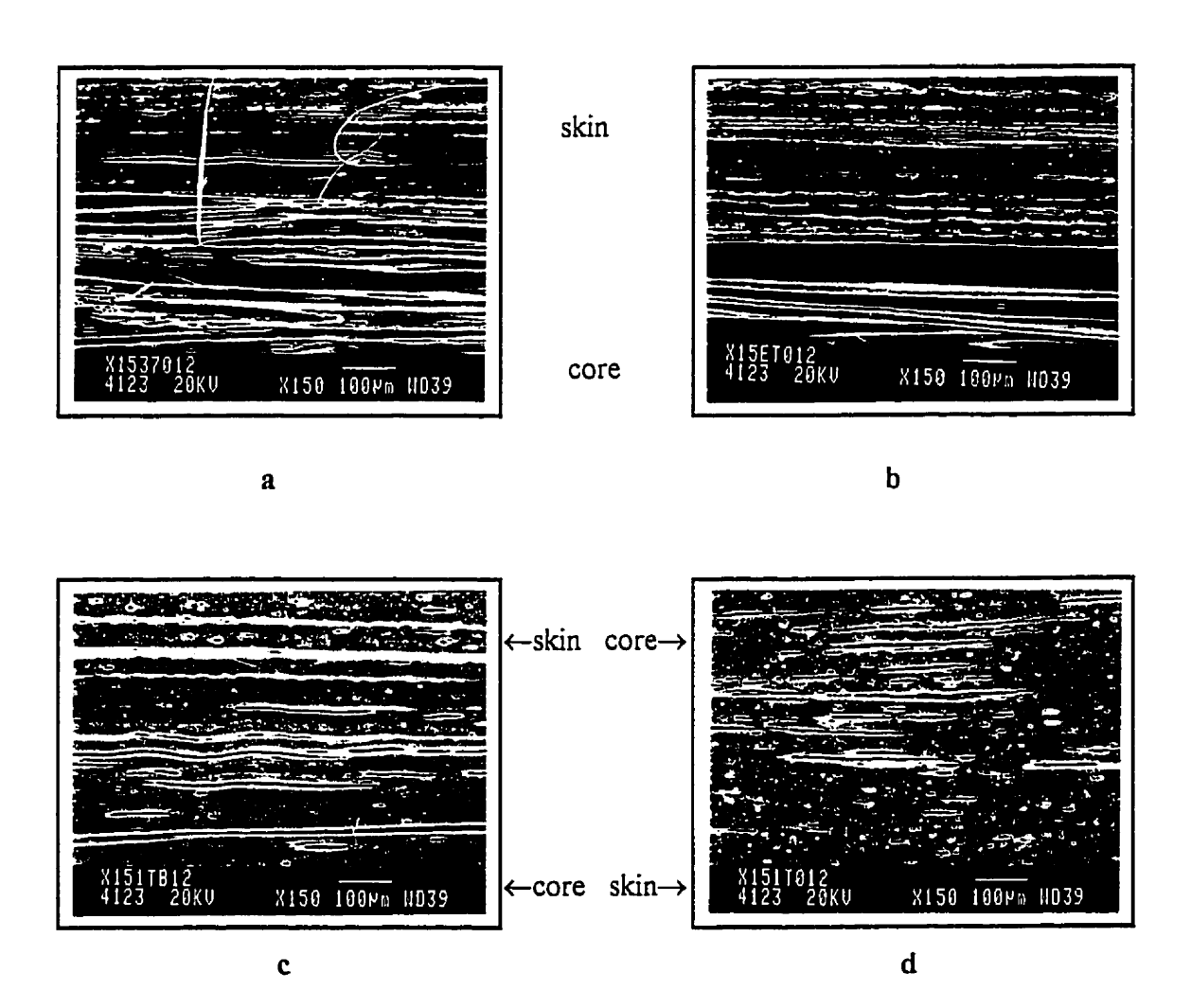


Figure 6.16: SEM micrographs showing effect of pre-compounding on the morphology of PEO/PE2/PA-6 (70/10/20 wt%) blends. a- dry-blending b- PE0 and PE2 were pre-mixed c- PE0, PE2, and PA-6 were pre-mixed in one pass d-PE0,PE2, and PA-6 were pre-mixed in two passes

Figure 6.17 shows the distribution of the number of particles in the same locations as in Figures (6.15) and (6.16). As indicated, dry blends yield a wide distribution of particle size with smaller number of particles. By increasing the mixing, narrower size distribution and a larger number of particles are observed (compare Figures 6.17.a and 6.17.d.)

It is recommended that using a twin-screw extruder with shorter length and incorporation of external lubricants like paraffin waxes to reduce shear heating and lower processing temperatures, would contribute to improved laminar morphology of twin-screw compounded blends of HDPE and PA-6.

6.1.2 PP/EVOH Blends

Due to the small difference between the melting points of the matrix, i.e. ADMER with a melting point of 160°C, and the dispersed phase, i.e. EVOH with a melting point of 181°C, the approach of using low temperature in the screw zone in not readily applicable to this system. Therefore, the generation of laminar morphology is more difficult than for the PE/PA-6 blend. Other researchers (16-20) have investigated the influences of some parameters on the morphology of PP/EVOH blends. The present study attempts to evaluate a novel approach to improving laminar morphology in this system, particularly by employing a lower temperature profile in the screw zone. It also attempts to overcome some of the limitations of earlier morphological studies by employing etching of the dispersed phase and obtaining quantitative image analysis data.

6.1.2.1 Variation of Microstructure Across the Ribbon Thickness

Figure 6.18 presents a SEM micrograph of a sample extruded using the mixing screw with die exit gap size of 0.25 mm, in conjunction with temperature profile #2 described in Table 4.4. Detailed processing conditions used to produce this sample are listed in appendix B. Although, the obtained morphology is not as good as the morphology of laminar blends of

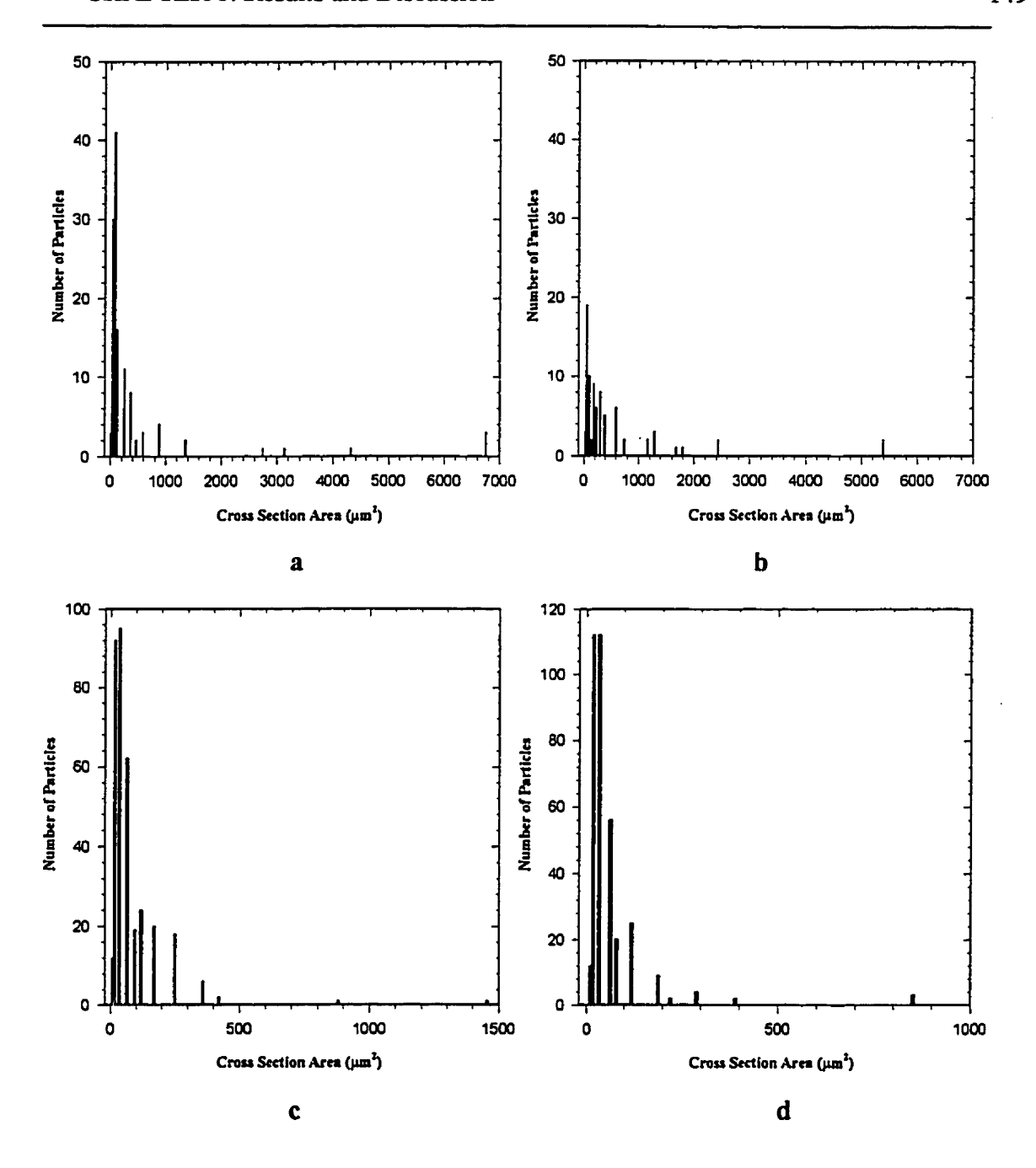


Figure 6.17:Distribution of cross section area for SEM micrographs of Figure 6.16 showing the effect of pre-compounding on particle size of PEO/PE2/PA-6 (70/10/20 wt%) blends. a- dry-blending b- PE0 and PE2 were pre-mixed c- PE0, PE2, and PA-6 were pre-mixed in one pass d- PE0, PE2, and PA-6 were pre-mixed in two passes

HDPE and PA-6 resins, the general trend explained in section 6.1.1.2 is also observed in this micrograph. In the core and intermediate regions, elongated particles of EVOH are present, while close to the surface; deformed droplets and agglomerates of dispersed phase are observed. However, layers of EVOH in the core and intermediate regions are not as long as in the previous system, especially in the intermediate region. The area close to the surface, where deformed droplets of dispersed phase are dominant, is larger. In other words, the intermediate zone includes both layered and droplet morphology. As in the HDPE/PA-6 system, due to migration of the dispersed phase particles towards the axis, the content of the EVOH phase decreases near the surface. Figure 6.19 provides the image analysis results for the micrograph shown in Figure 6.18. Contrary to the PE/PA-6 blend, moving from the core towards the intermediate region, a noticeable decrease in both aspect ratio and cross section area is observed. On the other hand, in the PE/PA-6 system, the intermediate and core regions show similar layered structure with comparable aspect ratio and particle size. These parameters are much smaller than the PE/PA-6 system indicating the importance of special low temperature processing conditions employed in extrusion of PE/PA-6 blends.

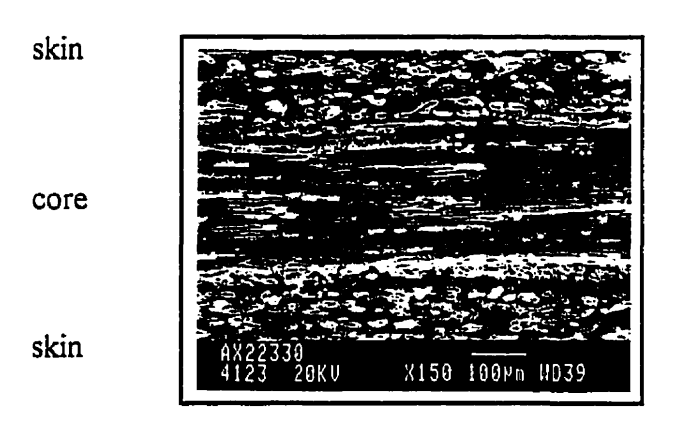
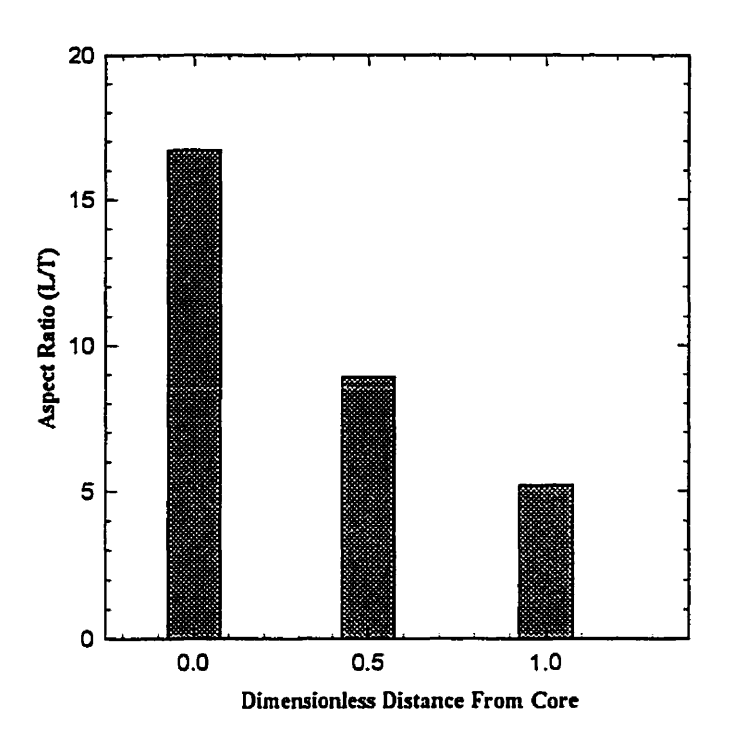


Figure 6.18: SEM micrograph of ADMER/EVOH (75/25wt%) blend showing the variation of morphology across the thickness of extruded ribbon



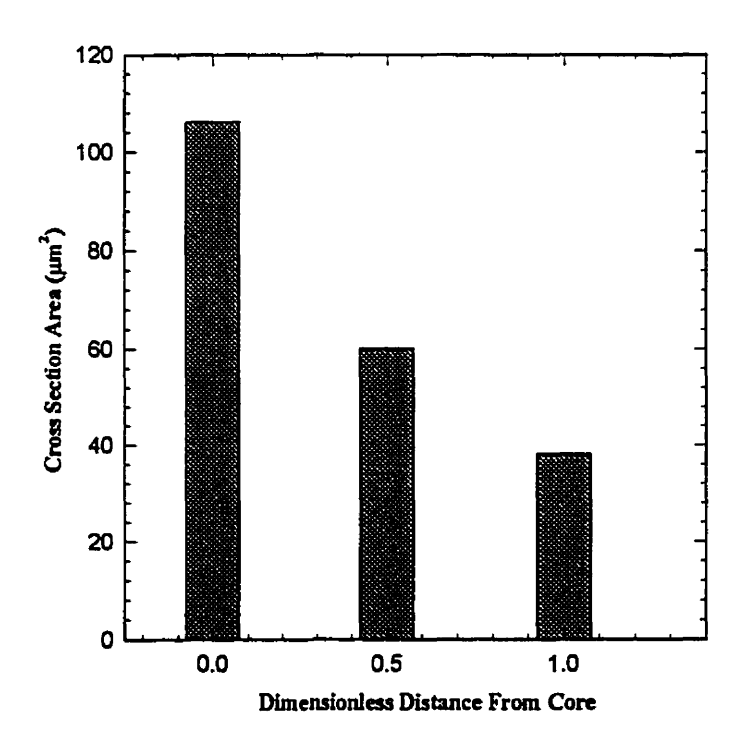


Figure 6.19: Variation of cross section area and aspect ratio across the ribbon thickness for ADMER/EVOH (75/25 wt%) blend.

6.1.2.2 Effect of Die Temperature on Morphology

It was suggested earlier that a viscosity ratio of unity is desirable for large deformations of dispersed phase particles, which are needed for developing laminar morphology. However, Figure 5.6 showed that at both 200 and 230°C, over the entire range of shear rates, the viscosity of EVOH is higher than the viscosity of ADMER. Therefore, as shown in Figure 5.7, the viscosity ratio of EVOH/ADMER is always larger than unity, in the practical processing range. Also, higher elasticity of EVOH at higher shear rates (Figure 5.10) does not favor large drop deformations.

Figure 6.20 presents the influence of die temperature on the morphology of ADMER/EVOH (75/25 wt%) blends. Although, the EVOH particles are stretched in the flow direction, the number, size and aspect ratio of dispersed phase particles are smaller than for the PE/PA-6 system. Figure 6.21 shows the image analysis results of morphology shown in the micrographs of Figure 6.20. It seems that the die temperature does not play a major role in developing laminar morphology in extrusion of ADMER/EVOH blends. However, it appears that higher temperature results in minor improvement of layered structure by providing slightly longer and larger particles. Increasing the die temperature leads to viscosity ratios closer to unity that might be responsible for minor improvement of layered structure. The crossover of elasticity of matrix and dispersed phase occurs at higher shear rates for higher temperatures, thus is expected to observe minor improvement of laminar morphology at higher temperatures.

Temperature also affects the interfacial tension, as shown in Figure 5.35 and by the large temperature coefficient of interfacial tension of the ADMER/EVOH pair depicted in Equation 5.27. This effect is large enough to have some impact on the deformation of EVOH particles in the matrix of ADMER. Smaller interfacial tension enhances deformation of EVOH particles under the extensional flow inside the die unit, thus results in longer and larger particles of dispersed phase at higher temperatures.

WX51325 4123 20KU X220 100Pm HD39

WX52325 4123 20KV X220 100 Mm ND39

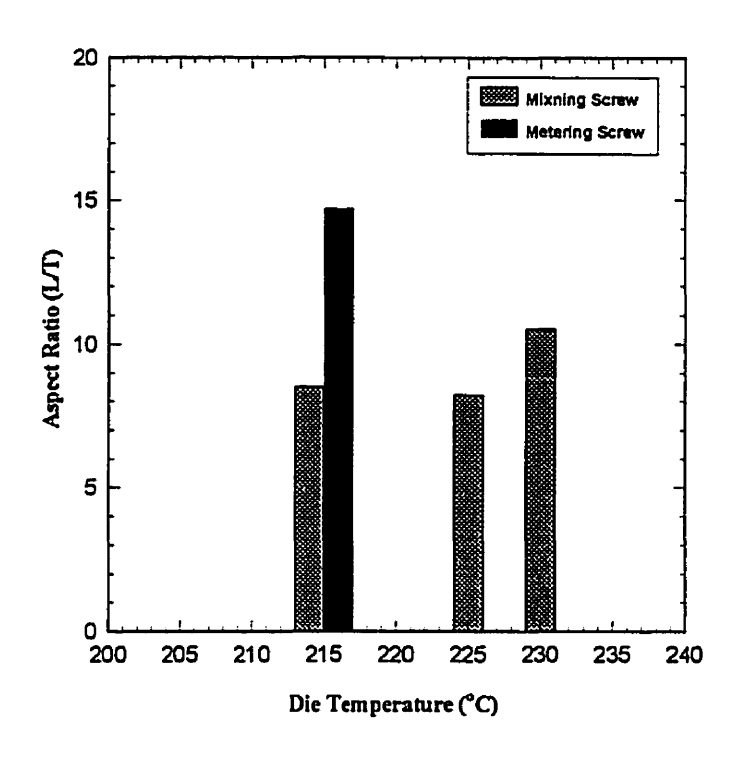
> MX53325 4123 20KU X220 100Pm N039

Figure 6.20: SEM micrographs of ADMER/EVOH (75/25 wt.%) blends showing the effect of die temperature on morphology: a-215 °C b-225 °C c-230 °C

a

b

C



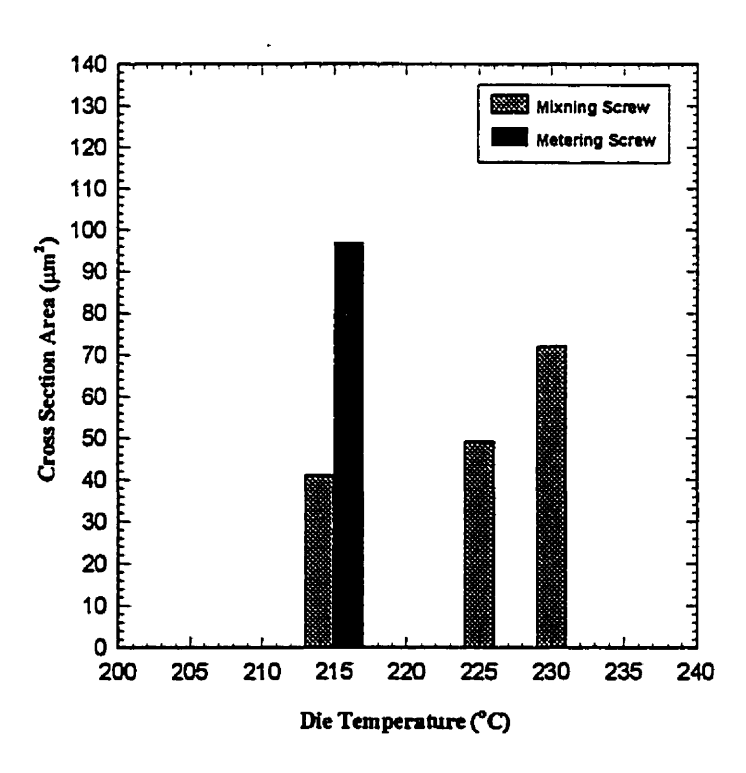


Figure 6.21: Effect of die temperature on the aspect ratio and area of dispersed phase particles for ADMER/EVOH (75/25 wt%) blends.

6.1.2.3 Influence of Screw Design on Morphology

The mixing screw used in this study has an extra channel with higher pitch in the metering zone. This design results in improved mixing efficiency of the mixing screw compared to the metering screw. Therefore, the EVOH particles entering the die unit should be smaller than the particles exiting the metering screw zone. With the metering screw, it is expected to obtain larger and longer particles of dispersed phase in the extruded sample.

Figure 6.22 reveals the microstructure of two samples, WX51325 and WT51325, extruded under the same processing conditions, except the screw design. Figure 6.20 presents the image analysis results done on the same micrographs. As shown in Figure 6.20, aspect ratio and particle size of the dispersed phase increase by 40 and 50%, respectively, by using a metering rather than a mixing screw. Screw design changes the microstructure pattern across the thickness. In the core region of the sample obtained employing a metering screw, i.e. micrograph 6.22.b, large elongated particles are observed, while the mixing screw gives more homogeneous distribution of dispersed phase in picture 6.22.a.

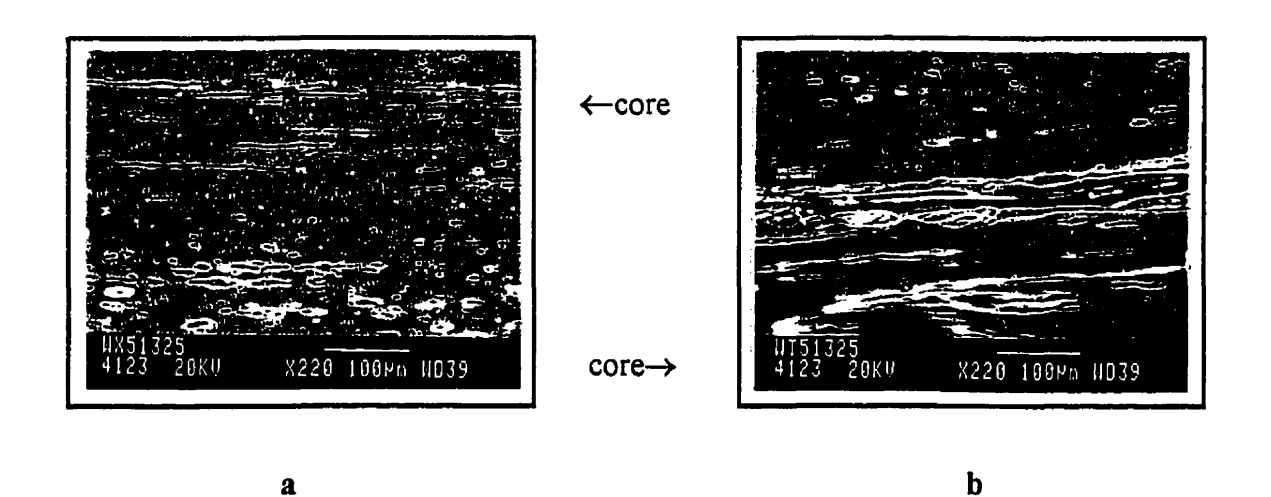


Figure 6.22: SEM micrographs showing effect of screw design on the morphology of ADMER/EVOH (75/25 wt%) a-Mixing screw b-Metering screw

6.1.2.4 Influence of Low Temperature Screw Zone on Morphology

The approach of using low temperature profile in the screw zone was successfully employed with the PE/PA-6 system. The processing window for this approach is as wide as the temperature difference between the melting points of dispersed phase and matrix. For the PE/PA-6 system, the processing window in the screw zone is 135-220°C, i.e. the melting points of HDPE and PA-6, respectively. This processing window is wide enough for using this technique. However, for the ADMER/EVOH system, the processing window is between 160 and 181°C, i.e. the melting points of ADMER and EVOH, respectively. The processing window becomes even narrower, considering the necessity of keeping the temperature well below the melting point of EVOH up to zone 3 of the extruder. Therefore, temperature profile #4, where zone 3 of the extruder was kept at 170°C was the lowest practical temperature profile.

Figure 6.23 presents the morphology of a sample extruded using temperature profile #4, where temperature of zone 3 is 170°C. In comparison to samples extruded under usual processing conditions, the particles of dispersed phase are much larger. Image analysis results showed an aspect ratio of 10 and particle area of 275µm², which is twice

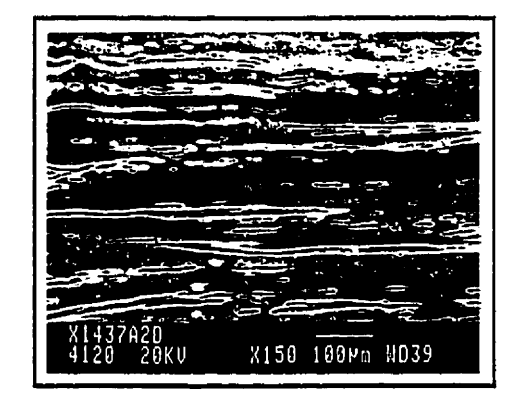


Figure 6.23: SEM micrograph of ADMER/EVOH (75/25wt%) blend showing the microstructure obtained at low temperature screw zone.

the range of particle areas obtained for other samples. Figure 6.23 reveals a clear distinction between ADMER/EVOH and PE/PA-6 blends, extruded using the technique of low temperature screw zone. Contrary to the PE/PA-6 micrographs, large particles of dispersed phase are observed only in the core region of Figure 6.23. Using a low temperature profile in the screw zone for PE/PA-6 blends results in large and elongated particles of dispersed phase in the core and intermediate regions. It appears that EVOH particles close to the walls, i.e. barrel and screw, are melted before reaching zone 4 of the extruder, causing breakdown to small particles. Due to technical limitations of the extruder and high torque, it was not possible to employ lower die gaps using the low temperature profile #4. However, employing appropriate lubricants might enhance the processing of ADMER/EVOH at low temperatures and also prevents breakdown of EVOH particles.

6.1.2.5 Effect of Die Exit Gap Size on Morphology

a

Figure 6.24 presents the effect of die exit gap size on the morphology of ADMER/EVOH (70/30 wt%) blends. Contrary to the PE/PA-6 blends, higher extension ratios provided by lower die exit gap, result in longer and thinner particles of the dispersed phase, i.e. EVOH. Figure 6.25 shows image analysis results obtained for the same micrographs. Both aspect

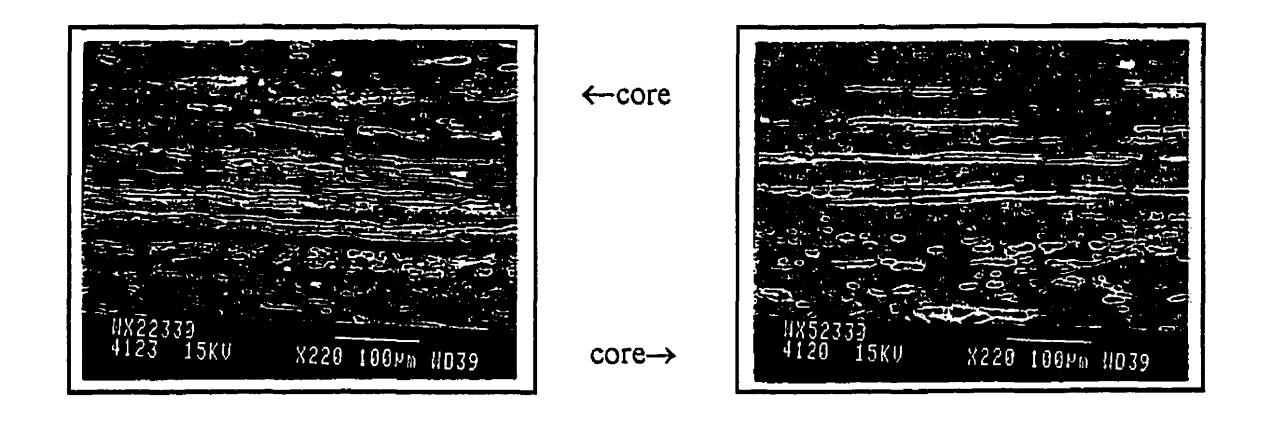
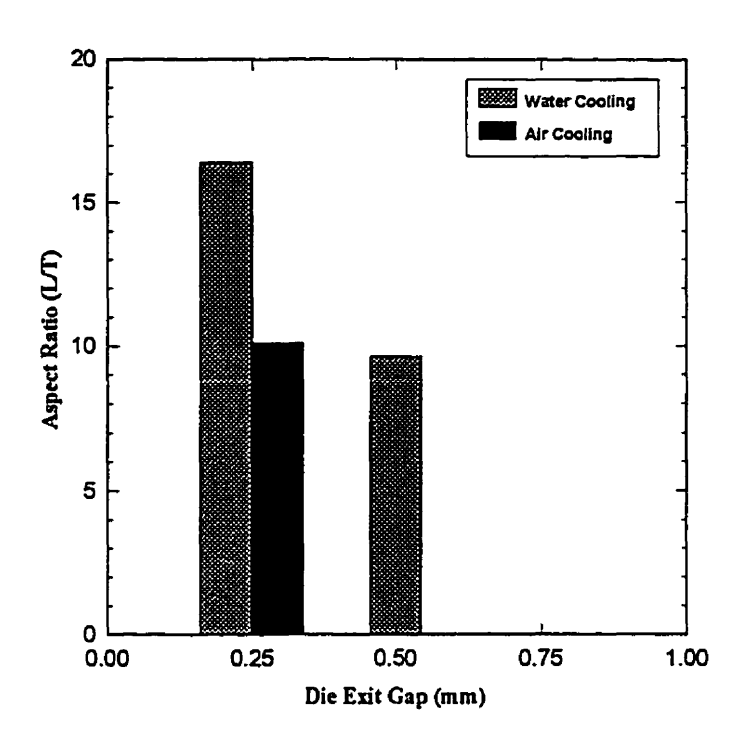


Figure 6.24: SEM micrographs showing effect of die exit gap size on the morphology of ADMER/EVOH (70/30 wt%) blends. a- 0.25 mm b- 0.5 mm

b



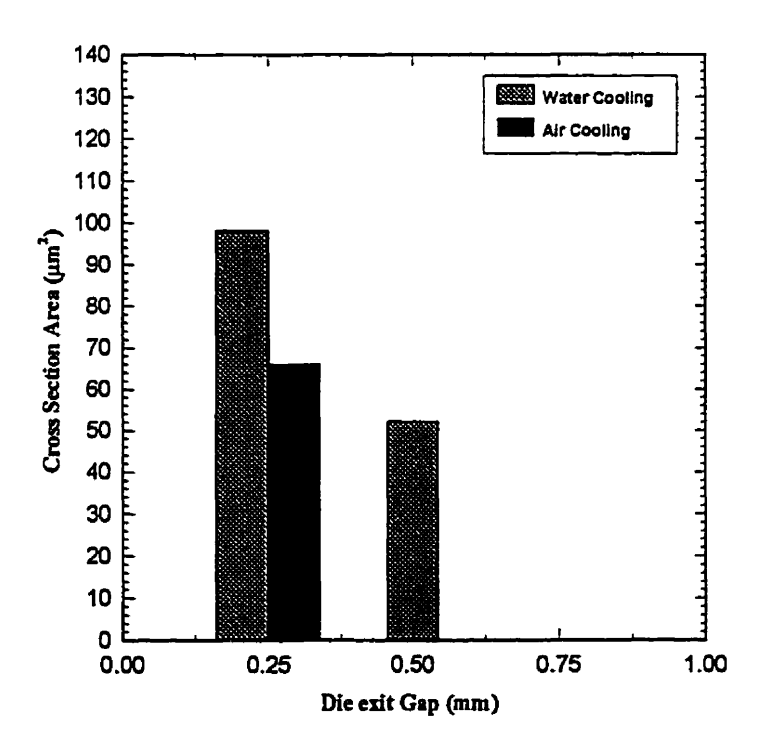


Figure 6.25: Effect of die exit gap size on the aspect ratio and area of dispersed phase particles for ADMER/EVOH (70/30 wt%) blends.

ratio and cross section area of the sample obtained with the gap size of 0.25 mm are considerably larger than for the sample extruded with die gap size of 0.5 mm. Smaller gap size produces stronger extensional flow and higher extension ratio, which is responsible for the larger and thinner particles of the dispersed phase.

Rheological studies in section 5.1 might help to explain some of differences between the PE/PA-6 and ADMER/EVOH blends. As the viscosity ratio is close to unity in PE/PA-6 blends, the extensional flow is more efficient in deforming the dispersed phase particles. Therefore, it is expected that strong extensional flow provided by low gap size would lead to break up of the dispersed phase particles, i.e. PA-6, and smaller particles are formed. On the other hand because of the high viscosity ratio in ADMER/EVOH blends, even strong extensional flow generated in the small gap size (0.25 mm), is not sufficient to break up the EVOH particles. However, the stronger extensional flow leads to larger deformations of EVOH particles, which produces longer particles.

It has been reported that high elasticity of droplets enhances resistance to deformation and breakup (76.). Chin and Han (88) reported that highly viscoelastic medium gave rise to large deformation of droplets. The shear storage modulus of of PA-6 shown in Figure 5.8, which is related to its elasticity, is always lower than the storage modulus of PE0. On the other hand, the storage modulus of EVOH is larger than of ADMER for frequencies larger than 50s⁻¹ (Figure 5.10). Therefore, EVOH particles are expected to show higher resistance against the high extensional flow, whereas the highly elastic matrix of PE0 produces large deformations that might lead to breakup of PA-6 particles.

6.1.2.6 Effect of Cooling System on Morphology

When the particles of dispersed phase that have been stretched by the extensional flow exit the die region, there is great chance of relaxation and returning to the original contracted position. Therefore, depending on the efficiency of cooling system, elongated particles of the dispersed phase exiting the die unit might experience different amounts of relaxation.

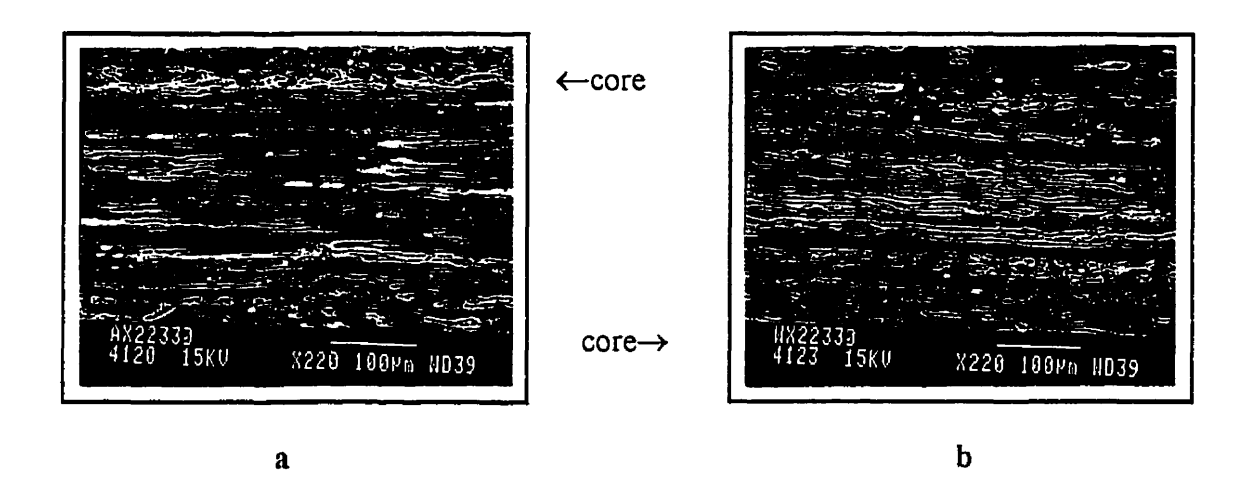


Figure 6.26: SEM micrographs showing effect of cooling system on the morphology of ADMER/EVOH (70/30 wt%) blends. a- air cooling b-water cooling

Thus, it is important to evaluate the influence of cooling system on the obtained morphology. Figure 6.26 shows a blend of 70/30 wt% of ADMER and EVOH extruded under the same conditions except for the cooling system. It appears that a water cooling system, which is more efficient in cooling the extruded ribbon, produces longer and larger particles of EVOH. In Figure 6.25, the image analysis results for the same micrographs are presented. The aspect ratio of water-cooled samples is higher than the air cooled samples by more than 60%, and enlargement of particle area is slightly smaller

6.2 Permeability Results

The barrier properties of polymer blends are determined by the chemical structure and physical properties of individual resins, the chemical nature of the penetrant, and by the system morphology. Also, orientation and crystallization of polymers influence the barrier properties of the material as a result of the increased packing efficiency of the polymer chains (162). However, their influence on the barrier properties is minor, in comparison

Table 6.1: Toluene and oxygen permeability of individual resins

Resin	Toluene Permeability (Measured ¹)	Toluene Permeability (Literature)	Oxygen Permeability (Measured²)	Oxygen Permeability (Literature)
PE0	24.8	27.08 (@22.8°C)	23.5	26.25 (@25°C)
PE1	30.7	-	•	•
PE2	32.9	-	25.0	•
PP	163	98.6 (@22.8°C)	48.0	65.2 (@23°C)
ADMER	176	-	61.5	•
PA-6	0.11	-	0.6	0.71 (@23°C)
EVOH	0.004	-	0.01	0.006@20°C

l-unit: mg.mm/m².min

2- unit: cm³.mm/m².day.atm

with the above factors. Barrier materials are needed in applications such as food packaging and gasoline tanks. Two blend systems of HDPE/PA-6 and PP/EVOH are evaluated for their barrier properties against oxygen and toluene as a typical hydrocarbon. Various parameters influencing system morphology including processing conditions and material characteristics have been investigated and will be presented in the following sections.

Oxygen and toluene permeability of individual resins used in this study were measured and reported in Table 6.1. All the reported values are for 50% relative humidity and a temperature of 23°C. The reproducibility of toluene permeability measurements was better than 5% and the oxygen permeability measurements were reproducible within 8%. For comparison purpose, reported values in the literature are also shown (122, 123).

Considering all the uncertainties like different crystallinity, orientation, relative humidity and test temperature; measured values agree with reported results reasonably.

As known, EVOH exhibits excellent barrier properties against both oxygen and toluene. PA-6 shows good barrier properties against toluene but it is not a good barrier for oxygen. Generally, increasing the maleation content of both polyethylene and polypropylene, raises oxygen and toluene permeability of these resins. However, it appears that oxygen permeability of maleated polypropylene increases more rapidly. One explanation might be the higher branching of these resins, that leads to lower packing efficiency of maleated polyethylene and polypropylene. Among the resins used as the matrix, ADMER shows the highest permeability to both oxygen and toluene.

6.2.1 Toluene Permeability of HDPE/PA-6 Blends

Laminar blends of HDPE and PA-6 have shown promise as solvent and hydrocarbon barriers. In order to evaluate the effect of different processing conditions and composition on barrier properties, toluene permeability of extruded samples was measured. Also, to evaluate the gas barrier properties of these blends, oxygen permeability of selected samples was measured.

6.2.1.1 Effect of Die Temperature on Permeability

It was shown in section 6.1.1.3 that, at a die temperature of 250°C, larger and longer particles of the dispersed phase, i.e. PA-6, were produced. Figure 6.27 reveals the influence of die temperature on toluene permeability of PE/PA-6 (80/20 wt%) blend.

Figure 6.27 shows about 30% lower toluene permeability values at die temperature of 250°C for both of compatibilized and non-compatibilized blends. This findings is in agreement with morphological studies, where higher aspect ratio was observed for samples produced at a die temperature of 250°C in Figure 6.5. Also it confirms that the die

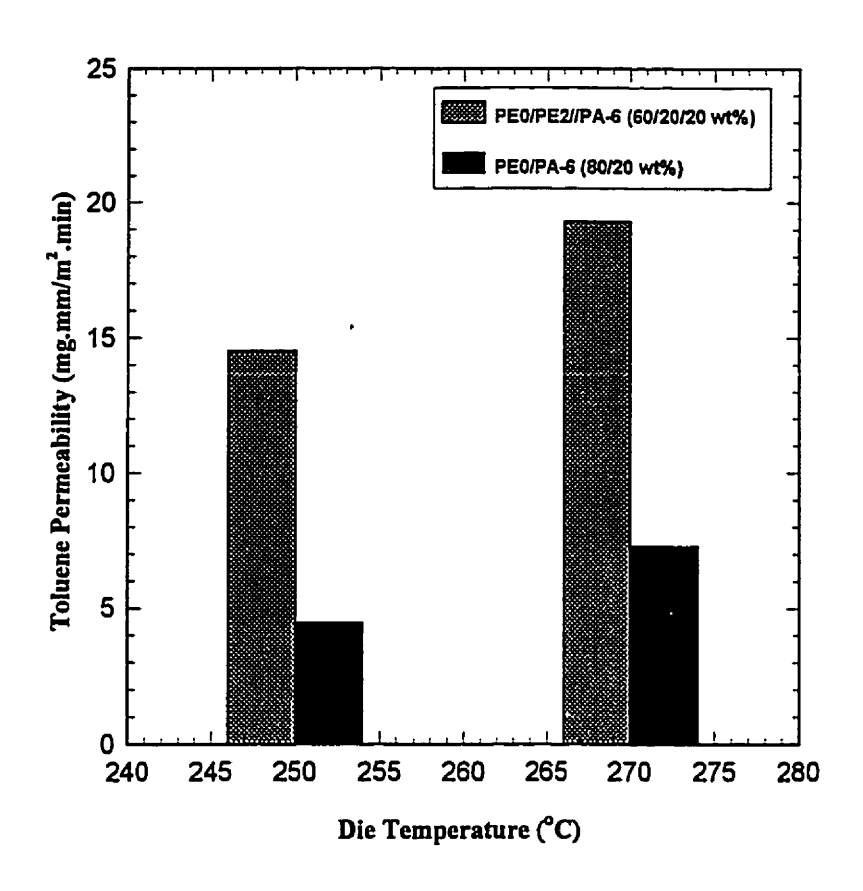


Figure 6.27: Effect of die temperature on toluene permeability of PE/PA-6 (80/20 wt%) blends.

temperature of 250°C, which is associated with viscosity ratio close to unity in Figure 5.5, gives good barrier properties.

Figure 6.27 also demonstrates the effect of compatibilizer or maleation content of polyethylene on the barrier properties of blends extruded under usual processing temperatures. A compatibilized blend that incorporates 20% of PE2, shows 3-4 times higher toluene permeability than the non-compatibilized blend. Lower interfacial tension of the compatibilized system leads to finer dispersion of dispersed phase. The smaller particle size is responsible for the observed reduction in barrier properties.

6.2.1.2 Effect of Screw Temperature on Permeability

In section 6.1.1.4, the key role of the temperature in the screw zone in development of laminar morphology during ribbon extrusion of polymer blends was discussed. The morphological studies and image analysis results presented in Figures 6.6 and 6.7 revealed the substantial increase of aspect ratio and particle size of the dispersed phase at low screw zone temperatures. Therefore, it is expected that the technique of low screw temperature leads to substantial improvement of barrier properties of PE/PA-6 laminar blends.

Figure 6.28 shows the dramatic influence of screw zone temperature on toluene permeability of PE0/PE2/PA-6 (70/10/20 wt%) blends. All three samples have the same composition and were extruded using the mixing screw and a die gap of 1.0 mm. Die

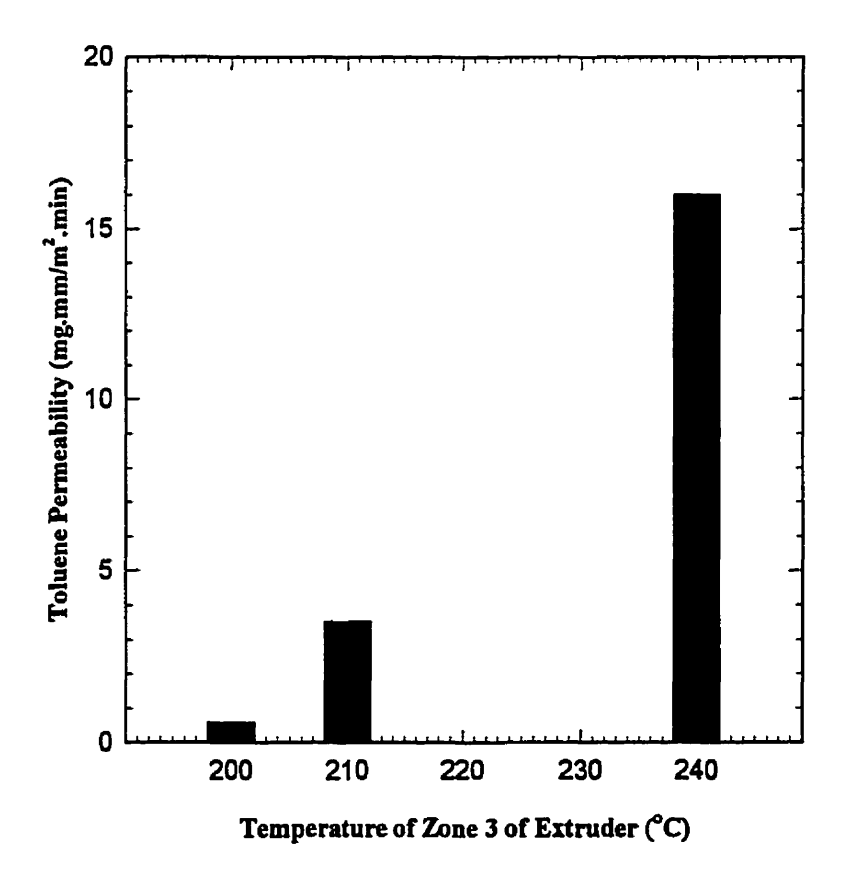


Figure 6.28: Effect of screw zone temperature on toluene permeability of PE0/PE2/PA-6 (70/10/20 wt%) blends

temperature was kept at 250°C for all samples. By reducing the temperature of zone 3 of the extruder from the usual processing temperature of 240°C to 200°C, the toluene permeability of the blend is decreased about 30 times. The change in permeability is also substantial from 210 to 200°C, where over such a small temperature difference, the permeability decreases from 3.5 to 0.62 mg.mm/m².min. These results show the effectiveness of the low screw temperature approach in improving the barrier properties of polymer blends. The substantial change in permeability over a small window of screw temperature confirms the results of Sundaraj et al (116), Lindt and Ghosh (113), and Lim and White (104). Their common findings showed major morphological changes during the initial softening stages and the importance of seconds of residence time or millimeters of screw length during the initial stages of melting.

6.2.1.3 Influence of Screw Design on Permeability

Figure 6.29 presents the impact of screw design on the barrier performance of PEO/PE2/PA-6 (70/10/20 wt%) blends. The metering screw produces samples that exhibit 25% lower permeability to toluene than the mixing screw. Figures 6.8 and 6.9 indicated 80% reduction in aspect ratio and 100% in particle size of samples when switching to the mixing screw from the metering screw. This explains the improvement in barrier properties of blends by changing from the mixing to metering screw. However, it should be pointed out that the mixing screw produces more efficient mixing of blend components, and is more likely to deliver the compatibilizer to the interface of polyethylene and polyamide. Therefore, samples obtained with the mixing screw might exhibit better adhesion at the interface. Consequently, both barrier and mechanical properties are likely to be enhanced. Therefore, despite the significant differences between the morphologies of samples extruded with the metering and mixing screws, the barrier properties are not affected notably.

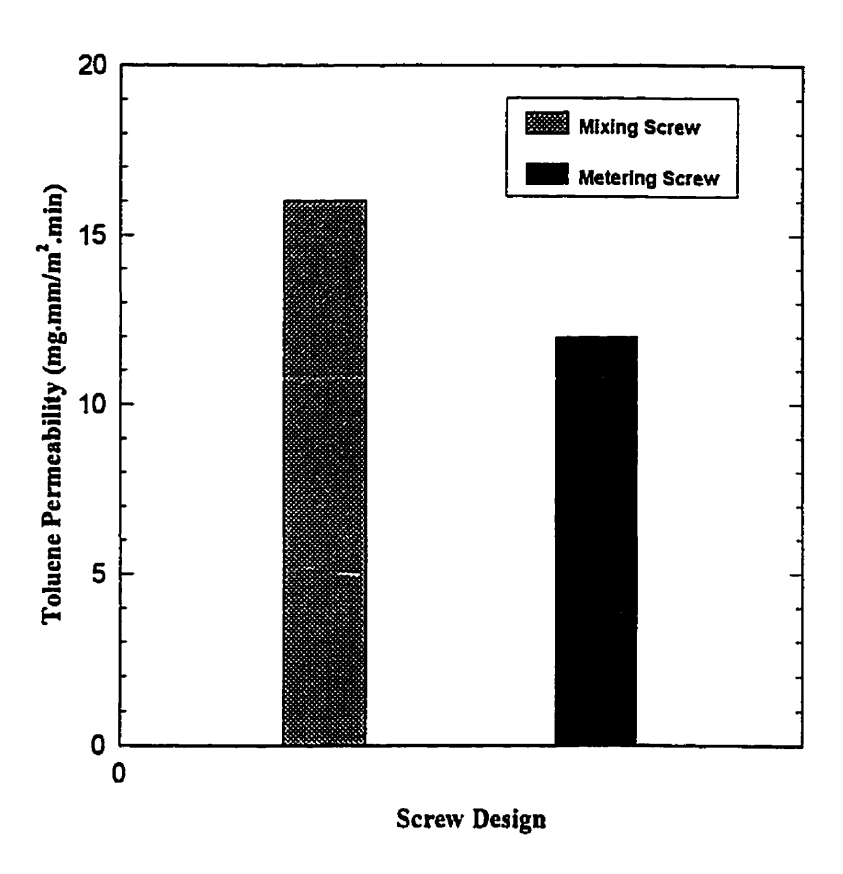


Figure 6.29: Influence of screw design on toluene permeability of PE/PE2/PA-6 (70/10/20 wt%) blends

6.2.1.4 Effect of Die Exit Gap Size on Barrier Performance

Figure 6.30 presents the results of toluene permeability measurements for the same samples of Figures 6.10 and 6.11 along with two other samples incorporating 10% of PE2 as compatibilizer. The compatibilized blend was obtained using a metering screw and temperature profile number 2. As was concluded from morphological analysis in Figures 6.10 and 6.11, the high stretch ratio prevailing in the small 0.5 mm gap, leads to breakup of PA-6 particles. Accordingly, smaller particles of the barrier dispersed phase result in lower barrier performance of blend. Permeability results, shown in Figure 6.30, confirm morphological observations. Samples obtained with a gap of 0.5 mm show toluene permeabilities as high as twice the permeability of samples obtained with a gap of 1.0 mm. The trend is similar for both of compatibilized and non-compatibilized blends. However,

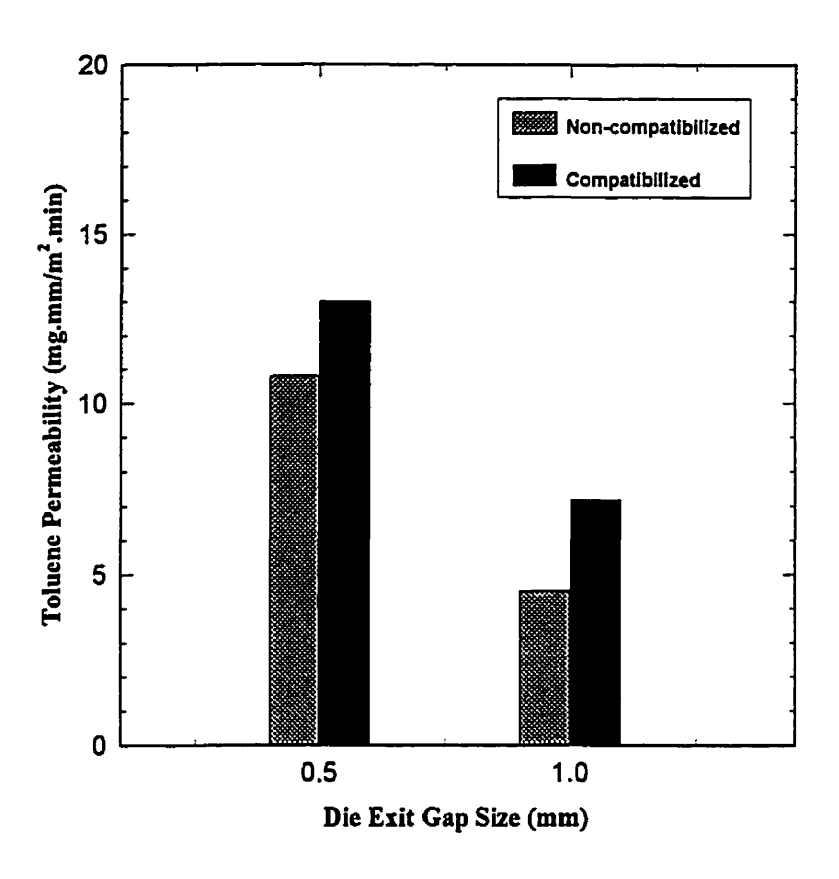


Figure 6.30: Effect of die exit gap size on toluene permeability of PE0/PE2/PA-6 (70/10/20 wt%) blends

for both gap sizes, compatibilized blends obtained at the usual processing temperature profile of number 2, exhibit higher toluene permeability. This suggests that a stretch ratio above 10 inside the die unit is not recommended for developing laminar morphology in blends of HDPE and PA-6 resins.

The permeability of samples extruded at a gap of 0.5 mm increases more than expected from the morphological analysis. It is believed that this difference may be attributed to crystallinity. Thinner samples obtained with a 0.5 mm gap experiences higher cooling rates than thicker ribbons obtained with a 1.0 mm gap. Therefore, it is expected to obtain higher crystallinity with the 1.0 mm gap. Crystallinity is known to improve the barrier properties of polymers (162).

6.2.1.5 Influence of Composition on Permeability

Figure 6.31 presents the impact of PA-6 content on toluene permeability of laminar blends of HDPE and PA-6 resins. In this figure, toluene permeability of 78.6/11.4/10 and 70/10/20 (PE0/PE2/PA-6 wt%) blends along with the toluene permeability of non-compatibilized blends obtained at high temperature profile of number 2 are shown. As expected, from morphological comparisons in section 6.1.1.7, samples extruded using the low screw zone temperature exhibit substantial improvement of one order of magnitude in toluene permeability, by increasing the PA-6 content from 10 to 20 wt%. It will be shown that the permeability of samples having 20 wt% PA-6 using the low screw zone temperature is comparable with co-extruded material. Therefore, it is not necessary to increase the PA-6 content beyond this value.

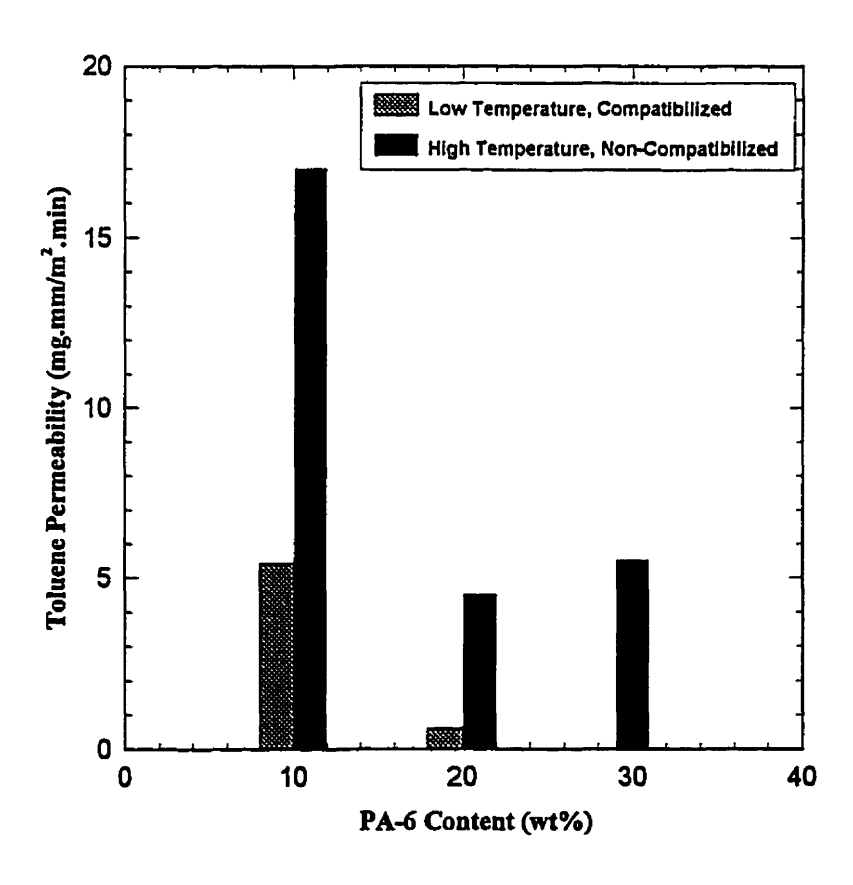


Figure 6.31: Effect of PA-6 content on toluene permeability of HDPE/PA-6 laminar blends

The effect of PA-6 content on non-compatibilized blends is similar, suggesting a leveling off at around 20 wt% PA-6 content. The results also confirm the important role of interfacial adhesion in improving the barrier performance of laminar blends. It is believed that lack of adhesion at high PA-6 content above 20 weight percent is responsible for the relatively high values of permeability in non-compatibilized blends.

6.2.1.6 Influence of MAH Content of PE on Permeability

Generally, by increasing the amount of interfacial agent, the particle size of dispersed phase decreases and smaller particles are expected to diminish the barrier performance of laminar blends. However, the low screw zone temperature approach proposed in this study demonstrated that, the particle area in the plane of extrusion and aspect ratio were increased upon increasing the MAH content of polyethylene. Furthermore, higher maleation content improves the interfacial adhesion in the solid state that should improve the barrier performance of these laminar blends.

Figure 6.32 shows the effect of maleation content of PE on toluene permeability of samples extruded using the low temperature profile of number 5 in Table 4.3. The Mixing screw and a die exit gap of 1.0 mm were employed. The toluene permeability of non-compatibilized blend, i.e. zero maleation content, is very high. When the maleation content is raised to 0.007 wt%, permeability decreases by one order of magnitude. By increasing the maleation content, more reduction in permeability is observed and above the maleation content of 0.014%, permeability levels off. Therefore, considering both morphological analysis and barrier performance, it seems that the optimum level of maleation content of polyethylene is in the 0.014-0.028 wt% range. The toluene permeability of blends within this range of MAH content, is 45 times lower than for the unmaleated PE matrix.

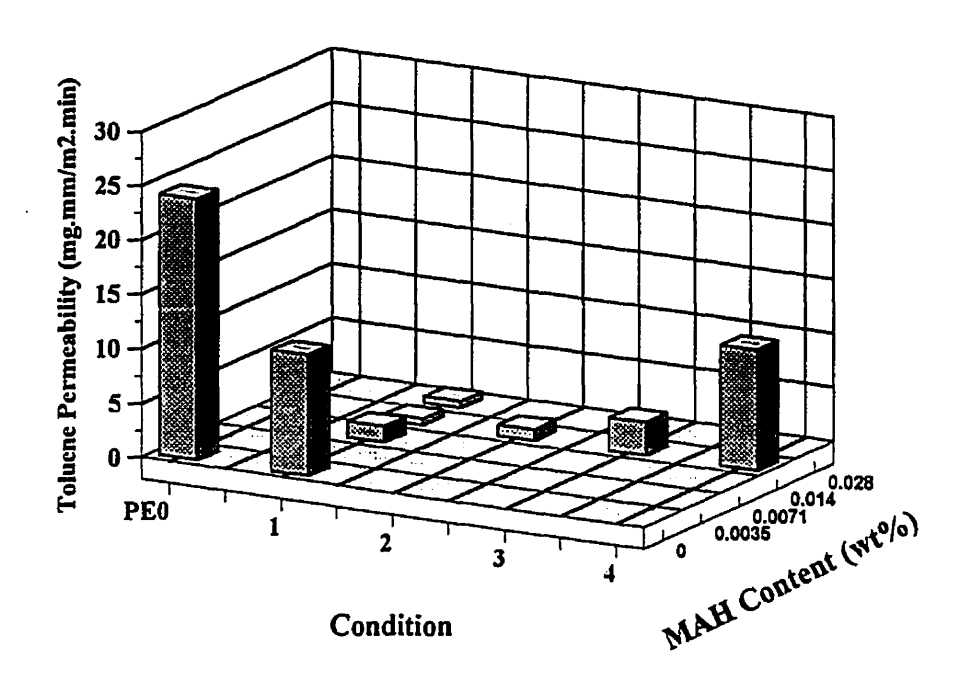


Figure 6.32: Effect of maleation content and pre-compounding on toluene permeability of PEO/PE2/PA-6 (70/10/20 wt%) blends extruded at low screw zone temperature.

6.2.1.7 Effect of Pre-compounding on Permeability

Morphological studies in section 6.1.1.9 revealed the influence of pre-compounding on particle size and aspect ratio of dispersed phase. It was concluded that longer residence time of polymer melt inside the screw zone and excessive mixing results in particle break-up and leads to microstructure that incorporates much smaller PA-6 particles than dry blended samples.

Figure 6.32 shows the toluene permeability of samples the morphology of which was given in Figures 6.15 and 6.16. Permeability result supports the morphological findings. The addition of mixing steps prolongs the residence time of the polymer melt in the screw zone, and thus tends to raise toluene permeability of laminar blends. However,

applying optimum screw configuration in twin-screw compounding of blend components in combination with low screw zone temperatures in both extruders, i.e. twin and single screw extruders (condition #3), results in one order of magnitude reduction in toluene permeability of polyethylene.

6.2.1.8 Effect of Screw Speed on Permeability

Changes in screw rotational speed influence the residence time or flow rate and shear rate. Raising the RPM (rotation per minute) reduces the residence time of the polymer melt in the extruder and increases the average shear rate applied to the particles of dispersed phase. As long as the PA-6 particles are melted before entering the die and the interfacial agent wets the interface of two phases, a reduction in residence time of the polymer melt inside the extruder should lead to larger particles entering die unit, which is desirable for developing laminar morphology. On the other hand, higher RPM associated with higher shear rate could produce finer particles of the minor phase which is not advantageous. Therefore, the balance of these two effects determines the net effect of RPM on morphology. It should be kept in mind that, for commercial extrusion lines, where production rate is an important consideration, higher RPM is generally desirable.

Figure 6.33 reveals the toluene permeability of two samples extruded at 30 and 60 RPM. To the extent possible, other processing conditions, including composition, are kept identical. The Mixing screw, in conjunction with high temperature profile # 3, was used with these samples. Raising the RPM from 30 to 60 leads to a 30% increase in toluene permeability. Yet, it may be possible to obtain different results for samples extruded with low screw zone temperature profile.

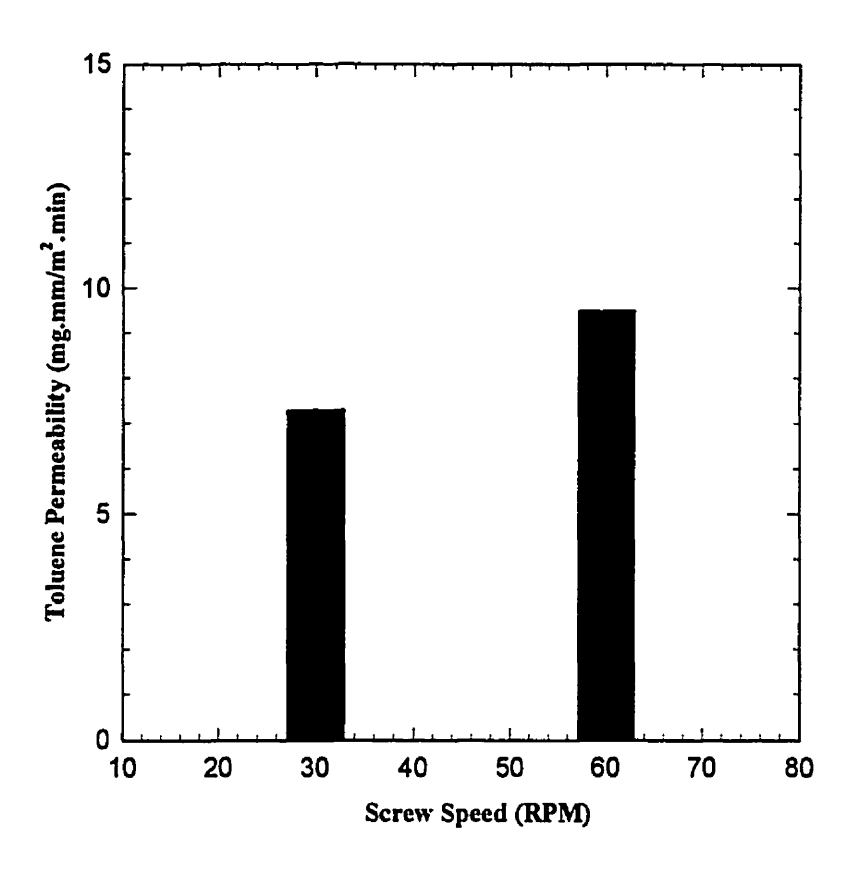


Figure 6.33: Effect of RPM on toluene permeability of PEO/PA-6 (80/20 wt%) laminar blends

6.2.1.9 Influence of Adapter Angle on Permeability

Streamlined flow in the converging cone tends to promote coalescence of minor phase particles (93). The amount of coalescence depends on the strength of convergence of cone, i.e. the angle of the cone. However, it has been reported that coalescence occurs to a smaller extent with compatibilized systems (69).

In this study, two different adapter angles, 30 and 70°, were used. Particles exiting the metering screw are coarse; thus, a 30° adapter angle was used for most of the runs with the metering screw. The mixing screw tends to provide finer particles; therefore, an adapter with 70° angle was employed to enhance coalescence to form larger particles. Two compatibilized samples using adapter angles of 30 and 70° were extruded. All other

processing parameters were identical. Results of toluene permeability measurements showed only 5% difference between two blends, which are considered identical within experimental error of measurements.

6.2.2. Permeability of ADMER/EVOH Blends

In general, the processing variables influence morphology, and therefore, the permeability of ADMER/EVOH extruded sheets in the same way as for PE/PA-6. Therefore, in the following discussion, we shall not repeat the arguments that were given in the preceding sections. Emphasis will be placed on presentation of the results and indicating and explaining differences in the pattern of behavior from those exhibited by PE/PA-6 blends.

6.2.2.1. Effect of Die Temperature on Permeability

Figure 6.34 shows the influence of die temperature on toluene permeability of ADMER/EVOH (75/25 wt%) blends. It appears that, within the temperature range of 215 to 230°C, die temperature does not affect toluene permeability substantially. As mentioned earlier, the viscosity ratio is larger than unity for the entire range of shear rates and processing temperatures covered in Figure 5.7. Such conditions are not ideal for the large deformations needed for good barrier performance. However, it seems that a higher temperature yields slightly better barrier properties. Lower interfacial tension at higher temperatures enhances deformation of EVOH particles. This might explain the minor improvement in barrier properties at higher die temperatures. These findings are in harmony with morphological results discussed in section 6.1.2.2.

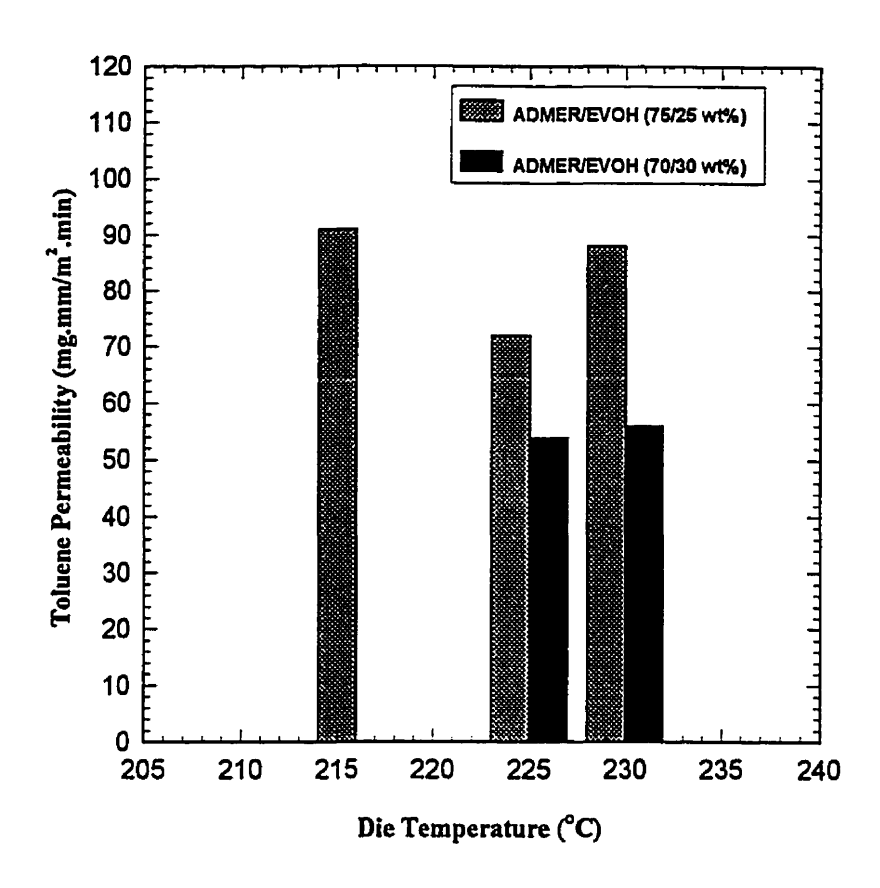


Figure 6.34: Effect of die temperature on toluene permeability of ADMER/EVOH (75/25 wt%) blends

6.2.2.2. Influence of Screw Design on Permeability

Figure 6.35 shows the effect of screw design on toluene and oxygen permeability of ADMER/EVOH blends. This graph also presents the influence of composition on toluene permeability. Two different compositions were tested for toluene permeability and one blend composition was tested for oxygen permeability. For all the samples tested for toluene or oxygen permeabilities, the mixing screw provided lower permeability. This supplies samples exhibit 15-25% lower permeability than the samples obtained with the metering screw. Although, Figures 6.20 and 6.21 revealed larger and longer EVOH particles for metering screw samples, it appears that lack of adhesion at the interface of ADMER and EVOH phases, tends to cause deterioration of barrier properties.

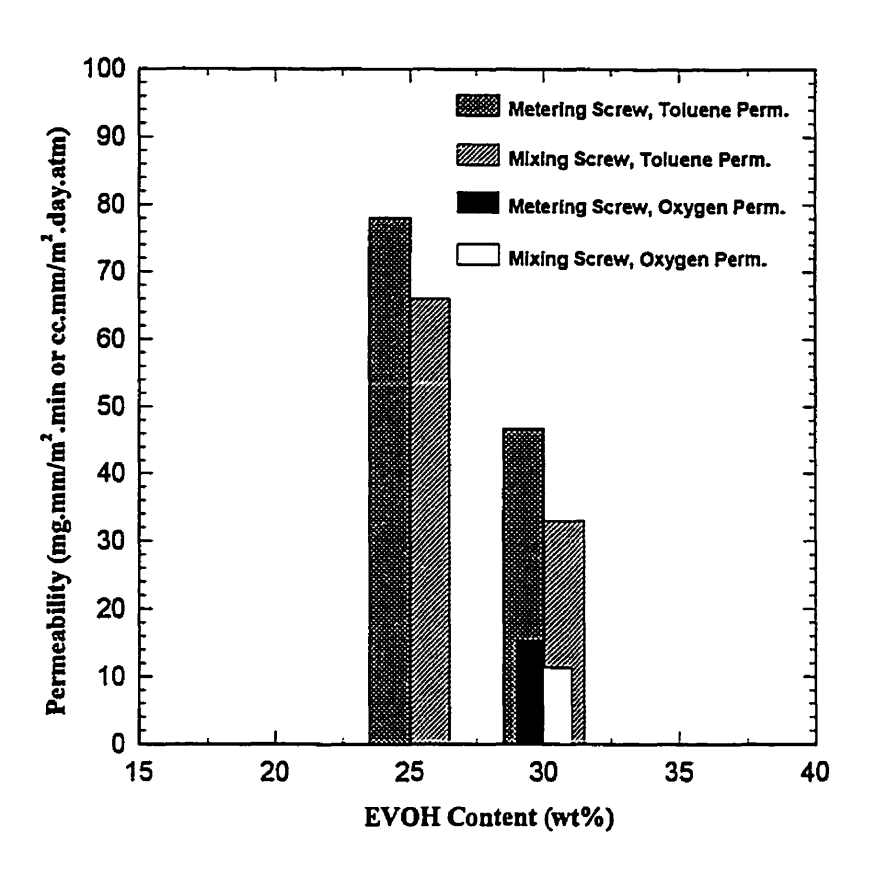


Figure 6.35: Influence of screw design on barrier performance of ADMER/EVOH blends

6.2.2.3. Influence of Die Exit Gap Size on Permeability

Variations of die exit gap size might affect the barrier performance of blends in two competitive manners. As shown in Figures 6.24 and 6.25, smaller gap size leads to stronger extensional flow that gives larger and longer particles of dispersed phase, i.e. EVOH. Thus, morphological analysis determines better barrier properties at lower gap size. On the other hand, extruded ribbon produced using smaller gap size, incorporates less crystallinity. Therefore, it diminishes the barrier performance of blend.

Figure 6.36 presents the effect of die exit gap size on the toluene and oxygen permeabilities of ADMER/EVOH (70/30 wt%) blends using temperature profile number 2 and the water cooling system. Toluene permeability is increased by 15% for the small gap

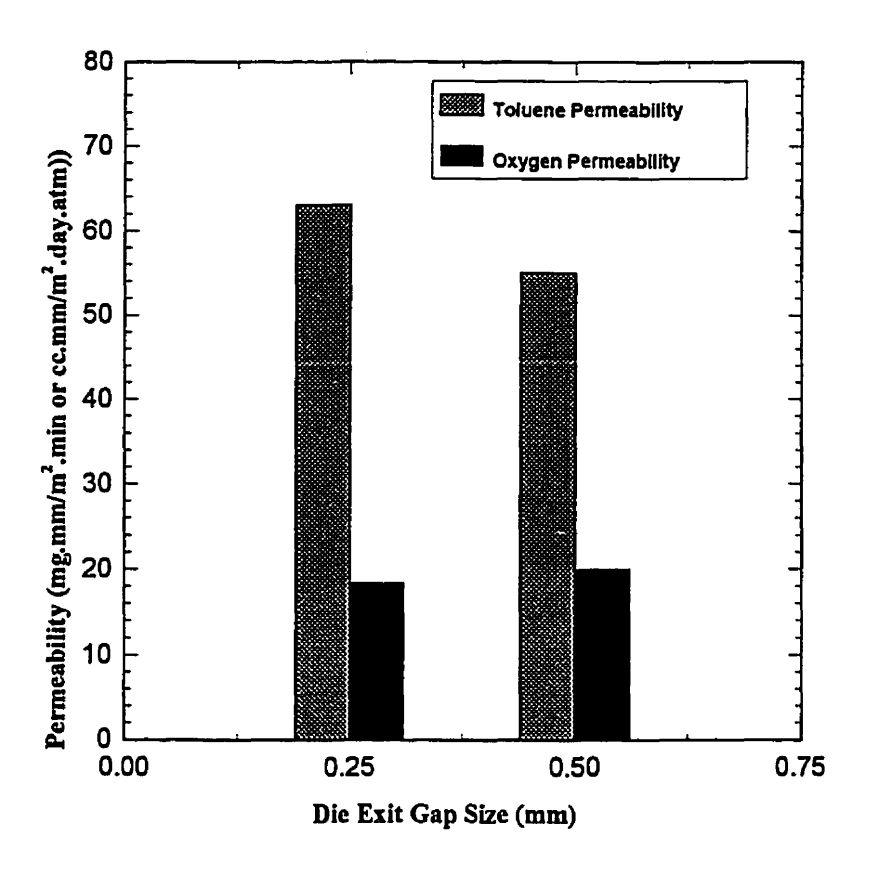


Figure 6.36: Influence of die exit gap size on barrier performance of ADMER/EVOH (70/30 wt%) blends

size, while oxygen permeability is reduced about 10%. Considering the experimental errors, it appears that the two competitive parameters (laminar quality and crystallinity) tend to balance each other, as discussed in earlier sections. Therefore, barrier properties of two blends produced using gap sizes of 0.25 and 0.5 mm are considered similar to each other. Further studies on the effect of crystallinity on the oxygen and toluene permeability of individual resins might help to explain these observations.

6.2.2.4. Influence of Cooling System on Permeability

In Figure 6.26, it was shown that water cooling in comparison of air cooling, could restrict relaxation of stretched particles of EVOH exiting the die. This produces larger and longer particles of the minor phase. On the other hand, it is likely that water cooling would lead to lower crystallinity than air cooling, due to the higher cooling rates.

Figure 6.37 shows the effect of the cooling system on toluene and oxygen permeability of ADMER/EVOH (70/30 wt%) blends extruded using a mixing screw. Aircooled samples exhibit lower toluene and oxygen permeabilities. Toluene permeability was reduced by about 50%, while oxygen permeability decreased by 40%. Therefore, it appears that the influence of crystallinity is more important than the minor improvement of laminar morphology, with regard to the barrier properties of extruded ribbons.

6.2.3. Comparison of Permeability Results of HDPE/PA-6 Blends with Predictions of Theoretical Models

The permeability coefficient is defined as the product of the effective diffusion, D, and solubility, S, coefficients

$$P = D.S ag{6.2}$$

A reduction of the solubility parameter or an increase of the length of diffusion path (tortuosity) caused by laminar structure may decrease permeability. The tortuosity factor, τ , is generally defined as the ratio of the effective path length for permeation to the thickness of composite or blend ($1 < \tau < \infty$).

Presently, there is no general reliable, predictive model for transport through a composite medium of arbitrary morphology (163). However, the permeability of homogenous blends may be estimated by a treatment similar to Maxwell's analysis of conductivity for systems containing conductive spherical particles dispersed in a conducting matrix (164).

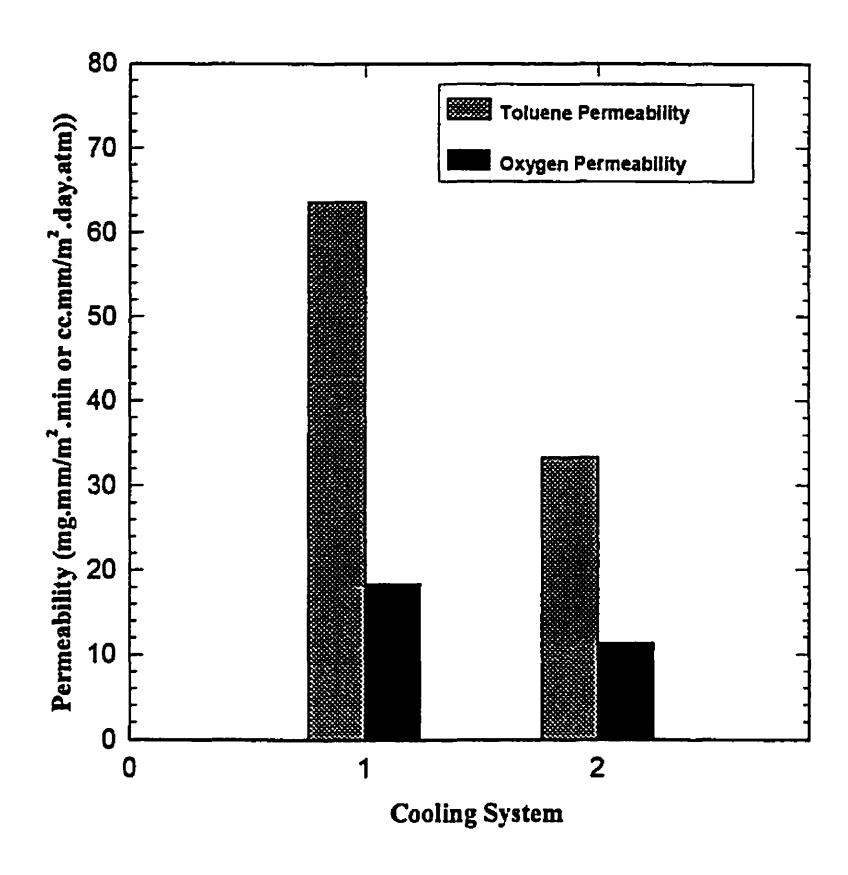


Figure 6.37: Influence of cooling system on barrier performance of ADMER/EVOH (70/30 wt%) blends

According to this analysis:

$$\tau = 1 + \frac{\phi_d}{2} \tag{6.3}$$

where τ is tortuosity and ϕ_d is the volume fraction of dispersed phase.

A commonly used estimation for the ratio between the permeability of a blend or composite and that of the conductive matrix phase as a function of the tortuosity and the volume fraction of matrix polymer, ϕ_m , has been proposed by Michaels and Bixler (165) and Barrer (166):

$$\frac{p_c}{p_m} = \frac{\phi_m}{\tau} \tag{6.4}$$

where p_c and p_m are the permeabilities of the composite (blend) and matrix, respectively.

For homogenous systems, permeability is given by (167):

$$p_{c} = p_{m} \left(\frac{p_{d} - 2p_{m} - 2\phi_{d}(p_{m} - p_{d})}{p_{d} + 2p_{m} + \phi_{d}(p_{m} - p_{d})} \right)$$
(6.5)

where p_d is the permeability of the dispersed phase.

For morphologies consisting of laminates stacked in series, as in the case of coextruded structures, Nielson's treatment (168) may be used:

$$\tau = 1 + \left(\frac{L}{2T}\right)\phi_d \tag{6.6}$$

where L and T are length and thickness of the platelet, respectively.

Permeability in this arrangement of phases is given by (168, 169):

$$\frac{1}{p_c} = \frac{\phi_d}{p_d} + \frac{\phi_m}{p_m} \tag{6.7}$$

we shall refer to this as the series model.

By comparing Equations of (6.3) and (6.5) with (6.6) and (6.7), it is observed that thin platelets with a large, but finite, L/T ratio can reduce permeability dramatically, even for small volume fractions. On the other hand, it is obvious that reduction of permeability in homogenous blends, even with a substantial volume fraction of the minor phase, is small.

6.2.3.1. HDPE/PA-6 Blends

6.2.3.1.1. Toluene Permeability of HDPE/PA-6 Blends

Figure 6.38 presents the variation of toluene permeability of extruded blends of HDPE/PA-6, at various concentrations of PA-6 along with predictions of Maxwell and Series models. Appendix B provides the detailed processing conditions for each sample code. As observed, depending on the processing conditions, a wide range of toluene permeability values might be obtained. Samples extruded under low screw temperature conditions, i.e. X153701 and X153702, exhibit the lowest permeability values closely approaching co-extruded ribbon permeability levels for PA-6 content above 15 vol%. As mentioned earlier, by using external lubricants at slightly lower screw temperature, it might even be possible to achieve permeability

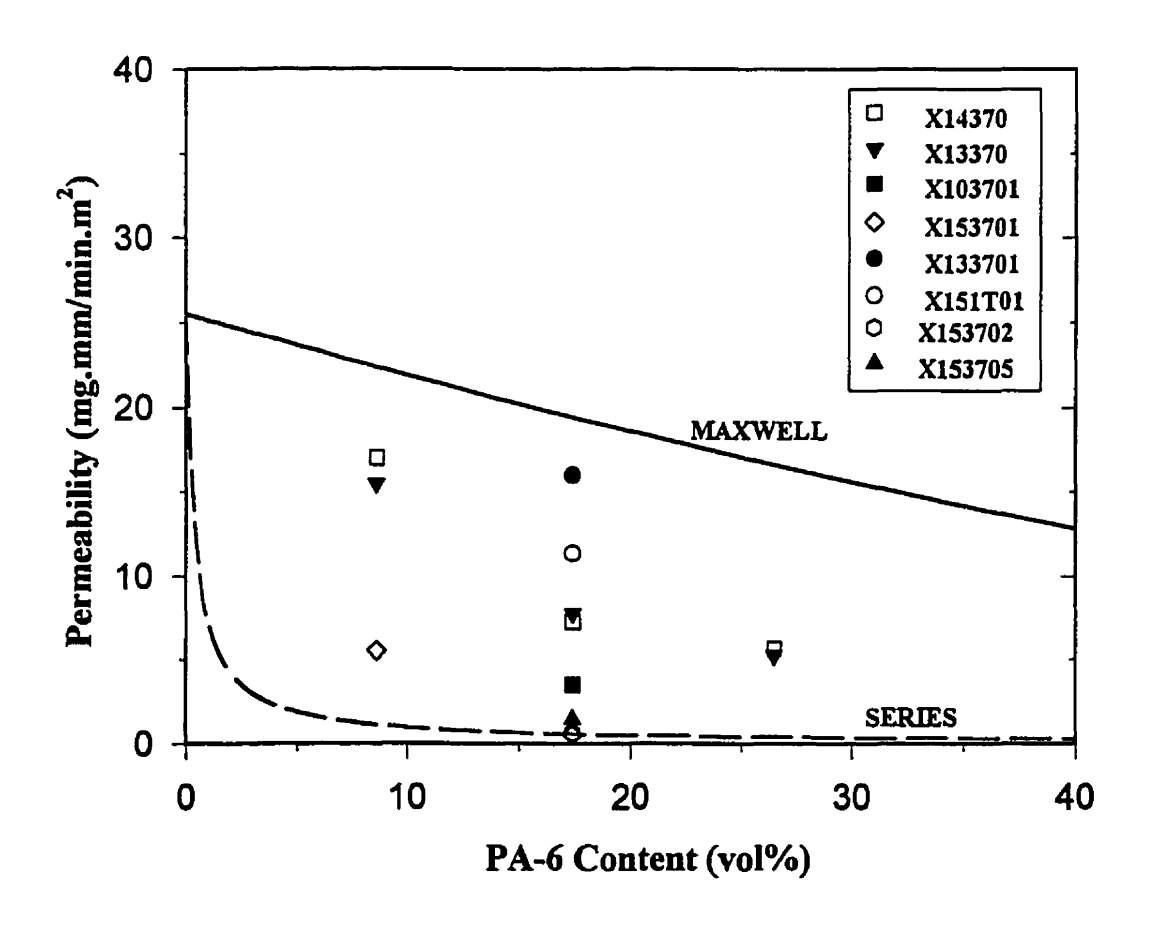


Figure 6.38: Variation of toluene permeability with respect to PA-6 content along with Maxwell and Series model predictions for HDPE/PA-6 blends.

values comparable to co-extruded material at lower PA-6 contents. Due to incorporating 10 to 20 wt% of PE2 resin as interfacial agent in these systems, it is expected that the samples would also exhibit good mechanical properties. Toluene permeability of compatibilized blends obtained under usual processing conditions (e.g. sample X133701) resembles that of homogeneous mixtures. The above suggests the possibility of obtaining a dramatic improvement in barrier properties, comparable to that achievable by co-extrusion, by causal extrusion of blends. Such a possibility would lead to significant reduction in capital and operating costs in the manufacturing of barrier materials.

6.2.3.1.2. Oxygen Permeability of HDPE/PA-6 Blends

Although, as shown in Table 6.1, PA-6 resin is not a good oxygen barrier, oxygen permeability measurements were done on selected samples, for comparison purposes. Figure 6.39 shows the oxygen permeability of selected PE0/PE2/PA-6 blends as a function of volume percent of PA-6, along with the predictions of Maxwell and series models. The experimental results are close to the predictions of the series model. Yet, due to the high oxygen permeability of PA-6, i.e. only 40 times lower than PE, the reduction in oxygen permeability is not large. A maximum reduction of 4 times in oxygen permeability of sample X1537012 is obtained. Therefore, PE/PA-6 laminar blends are not a good candidate for applications where oxygen barrier property is needed.

6.2.3.2. ADMER/EVOH Blends

6.2.3.2.1. Toluene Permeability of ADMER/EVOH Blends

In Figure 6.40, the toluene permeability of ADMER/EVOH blends is compared with the calculated permeability for conventional homogeneous blends and co-extruded materials; as predicted by the Maxwell and Series models, respectively. The barrier performance of sample X1437A, which is extruded using the low screw temperature, approaches that of

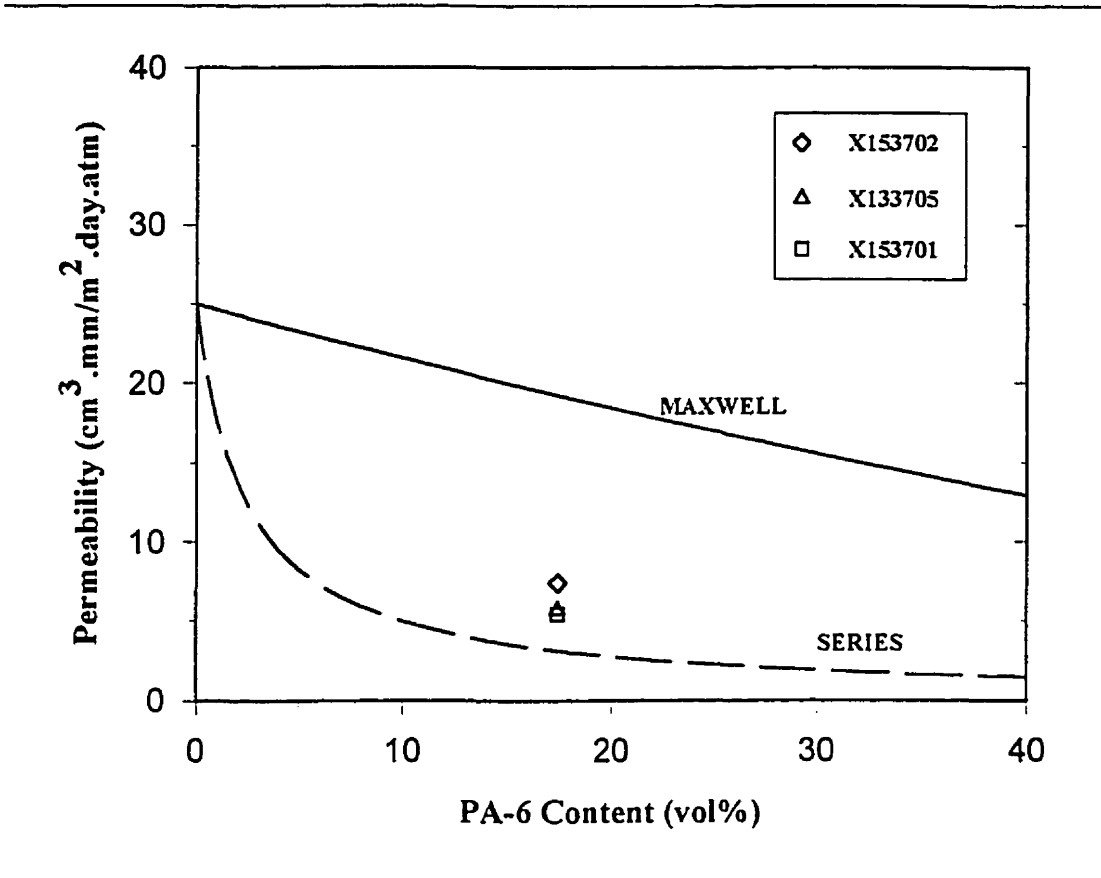


Figure 6.39: Variation of oxygen permeability with respect to PA-6 content along with Maxwell and Series model predictions for HDPE PA-6 blends

co-extruded materials. A maximum reduction of 9 times in toluene permeability is obtained, which is 3 times better than results reported by Hozhabr (19). However, considering the excellent toluene barrier properties of EVOH, i.e. 0.004 mg.mm/m².min, which is 28 times lower than toluene permeability of PA-6, these results are not very encouraging. The narrow processing window, a viscosity ratio larger than unity, large elasticity ratio, weak adhesion at the interface, and relatively high permeability of maleated polypropylene are among the factors that limit barrier performance of ADMER/EVOH blends. To overcome some of these problems, it is suggested that manipulation of the molecular weight of PP, combined with changes in the type and concentration of compatibilizer, might lead to significant improvement. Changes should be oriented

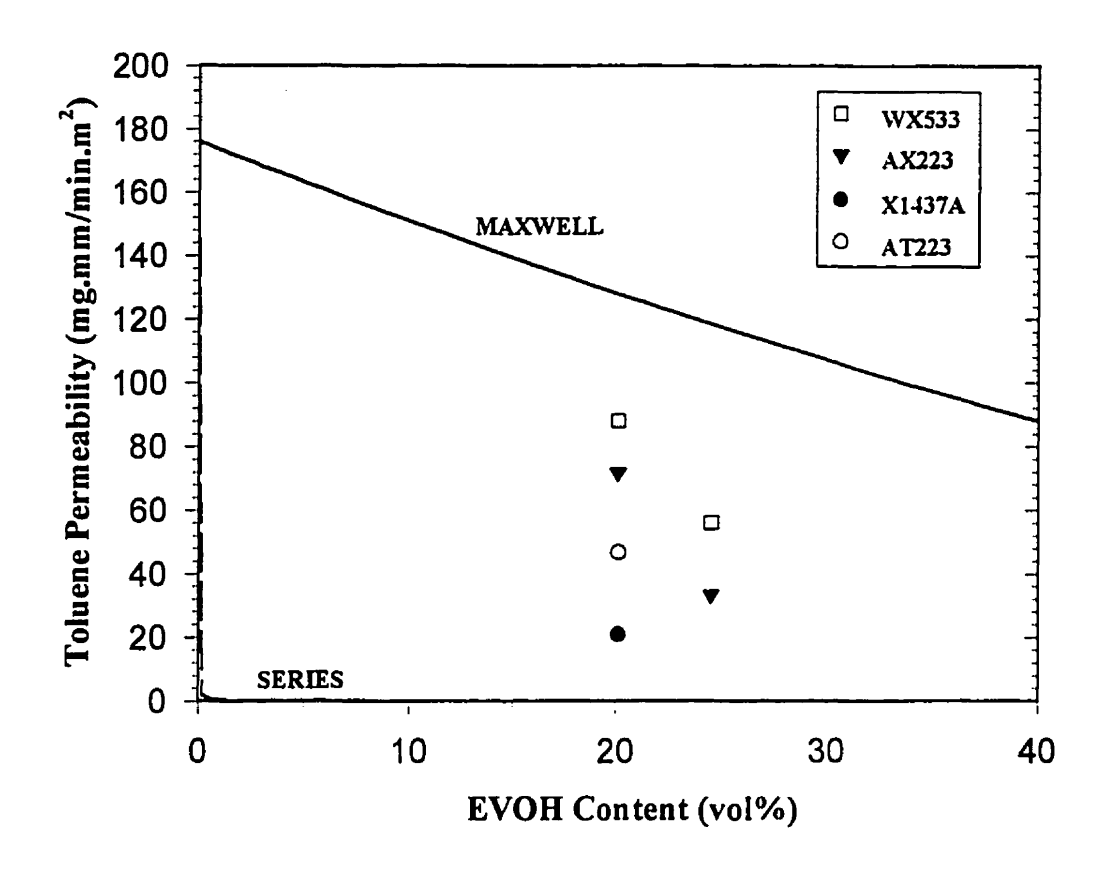


Figure 6.40: Variation of toluene permeability with respect to EVOH content along with Maxwell and Series model predictions for ADMER/EVOH blends

towards widening the processing window, improving the barrier characteristics of the compatibilizer, reducing the elasticity ratio, and lowering the viscosity ratio towards unity. Also, using lubricants might prevent extra shearing in the screw zone, thus reducing particle breakup. The manipulation of cooling rates to enhance crystallinity may prove to be helpful.

6.2.3.2.2. Oxygen Permeability of ADMER/EVOH Blends

Figure 6.41 shows the oxygen permeability of ADMER/EVOH blends with respect to volume percent of EVOH along with predictions of the Maxwell and Series models.

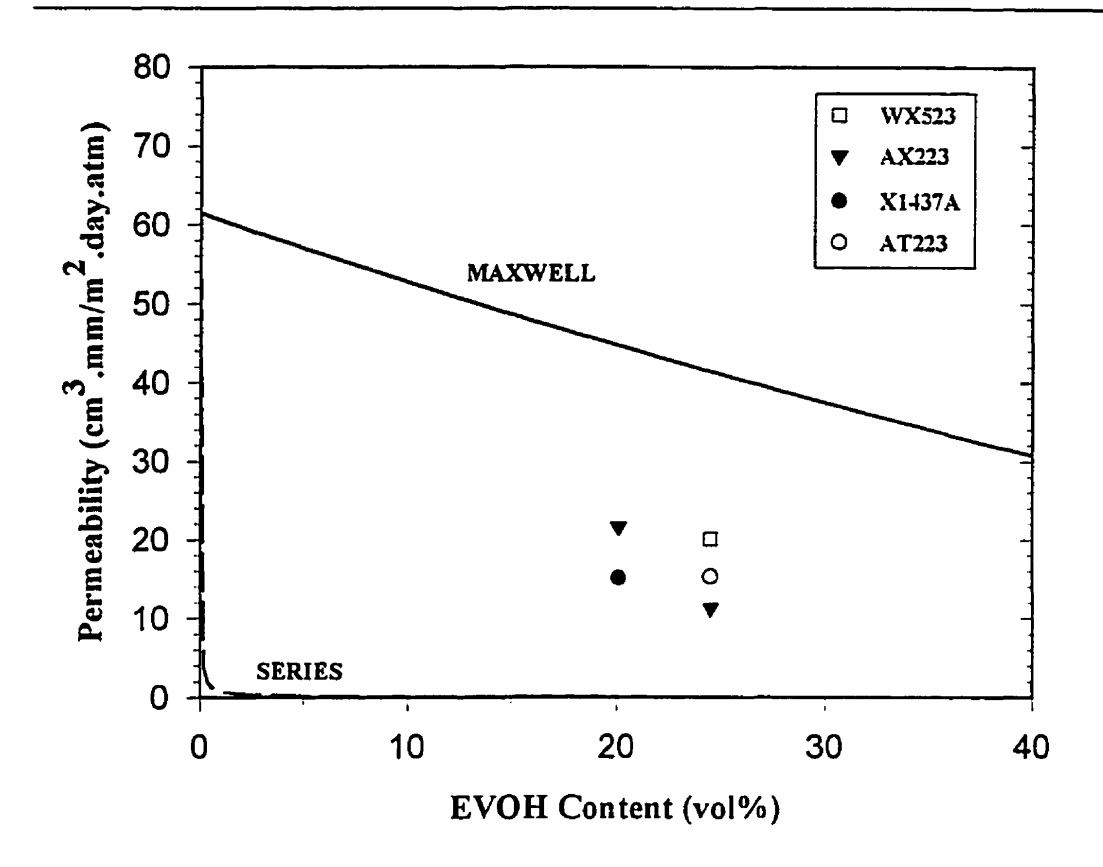


Figure 6.41: Variation of oxygen permeability with respect to EVOH content along with Maxwell and Series model predictions for ADMER EVOH blends

Sample X1437A, extruded with the low temperature profile number 4, yields maximum reduction of 4 times in oxygen permeability of the ADMER matrix. Although, the results are not fully satisfactory, significant improvement in oxygen barrier performance are obtained in comparison with the results of Lohfink (18) and Hozhabr (19).

6.3. Evaluating Mechanical Performance of Blends

The instrumented impact test was used for evaluation of mechanical strength of extruded samples. The instrumented impact test provides force, deflection, stiffness, and energy data for each sample. Depending on the application, one of these parameters or a combination of them might be the controlling variable during an impact event. However,

among them, energy, which is the area under the load-deflection curve, is used more often as critical variable for the ultimate strength of materials (170). Both of ultimate energy and ultimate force are presented below.

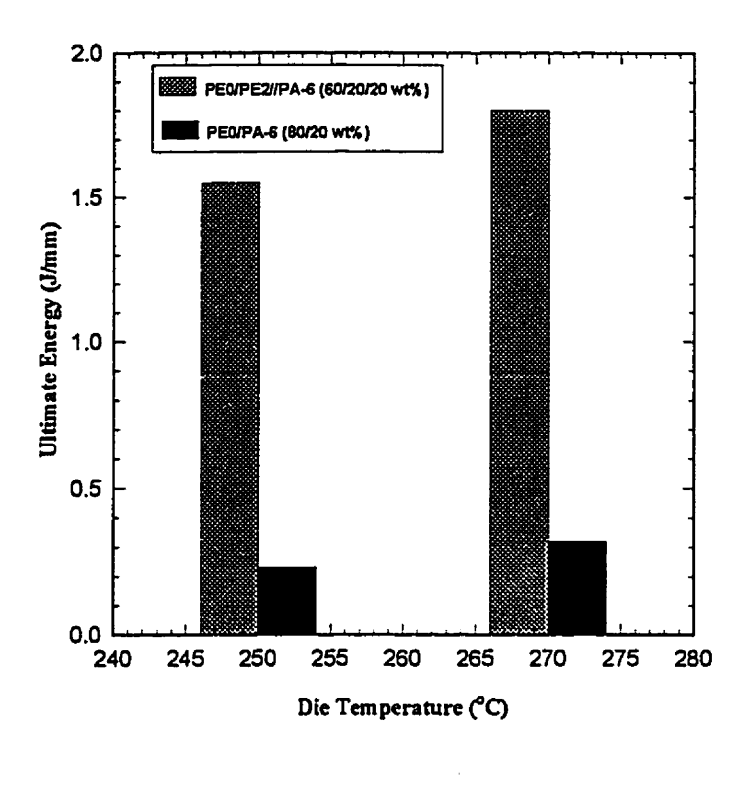
There are problems associated with impact testing of specimens with different thicknesses (171). Thin specimens tend to fail in flexure (either tensile fracture or compressive buckling), while thick specimens fail in shear (one or more delaminations running along the length of sample). Generally, thicker specimens exhibit higher impact energies, although not always with the same ratio from one material to another. Since this study involves samples with different thicknesses, a normalization procedure, explained in Appendix D, was used to normalize the impact properties with reference to a thickness of 1 mm.

6.3.1. Impact Strength of HDPE/PA-6 Blends

Both polyethylene and polyamide-6 exhibit ductile fracture in the impact test. Samples of load-deflection curves are given in Appendix F. Influences of different parameters on the impact strength of blends were studied and are discussed here. A standard deviation of 15% was observed for samples having medium to good impact properties. While, for the non-compatibilized blends, which showed poor mechanical properties, larger standard deviations up to 25% was observed.

6.3.1.1. Influence of Die Temperature

Figure 6.42 shows the ultimate energy and force versus die temperature for both compatibilized, i.e. PE0/PE2/PA-6 (60/20/20 wt%), and non-compatibilized blends of PE0/PA-6 (80/20 wt%). It is evident that adding 20% of compatibilizer, corresponding to a maleation level of 0.028 wt%, increases impact properties substantially. It appears that higher temperature results in a minor increase of ultimate force or energy. The maximum increase of about 15%, which observed for the compatibilized blend, is within the



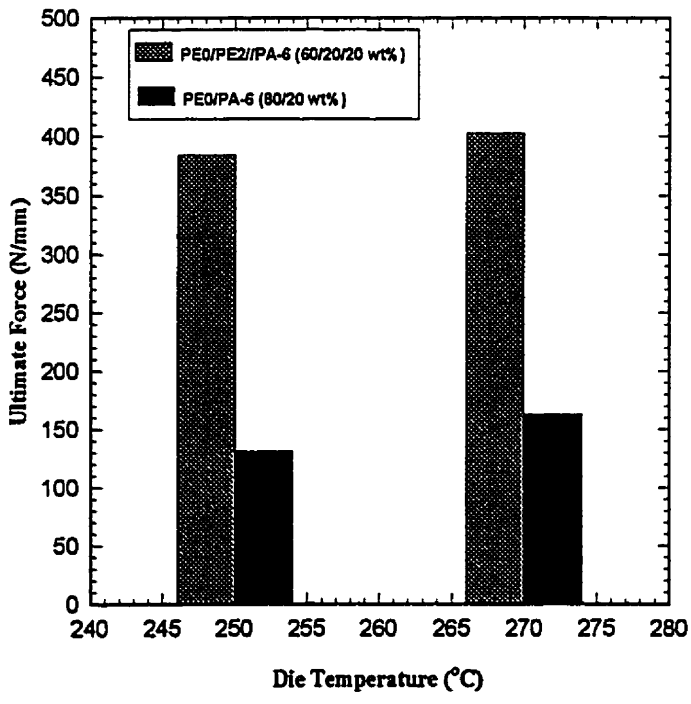


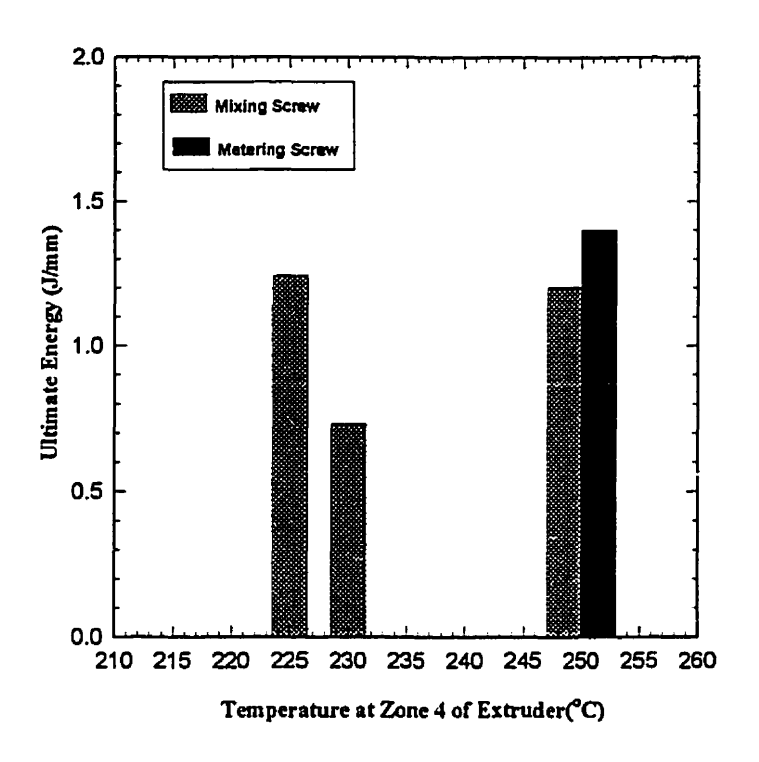
Figure 6.42: Influence of die temperature on ultimate force and energy of PE/PA-6 blends

experimental error of tests. Lower viscosities at elevated temperatures could lead to improved coating of interface with the compatibilizer and a lower interfacial tension, which result in minor improvement of mechanical properties. However, Figure 5.30 reveals that interfacial tension of PE/PA-6 is not very sensitive to variations of temperature. It should be mentioned that a die temperature of 250°C produced better laminar morphology and barrier properties. Thus, considering the minor improvement in mechanical properties, and taking into account both barrier and mechanical properties, a die temperature of 250°C is favored.

6.3.1.2. Effect of Screw Design and Screw Zone Temperature

Figure 6.43 reveals the effect of screw zone temperature and screw design on impact properties of HDPE/PA-6 blends. By lowering the temperature of zone 4 of the extruder from 250 to 230°C, the ultimate energy and force reduced. This follows the general trend observed for the effect of die temperature. Reducing the temperature of zone 4 from 230 to 225°C and applying the method of low screw zone temperature changes the direction of variations. Samples extruded using low temperature profile # 5 showed improved laminar morphology and extraordinary barrier properties, and show improved impact properties comparable to the PE0 matrix. This issue will be discussed in more details later.

In the same figure, the effect of screw design on impact properties is also presented. Within the experimental error of tests, the ultimate force and energy of samples obtained with different screw designs are similar. However, standard deviations for the impact properties of samples obtained with a metering screw, are larger, indicating the lack of sufficient homogeneity in samples. This observation is confirmed by morphological studies in section 6.1.1.5.



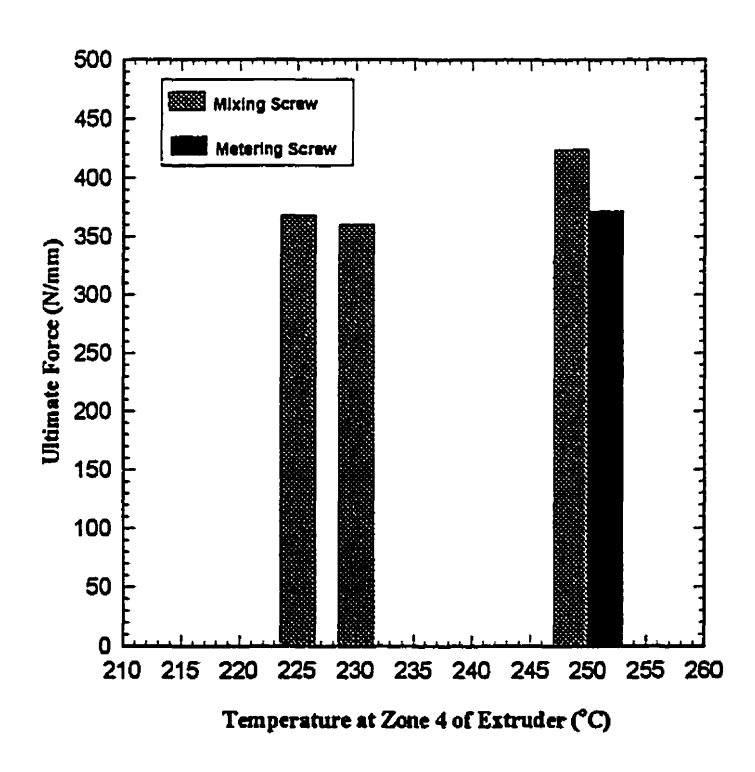


Figure 6.43: Variations of ultimate force and energy versus screw design and screw zone temperature for PE0/PE2//PA-6 (70/10/20 wt%) blends

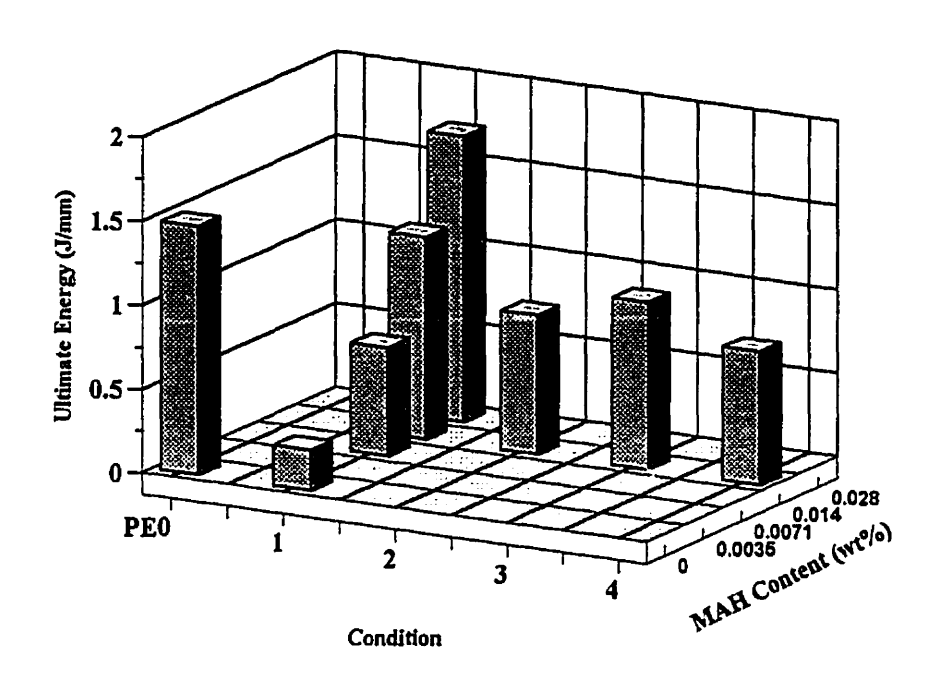
6.3.1.3. Influence of MAH Content of PE on Impact Properties

Raising the compatibilizer level improves the interfacial adhesion, which results in improved mechanical properties of blends (108,109). Figure 6.44 shows the effect of increasing the level of maleic anhydride on the ultimate energy and force of dry-blended samples. Blends without any compatibilizer give poor impact properties, while there is a substantial increase in ultimate energy and force at a MAH level of 0.007 wt%. As the level of MAH is raised further, the ultimate energy and force become comparable to those of matrix of PE. In section 6.2.1.6, it was shown that blends having 0.014 to 0.028 wt% maleic anhydride exhibit extraordinary barrier properties. Figure 6.44 reveals that the same levels of maleic anhydride, provides good mechanical properties.

Enhancement of mechanical properties by increasing the level of compatibilizer follows the general trend observed for homogenous blends. However, a principal difference exists between improvement of mechanical properties of laminar blends studied in this work and conventional blends. In homogeneous blends, increasing the compatibilizer level, enhances the deformation and break up of dispersed phase particles. Thus, it results in lower average particle size and better mechanical properties. On the other hand, in the case of laminar blends studied here, morphological results presented in section 6.1.1.8, showed longer and larger particles in the plane of extrusion for highly maleated blends. Therefore, it is evident that there is an important difference between the mechanisms of toughening in laminar blends and homogeneous blends. This issue will be discussed below.

6.3.1.4. Effect of Pre-compounding on Impact Properties of PE/PA-6 Blends

The twin-screw extruder is an efficient mixer for compounding of blend components. Precompounding of blend components in a twin-screw extruder is expected to yield smaller particles of the dispersed phase and improved distribution of interfacial agent at the interface. However, the purpose of using the twin-screw in this work has been to obtain good distributive mixing of the minor phase and of compatibilizer, but to limit the extent of dispersive mixing and size reduction. The special low shear screw configuration and low



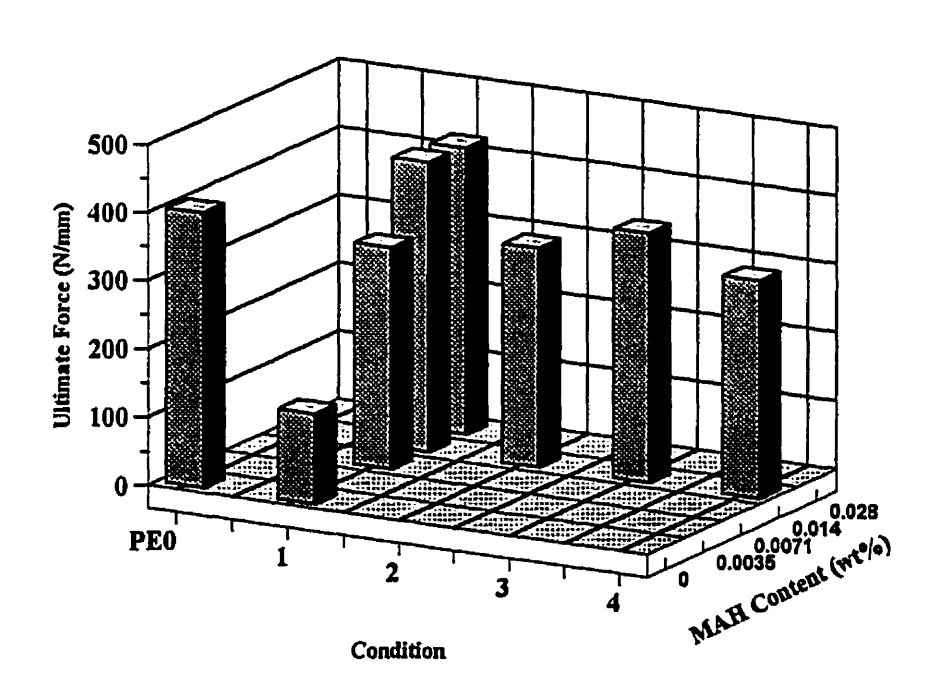


Figure 6.44: Influence of MAH content and pre-compounding on ultimate force and energy for HDPE/PA-6 blends

screw zone temperature in addition with other optimized processing conditions explained in section 4.2.2.1.2, are expected to help to achieve this purpose.

Results presented in Figure 6.44 indicating the effect of pre-compounding on the ultimate energy and force, show a reduction of impact properties by increasing the mixing intensity, which is opposite to the common trend observed for homogeneous blends. It shows that samples extruded with Condition # 1, which indicates dry blending, yield higher energy and force than twin-screw compounded blends. This appears to contradict theories of fracture mechanics which suggests that, in order to improve fracture toughness of the blends, particles of the minor phase should be as fine as possible. The resulting fine particles can distribute the applied stresses much better than large particles that can initiate large cracks and result in failure (172). Therefore, another explanation for the results should be found.

It is well known that the mechanical properties of fiber reinforced materials (173,174) and mica composites (175,176.) depends strongly on aspect ratio of the reinforcement. The most important property improvement attributable to increased fiber length is fracture toughness. Long fiber reinforced thermoplastics exhibit an order of magnitude higher impact strength than short fiber composites of similar composition. The increased impact strength of the long fiber materials is due to two major factors: reduction in the number of Griffin flaws and increased pullout force. Substantial increase in flexural and tensile moduli of mica composites have been reported at higher aspect ratios of mica particles (175,176).

During an impact event, fiber reinforced materials absorb energy via three major mechanisms: fiber breakage, fiber pullout, and matrix crack propagation. Reinforcing fibers form a three dimensional crack arresting network, which tends to shift failure modes to the more highly energy absorptive pullout and breakage modes. The end of each fiber, however, acts as a Griffin flaw and is, therefore, a crack initiation site. By increasing fiber length, the benefits of the crack arresting network are retained, while substantially (as much as ten or twenty-fold) reducing the crack initiation sites. The end result is a much

higher energy absorption. As well, the reduced number of crack initiation sites provides a much higher level of impact strength.

In the case of laminar blends with much larger particles in comparison to the conventional blends, it is possible to consider a similar mechanism of toughening. In this case, the dispersed phase particles operate similar to fibers or mica particles, and larger particles which provide less crack initiation sites will result in higher impact strength. According to this mechanism, larger particles are favored for improving both mechanical and barrier properties. We are not aware of earlier research on this aspect of laminar blends. In a later section, we shall discuss some quantitative aspects for the relationship between mechanical properties and dimensions of the dispersed phase particles.

6.3.1.5. Influence of PA-6 Content on Impact Properties of PE/PA-6 Blends

The effect of varying PA-6 content on morphology of laminar blends of HDPE and PA-6 was discussed in section 6.1.1.7. It was also shown in Figure 6.31 that changing PA-6 content from 10 to 20 weight percent reduces the permeability by one order of magnitude. Despite the large difference between toluene permeabilities of PE and PA-6 resins, the mechanical properties of the individual resins, shown in Tables 4.1 and 4.2, are of the same order of magnitude. Therefore, although, varying PA-6 content changes morphology and permeability substantially, it does not seem to affect impact properties considerably.

Figure 6.45 shows variations of ultimate energy and force versus PA-6 content for extruded samples using the mixing screw and low temperature profile #5. Blends incorporating higher PA-6 content exhibit better impact properties. By increasing the PA-6 content from 10 to 20 weight percent, the ultimate energy increases by 25%, while a minor improvement in ultimate force is observed. It is believed that the higher ultimate energy originates from incorporating larger PA-6 particles.

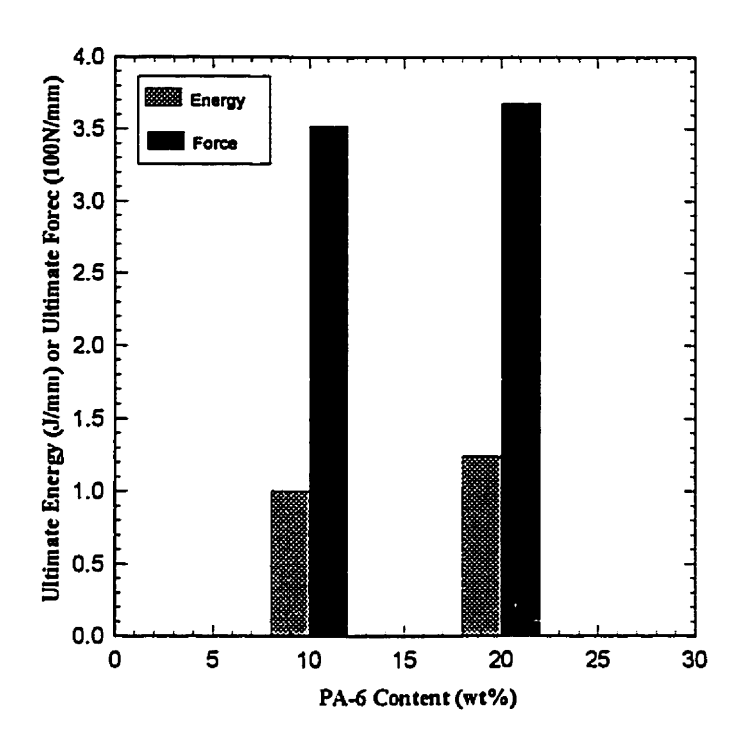


Figure 6.45: Variation of ultimate force and energy versus PA-6 content for HDPE/PA-6 blends.

6.3.1.6. Effect of Screw Speed on Impact Properties of PE/PA-6 Blends

Figure 6.46 shows variations of ultimate force and energy versus screw speed for non-compatibilized blends of PEO/PA-6 (80/20 wt%). The mixing screw, die exit gap size of 1mm and temperature profile # 3 were used for extrusion of these samples. It appears that, within the range of experimental error of measurements, screw speed does not influence impact properties significantly.

6.3.1.7. Influence of Adapter Angle on Impact Properties of PE/PA-6 Blends

Variations of adapter angle might affect the coalescence of minor phase particles of non-compatibilized blends. Previous studies have shown that for compatibilized blends, coalescence is inhibited (54, 69). Compatibilized laminar blends of PE and PA-6

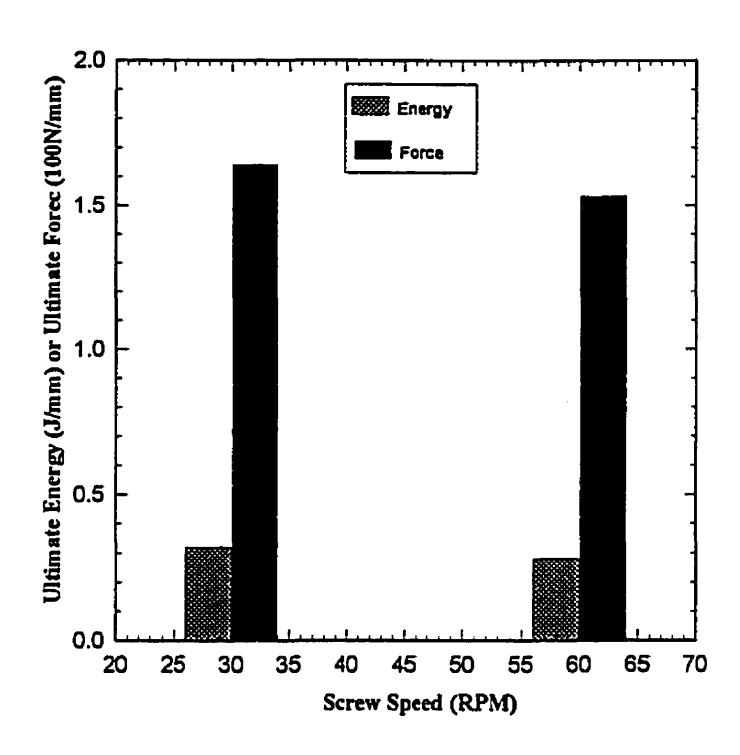


Figure 6.46: Variation of ultimate force and energy versus Screw Speed for HDPE/PA-6 blends

introduced in this work revealed superior barrier and good mechanical properties. Samples having the same composition of PE1/PA-6 (80/20 wt%) were extruded under identical processing conditions, except two adapter angles of 30 and 70°, were employed. Impact strength measurements showed variations of less than 10% for the ultimate energy and force. Thus, it is concluded that the effect of adapter angle on impact properties is small.

6.3.2. Impact Strength of ADMER/EVOH Blends

The load-deflection curve of ADMER and EVOH are quite dissimilar. Samples of load-deflection curves are given in Appendix F. The load-deflection curve of EVOH is similar to that of rigid-brittle materials. It has high slope and ultimate force but small deflection,

thus indicating small ultimate energy. Low slope and ultimate force, with large displacement and high energy, indicate ductility of ADMER resin. The effects of parameters that might influence impact strength but were not studied exclusively in previous works (18-20) are discussed here.

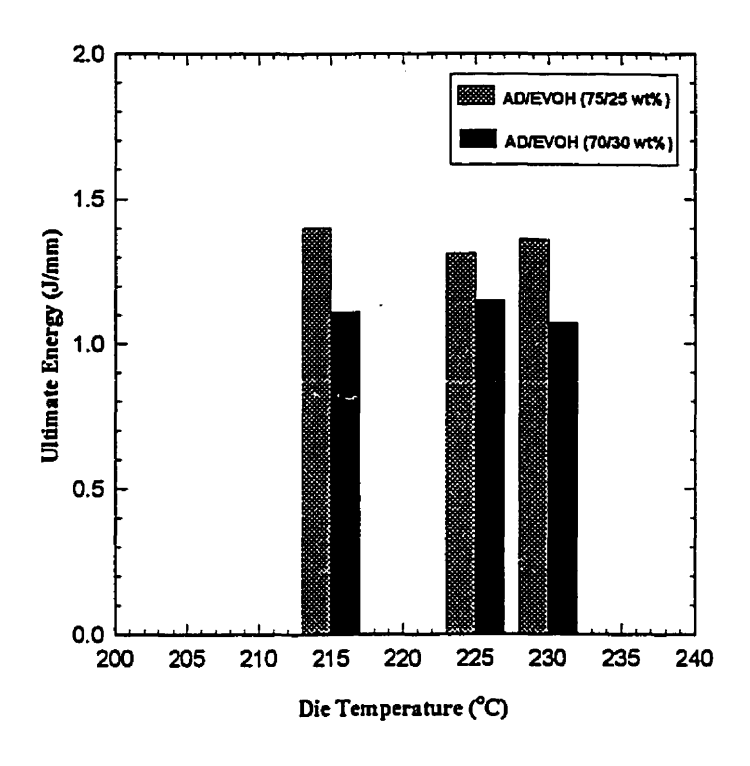
6.3.2.1. Effect of Die Temperature at Various Compositions

Load-deflection curves shown in Appendix F indicate that the sample shows a linear elastic deformation and then shatters. Figure 6.47 shows the variations of ultimate energy and force versus die temperature for ADMER/EVOH (75/25 and 70/30 wt%) blends. Ultimate energy and force for ADMER were measured as 2.5 J/mm and 537N/mm, respectively. High ultimate forces comparable to the matrix, and 40 to 50 percent reduction in ultimate energy of blends compared to ADMER, indicate brittle impact behavior.

It is evident that die temperature does not affect either ultimate energy or ultimate force considerably. By increasing the EVOH content from 25 to 30 weight percent, the ultimate energy is reduced about 20%. However, within the experimental error of the measurements, ultimate force does not change considerably. Lack of sufficient adhesion at the interface and brittle behavior of dispersed phase, i.e. EVOH, might be responsible for the inefficient impact performance of these blends.

6.3.2.2. Influence of Screw Design at Different Die Temperatures

Figure 6.48 shows the effect of screw design, at different die temperatures, on ultimate energy and force of ADMER/EVOH (75/25 wt%) blends. Both ultimate energy and ultimate force results indicate improvement of impact properties for the samples obtained with the mixing screw. The influence is more dramatic at lower die temperatures. Enhanced distributive and dispersive mixing of a mixing screw and longer residence time



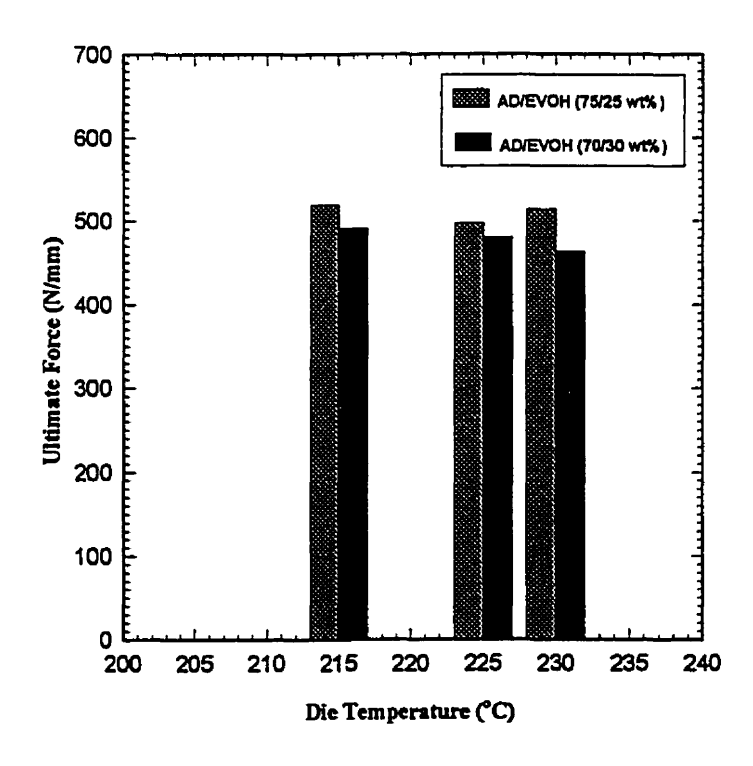
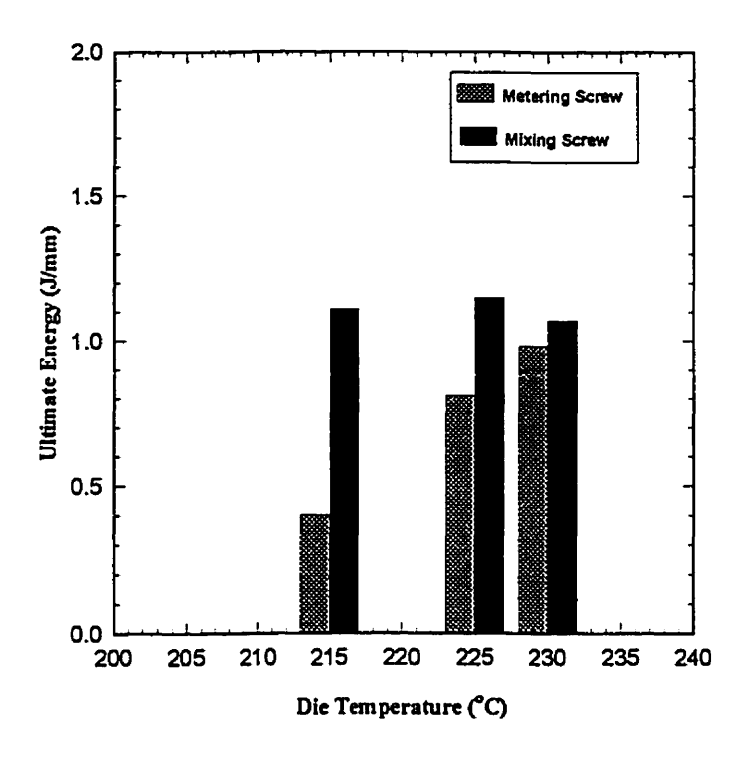


Figure 6.47: Variation of ultimate energy and force versus die temperature for various compositions of ADMER/EVOH blends



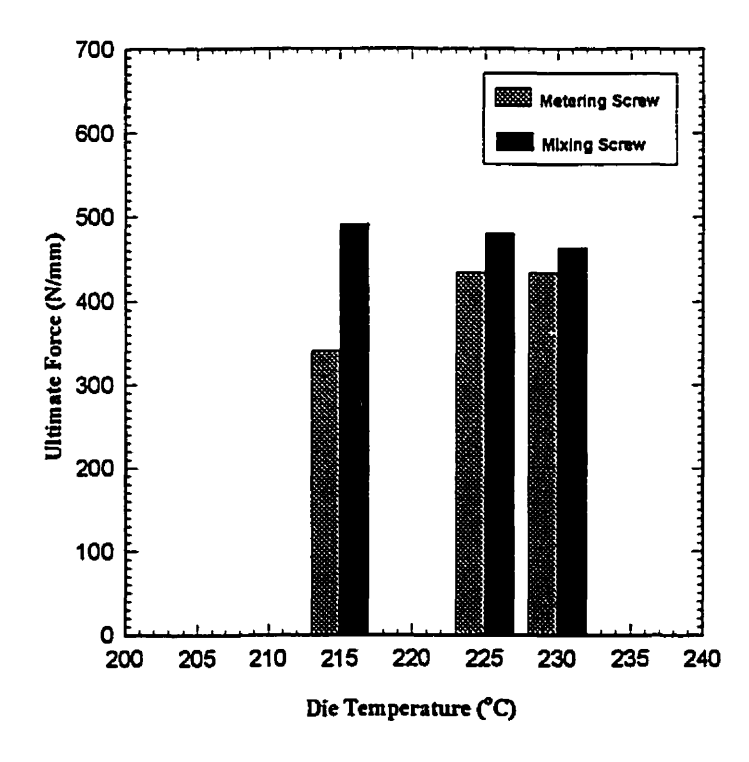


Figure 6.48: Variation of ultimate energy and force versus die temperature for various screw designs for ADMER/EVOH (75/25 wt%) blends

of the polymer melt inside the mixing screw might be possible explanations for the improved impact performance of these samples.

6.3.2.3. Effect of Cooling System on Impact Properties

It has been reported (177) that for a ductile material like polypropylene, the presence of a crystalline phase produces quite different stress-strain curve. The stress-strain curve changes from that of an uncrosslinked rubber, for low crystallinity, to one which is similar to that of crosslinked rubber, at high crystallinity. At very high degree of crystallinity, especially if large spherulites are present, the polymer exhibits a stress-strain curve of a brittle material in many cases.

Figure 6.49 shows the variation of ultimate energy and force versus cooling system for ADMER/EVOH (75/25 wt%) blends. A water-cooled sample that should have lower degree of crystallinity, yields considerably higher ultimate energy, but ultimate force is not increased substantially. Load-deflection curves presented in Appendix F show similar results; however, the water-cooled samples show higher forces and deflections. Although, it appears that water-cooling produces better mechanical properties, permeability results showed better performance for air-cooled samples. Further studies are needed to balance the crystallinity and particle size effects.

6.3.2.4. Influence of EVOH Content at Low Screw Temperature

In section 6.3.1, it was discussed that HDPE/PA-6 blends extruded at low screw zone temperature exhibit better mechanical performance than samples obtained with higher temperature profiles. It was also found that, by increasing the PA-6 content from 10 to 20 weight percent, improvement in impact properties was observed. However, in the case of ADMER/EVOH blends, the opposite trend is observed.

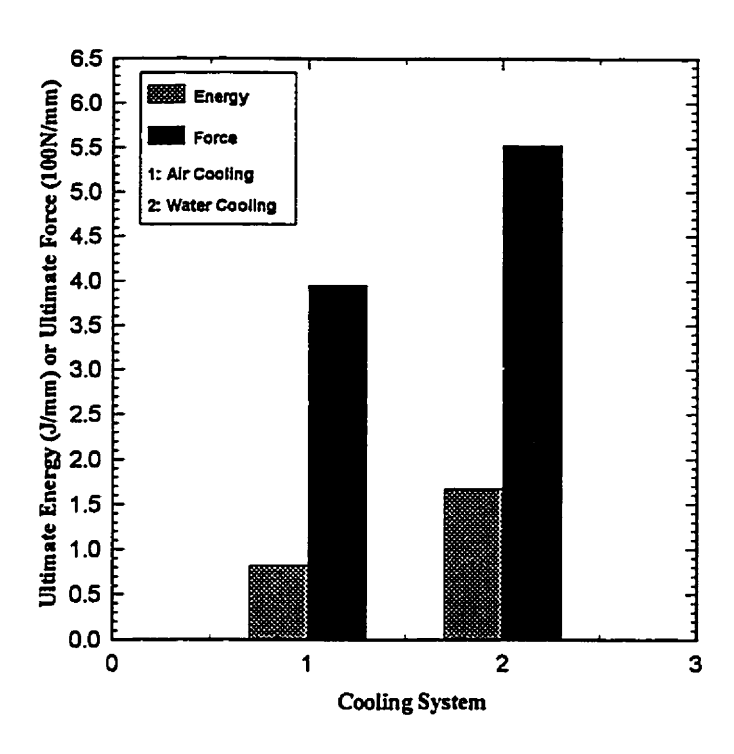


Figure 6.49: Variation of ultimate energy and force versus cooling systems for ADMER/EVOH (75/25 wt%) blends

Figure 6.50 shows the impact properties of ADMER/EVOH blends versus EVOH content. By increasing the EVOH content from 15 to 25 weight percent, a visible reduction in impact properties, especially in ultimate energy is indicated. Morphological analysis in section 6.1.2, revealed that contrary to PE/PA-6 blends, ADMER/EVOH blends extruded at low temperature do not produce large particles of the dispersed phase. Thus, it appears that these samples do not satisfy the requirements of the toughening mechanism proposed for PE/PA-6 laminar blends. Short residence time of the polymer melt inside extruder and die unit and insufficient amount of functionalized groups at the interface in addition to the brittle behavior of EVOH lead to weak mechanical performance of these blends. In order to develop laminar blends of PP and EVOH with good barrier properties, larger and longer particles of the EVOH dispersed phase are needed. Also, to achieve improved mechanical performance of these blends, better adhesion at the interface is necessary.

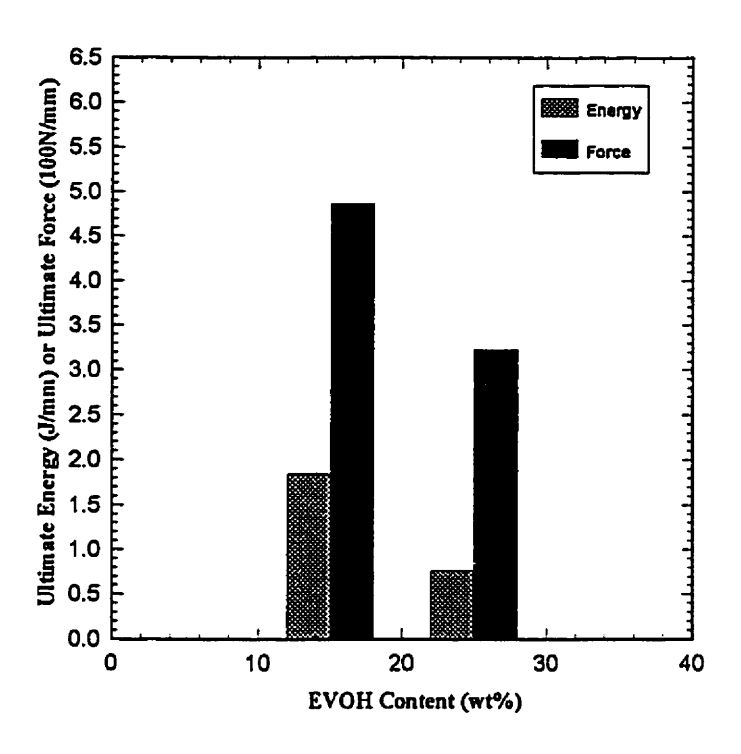


Figure 6.50: Variation of ultimate energy and force versus EVOH content for ADMER/EVOH blends extruded at low screw zone temperature.

6.4. Theoretical Prediction of Barrier and Mechanical Properties

6.4.1. Prediction of Permeability of Laminar Polymer Blends From Morphology

Higuchi (178) proposed the following equation to correlate the permeability of a composite (c) with the concentration and shape of dispersed phase (d):

$$p = 1 + \frac{(f+1)(p_2-1)\phi_d}{(p_2+f)-(p_2-1)\phi_d}$$
(6.8)

where $p=p_c/p_m$, $p_2=p_d/p_m$, m denotes the matrix, ϕ_d is the volume fraction and "f" is a shape factor.

This is a generalized form of the equation of permeability, which is useful to estimate the permeability of polymer blends with various morphologies. It reduces to the well-known equation of Maxwell, i.e. Equation (6.5), for spherical particles with f=2. Also, the series model, i.e. Equation (6.7), can be derived from this equation by assuming f=0. For f=1, it provides the Raleigh relationship for cylindrical particles (174):

$$p = \frac{(p_m + p_d) - \phi_d(p_m - p_d)}{(p_m + p_d) + \phi_d(p_m - p_d)}$$
(6.9)

Although there is fixed no physical definition for the shape factor of "f", it is an indication of dimensions and geometrical shape of particles of the dispersed phase. For convenience, we define as follows:

$$f = \frac{T}{L_1} + \frac{T}{L_2} \tag{6.10}$$

where T is the characteristic dimension of the particle in the direction of diffusion and L_1 and L_2 are the characteristic length of the particles in transverse directions, along a plane normal to T.

In the case of laminar morphology, that consists of laminates stacked in series, the shape factor can be expressed as:

$$f \approx 2\frac{T}{L} = \frac{2}{\alpha} \tag{6.11}$$

where L is the average length of a face of the platelets, T is the thickness, and α is the aspect ratio.

If one considers the tortuosity of series laminates as given in Equation (6.3), it can be seen that the shape factor "f" varies inversely with tortuosity, which is a commonly used parameter for characterizing the permeability of composite materials. Therefore, having the dimensions of dispersed phase, i.e. thickness and length, from image analysis results, enables us to calculate the shape factor "f". With such a value of "f" and the permeability values for individual resins, i.e. dispersed phase and matrix, it is possible to predict the permeability of a laminar blend from Equation (6.8). Alternatively, one can manipulate Equation (6.8), to find an expression for the shape factor of "f":

$$f = \frac{p_2(p-1) - p\phi_d(p_2 - 1)}{\phi_d(p_2 - 1) + (1 - p)}$$
(6.12)

Then, in order to evaluate the accuracy of this approach, the values of shape factor "f" may be calculated from Equations (6.11) and (6.12) and compared with each other. This provides a comparison of values of the shape factor as obtained from permeability data to values obtained by morphological measurements and associated image analysis. However, Equation (6.11) is valid for ideal conditions, where there is enough adhesion at the interface. In order to consider the effect of adhesion at the interface, which affects the barrier properties of the blends adversely, we introduce an efficiency factor " Λ " in equation (6.11) as follows:

$$f = 2\frac{T}{\Lambda L} \tag{6.13}$$

where $1 \ge \Lambda \ge 0$. Λ indicates adhesion at the interface and is inversely proportional to interfacial tension. Equation (6.13) reduces to Equation (6.11) for an ideal condition, i.e $\Lambda=1$. The value of Λ can be estimated by the ratio of "f" from Equation (6.11) to its value from Equation (6.12).

Tables 6.2 and 6.3 present the comparison between the "f" shape factor using these two methods for HDPE/PA-6 and ADMER/EVOH blends, respectively. For the PE/PA-6 system, p₂=0.004, and for ADMER/EVOH blends, p₂=0.000023 were calculated.

By comparing the "f" shape factors obtained from the two different methods, it is concluded that:

- Allowing for the experimental errors, especially in calculating the aspect ratio from image analysis, it appears that the calculated values are of the same order of magnitude, as the experimental values.
- The values of "f" shape factor obtained from the two methods are in better agreement in the case of ADMER/EVOH blends, i.e. Table 6.3. Shorter particles are observed in the micrographs of these blends. Thus, the measured length of particles and, consequently, the aspect ratio are estimated more accurately.
- For the PE/PA-6 blends that show superior barrier properties and dominant laminar morphology, the image analysis method underestimates the length of particles. In fact, the particles are so long that even at magnifications below 100X, the particles of PA-6 are longer than the entire length of the micrograph. Therefore, the calculated "f" values are larger than estimated from permeability measurements.
- For non-compatibilized blends, like X153702, the "f" values calculated from permeability measurements, are larger than values estimated from image analysis. It appears that the lack of adhesion at the interface, which is not considered in calculating "f" shape factor, using the image analysis method, is responsible for lower "f" shape factors.
- More accurate image analysis data are needed, especially incorporating both the length and width of layers and allowing for the non-uniformity of the layers and their distribution.
- -. Values in the last column in both tables, which can be considered as rough estimates for the values of "Λ", shows better agreement for ADMER/EVOH system. More accurate image analysis results for this system is responsible for this agreement.

Table 6.2: Comparison between "f" shape factors obtained from Equations (6.10) and (6.11) for HDPE/PA-6 blends.

Sample	фа	Aspect	"f" From	p=pc/pm	P _{exp} /P _{series}	"f" From	f 6.11/f 6.12
		Ratio (α)	Eq. (6.11)			Eq. (6.12)	
X133702	0.174	21	0.095	0.181	8.01	0.044	2.1
X143702	0.174	16	0.125	0.294	13.02	0.090	1.3
X1037012	0.174	34	0.059	0.141	6.24	0.031	1.9
X1337012	0.174	8	0.250	0.645	28.6	0.611	0.5
X1537012	0.174	107	0.018	0.025	1.1	0.0005	36.0
X1537022	0.174	122	0.016	0.025	1.1	0.0005	32.0
X1537052	0.174	67	0.030	0.058	2.57	0.008	3.7
X153702	0.174	48	0.042	0.447	19.79	0.199	0.2
T1337012	0.174	16	0.111	0.483	21.39	0.239	0.6
X533702	0.174	17	0.133	0.435	19.26	0.187	0.6
X1537011	0.086	43	0.046	0.218	4.87	0.023	2.0
X15ET012	0.174	51	0.039	0.041	1.81	0.004	9.8
X151B12	0.174	41	0.048	0.124	5.49	0.025	1.9
X151T012	0.174	13	0.154	0.447	19.8	0.199	0.8

Table 6.3: Comparison between "f" shape factors obtained from Equations (6.10) and (6.11) for ADMER/EVOH blends.

Sample	фа	Aspect Ratio (α)	"f" From Eq. (6.11)	p=p _c /p _m	P _{exp} /P _{series}	"f" From Eq. (6.12)	
WX51325	0.201	9.1	0.220	0.517	455	0.370	0.6
WX52325	0.201	8.2	0.244	0.409	360	0.211	1.1
WX53325	0.201	11.0	0.182	0.500	440	0.337	0.6
WT51325	0.201	14.7	0.136	0.443	390	0.251	0.6
X1437A2D	0.201	10.4	0.192	0.130	114	0.053	3.6
WX22330	0.245	16.4	0.123	0.357	392	0.228	0.6
WX52330	0.245	9.6	0.208	0.306	336	0.173	1.2
AX22330	0.245	10.0	0.200	0.189	207	0.085	2.3

-. Since Equations (6.11) and (6.12) did not allow for the nature of the interface and interphase for both compatibilized and non-compatibilized systems, we propose Equation (6.13) to account for those effects. More studies are needed for refinement of this equation. Obviously, other factors are important, since values of " Λ " are substantially larger than 1.0 in some cases.

6.4.2. Prediction of Elastic Modulus of Laminar Blends

In section 6.3.1.4, it was found that laminar blends of HDPE and PA-6 having larger particles of the dispersed phase exhibit improved impact properties. Also, it was suggested that the mechanism of toughening of laminar blends incorporating large particles

of PA-6 resembles that encountered with platelet reinforced systems, such as mica composites. In order to evaluate this hypothesis, it was decided to study the tensile properties of laminar blends and to employ modified models of predicting modulus of mica composites for prediction tensile modulus of laminar blends.

There have been a number of studies to predict the mechanical properties of mica composites (175, 176, 179.). These studies have shown that the flexural strength and modulus of mica composites increase rapidly as the aspect ratio of mica is raised up to a value of about 100, after which a plateau is obtained.

The modified rule of mixtures relationship can be written as:

$$E_c = V_f E_f (MRF) + (1 - V_f) E_m$$
 (6.14)

where:

 E_c , E_h = modulus of composite, flake and matrix respectively

 V_f = volume fraction of flake

The Modulus Reduction Factor (MRF) as modified for flakes by Padawar and Beecher (179) is given by:

$$MRF = \left(1 - \frac{\tanh u}{u}\right) \tag{6.15}$$

where

$$u = \alpha \left(\frac{G_m N_f}{E_f (1 - V_f)}\right)^{1/2}$$
(6.16)

 α is the flake aspect ratio, and G_m is the matrix shear modulus. This equation is based on a shear lag analysis representing the case for an isolated single flake, neglecting flake-flake interactions. The virtual work analysis of Riley (180), for fiber composites takes fiber interaction into account. Riley's treatment has been modified for a simple lap joint

(rectangle flakes) with the result that

$$MRF = 1 - \frac{\ln(u+1)}{u}$$
 (6.17)

where MRF includes the effects of flake-flake interactions and equals 1 for long ribbons with large overlapping areas. Equation (6.15) was modified by the efficiency factor K (K<1) on the basis of microscopic observations. The u values can be described by the equation:

$$u = K\alpha \left(\frac{G_m V_f}{E_f (1 - V_f)}\right)^{1/2}$$
(6.18)

K includes the origin of weakening due to misalignment, and non-uniformity of flake shape, size and distribution in the matrix. It also depends on the degree of adhesion between matrix and reinforcing material. Equation (6.18) reduces to Equation (6.16) for an ideal system (K=1).

If mica flakes are replaced with platelet particles of PA-6, the same analogy can be applied. However, there is two orders of magnitude difference between the modulus of mica and plastics. In the case of laminar blends, the modulus of PA-6 is about twice the modulus of HDPE. Therefore, instead of the substantial improvement achieved in modulus for mica composites by increasing the aspect ratio, it is expected that relatively minor improvement of modulus of laminar blends is achieved by increasing the aspect ratio of PA-6 particles.

Tensile moduli of individual resins as well as the blends were measured and are reported here. The shear modulus of HDPE was obtained from literature (181). The following values were used in the calculations:

 $E_m=702 MPA$

 $E_d=1210 MPA$

 $G_m=230 \text{ MPA}$

 $V_d = 0.1746$

K=1 (assuming ideal case)

For the dilute systems encountered in this work, the Padawar and Beecher equation, i.e. Equation (6.15) provides better results. Therefore, substituting numerical values in the appropriate equations yields:

 $u=0.200 \alpha$

MRF=1-(tanh u/u)

 $E_b = V_d \cdot E_d + (1 - V_d) E_m$

 $E_b=212.3 (MRF)+579.4$

The latter equation was applied for PEO/PE2/PA-6 (70/10/20 wt%) blends precompounded in the twin-screw extruder and extruded employing low screw zone temperature of #5. The results are presented in Table 6.4.

As the result show, good agreement is obtained between the calculated and measured values of tensile modulus. Calculated MRF values are close to 1 for samples representing high aspect ratios, while for the samples with smaller aspect ratios, smaller MRF values are obtained. Since there is only a small difference between the modulus of the dispersed phase and the matrix, improvement in modulus, even at high aspect ratios of more than 100, is not considerable.

Table 6.4: Comparison between predicted and measured elastic modulus for PE0/PE2/PA-6 (70/10/20 wt%) blends.

Sample	X151T012	X151B12	X15ET012	X1537012
α	13	41	51	107
и	2.6	8.2	10.2	21.4
MRF	0.620	0.878	0.902	0.953
Predicted Modulus (MPA)	711	766	771	782
Measured Modulus (MPA)	787	812	779	786

CHAPTER 7

CONCLUSIONS AND RECOMMENDATIONS

7.1. Conclusions

The material characteristics, processing conditions and flow field were manipulated in a manner that ribbon extrusion of polymer blends incorporating a polyolefin matrix such as high density polyethylene (PE) or polypropylene (PP), and a dispersed phase of a barrier polymer like ethylene vinyl alcohol (EVOH) or polyamide-6 (PA-6) produced samples exhibiting substantial (up to 45 times) improvement in barrier properties. The reason for the significant low permeability is the existence of laminar morphology in the extruded samples, where thin, large and long particles of the dispersed phase were generated in the plane of extrusion to produce a layered structure that formed a tortuous path for the diffusion of gases and solvents. The above was achieved and optimized by controlling the mixing and melting steps in the screw zone to maximize the size of melted particles of the dispersed phase, upon entering the die unit. In the die region, a special design incorporating converging and diverging sections, causes the large particles entering the die to be stretched in both directions (machine and traverse direction), thus producing platelets in the plane of extrusion. Large melted particles of the dispersed phase at the die entrance were formed by employing a special low temperature profile in the screw zone. This approach delayed the melting of the minor phase until it reached to the last zone of the extruder. It was also desirable to employ low shear rates, in order to minimize the particle breakup.

In order to carry out a systematic treatment of the above issues, it was necessary to obtain detailed, reliable information about the characteristics of the components, including viscosity ratio, interfacial tension and elasticity ratio. Also, it was necessary to conduct a

detailed experimental analysis of the relation between morphology, permeability and mechanical properties of the blends. The following conclusions are based on the results of a large number of experiments carried out under a wide range of processing conditions:

- 1. The most promising approach for the development of effective laminar structure in ribbon extrusion of immiscible polymer blends involves the use of a low temperature profile in the extruder to delay the melting process until the particles reach the last zone of the extruder, coupled with the stretching of the large particles entering the die in two directions by incorporating appropriate converging and diverging sections in the die.
- 2. Appropriate selection of components with large differences in melting range is desirable to obtain a broad processing window.
- 3. Viscosity ratios (dispersed phase/ matrix) close to unity, low interfacial tensions and small elasticity ratios (dispersed phase/ matrix) in the die region favour the development of laminar morphology.
- 4. Among the processing variables, screw design and die exit gap size have a significant influence on the morphology. The effects of screw speed, adapter angle, and cooling system are smaller.
- 5. Compatibilization of the HDPE/PA-6 blend through controlling the maleation level of polyethylene leads to improved mechanical and barrier properties. A maleation level between 0.014 and 0.028 wt% provides good mechanical and barrier properties. However, the proposed low extrusion temperature profile is important in achieving the desired barrier properties.
- 6. The interfacial tension measurements of PE/PA-6 system confirm that, from economical point of view, maleation level of 0.014-0.028 wt%, is close to the optimum value.
- 7. PVT studies verify that the Tait equation with appropriate parameters provides good prediction for the PVT behaviour of EVOH, maleated PP and PE, and blends

of PE and PA-6 resins. The Spencer-Gilmore equation of state provides better prediction of PVT behaviour of PA-6.

7.2. Recommendation for Future Work

The results of this work, in combination with previous efforts, contribute to the pool of knowledge regarding the preferred compositional and processing parameters for producing laminar morphology in ribbon extrusion of polymer blends. Still, many issues and questions require further classification. Therefore, the following recommendations suggests some important avenues of future research in this area:

- 1. An important application for high barrier plastic materials is fuel system tubing in the automotive industry. This work can be extended to tube extrusion in annular dies.
- 2. Reactive compatibilization may be useful. Reactive compatibilization can provide gradual lowering of interfacial tension, which might be helpful in avoiding drop deformation in the screw zone. Thus, maximum deformation would be achieved in the die region. Also reactive compatibilization may produce more stable structure than the non-reactive case.
- 3. The proposed techniques can be applied successfully to any pair of barrier polymer and polyolefins, with large difference in melting point and appropriate rheological and interfacial tension characteristics. It is recommended to evaluate these techniques for developing laminar morphology in PE/EVOH or PE/PET systems.
- 4. Using grades of polypropylene with slightly lower melting point and applying external lubricants to limit shear heating in the screw zone might be helpful in improving the barrier properties of PP/EVOH system. Also it appears, that the level of maleation that was used in this work, is not enough for producing good barrier and mechanical properties. Moreover, due to increased permeability of maleated PP to oxygen, it is recommended that other compatibilizer systems should be considered.

- 5. The use of external lubricants with the PE/PA-6 system could help to improve the barrier properties of twin-screw compounded blends. This approach is worthy of evaluation.
- 6. The method should be evaluated with the blow-moulding and film-blowing processes. It is evident that in these two processes, due to controlled stretching in both directions, there is a great possibility of extruding laminar morphology.

7.3. Original Contributions

The present work has introduced processing method in sheet extrusion of polymer blends that may lead to developing laminar morphology. Particular contributions include:

- A low temperature extrusion approach has been proposed. This approach in combination with special die design, produces laminar morphology in immiscible polymer blends.
- 2. Mechanical and barrier properties of HDPE/PA-6 laminar blends were improved by optimization of the level of maleation of PE.
- 3. Interfacial tension of PP/EVOH and PE/PA-6 system were measured, using the pendant drop and spinning drop techniques. Comparison between the two methods was done. Also the influences of temperature and maleation content of PE and PP on the interfacial tension were evaluated.
- 4. Experimental data were obtained regarding the PVT behaviour of EVOH, maleated PE and PE/PA-6 blends with various amounts of compatibilizer. Such data are not available in the literature. Thus, should be useful for the development and evaluation of equations of state and other thermodynamic relationships for compatibilized and non-compatibilized blends.

5. Various quantitative relationships adapted and evaluated for the estimation of permeability and tensile modulus of laminar blends on the basis of morphological information.

REFRENCES

- 1. A. Ajji and L. A. Utracki, *Polym. Eng. Sci.*, 36, 1574 (1996).
- 2. L. A. Utracki, Polym. Eng. Sci., 35, 2 (1995).
- 3. M. M. Alger, T. J. Stanley, and J. Day, in "Barrier Polymers and Strutures". Ch. 10, p.203, American chemical Society, Washington, DC, 1990.
- 4. F. Kerschbaumer, and B. Zeh, *Kunstsoffe*, 78, 1095, (1988)
- 5. L. B. Ryder, *Plastics Eng.*, 5, 41 (1984).
- 6. M. Harada, Plast. Eng., p.27, Jan. 1988.
- 7. W. Michaeli, Extrusion Dies: Design and Engineering, Hanser Publishers, Munich; Vienna; New York, 1984, p.266.
- 8. A. Rincon, A. N. Hrymak, J. Volachopoulas and J. Dooly, SPE Antec Tech. Papers, 55, 335 (1997).
- 9. R. Diluccio, and W. Del, "Laminates of Lamellar Articles and Polyolefins", *U.S.Patent No.4,416,942*, Issued November 22, 1983 to E. I. Du pont de Nemours & Co.
- 10. P. Mapleson, Modern Plastics, P. 418, Aug. 1992.
- 11. K. Miura, E. Mori, K. Yoshizumi, A. Hiraku, and T. Goto, *Toyota Technical Review*, 44, 1133 (1994).
- W. E. Walles, in "Barrier Polymers and Strutures". Ch. 14, p. 266, American chemical Society, Washington, DC, 1990.
- 13. H. Garmabi, M. R. Kamal, SPE Antec Tech. Papers, 55, 2687 (1997)
- 14. M. R. Kamal, H. Garmabi, S. Hozhabr, and L. Arghyris, *Polym. Eng. Sci.*, 35,41, (1995).
- 15. H. Garmabi, M.R. Kamal. SPE Antec Tech. Papers, 53, p.3182 (1995).
- 16. H. Garmabi, M. R. Kamal, Polyblend Conference, Oct. 1993,
- 17. M. R. Kamal, G. Lohfink, L. Arghyris, and S. Hozhabr-Ghelichi, "Process for Laminar Extrusion", U.S.Patent No.5,188,784, issued February 23,(1993).
- 18. G. Lohfink, Ph.D. Thesis, Dept. of Chemical Engineering, McGill University (1990).
- 19. S. Hozhabr-Ghelichi, M.Eng. Thesis, Dept. of Chemical Engineering, McGill University (1991).
- 20. L. Arghyris, M.Eng. Thesis, Dept. of Chemical Engineering, McGill University (1991).
- 21. G. W. Lohfink and M.R. Kamal, Polym. Eng. Sci., 33, 1404, (1993).
- 22. P.M.Subramanian and V.Mehra, *Polym. Eng.Sci.*, 27, 663 (1987).

- 23. P. M. Subramanian, Polym. Eng. Sci., 25, 483 (1985).
- 24. J.M. Torradas and D. Zhang, S.P.E. ANTEC Proc., Montreal, 1468 (1991).
- 25. P. M. Subramanian, "Process for Making Laminar Articles of polyolefin and Condensation Polymer", U.S.Patent No.4,410,482, issued Oct. 18, 1983.
- 26. P. M. Subramanian, "Laminar Articles of Polyolefin and a condensation Polymer", U.S.Patent No.4,444,817, issued Apr. 24,1984.
- 27. P. M. Subramanian, in "Barrier Polymers and Strutures". Ch.13, p.252, American chemical Society, Washington, DC, 1990
- 28. M. S. Lee, and Y. G. Cho, "Polyolefin based blend containing reactive low molecular weight compound and process for making the same" EU. Patent No. EP0526230B, issued May 1993.
- 29. D. R. Paul and S. Newman, "Polymer Blends", vol1, Ch.3, Academic Press, New York, (1978).
- **30.** J. W. Barlow and D. R. Paul, *Polym. Eng. Sci*, 21, 985, (1981).
- 31. M. R. Kamal, I. A. Jinah and L. A. Utracki, *Polym. Eng. Sci*, 24, 1337 (1984).
- 32. R. M. Barrer, J. A. Barrie and M. G. Rogers, J. Polym. Sci., Part A1, 2565 (1963).
- **33.** G.I. Taylor, *Proc. Roy. Soc.*, **A138**, 41 (1932).
- **34.** G.I. Taylor, *Proc. Roy. Soc. A146*, 501 (1934).
- **35.** R. G. Cox, J. Fluid Mech., **37**, 601 (1969).
- 36. G. I. Taylor, proc. 11th Int. Cong. Appl. Mech., Munich (1964).
- 37. C.E.Chaffey and H.Brenner, J.Colloid Interface.Sci.24,258 (1967).
- 38. A. Acrivos and T. S. Lo, J. Fluid Mech., 88, 641 (1978).
- 39. D.Barthes-Biesel and A.Acrivos, J. Fluid Mech., 61, Part 1, PP. 1-21, (1973).
- **40.** J.D.Buckmaster, *J. Fluid Mech.* 55, 385, (1972).
- 41. J.D Buckmaster, J. Appl. Mech. E, 40, 18, (1973).
- **42.** A. Acrivos and T.S.Lo, *J. Fluid Mech.* ,88 ,641 (1978).
- 43. S.Choi and W.R.Schowalter, Phys. of Fluids, Vol. 18, No. 4, (1975).
- **44.** R.W.Flumerfelt, J. *Colloid and Interface Sci.*, vol. 76, No. 2, pp. 330-349, (1980).
- 45. W.J.Philips, R.W.Graves, and R.W.Flumerfelt, J. Colloid and Interface Sci., vol. 76, No.2, pp. 350-371, (1980).
- 46. W. Bartok, and S. G. Mason, J. Colloid and Interface Sci., 14, 13, (1959).
- 47. G.K. Youngern and A. Acrivos, J. Fluid Mech. vol. 69, Part 2, pp. 377-403, (1975).
- 48. J.M.Rallison and A.Acrivos J. Fluid Mech., 89, 191-200, (1978).
- 49. H.A. Stone and L.G.Leal, J. Fluid Mech., vol. 206, pp. 223-263, (1989).

217

- 50. H.A.Stone and L.G.Leal J. Fluid Mech, 198, 399 (1989).
- 51. H.A.Stone and L.G.Leal, J. Colloid and Interface Sci., 133, No. 2, pp. 340 (1989).
- 52. L. Rayleigh, Proc. London Math. Soc. 10, 4 (1879); Proc. R. Soc., 29, 71 (1879).
- 53. S. Tomotika, *Proc. R. Soc.*, A150, 322 (1935); A153, 302 (1936).
- 54. L. A. Utracki, and Z.H. Shi, *Polym. Eng. Sci.*, 32, 1824 (1992).
- 55. H.B.Chin and C.D.Han, J. Rheology, 23, 557 (1979).
- **56.** J. F. Palierne, *Rheol. Acta.*, **29**, 204 (1990).
- 57. I. Delaby, B. Ernest, D. Froelich, and R. Muller, *Polym. Eng. Sci.*, 36, 1627 (1996).
- 58. I. Delaby, B. Ernest, D. Froelich, and R. Muller, Rheol. Acta, 34, 525 (1995).
- 59. I. Delaby, B. Ernest, Y. Germian, and R. Muller, J. Rheol., 38, 1705 (1994).
- 60. L. Stradins, and T. A. Osswald, *Polym. Eng. Sci.*, 36,979 (1996).
- 61. L. Levitt, and C. W. Macosko, , *Polym. Eng. Sci.*, 36,1647 (1996).
- 62. P. G. Ghodgaonkar, and U. Sundararaj, , *Polym. Eng. Sci.*, 36,1656 (1996).
- 63. F. D. Rumscheidt, and S. G. Mason, J. Colloid Sci., 16, 238, (1961).
- 64. W. J. Phillips, R. W. Graves, and R. W. Flumerfelt, J. Colloid Interface Sci., 76, 350, (1980).
- 65. H. P. Grace, Chem. Eng. Commun., 14, 225 (1982).
- 66. H.L.Goldsmith and S.G.Mason, J. Colloid and Intrface Sci., 17, 448 (1962).
- 67. C. Vander Reijden-stolk and A.Sara, Polym. Eng. Sci., 26, 1229 (1986).
- 68. S. Torza, R.G.Cox and S.G.Mason, J. Colloid and Interface Sci., 38, 395 (1972).
- 69. H.J.Karam and J.C. Bellinger, I & EC Fundamentals, 7,576 (1968).
- 70. H. Van Oene, J. Colloid Interface Sci., 40, 448 (1972).
- 71. J. M. Starita, Trans. Soc. Rheol., 16, 339 (1972).
- 72. F. Gauthier, H. L. Goldsmith and S. G. Mason, *Rheol. Acta*, 10, 344 (1971).
- 73. J. J. Elmendorp and R. J. Maalcke, *Polym. Eng. Sci.*, 25, 1a, 11 (1985).
- 74. F. Gauthier, H. L. Goldsmith and S. G. Mason, Trans. Soc. Rheol. Trans., 15, 297 (1971).
- 75. R. w. Flumerfelt, Ind. Eng. Chem. Fundam., 11, 312 (1972).
- 76. C. D. Han and K. Funatsa, J. Rheology, 22, 113 (1978).
- 77. J. D. Goddard, and C. Miller, J. Fluid Mech., 28, 657 ((1967).
- 78. R. Roscoe, J. Fluid Mech., 28, 273 (1967).
- 79. A. P. Plochocki, Polym. Eng. Sci., 26, 82 (1986).

- 80. A. P. Plochocki, Polym. Eng. Sci., 23, 618 (1985).
- 81. S. Wu, Polym. Eng. Sci., 27, 335 (1987).
- 82. G. Serpe, J. Jarrin, and F. Dawans, *Polym. Eng. Sci.*, 30, 553 (1990).
- 83. E.Bartram, H.L.Goldsmith and S.G.Mason, *Rheol.Act.*, 14, 776 (1975).
- 84. F. Gonzalez, B. D. Favis, P. J. Carreau, and C. Lavallee, *Polym. Eng. Sci.*, 33, 851 (1993).
- 85. B. D. Favis, J. Appl. Polym. Sci., 39, 285 (1990).
- 86. K. Min., and J. L. White, *Polym. Eng. Sci.*, 24,1327 (1984).
- 87. V. E. Dreval, G. V. Vinogradov, M. P. Zabugina, N. P. Krasnikova, E. v. Kotova, and Z.Pelzbauer, *Rheol. Acta*, 22, 102 (1983).
- 88. H. B. Chin and C.D. Han, J. Rheol., 24, 1 (1980).
- 89. H. B. Chin and C.D. Han, J. Rheol., 23,557 (1979).
- 90. Z.H. Shi, and L. A. Utracki, Polym. Eng. Sci., 32, 1834 (1992).
- 91. C. C. Chen, E. Fantan, K. Min, and J. L. White, *Polym. Eng. Sci.*, 28, 69 (1988).
- 92. H. Y. Tsai, and K. Min, Polym. Eng. Sci., 35, 619 (1995).
- 93. L. A. Utracki, and P. Toma, *Polym. Eng. Sci.*, 26,34 (1986).
- 94. C. David, M. Getlichermann, M. Trojan, *Polym. Eng. Sci.*, 32, 6 (1992).
- 95. V. Bordereau, Z. H. Shi, L. A. Utracki, P. sammut, and M. Carrega, *Polym. Eng. Sci.*, 32, 1846 (1992).
- 96. N. Tokita, Rubber Chem. Technol., 50, 292 (1977).
- 97. L. A. Utracki, J. Colloid Interf. Sci., 42, 185 (1973).
- 98. J. J. Elmendorp and A. K. Van der Vegt, *Polym. Eng. Sci.*, 26, 1332 (1986).
- 99. I. Fortenly and J. Kovar, *Polym. Compos.*, 9,119 (1988).
- 100. I. Fortenly and J. Kovar, Eur. Plym. J., 25, 317 (1989).
- 101. J. Lyngaae-Jorgenson and L. A. Utracki, makromol. Chem. Macromol. Symp., 48/49, 189 (1991).
- 102. L. A. Utracki, Polymer *Alloy and Blends-Thermodynamics and rheology*, Hanser Publishers, Munich-Vienna, New York 91989).
- 103. A. P. Plochoki, S. S. Dagli, and R. D. Andrews, *Polym. Eng. Sci.*, 30, 741 (1990).
- 104. S. Lim and J. J. white, *Polym. Eng. Sci.*, 34, 221 (1994).
- 105. C. C. Chen and J. J. White, *Polym. Eng. Sci.*, 33, 923 (1993).
- 106. H. Chuang and C. D. Han, J. Appl. Polym. Sci., 30, 165 (1985).
- 107. R. Holsti-Miettinen and J. Seppala, *Polym. Eng. Sci.*, 32, 868 (1992).

- 108. J. M. Willis and B. D. Favis, *Polym. Eng. Sci.*, 28, 1416 91988).
- 109. A. R. Padwa, Polym. Eng. Sci., 32, 1703 (1992).
- 110. K. Chandramouli and S. A. Jabarin, Adv. In polym. Tech., 14 No.1, 35 (1995).
- 111. A. Ajji and L. A. Utracki, *Polym. Eng. Sci.*, 36, 1547 (1996).
- 112. J. T. Lindt, *Polym. Eng. Sci.*, 25, 585 (1985)
- 113. J. T. Lindt and K. Ghosh, Polym. Eng. Sci., 32, 1802 (1992).
- 114. K. Ghosh, J. T. Lindt, and S. Lorek, SPE ANTECH Tech. Papers, 37, 232 (1991).
- 115. K. Y. Lee and C. D. Han, *Polym. Eng. Sci.*, 30, 665 (1990)
- 116. U. Sondararaj and C. W. Macosko, Polym. Eng. Sci., 32, 1814 (1992).
- 117. C. E. Scott and C. W. Macosko, *Polym. Bull.*, 26, 341 (1991).
- 118. L. Levitt and C. W. Macosko, SPE RETEC Polyblend 95 Proceedings, 325 (1995).
- 119. C. E. scott and C. W. Macosko, *Polym. Bull*, 26, 341 (1991).
- **120.** C. E. scott and C. W. Macosko, *Polym.*, 36, 3 (1995).
- 121. Personal communication with S. Y. Lee and S. C. Kim, Korea Advanced Institute of Science and Technology 1997.
- 122. Technical Information on EVAL® EP-F Series, EVAL® Company of Americal (1994).
- 123. J. Brandrup and E. H. immmergut, "Polymer Handbook", John Wiley, New York (1989).
- 124. J. M. Dealy and K. F. Wissbrun, "Melt Rheology and its Role in Plastics processing", Van Nostrand reinhold book, New York 1990.
- 125. N. G. Gaylord, J. Polym. Sci. Polym. Lett. Ed., 21, 23 (1983).
- 126. P. Zoller, P. Bolli, V. Pahud, and H. Ackerman, Rev. Sci. Instrum., 47, 948 (1976).
- 127. Manual of PVT Apparatus, Gnomix Inc. (1994).
- 128. M. R. Kamal, R. Lai-Fook, and N. R. Demarquette, *Polym. Eng. Sci.*, 34, 1834 (1994).
- 129. N. R. Demarquette and M. R. Kamal, Polym. Eng. Sci., 34, 1823 (1994).
- 130. S. H. Anastasiadis, J. K. Chen, J. T. Koberstein, A. F. Siegel, J. E. Sohn, and J. A. emerson, J. Colloid Interf. Sci., 119, 55(1987).
- 131. H. T. Patterson, K. H. Hu, and T. H. Grindstaff, J. Polym. Sci., Part C, 34, 31 (1971).
- D. D. Joseph, M. S. Arney, G. Gillberg, D. Hultman, C. Verdier, and T. M. Vinagre, J. Rheol. 36(4), 623 (1992).
- 133. S. Bashforth and J. C. Adams, "An attempt to test the Theory of Capillary Action", Cambridge University Press and Deighton, Bell and Co., London (1882).
- 134. N. R. Demarquette, , Ph.D. Thesis, Dept. of Chemical Engineering, McGill University (1994).

REFRENCES 220

- 135. B Vonnegut, Rev. Sci. Instrum., 13, 6 (1942).
- 136. H. M Princen, I. Y. Z. Zia, and S. G. Mason, J. Colloid Interf. Sci., 23, 99 (1967).
- 137. P. Than, L. Preziosi, D. D. Joseph and Arny, J. Colloid Interf. Sci., 124, 552 (1988).
- 138. Y. Seeto and L. E. Scriven, Rev. Sci. Instr., 53(11), 1757 91982).
- 139. C. D. Manning, M.Sc. Thesis, University of Minesota (1976).
- 140. R. S. Spencer, G. D. Gilmore, J. Appl. Phys., 20, 502 (1949).
- 141. R. Simha and T. Somcynsky, Macromolecules, 2, 342 (1969).
- 142. Y. X. Yi and P. Zoller, J. polym. Sci. Part B: Polym. Phys., 31, 779 (1993).
- 143. P. G. Tait, Phys. Chem., 2, 1 (1888).
- 144. C. Zhong, W. Wang, and H. Lu, *Macromol.* 28, 7737 (1995).
- 145. P. Zoller, J. Appl. Polym. Sci., 23, 1057 (1979).
- 146. P. Zoller, and H. H. Hoehn, J. polym. Sci. polym. Phys., 20, 1385 (1982).
- 147. A. F. Yee, Polym. Eng. Sci., 17, 213 (1977).
- 148. L. W. Kleiner, F. E. Karasz, and W.J. Macknight, *Polym. Eng. Sci.*, 19, 519 (1979).
- 149. M. R. Kamal, W. Frydrychowicz, and I. Ansari, in "High-Temperature Properties and Applications of Polymeric Materials" M. R. Tant, J. W. Connell, and H. L. N. Mcmanus, eds, American Chemical Scociety, Washington, DC (1995).
- 150. D. W. Van Krevelen, *Chimia*, 32, 279 (1978).
- 151. Y. X. Yi and P. Zoller, J. Appl. Polym. Sci., 31, 779 (1993).
- 152. P. Rodgers, J. Appl. Polym. Sci., 48, 1061 (1993).
- 153. S. Wu, "Polymer Interface and Adhesion", Marcell Dekker, Inc. New York, (1982).
- 154. M. R. Kamal and N. R. Demarquette, R. A. Lai-Fook, and T. A. Price, *Polym. Eng. Sci.*, 37, 813 (1997).
- 155. E. F. H. Cho, Ph.D. Thesis, Dept. of Chemical Engineering, McGill University (1992).
- 156. E. Helfand, and Y. Tagami, J. Polym. Sci. Polym. Lett., 9, 741 (1971).
- 157. E. Helfand, and Y. Tagami, J. Chem. Phys. 56, 3592 (1972).
- 158. J. W. Cahn and J. E. Hillard, J. Chem. Phys. 28, 258 (1958).
- 159. E. Helfand, S. M. Bhattacharjee, and G. H. Fredrickson, *J. Chem. Phys.* 91, 7200 (1989).
- 160. D. Broseta, G. H. fredrickson, E. Helfland, and L. Leibler, *Macromolecules*, 23, 132 (1990).
- 161. P. L. Shah, SPE Antec Tech. Papers, 50, 937 (1992).
- 162. D. H. Weinkauf and D. R. Paul, in "Barrier Polymers and Strutures". Ch.3, p.61, American Chemical Society, Washington, DC, 1990

REFRENCES 221

- 163. J. Sax. And J. M. Ottino, Polym. Eng. Sci., 23, 165 (1983).
- 164. J. C. Maxwell, "Electricity and Magnetism", 3rd edn, Vol. 1, Dover, New York (1904).
- 165. A. S. Michaels and H. J. Bixler, J. Polym. Sci., 50, 413 (1961).
- 166. R. M Barrer, J. A. Barrie, and M. G. Rogers, J. Polymer Sci. Part A 1, 2565 (1963).
- 167. L. M. Robeson, A. Noshay, M. Matzner and C. N. Merriam, *Angew. Makromol. Chem.*, 29/30, 47 (1973).
- 168. L. E. Nielsen, J. Macromol. Sci. (Chem) A15, 929 (1967).
- 169. H. B. Hopfenberg, D. R. Paul in, "Polymer Blends", D. R. Paul and S.Newman, eds., Vol.1, ch. 10, Academic Press, New York, 1978.
- 170. J. L. Roche and S. N. Kakarala in 'Instrumented Impact Testing of Plastics and Composite Materials' Kessler, Adams, driscls and Ireland, eds, P163, ASTM Publications, Baltimore (1986).
- 171. S. B. driscoll in 'Instrumented Impact Testing of Plastics and Composite Materials' Kessler, Adams, driscls and Ireland, eds, P24, ASTM Publications, Baltimore (1986).
- 172. W. H. Lee in 'Polymer Blends and Alloys' M. J. Folkes and P.S. Hope, eds., Blackie Academic and Professional, Glasgow 91993).
- 173. A. Youngs, SPE Antec Tech. Papers, 42, p5-c-1, (1995).
- 174. J. M. Charrier, Polym. Eng. Sci., 15, 731 (1975).
- 175. S. Inubushi, T. Ikeda, S. Tazuke, T. Satoh, Y. Terada, and Y. Kumagai, *J. Mater. Sci.*, 23, 1182 (1988).
- 176. J. Lusis, R.T. woodhams and M. Xanthos, Polym. eng. sci, 13, 139, 1973.
- 177. L. E. Nelson and A. F. Landel, "Mechanical Properties of Polymers and Composites" Secon edition, Marcel dekker, New York, 1994.
- 178. W. I. Higuichi and T. Higuichi, J. AM. Pharm. Assoc., Sci. Ed., 49, 598 (1960).
- 179. C. E. Padawer and N. Beecher, *Polym. Eng. Sci.*, 10,185 (1970).
- 180. V R. Riley, "Interaction Effects in Fiber composites", Polymer Series Conference, University of Utah, June 1970.
- 181. S. Casenave, A. Ait-Kadi and B. Riedl, Can. J. Chem. Eng., 74, 308 (1996).
- 2. Tadmor and C. G. Gogos, "Principles of Polymer Processing", John Wiley & sons, New York (1979).

Appendix A Detailed Design of Screw and Barrel of the Single Screw Extruder

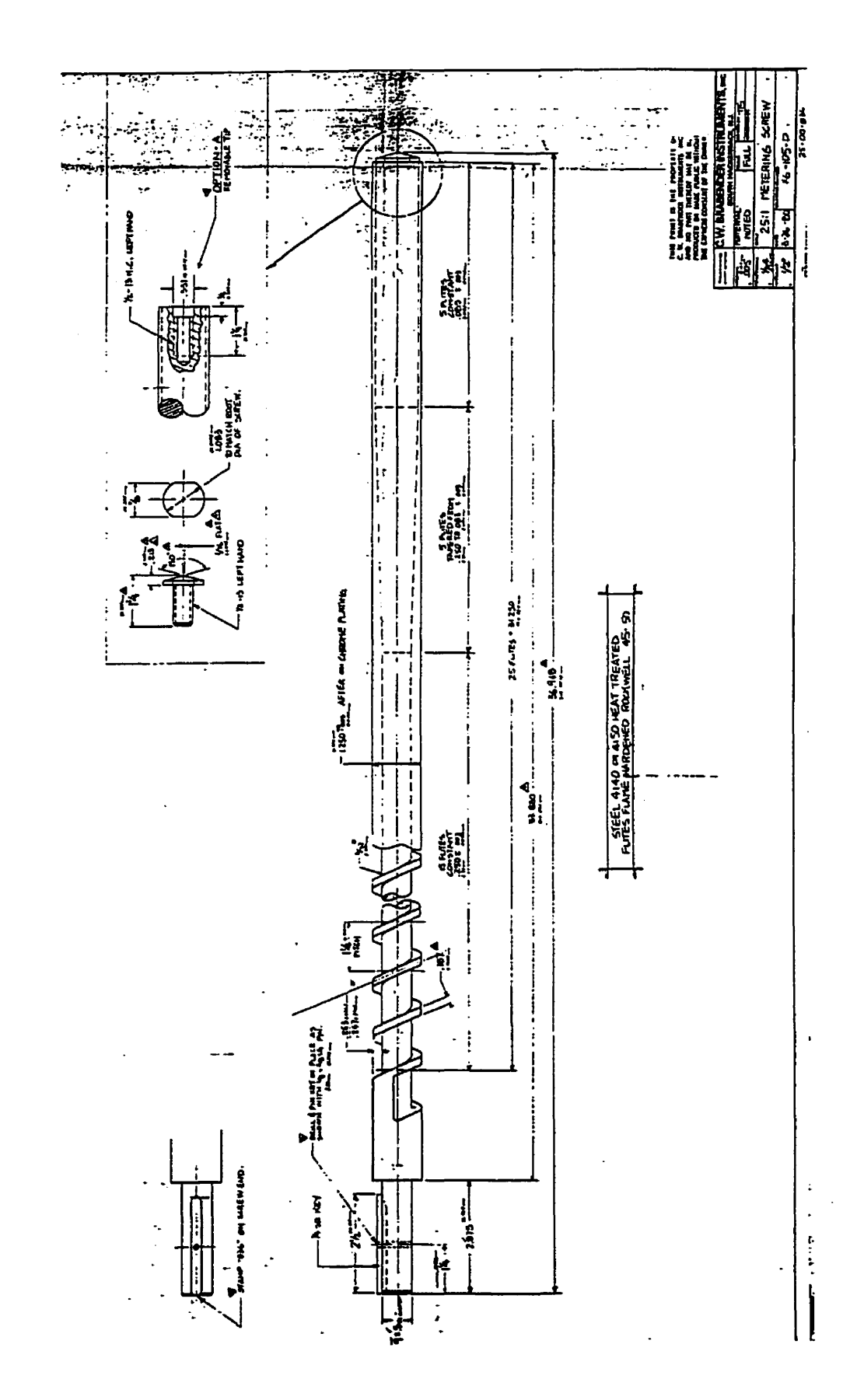


Figure A1: Detailed Design of Metering Screw (C. W. Brabender Instruments Inc)

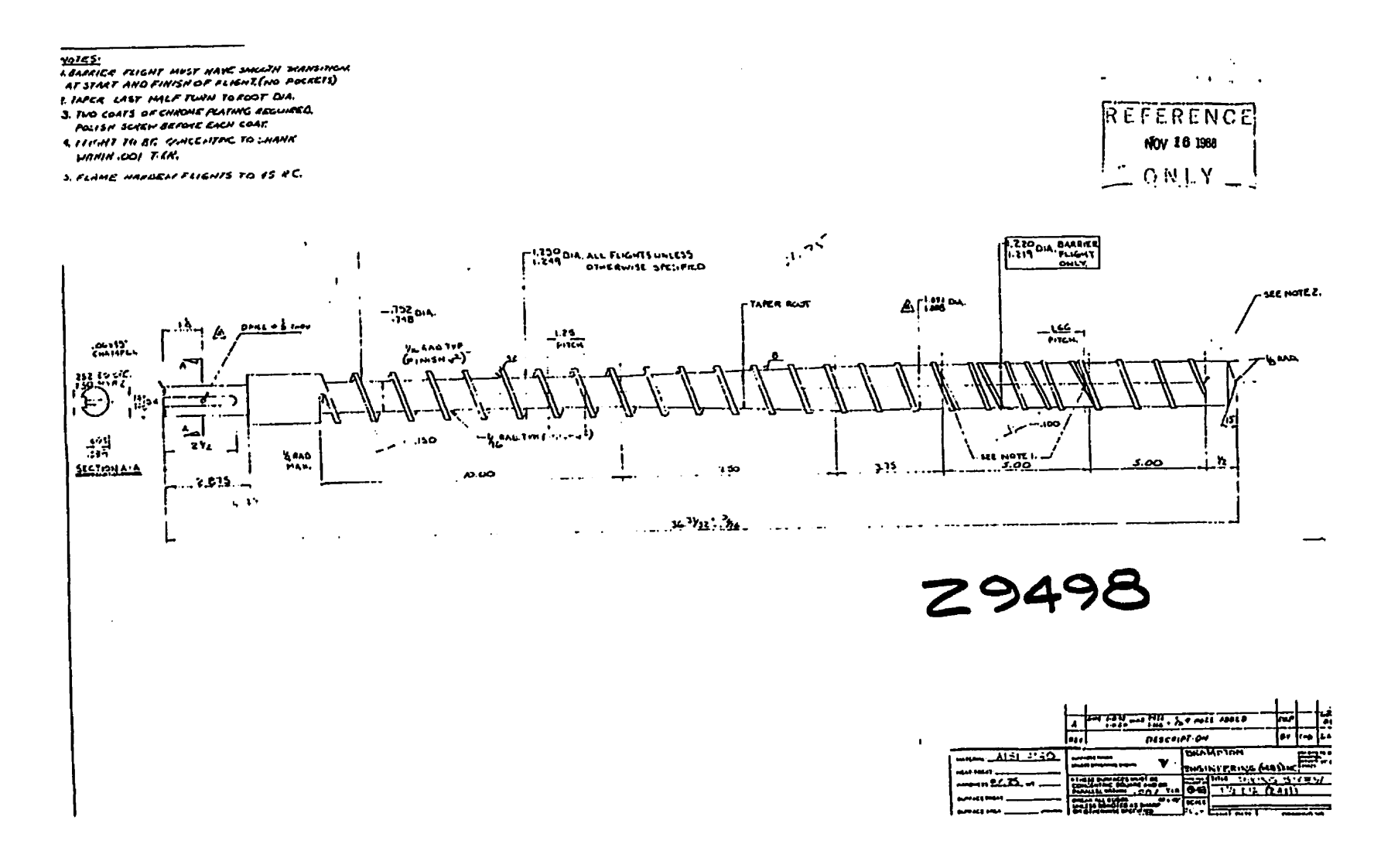


Figure A2: Detailed Design of Mixing Screw (C. W. Brabender Instruments Inc)

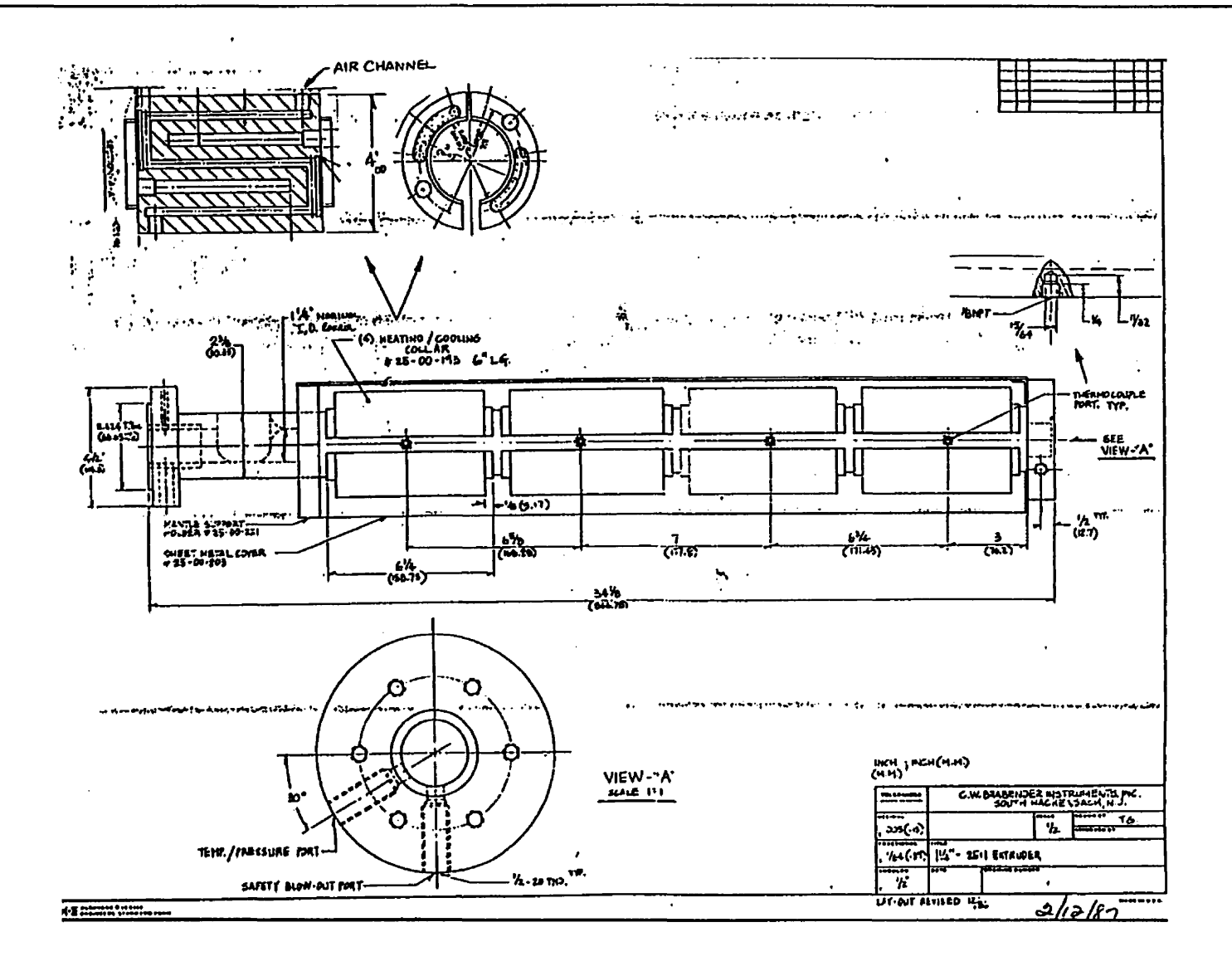


Figure A3: Heating/cooling Collar Design (C. W. Brabender Instruments Inc)

Appendix B

Sample Codes and Processing Conditions

Detailed processing conditions used to extrude PE/PA-6 and ADMER/EVOH blends are listed in Tables B1 and B2. On the basis of MAH content of individual resins presented in Table 4.2, and applying the additive rule, the maleation level for each blend can be calculated. Tables 4.3 and 4.4 present the description of temperature profiles used in Table B1 and Table B2, respectively.

Table B1: Processing conditions used for extruding HDPE/PA-6 blends:

Sample	Screw Design	Die Gap Size (mm)	Temperature Profile	Screw Speed (RPM)	Adapter Angle (°)	Composition (PE0/PE1/PE2/ PA-6 wt%)	Twin-Screw Compounding
X143712 (A06094)	Mixing	1.0	3	30	70	0/80/0/20	No
X143703 (C06214)	Mixing	1.0	3	30	70	70/0/0/30	No
X1437PE0 (D06214)	Mixing	1.0	3	30	70	100/0/0/0	N0
X143713 (A06234)	Mixing	1.0	3	30	70	0/70/0/30	No
X143723 (B06234)	Mixing	1.0	3	30	70	0/0/70/30	No

Table B1: Processing conditions used for extruding HDPE/PA-6 blends (continued):

Sample	Screw Design	Die Gap Size (mm)	Temperature Profile	Screw Speed (RPM)	Adapter Angle (°)	Composition (PE0/PE1/PE2/ PA-6 wt%)	Twin-Screw Compounding
X133702	Mixing	1.0	2	30	70	80/0/0/20	No
X143701	Mixing	1.0	3	30	70	90/0/0/10	No
X146702	Mixing	1.0	3	60	70	80/0/0/20	No
X143302	Mixing	1.0	3	30	70	80/0/0/20	No
X143312	Mixing	1.0	3	30	30	0/80/0/20	No
X533702	Mixing	0.5	2	30	70	80/0/0/20	No
X533703	Mixing	0.5	2	30	70	70/0/0/30	No
X5337012	Mixing	0.5	2	30	70	70/0/10/20	No
X5337052	Mixing	0.5	2	30	70	75/0/5/20	N0
X5437PE0	Mixing	0.5	3	30	70	100/0/0/0	No
T543302	Metering	0.5	3	30	30	80/0/0/20	No
T543312	Metering	0.5	3	30	30	0/80/0/20	· No
T533302	Metering	0.5	2	30	30	80/0/0/20	No
T533303	Metering	0.5	2	30	30	70/0/030	No
T5333052	Metering	0.5	2	30	30	75/0/5/20	No
T133301	Metering	1.0	2	30	30	90/0/010	No
T133302	Metering	1.0	2	30	30	80/0/0/20	No
T133303	Metering	1.0	2	30	30	70/0/0/30	No

Table B1: Processing conditions used for extruding HDPE/PA-6 blends (continued):

Sample	Screw Design	Die Gap Size (mm)	Temperature Profile	Screw Speed (RPM)	Adapter Angle (°)	Composition (PE0/PE1/PE2/ PA-6 wt%)	Twin-Screw Compounding
T1333052	Metering	1.0	2	30	30	75/0/5/20	No
T1333032	Metering	1.0	2	30	30	77.5/0/2.5/20	N0
T1333012	Metering	1.0	2	30	30	70/0/10/20	No
T143302	Metering	1.0	3	30	30	80/0/0/20	No
X133701	Mixing	1.0	2	30	30	90/0/0/10	No
X133703	Mixing	1.0	2	30	70	70/0/0/30	No
X1337032	Mixing	1.0	2	30	70	77.5/0/2.5/20	No
X1337052	Mixing	0.5	2	30	70	75/0/5/20	N0
X1437022	Mixing	1.0	3	30	70	60/0/20/20	No
X1437042	Mixing	1.0	3	30	70	40/0/40/20	No
X1337022	Mixing	1.0	2	30	70	60/0/20/20	No
X5337022	Mixing	0.5	2	30	70	60/0/20/20	No
T1333022	Metering	1.0	2	30	30	60/0/20/20	Yes
T133302	Metering	1.0	2	30	30	80/0/0/20	Yes
T1333022	Metering	1.0	2	30	30	60/0/20/20	Yes
T1333042	Metering	1.0	2	30	30	40/0/40/20	No
X1337012	Mixing	1.0	2	30	70	70/0/10/20	No
X1037012	Mixing	1.0	4	30	70	70/0/10/20	No

Table B1: Processing conditions used for extruding HDPE/PA-6 blends (continued):

Sample	Screw Design	Die Gap Size (mm)	Temperature Profile	Screw Speed (RPM)	Adapter Angle (°)	Composition (PE0/PE1/PE2/ PA-6 wt%)	Twin-Screw Compounding
X1037022	Mixing	1.0	4	30	70	60/0/20/20	No
X1537012	Mixing	1.0	5	30	70	70/0/10/20	No
X153701	Mixing	1.0	5	30	70	90/0/0/10	No
X153702	Mixing	1.0	5	30	70	80/0/0/20	No
X153703	Mixing	1.0	5	30	70	70/0/0/30	No
X1537052	Mixing	1.0	5	30	70	75/0/5/20	No
X1537022	Mixing	1.0	5	30	70	60/0/20/20	N0
X151T012	Mixing	1.0	5	30	70	70/0/10/20	Yes
X15ET012	Mixing	1.0	5	30	70	70/0/10/20	Yes (PE0 &PE2)
X1537011	Mixing	1.0	5	30	70	77.2/0/12.8/10	No
X103702	Mixing	1.0	5	30	70	80/0/0/20	No
X1037022	Mixing	1.0	4	30	70	60/0/20/20	No
X151TB12	Mixing	1.0	5	30	70	70/0/10/20	Yes

Table B2: Processing conditions used for extruding ADMER/EVOH blends (continued):

Sample	Screw Design	Die Gap Size (mm)	Temperature Profile	Screw Speed (RPM)	Adapter Angle (°)	Composition (AD/EVOH wt%)	Cooling System
AT52325 (EXS 3-4)	Metering	0.5	2	30	30	75/25	Air
AT22330 (E04033)	Metering	0.25	2	30	30	70/30	Air
AX22325 (D15013)	Mixing	0.25	2	30	70	75/25	Air
AX22330 (E20013)	Mixing	0.25	2	30	70	70/30	Air
AT52625 (EXS421)	Mixing	0.5	2	60	30	75/25	Air
WT52325 (EXS422)	Metering	0.5	2	30	30	75/25	Water
WT51325 (AXS504)	Metering	0.5	I	30	30	75/25	Water
WT53325 (CXS505)	Metering	0.5	3	30	30	75/25	Water
WT53625 (DXS429)	Metering	0.5	3	60	30	75/25	Water
WX51325 (EX1030)	Mixing	0.5	1	30	70	75/25	Water
WX52325 (DX1027)	Mixing	0.5	2	30	70	75/25	Water

Table B2: Processing conditions used for extruding ADMER/EVOH blends (continued):

Sample	Screw Design	Die Gap Size (mm)	Temperature Profile	Screw Speed (RPM)	Adapter Angle (°)	Composition (AD/EVOH wt%)	Cooling System
WX53325 (EX1117)	Mixing	0.5	3	30	70	75/25	Water
WX51330 (EX610)	Mixing	0.5	1	30	70	70/30	Water
WX52330 (EX925)	Mixing	0.5	2	30	70	70/30	Water
WX22330 (E26013)	Mixing	0.25	2	30	70	70/30	Water
WX53330 (EX1410)	Mixing	0.5	3	30	70	70/30	Water
X1437A2 D	Mixing	1.0	4	30	70	80/20	Air
X1437A1 D	Mixing	1.0	4	30	70	90/10	Water

Appendix C

Error Analysis of Experimental Measurements:

If a calculated result, y, is a function of $x_1, x_2, \dots x_n$

$$y = f(x_1, x_2, ...x_n)$$
 (C.1)

then the total error in determination of y is given by:

$$\varepsilon_{y} = \left[\left(\frac{\partial y}{\partial x_{1}} \varepsilon_{1} \right)^{2} + \left(\frac{\partial y}{\partial x_{2}} \varepsilon_{2} \right)^{2} + \dots + \left(\frac{\partial y}{\partial x_{n}} \varepsilon_{n} \right)^{2} \right]^{1/2}$$
(C.2)

where $\varepsilon_1, \varepsilon_2, ..., \varepsilon_n$ are the errors in the variables $x_1, x_2, ..., x_n$.

C.1. Capillary Rheometry

The true viscosity is given by the following equation:

$$\eta = \frac{\tau_w}{\gamma_w} = \frac{\Delta P/((2L/R) + e)}{((3+b)/4)\gamma_{app}} = \frac{960.R_d^3.((2L/R) + e))}{4\pi(3+b)R_b^4V_E}$$
 (C.3)

where F is the force in Kg, V_E is the speed of the piston in cm/min, R_d and R_b are the diameters of the die and barrel, respectively. The error associated with each variable is estimated to be:

<u>VARIABLE</u>	VALUE	ABSOLUTE ERROR	%ERROR
F	40-500 Kg	1	1
$\mathbf{V}_{\mathtt{E}}$	0.05-50 cm/min	0.01	0.1
$\mathbf{R}_{d.}$	0.76, 2.54 mm	0.01	0.7
R_b	0.95 mm	0.01	1
L/R	5-40	0.01	0.05

If Equation (C.2) is applied to Equation (C.3) using the above values for the errors of each variable, the estimated total error in viscosity measurements will be %7.2.

C.2. PVT Measurements

The specific volume is calculated using the following equation:

$$V = \frac{V_{init} + (L \times A)}{m}$$
 (C.4)

where V_{ini} is the specific volume at room temperature in cm³/g, L is the deflection of the LVDT in the PVT apparatus in mm, A is the effective area of the bellows in cm², and m is the weight of the sample in gram. The error in the measured variables is estimated to be:

VARIABLE	VALUE	ABSOLUTE ERROR	<u>%ERROR</u>
$\mathbf{V}_{ ext{ini}}$	1.0-1.2 cm ³ /gr	0.001	0.09
L	0.0-4.0 mm	0.001	0.025
A .	1.184	0.001	0.08
m	1.0-1.5 gr	0.00001	0.09

Appendix C XIII

The calculated error for the specific volume measurements is 0.2%.

C.3. Interfacial Tension Measurements

Interfacial tension, γ , is given by equation (C.5) as:

$$\gamma = \frac{\Delta \rho . \omega^2 . d^3}{32} = \frac{\Delta \rho \omega^2 P^3}{32n^3 M^3}$$
 (C.5)

where P is the number of pixels read from the screen of the computer, M is the magnification and the other variables have been already identified. The errors associated with each of the variables are estimated to be:

VARIABLE	VALUE	ABSOLUTE ERROR	%ERROR
Δρ	0.8-1.2	0.005	0.5
ω	20,000-25,000	100	0.4
P	150-300	2	1
n.	1.45-1.47	0.003	0.2
M	955-965	5	0.5

The estimated total error in interfacial tension measurements is %15.

C.4. Toluene Permeability Measurements

The toluene permeability is calculated using the following equation:

$$P = f.t.c.\frac{F}{A}$$
 (C.6)

where "f" is the calibration factor, P is the permeability in mg.mm/m².min, t is the thickness of the sample in mm, c is the concentration in mg/cm³, F is the flow rate of the carrier gas in cm³/min, and A is the area of the sample under the permeation. The error associated with each of the above variables are estimated to be:

VARIABLE	VALUE	ABSOLUTE ERROR	%ERROR
f	1.101×10 ⁻⁵	1×10 ⁻⁷	0.9
t	0.5-1.5 mm	0.01	1
c	0.1-1000 ppm	0.1	0.01
F	50 cm ³ /min	1	2.0
A	18.2 cm ²	0.2	1.01

The estimated total error in toluene permeability measurements is %5.16.

C.5. Oxygen Permeability Tension Measurements

The oxygen permeability is obtained using the following equation:

$$P = v.f.t \tag{C.7}$$

where P is the permeability in cm³.mm/m².day.atm, v is the voltage in mv, f is a factor which depends on the area and the resistor used in the apparatus, and t is the thickness in mm. The errors associated with each of the variables are estimated to be:

VARIABLE	VALUE	ABSOLUTE ERROR	%ERROR
v	0.01-1 mv	0.005	5
f	53	0.5	0.94
t	0.5-1.5 mm	0.01	1.0

Appendix C

Thus, it is estimated that a total error of 6.94% is associated with oxygen permeability measurements.

C.6. Impact Strength Measurements

The impact strength of the samples are obtained using the following relationship:

$$E = F.D/t (C.8)$$

XV

where E is the impact energy in $\mathrm{ft.lb_f}$, F is the force measured by the force transducer in lb, D is the deflection in mil, and t is the thickness of the sample in mm. It should be mentioned that the presence of the "t" as the denominator in Equation (C.8), indicates that the value is normalized for the thickness of 1 mm. The errors associated with each variable is estimated to be:

<u>VARIABLE</u>	VALUE	ABSOLUTE ERROR	%ERROR
F	10-150	1	1.3
D	50-300 mil	1	1
t	0.5-1.5	0.01	1

The estimated total error in impact strength measurements is estimated to be %3.3.

7. Image Analysis

The error in determination of aspect ratio and particle area using the image analysis could not be calculated, but may be significant. The main limitation of the image analysis that can introduce considerable error in the results, is the wide range of particle sizes. In some samples, especially samples having dominant laminar morphology, the micron size particles

exist with the mm size particles, simultaneously. The above makes the image analysis results to be associated with larger errors. Also, due to the coarse morphology of these blends, it appears that analysing a sample with area of about 5 mm² is not a good representative of the sample.

Appendix D

Normalization Procedure for Impact Tests

ASTM method D4272-85 report points out that impact tests are comparable only for specimens with thickness that differ by no more than ± 15%. Since we are dealing with higher variations in thickness of specimens, a normalization method, explained in this section, was used to compare the impact strength of samples with various thicknesses. In order to keep the same conditions that were employed for extruding the blends, extrusion rather than compression molding was used to produce samples with different thicknesses. To obtain specimens with various thicknesses, the speed of the take off system was varied over a wide range. The normalization was done for both the PEO resin and PEO/PE2/PA-6 (60/20/20 wt%) blend. Specimens with various thicknesses were tested and the ultimate force and the energy were plotted versus thickness in Figure D1 and Figure D2 for PEO and the blend, respectively. A least square curve fitting was used to obtain the linear relationship between the variables. The following equations were obtained:

PE0:

$$F=432.2t-39.3$$
 $r^2=0.9928$ (D.1)

$$E=1.384t-0.002$$
 $r^2=0.9783$ (D.2)

PE0/PE2/PA-6 (60/20/20 wt%) blend:

$$F=598.5t-199.1$$
 $r^2=0.9748$ (D.3)

$$E=2.46t-1.20$$
 $r^2=0.9728$ (D.4)

where F is the ultimate force in Newton; E is ultimate energy in Joules, and t is thickness in mm.

Appendix D XVIII

Then assuming that all the blends follows the same relationship as the tested blend, i.e. PE0/PE2/PA-6 (60/20/20 wt%) blend, and having the thickness of specimen and measured values of force and energy, the following equations were used to obtain the values for a specimen with thickness of 1 mm:

$$F_{1mm} = F_t \cdot \frac{F_{N,1mm}}{F_{N,t}}$$
 (D.5)

$$E_{1mm} = E_t \cdot \frac{E_{N,1mm}}{E_{N,t}} \tag{D.6}$$

where F_{lmm} and E_{lmm} are the normalized values of force and energy, respectively, F_t and E_t are the measured values, $F_{N,lmm}$ and $E_{N,lmm}$ are calculated values for thickness of 1 mm from Equations (D.3) to (D.4) for the reference tested sample with thickness of 1 mm, and $E_{N,t}$ and $F_{N,t}$ are those values for thickness of t mm.

It should be mentioned that, as different draw down ratios and various thicknesses might lead to different orientation and crystallinity, care must be taken in extrapolating these data.

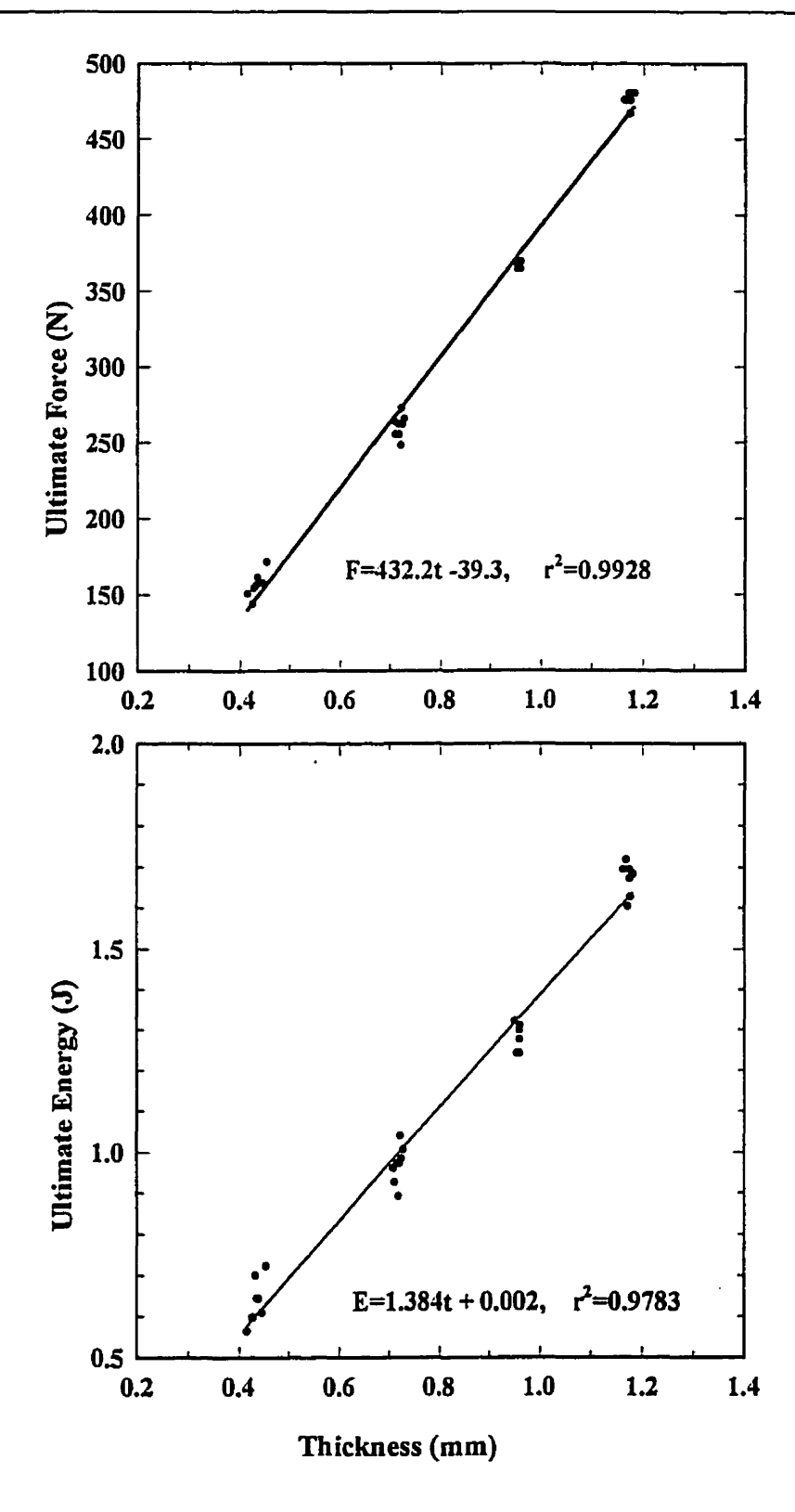


Figure D1: Normalization curves for ultimate energy and ultimate force for PE0

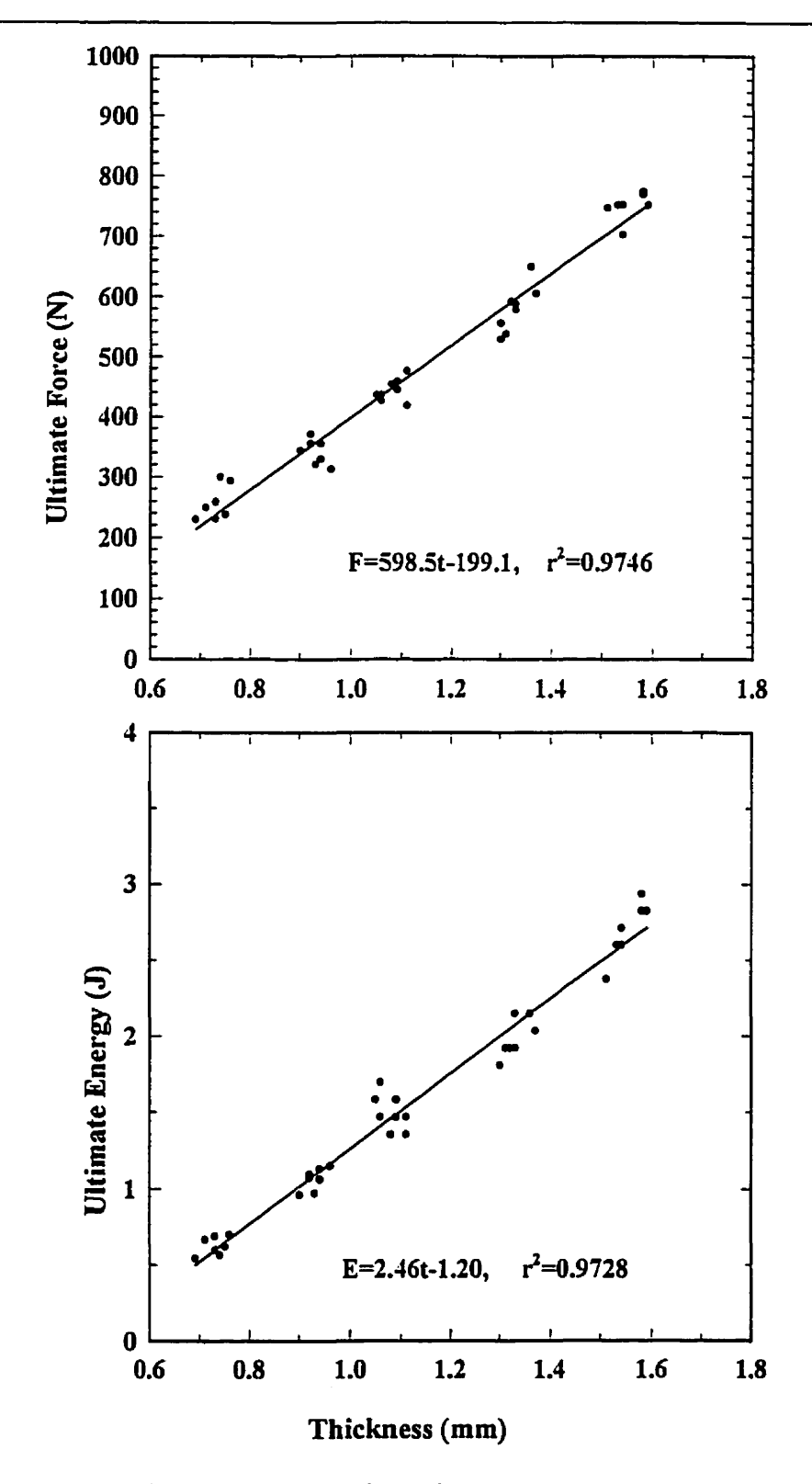


Figure D2: Normalization curves for ultimate energy and ultimate force for PE0/PE2/PA-6 (60/20/20 wt%) blend

Appendix E

Calculation of Shear Rates in Different Parts of the Die

The following equations have been used to estimate the shear rate in different parts of the die (182):

Tube:

$$\dot{\gamma}_{w} = \left(\frac{3n+1}{4n}\right) \left(\frac{4Q}{\pi R^{3}}\right) \tag{E.1}$$

Slit:

$$\dot{\gamma}_{w} = \left(\frac{2+b}{3}\right) \left(\frac{6Q}{H^2W}\right) \tag{E.2}$$

where "n" is the power law index, "b" is the Rabinowitsch correction factor (b=1/n), Q is the volumetric flow rate, R is the diameter of the tube, and H and W are the height and the width of the slit, respectively. Using one of the above equations, a range of shear rate is estimated for the converging and diverging section of the die. The power law approximation has been used for both systems. Table E.1 shows the Rabinowitsch correction factor (b=1/n) for PE/PA-6 system. Different values of "n" have been used for the correspondent shear rates. For the ADMER/EVOH system a value of 0.4 has been used for calculations (19).

Although, the mass flow rates measured during the different experimental runs, were not identical, but they can fairly be represented by an average value with standard deviation of less than 10%. The PVT data obtained in section 5.1 is used to calculate the volumetric flow rate at the temperatures and pressures inside the die. Based on the experimental data during the extrusion runs, average pressures of 700 psi (4.8 MPA) for

Table E.1: Rabinowitsch correction for PE and PA-6 resins

Shear Rate (s ⁻¹)	0.73	1.46	3.65	7.3	14.6	27.55	55.1	137.8	275.5	551	1371
Temp.	-					PE0					
230	1.4	1.54	1.62	1.69	1.78	2.08	2.2	2.3	2.3	2.4	2.7
250	1.52	1.58	1.71	1.73	1.76	2.0	2.05	2.2	2.2	2.5	2.5
270	1.48	1.7	1.68	1.75	1.75	1.9	1.95	2.0	2.2	2.3	2.6
	PE1										
230	1.12	1.31	1.48	1.54	1.55	1.89	1.83	1.95	2.2	2.46	2.5
250	1.2	1.42	1.53	1.57	1.63	1.85	1.75	1.9	2.2	2.4	2.4
270	1.26	1.5	1.6	1.56	1.57	1.80	1.83	1.84	1.95	2.3	2.5
						PE2					
230	1.34	1.47	1.56	1.66	1.69	2.0	2.1	2.3	2.2	2.3	2.6
250	1.4	1.53	1.6	1.61	1.67	1.9	2.0	2.1	2.2	2.4	2.4
270	1.47	1.62	1.63	1.68	1.7	1.8	1.85	1.96	2.1	2.4	2.6
	PA-6										
230	1.0	1.09	1.17	1.25	1.3	1.6	1.5	1.7	2.1	2.6	2.9
250	0.97	1.1	1.2	1.14	1.2	1.60	1.65	1.6	1.7	2.4	2.8
270	1.1	1.2	1.2	1.3	1.25	1.4	1.42	1.45	1.52	1.7	2.2

Table E.2: Estimated Shear Rates in Different parts of the Die Unit

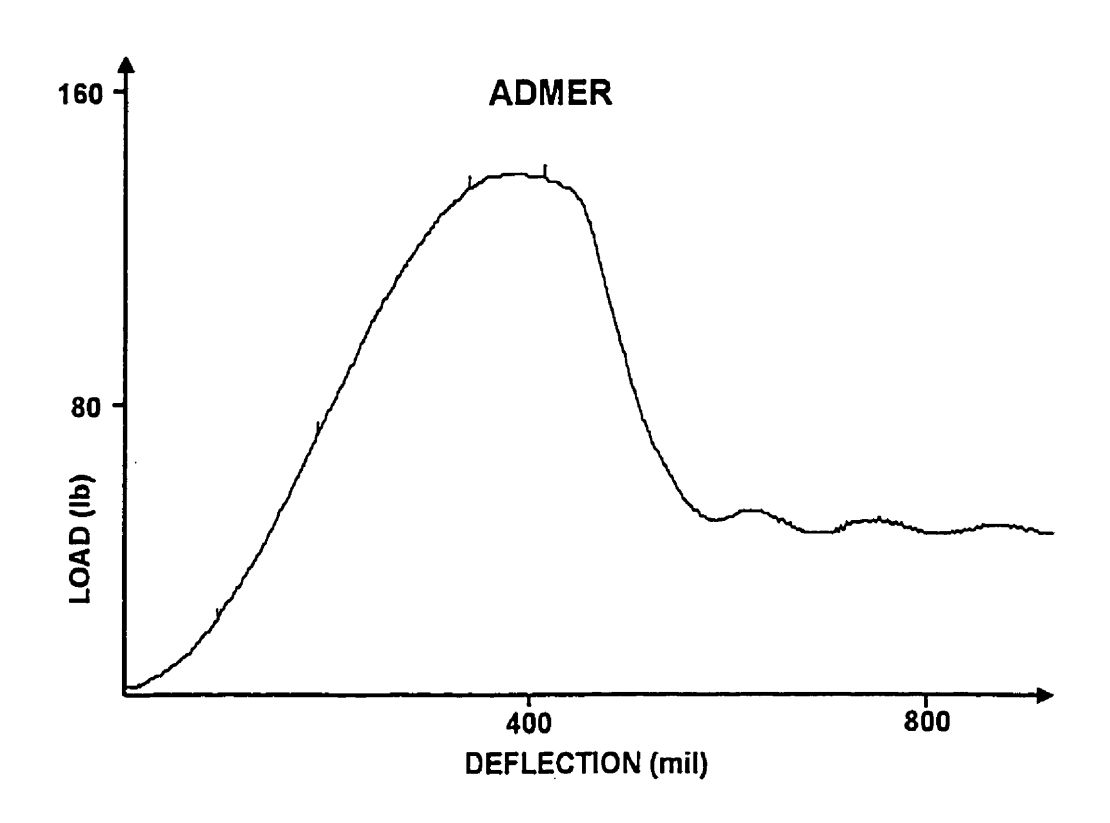
Part of the Die ¹	Shear Rate (PE/PA-6)	Shear Rate (ADMER/EVOH)
A	0.5-18.8	0.5-19.4
В	18.8	19.4
С	18.8-63.6	19.4-65.5
D	13.2-159.2	14.1-168.7
E	13.2	14.1
F	133.7	141.8

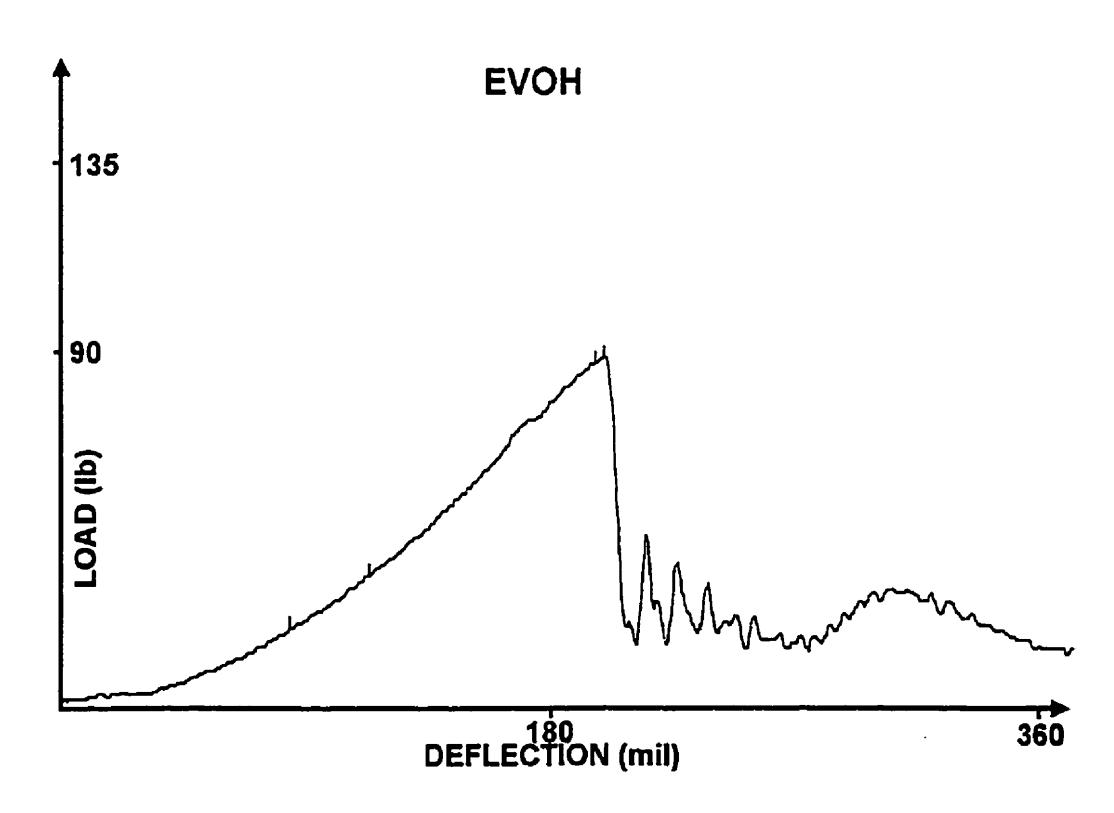
1- refer to Figure (4.6)

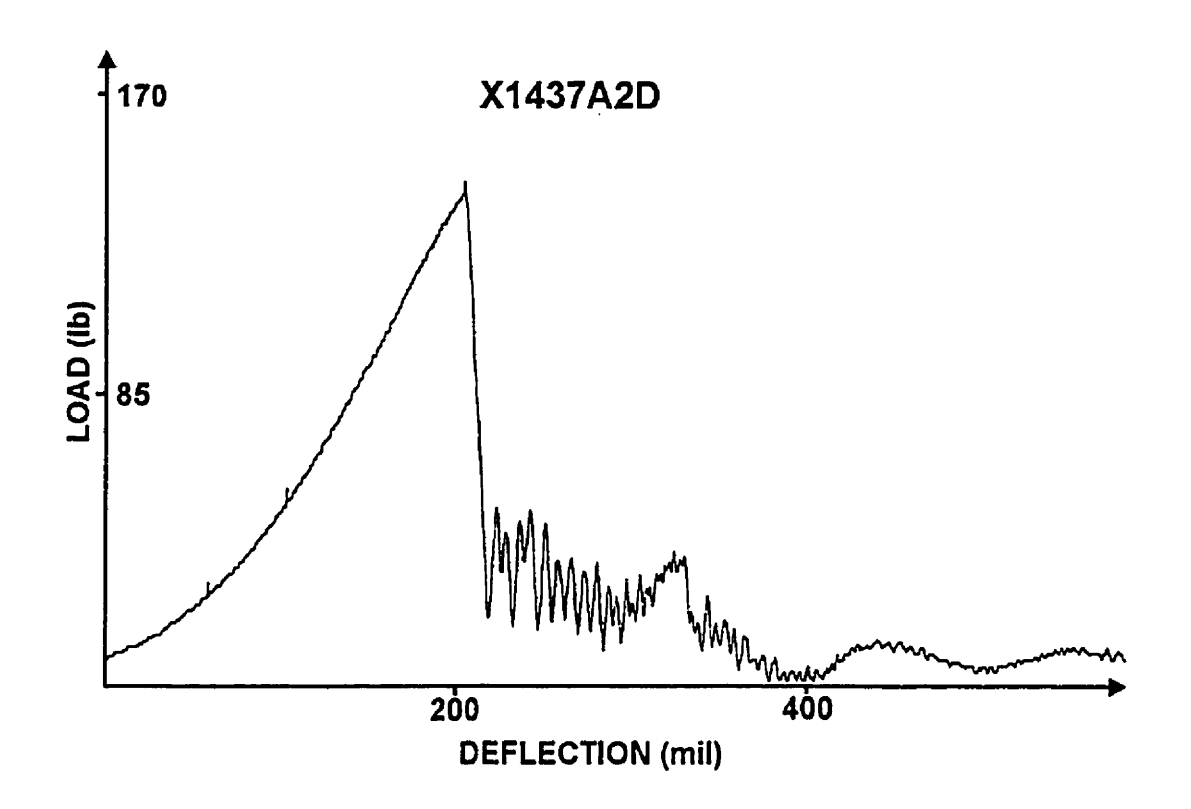
the PE/PA-6 system and 500 psi (3.4 MPA) for the ADMER/EVOH system were considered. The volumetric flow rates were calculated as 1.29 and 1.19 ccm³/sec for the PE/PA-6 (80/20 wt%) and ADMER/EVOH (75/25 wt%) systems, respectively. Table E.2 shows the estimated shear rates in different parts of the die for both systems.

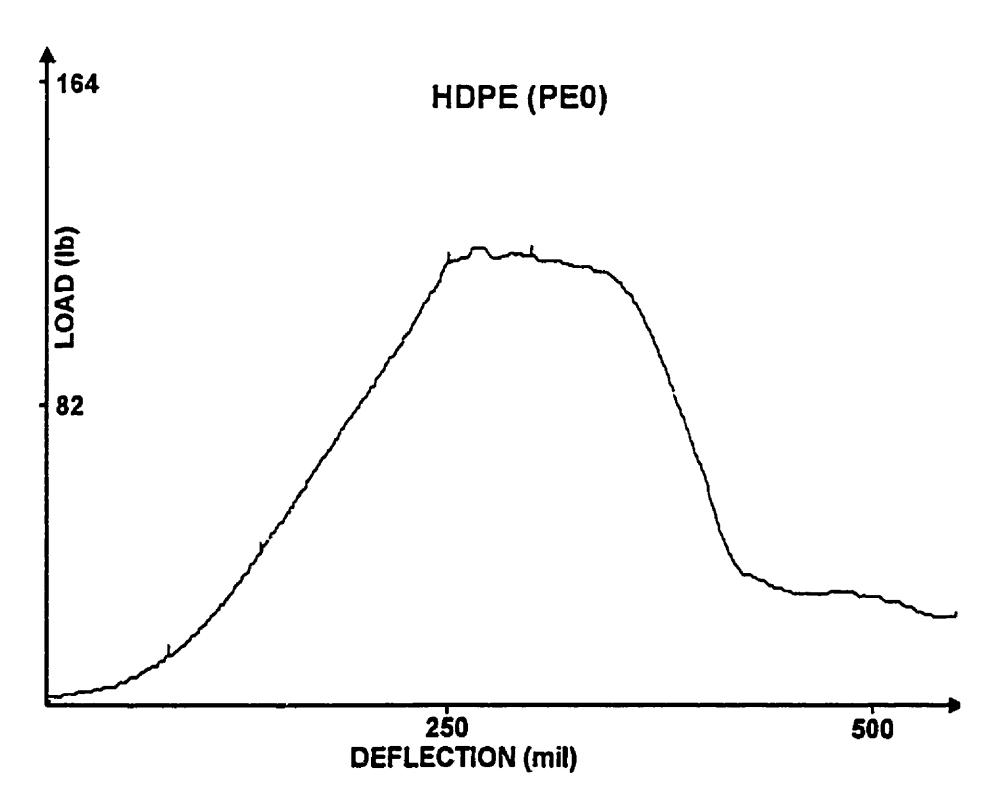
Appendix F Typical Load-Displacement Curves of Individual Resins and Blends

Appendix F XXV

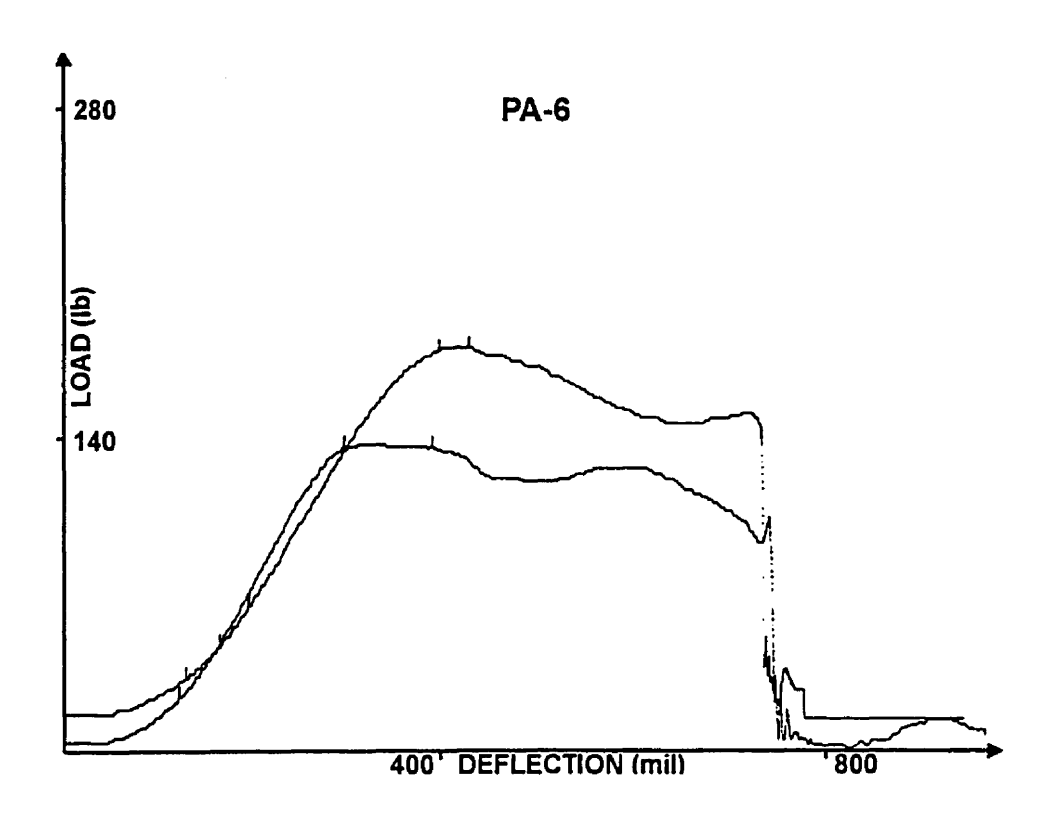


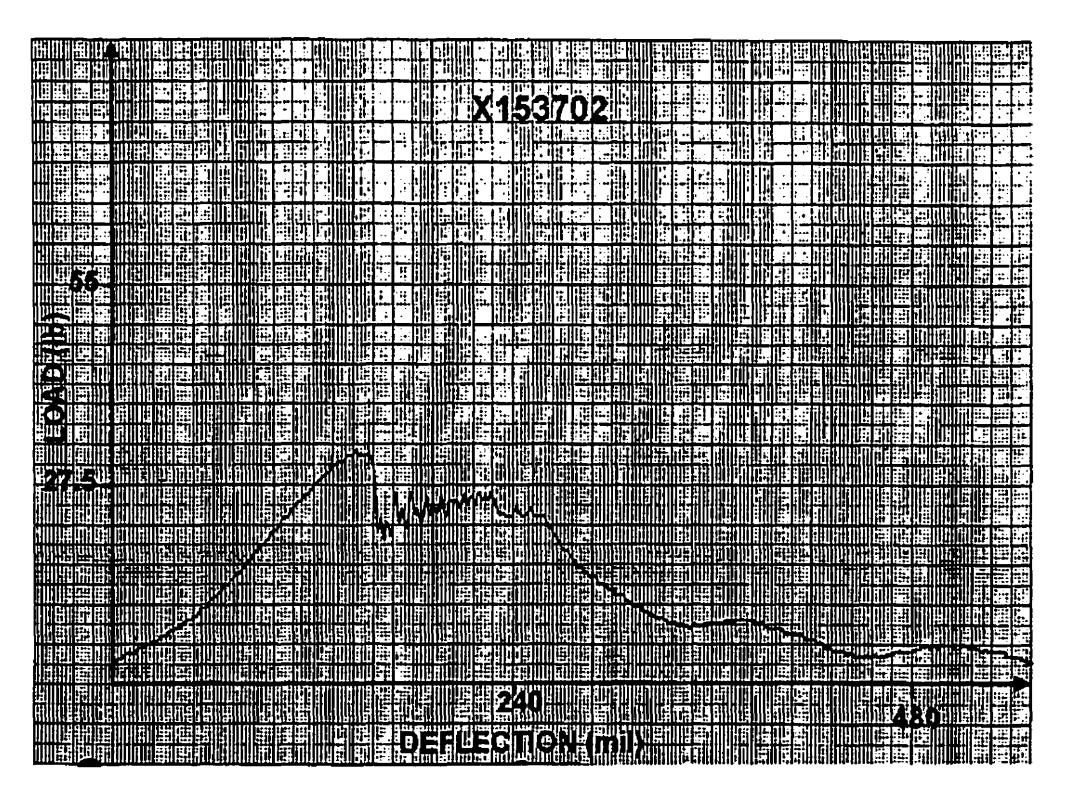






XXVII





Appendix F XXVIII

